Department of Naval Architecture, Ocean and Marine Engineering

University of Strathclyde

Investigation and Improvement of Wells Turbine Performance- Fluid Analysis & 2nd Law of Thermodynamics Study

Ahmed Samir Shehata

A thesis presented in fulfilment of the requirements for the degree of Doctor of Philosophy

January 2017

Declaration

I hereby declare that this thesis and all material contained herein is a record of work carried out in the Department of Naval Architecture, Ocean and Marine Engineering of Engineering Faculty, University of Strathclyde during the period from April 2013 to January 2017.

This thesis is the result of the author's original research except where otherwise indicated. It has been composed by the author and has not been previously submitted for examination, which has led to the award of a degree.

Signed: Date:

Acknowledgements

This thesis would not have been possible without the support and help of a great number of people, and it is impossible to properly acknowledge everyone who made this work possible. First of all, I gratefully acknowledge my sincere veneration and indebtedness and express my profound gratitude and deep respect to my primary supervisor, Dr. Qing Xiao, for her valuable guidance, suggestions and encouragement throughout all phases of this research work. It is also a great honour and privilege for me to work with her and to share her valuable knowledge and expertise. I have been extremely lucky to have such a supervisor who was always present to respond to my questions and queries so promptly. I would also like to give my deepest thanks to my secondary supervisor, Prof. Sandy Day, for his valuable support and help during my studies.

I express my sincerest gratitude to Dr. Samir Shehata for his patronization, guidance and support during my preparation for this doctoral study.

I also wish to pay my gratefulness to Dr. Khaled Saqr for his encouragement and suggestions. He taught me how to be a better researcher.

I am grateful to Prof. Amr Ali Hassan, Dean of College of Engineering and Technology, Arab Academy for Science, Technology and Maritime Transport, for his continuous support and valuable suggestions during my research work.

I would like to thank Dr. Mohamed M. Selim for his kind support and guidance during my Ph.D. study.

I am also grateful to Prof. Mohamed Shehadeh, Dr. Mohamed Anany, and Dr. Ashraf Sharara for their patronization, guidance and support.

I would like to take this opportunity to express my gratitude to my colleagues Eng. Amr Ibrahim, Dr. Mohamed N. El-Shaib, Dr. Islam Amin and Dr. Wendi Liu for their kind guidance and support during my Ph.D. study.

I would like to thank Mrs. Thelma Will and Mrs. Susan Pawson, the department's research secretary, for their kind assistance and support. I would like also to thank Mrs. Carole Muir, Senior Credit Control Assistant, University of Strathclyde for her kind support.

I would like to thank the Department of Naval Architecture, Ocean and Marine Engineering, Faculty of Engineering, University of Strathclyde. I always feel lucky to be a student of such a great department.

I would like to thank my external examiner, Dr Manosh C Paul, and my internal examiner, Dr. Tahsin Tezdogan, on their time and effort to review my thesis.

I am indebted forever to my parents for their support in all respects. I wish to acknowledge with love my wife's support, encouragement and patience

Finally, the financial assistance from the Arab Academy for Science and Technology and Maritime Transport (AASTMT) is greatly appreciated; without this help and support, this work would not have been possible. AASTMT provided me with the proper education and research experience during my B.Sc. and M.Sc. studies which gave me the qualifications and the capabilities to perform this Ph.D. level work.

Publications

- **Ahmed S. Shehata**, K.M. Saqr, M. Shehadeh, Q. Xiao, A.H. Day, Entropy Generation due to Viscous Dissipation around a Wells Turbine Blade: A Preliminary Numerical Study (Energy Procedia, 50 (2014) 808-816)

- **Ahmed S. Shehata**, K.M. Saqr, Q. Xiao, M.F. Shehadeh, A. Day, Performance analysis of Wells turbine blades using the entropy generation minimization method (Renewable Energy, 86 (2016) 1123-1133)

- **Ahmed S. Shehata**, Q. Xiao, K.M. Saqr, D. Alexander, Wells turbine for wave energy conversion: a review (International Journal of Energy Research, 41 (2017) 6-38)

- **Ahmed S. Shehata**, Q. Xiao, M.N. El-Shaib, A. Sharara, D. Alexander , Comparative analysis of different wave turbine designs based on conditions relevant to northern coast of Egypt (Energy (2016)- In Press)

- **Ahmed S. Shehata**, Q. Xiao, K.M. Saqr, D. Alexander, Improvement of the performance of air turbine for wave energy conversion using first and second law analysis (under review in Ocean Engineering)

- **Ahmed S. Shehata**, Q. Xiao, D. Alexander , Enhancement of performance of wave turbine during stall using passive flow control: first and second law analysis (under review in Renewable Energy)

- **Ahmed S. Shehata**, Q. Xiao, D. Alexander , Improvement of aerodynamic performance of axial turbines for wave energy extractor (under review in Applied Ocean Research)

Abstract

There have been several attempts to establish efficient methods to convert the energy of marine waves into electrical power. Wells turbine, with an Oscillating Water Column (OWC), is one of such methods. Wells turbine is the most common type of self-rectifying air turbine employed by OWC wave energy devices due to its technical simplicity, reliability, and design robustness. Because Wells turbine is subject to early stall, which negatively limits its performance, there were many endeavours to improve the energy extraction performance of Wells turbine within the stall regime. However, those endeavours were based only on the first law of thermodynamics analysis, without relying on the second law analysis. Since the second law of thermodynamics is concerned with the generation rate of entropy and accordingly the useful work, it is important to take the entropy generation rate into account while improve the performance of Wells turbine.

The main objective of this thesis is to analyse and improve the performance of Wells turbine under sinusoidal wave based on the entropy generation minimization method for various passive flow control technique parameters. To achieve this purpose, two-dimensional numerical models for Wells turbine aerofoils under sinusoidal wave flow conditions were built and used to investigate the single and multi-slots as passive flow control means. Different operating conditions with various design parameters were investigated. Furthermore, the turbine blade with optimum slots number, location and angle were investigated using the oscillating water system based on the real data from the northern coast of Egypt.

Firstly, in addition to the commonly used first law analysis, the present study utilized an entropy generation minimization method to examine the impact of the flow control method on the entropy generation characteristics around the turbine blade. The obtained results indicate that the global entropy generation rate has a different value according to the aerofoil design. It was determined that a certain aerofoil geometry always gives a

global entropy generation rate less than that of other aerofoil geometries under sinusoidal inlet velocity. Furthermore, the angle of attack radically affects the second law efficiency.

Subsequently, a comprehensive investigation was carried out on the passive flow control effect on the entropy generation as well as the torque coefficient. It was found that with the use of passive flow control, the entropy generation around the aerofoil section increases. On the other hand, torque coefficient of aerofoil increases before the stall happens and continues to increase within the stall regime. A significantly delayed stall is also observed with the use of the passive flow control. Moreover, aerofoils with two, three and four slots were investigated to improve the performance of Wells turbine in the stall regime. The optimum slots number and locations were determined based on minimizing the global entropy generation rate in addition to increasing the torque coefficient. Furthermore, the optimum angle for single slot aerofoil was confirmed to provide a lower global entropy generation rate as well as a higher torque coefficient than the zero angle slot before and after the stall.

Finally, from the modelling results, it can be concluded that the operating conditions based on real data for the northern coast of Egypt are very suitable for the oscillating water column system with Wells turbine as a wave energy converter. Moreover, by adopting the optimum slots number, location, and angle, the performance of Wells turbine can be significantly improved for a wide range of operating conditions.

Contents

List of Tables

List of Figures

Nomenclature

A	Total blade area (m^2)
A_r	Rotor area $=\pi R_m^2$ (m^2)
a	Margin distance for the endplate (m)
b	Blade Span (m)
c	Blade chord (m)
C_D	Drag force coefficient $= \frac{D}{\frac{1}{2}\rho(V_r)^2 A}$
C_L	Lift force coefficient $= \frac{L}{\frac{1}{2}\rho(V_r)^2 A}$
C_P	Power coefficient
C_T	Torque coefficient
D	Drag Force (N)
D_r	Rotor diameter (m)
D_{ss}	Suction slot diameter (m)
f	Cycle frequency (Hz)
F_A	Axial Force $= \frac{1}{2}\rho V_r^2 A C_A$ (N)
F_D	In-line force acting on cylinder per unit length (gf)
FD	The fluid domain
F_t	Tangential Force $= \frac{1}{2}\rho V_r^2 A C_t$ (N)
G	The filter function
g	Leading edge offsetting of a blade from an axis (m)
I	Moment of inertia (kg m^2)

K	Turbulent kinetic energy (J/kg)
KE	Kinetic Energy (J)
L	Lift Force (N)
L_{ss}	Suction slot location from leading edge in chord percentage %
L_{Rss}	Reference suction slot location from leading edge in chord percentage %
Δp	Pressure difference across the turbine (N/m^2)
P_{ss}	Suction slot pitch distance on x axis
ΔP_{ss}	Minimum distance between any two suction slot on x axis
Q	Flow rate through the rotor area (m^3/sec)
R_h	Rotor radius at hub (m)
R_m	Mean rotor radius $=\frac{R_t+R_h}{2}$ (m)
R_r	Rotor radius (m)
R_t	Rotor radius at tip (m)
S_{gen}	Local entropy generation rate (W/m^2K)
S_G	Global entropy generation rate (W/K)
S_{ij}	Mean strain rate (1/s)
S_t	Thermal entropy generation rate (W/m^2K)
S_V	Viscous entropy generation rate (W/m^2K)
t	Rotor blade thickness (m)
T_L	Loading torque (N m)
T_o	Reservoir temperature (K)

t_{sin}	The time period for sinusoidal wave $= {}^{1}/_{f}$ (second)
TSR	Tip speed ratio $= \frac{\omega Rm}{V_{Am}}$
$\bar{u}_i$	Reynolds Averaged velocity component in i direction (m/s)
V	Volume of a computation cell (m^3)
V_a	Instantaneous Velocity (m/s)
V_{am}	Highest speed of axial direction (m/s)
V_o	Initial velocity for computation (m/s)
V_r	Resultant air velocity $= \sqrt{V_A^2(t) + \omega^2(t)R_m^2}$ (m/s)
$\dot{W}$	The net-work transfer rate (W/s)
$\dot{W}_{rev}$	Reversible work (W)
W^*	Output power coefficient
X_i	Inertia coefficient
X_L	Loading torque coefficient $= \frac{T_L}{\rho\pi R_m^3 V_{Am}^2}$
Z	Number of blades
α	Angle of attack- the angle between the chord line and the direction of the fluid velocity ,degree
α_{SS}	Angle of suction slot (Degree)
η_F	The efficiency in first law of thermodynamics
η_S	The second law efficiency
μ	Viscosity (kg/ms)
μ_t	Turbulent viscosity ($N.s/m^2$)
ρ	Density (kg/m^3)
σ	Turbine solidity $= \frac{Z\,C}{2\,\pi\,R_m}$
∅	Flow coefficient

ω	Rotor angular speed (rad/sec)
$\bar{\omega}^*$	Non-dimensional angular velocity under irregular flow condition
$\left(-\overline{\rho u_i' u_j'}\right)$	Reynolds stress tensor

List of Abbreviations

CFD	Computational Fluid Dynamics
LES	Large Eddy Simulation
NACA	National Advisory Committee for Aeronautics
OWC	Oscillating Water Column
RANS	Reynolds Averaged Navier Stokes
TC	Tip clearance
2D	Two Dimensional
3D	Three Dimensional

PART I Introduction and Literature Review

Chapter 1 Introduction

1.1 Renewable energy and wave energy

Generating renewable energy has been increasing considerably in the past decade, achieving almost 22% of the global energy production in 2013, compared to 14% in 2005 (IEA, 2014). The ocean is a potential goldmine for renewable energy generation for several reasons, most important of which is that, unlike wind and solar power, power from ocean waves continues to be produced around the clock (Bogart et al., 2011). In addition, wave energy varies with the square of wave height, whereas wind energy varies with the cube of air speed. This results in a much higher average power production from waves per unit of time (DBEDT, 2002). Moreover, marine waves travel great distances without significant energy losses, therefore they act as a renewable and an efficient energy transport mechanism across thousands of kilometres. Such renewable energy can be produced through different devices, which produce sufficient work to drive electrical generators that convert such work into electricity.Wave energy extractors can be classified according to the water depth at which they operate. This classification is presented in Figure 1.1. Another classification based mostly on working principle is presented in Table 1.1.

Most of fixed-structure OWC systems are located on the shoreline or near the shore. Shoreline devices are characterized by relatively easier maintenance and installation, and they do not require deep water moorings and long underwater electrical cables. The floating OWC devices are slack-moored to the sea bed and so are largely free to oscillate, enhancing the wave energy absorption if the device is properly designed for that purpose (Mamun, 2006).

Offshore devices are basically oscillating bodies, either floating or fully submerged. They take advantage of the most powerful wave systems available in deep water. Offshore wave energy converters are in general more complex compared to fixed-

structure OWC. This, together with additional problems related to mooring and access for maintenance and the need of long underwater electrical cables, has hindered the converters' development, and only recently have some systems reached, or come close to, the full-scale demonstration stage (Cruz, 2008).

Overtopping systems are a different way of converting wave energy to capture the water that is close to the wave crest and introduce it, by over spilling, into a reservoir where it is stored at a level higher than the average free-surface level of the surrounding sea (Falcão, 2010, Twidell and Weir, 2006). The potential energy of the stored water is converted into useful energy through more or less conventional low head hydraulic turbines. The hydrodynamics of overtopping devices is strongly nonlinear and, unlike the cases of oscillating body and OWC wave energy converters, cannot be interpreted by linear water wave theory.

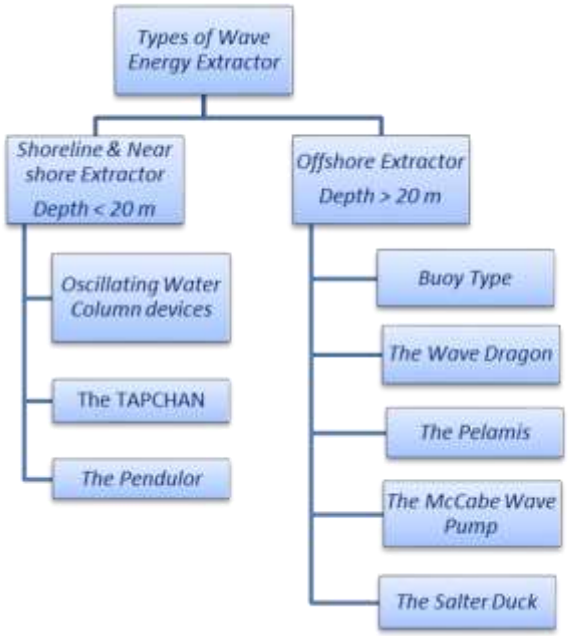

Figure 1.1 Types of wave energy extractors with respect to water depth

OWC energy converters operate much like a wind turbine via the principle of wave induced air pressurization (Marimuthu and Kirubakaran, 2014, Masters, 2004, Johnson, 2006). A containment housing (air chamber) is placed above the water, allowing the

passage of waves to change the water level. The frequently rising and falling water level increases and decreases the air pressure respectively within the housing. With regard to this notion, a turbine could be placed on top of the housing through which air may pass. Air would flow into the housing during a wave trough and out of the housing during a wave crest. Such an operation principle is illustrated in Figure 1.2**.** Because of this bidirectional air flow, the turbine must be designed to rotate only in one direction, regardless of the air flow direction (Rosa, 2012, Falcão, 2010, Twidell and Weir, 2006).

Table 1.1 Types of wave energy extractors based on working principle (Falcão, 2010)

System	Energy extractor	Structure types	Example	Remarks
Oscillating water column	Air turbine	Fixed structure	Pico	Isolated
			LIMPET	
			Sakata	Breakwater
			Mutriku	
		Floating	Mighty Whale	----------
			Sperboy	
			Oceanlinx	
Oscillating bodies	Hydraulic motor, hydraulic turbine and linear electrical generator	Floating	AquaBuoy	Essentially translation
			IPS Buoy	
			FO3	
			Wavebob	
			PowerBuoy	
			Pelamis	Essentially rotation
			PS Frog	
			SEAREV	
		Submerged	AWS	Essentially translation
			WaveRoller	Rotation with bottom hinged
			Oyster	
Overtopping	Low head hydraulic turbine	Fixed structure	TAPCHAN	Shoreline
			SSG	Breakwater
		Floating	Wave Dragon	--------

Finding an efficient and an economical means of converting oscillating flow energy to unidirectional rotary motion for driving electrical generators is the major challenge facing OWC systems. A novel solution for such a challenge is the Wells turbine (T. J. T. Whittaker, 1985b, T. J. T. Whittaker, 1985a, Whittaker, 1993a, Raghunathan, 1980, Raghunathan, 1995b), a version of the axial-flow turbine. Wells turbine is named after Professor Alan Wells of the Queen's University of Belfast in the 80's. It is unique as it contains a rotor with untwisted aerofoil blades of symmetrical cross section, usually belonging to the symmetrical NACA four digit series (Curran and M. Folley 2008, Falcão and Gato, 2012, Starzmann, 2012, Setoguchi and Takao, 2006), see Figure 1.3. A typical Wells turbine consists of a rotor with about eight aerofoil sectioned blades, installed on the hub with their chord lines lying in the plane of rotation. Once the blades have attained design speed, the turbine produces with a fair efficiency time-averaged positive power output from the oscillating air flow (Dixon, 1998, Mamun, 2006).

The Wells turbine is one of the simplest and probably the most economical turbines for wave energy conversion. It does not require rectifying air valves and can extract power at a low airflow rate, when other turbines would be inefficient. Therefore, it has been extensively researched and developed in many countries. Most self-rectifying air turbines for wave energy conversion proposed and tested so far are axial-flow machines of two basic types: the Wells turbine and the impulse turbine. The impulse turbine was patented by I. A. Babintsev in 1975 (IA, 1975). Its rotor is basically identical to the rotor of a conventional single-stage steam turbine of axial-flow impulse type. Since the turbine is required to be self-rectifying, there are two rows of guide vanes, placed symmetrically on both sides of the rotor, instead of a single row. These two rows of guide vanes are the reflection of each other, with respect to a plane through the rotor disc (Setoguchi T, 2000, T. Setoguchi, 2001, T. Setoguchi, 2004). Therefore, it is more complex and more costly than Wells turbine. The efficiency of Wells turbine is higher than that of the impulse turbine when the flow coefficient is less than the stall point. But after the stall point of Wells turbine, the efficiency of impulse turbine is considerably

higher than that of Wells turbine. However, the peak efficiencies are almost the same (Okuhara et al., 2013).

It is worth mentioning that the Wells turbine (with or without guide vanes) and the contra-rotating Wells turbine are approximately linear turbines (i.e., the pressure drop is approximately proportional to the flow rate at constant rotational speed). Other turbines behave quite differently (like impulse turbines) (Falcão and Gato, 2012).The principle of Wells turbine is explained in details next in this chapter.

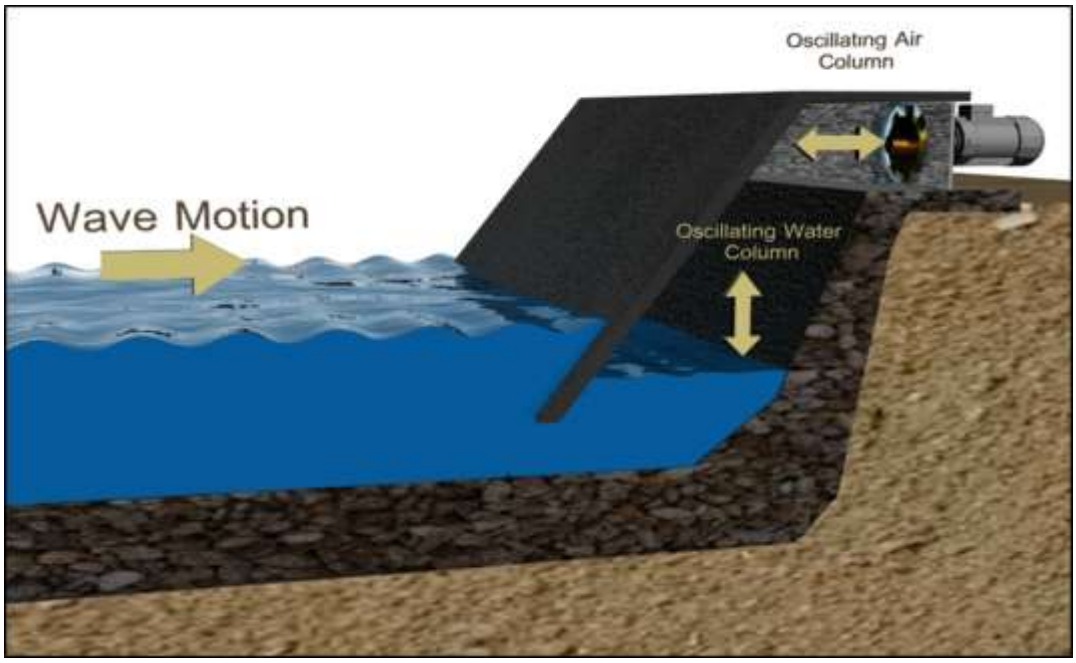

Figure 1.2 An illustration of the principle of operation of OWC system, where the wave motion is used to drive a turbine through the oscillation of air column

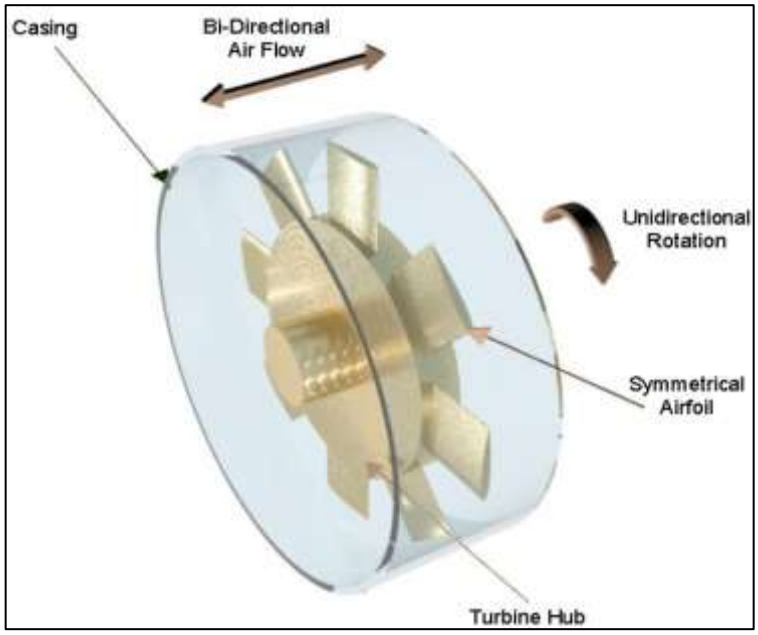

Figure 1.3 Typical structure of W-T rotor

1.2 Operation principle of Wells turbine

The distinguishing feature of Wells turbine is that oscillating air flow produces a single direction rotation of the rotor without the use of a rectifying valve. It is usually characterized by four digit double zero NACA profiles (SHERMAN, 1937, Sheldahl and Klimas, 1981, Raghunathan et al., 1981b), where the shape of the NACA four Digit profiles is determined by three parameters: the camber (first digit), the position of the camber (second digit) and the thickness of the chord in percent (last two digits). Hence, profiles without a camber are symmetrical (NACA 00XX). According to the classical aerofoil theory, an aerofoil set at α in a fluid flow generates L, normal to the free stream. The aerofoil also experiences D, in the direction of the free stream, see Figure 1.4 (a) and (b). For real fluids, Lift and Drag increase with the increase in α, however only up to a certain value of α beyond which the flow around the aerofoil separates. The angle of incidence at which the flow separates from the surface of the aerofoil is known as the stall angle (Wolfe and Ochs, 1997), see Figure 1.5. Further increase in α beyond the stall angle results in a decrease in lift and a significant increase in drag (Sheldahl and Klimas,

1981, Raghunathan, 1995b, Dixon, 1998). Because the flow between adjacent blades in cylindrical or liner series of blades (cascade) can be quite different to that over isolated aerofoils, the cascade lift and drag are different to those of isolated aerofoil due to the interference that each blade has on the flow field around its neighbours (Gareev et al., 2013, Weinig, 1964, Scholz, 1978).

1.2.1 Operation cycle

The operation cycle of Wells turbine is classified into two stages according to the action of the OWC. First, the Compression Stage, in which the water level rises inside the housing, see Figure 1.4 (a). The resultant aerodynamic force F_R due to lift and drag forces is given by

$$F_R = \sqrt{L^2 + D^2} \tag{1.1}$$

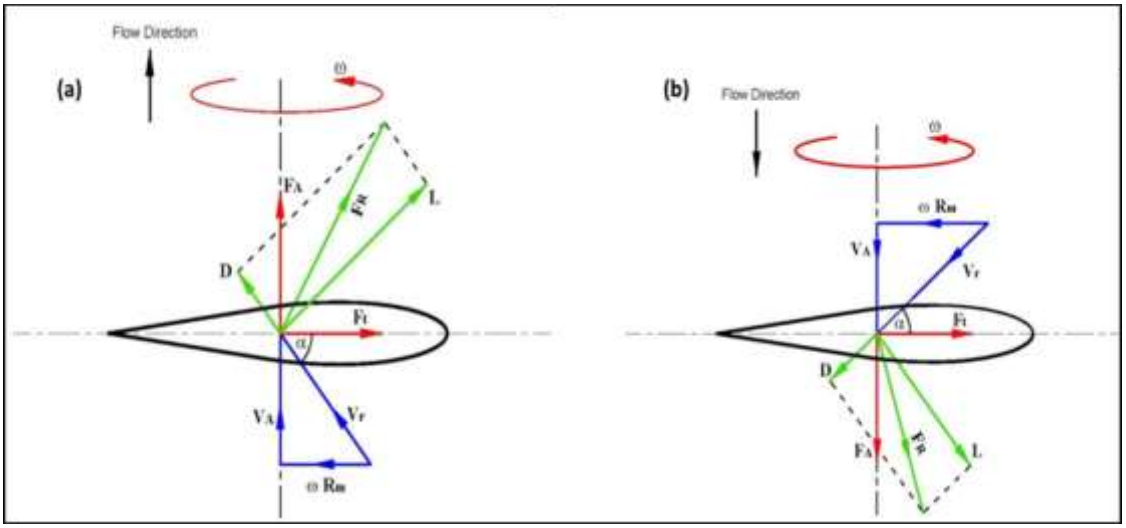

Figure 1.4 Aerodynamic forces in (a) compression and (b) suction stages

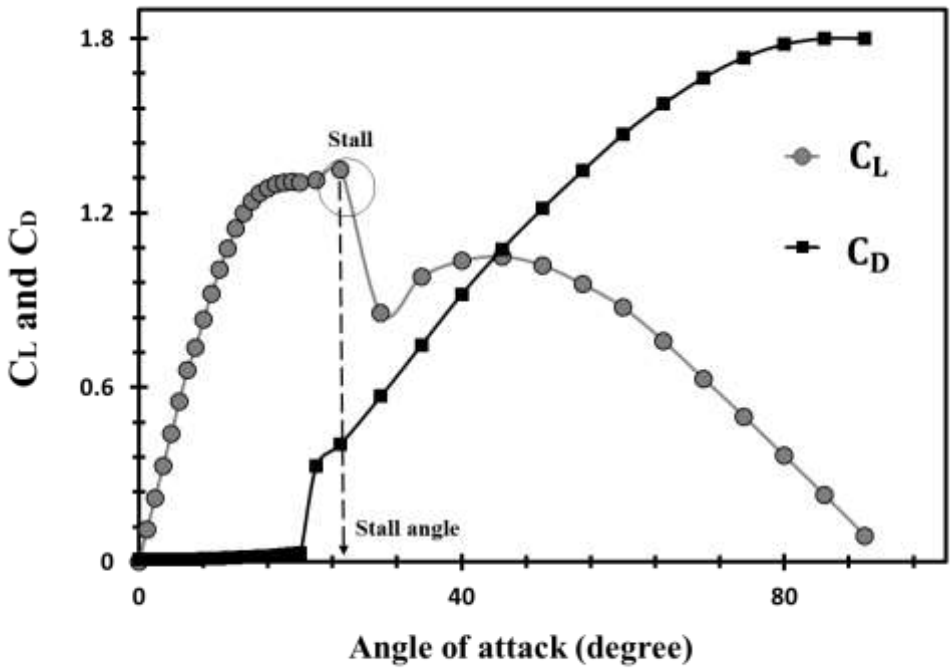

Figure 1.5 Lift and drag coefficient variation with angle of attack. Graph reproduced after (Sheldahl and Klimas, 1981)

This force can be decomposed in two components into the axial and tangential directions in terms of lift and drag components as:

$$F_A = L\cos\alpha + D\sin\alpha \quad (1.2)$$

and

$$F_t = L\sin\alpha - D\cos\alpha \quad (1.3)$$

where F_A and F_t are the axial and tangential forces, respectively.

Second, the Suction Stage - in which the water level drops, sucking air into the duct with a similar velocity and force analysis - can be described as shown in Figure 1.4 (b).

A comparison between Figures 1.4 (a) and 1.4 (b) shows that the tangential force maintains the same direction during the two stages, while the axial force reverses its direction. For a symmetrical aerofoil section, the direction of tangential force F_t remains the same for both positive and negative values of α. Such aerofoil blades are set around

an axis of rotation. The rotor rotates in the direction of F_t or upward and downward strokes, regardless of the direction of airflow.

There have been some studies citing the relevance of the radial force components. In such studies, it was assumed that the force resulting from the radial velocity component was far from being negligible (Torresi et al., 2009, Torresi et al., 2008, Torresi et al., 2011). Also, Falcao et al. reported that a fully three-dimensional force analysis should be performed, or at least corrections to two-dimensional flow results should be introduced. (Falcão and Gato, 2012). The vast majority of researchers assume that the force analysis resulting from the flow through the rotor can be reduced to a two-dimensional analysis (Mohamed and Shaaban, 2014, Mohamed and Shaaban, 2013, Mohamed et al., 2011, Thakker and Abdulhadi, 2007). This assumption is based on the Radial Equilibrium Theory (Csanady, 1964, Horlock, 1958) where the force resulting from the radial velocity component is assumed to be negligible everywhere in the flow field, except within the blade rows (Raghunathan, 1995b).

From the electrical power engineering point of view, the Wells turbine system can be seen as an AC/AC converter, which converts a mechanical power signal with variable force and frequency into an electrical power signal with constant voltage and frequency (Prado and Polinder, 2013). Wells turbine converts the bi-directional airflow into mechanical energy in the form of unidirectional shaft power, which is in turn used to move the wound rotor induction machine. The wound rotor machine controlled by rotor resistance has several advantages, such as high line power factor, absence of line current harmonics and smooth and wide range of speed control. As the external resistance is increased, the torque/slip curve becomes flatter, giving less speed, until the speed becomes zero at high resistance (Bose, 2002).

The squirrel cage induction generator is normally preferred since it is cheap, small, rugged, maintenance-free, and does not require separate excitation and synchronization to the grid. It works as a motor when running below synchronous speed, and as a generator above synchronous speed. However, the use of double-fed induction generator

has a huge potential in the development of distributed renewable energy sources. The double-fed induction generator is essentially an asynchronous machine, but instead of the rotor windings being shorted (as in a squirrel-cage induction machine), it is arranged to allow an AC current to be injected into the rotor, via the power converter. By varying the phase and frequency of the rotor excitation, it is possible to optimize the energy conversion. The frequency converter only has to process the generator's slip power fraction, which is generally no higher than 30% of the generator rated power. This reduced rating for the frequency converter implies an important cost saving, compared to a fully rated converter (Amundarain et al., 2010, Bose, 2002).

1.3 Evaluation of techno-economic aspects

The utilization of the sea wave was rarely considered on a practical scale prior to 1973. However, a great deal of research has been conducted since 1973, the year of the so-called oil crisis (McCormick, 2003). In recent years, interest has revived, particularly in Japan, Britain and Scandinavia, therefore the research and small-scale development have progressed to the stage of commercial construction for power extraction. As with all renewable energy supplies, the scale of operation has to be determined, and present trends support moderate power generation levels at about 1 MW from modular devices about 50 m wide across the wave front. Such devices should be economic to replace diesel-generated electricity, especially on islands (Twidell and Weir, 2006).

The predicted costs of wave power, in particular, have been falling against those of fossil fuels. The World Energy Council estimates that electricity from "arrays of mature devices located in promising wave energy sites" could cost from 5 cents to 10 cents per kilowatt-hour (kWh). In fact, the LIMPET, an on-shore oscillating water column device, began commercially generating electricity in Scotland in late 2000. At that time, the expected cost of Limpet's electricity was 7 cents to 8 cents per kWh (Alain Cle´ment et al., 2002). And according to the Electric Power Research Institute (EPRI), the cost of ocean electricity production will drop significantly as the volume of production increases, as usually happens in the development and commercialization of any new

technology. The electricity price produced from wave energy is still high but is forecasted to decrease with the development of the technology. This can be speeded up with initial financial and market support as it has been done in the past for preceding technologies such as wind, nuclear energy and oil.

Energy production costs are a major drive for the development of wave power – the lower they are, the faster the market grows. There are several levers to bring down costs of energy production systematically (Webb et al., 2005, Suzuki M, 2004, Jayakumar et al., 1993, VS et al., 1993), including, in order:

1- Reliability of the equipment: The degree of reliability of a wave power concept largely drives project risk and thus the rate at which an investor expects a new investment to earn. Therefore, reliability is an important key for the customer.

2- Efficiency of the machine: Costs per kWh are, in simple terms, discounted cash-outflows for capital investments, operations and maintenance, divided by discounted number of kWhs produced. Hence, an increase of energy output works on the total investment – not only the turbine – and can considerably bring costs down.

3- Reduction of capital investment costs: The largest cost item on an OWC plant is the collector. Bringing this cost down has a significant influence on energy production costs. Apart from creative engineering, the best idea is to avoid spending large sums on the collector by sharing it with other applications. This is how the idea of the active breakwater application was born.

For coastal protection, large concrete structures are built in order to protect harbours from waves. If these structures are modified so that OWCs can be included in the front wall, costs can be shared and, according to laboratory measurements, loads on the walls can be significantly reduced. For a caisson type breakwater, an empty concrete structure with a rectangular structure of concrete enforcement walls is cast. In this state, the structures are floating and can be towed into position by a ship. The empty chambers are then filled with stones or sand so that the structure can sink and sit rigidly on the seabed.

If the front chambers of the wall are only partly filled and openings under water are included, an OWC chamber can be formed (TV, 2007, Torre-Enciso et al., 2009). The Wells turbine is placed into the airflow. In this configuration, the breakwater is converted into an active breakwater, which not only protects the coast but also produces energy. Harbours usually require a high level of electrical energy and therefore offer good opportunities for grid connection. In effect, a fully integrated engineering development approach would appropriately design a shoreline OWC in order to find the best compromise between cost and performance. Following this path would lead to differences between a Wells turbine configuration, notably in terms of the OWC design and choice of location (Teillant, 2015). However, compared to Wells turbine, other types of wave energy converters are more expensive and have more complex designs.

1.4 Existing Wells turbine stations

Since the 1970s, there have been a number of wave energy projects based on Wells turbine. Table 1.2 provides a summary of all reported Wells turbine projects. The LIMPET (Boake et al., 2002, Whittaker, 1993b, Heath, 2002, Wavegen, 2002, Heath, 2000, Belfast, 2002) and Pico projects (Falcao, 1995, Falcao, 2000, Falcao, 1999, Falcao, 2003, Falcao, 2004, Falcao, 2002) are shoreline mounted systems. The OSPREY (Thorpe, 1995) is an example of near shore Wells turbine projects with the Trivandrum (Jayakumar et al., 1993, VS et al., 1993) and Sakata projects (Webb et al., 2005, Suzuki M, 2004) are examples of breakwater devices. In addition, the Mighty Whale is an offshore floating type (Y. Washio et al., 2000). These projects are necessary to the current understanding and improvement of Wells turbine technology and in many cases serve as test beds and data collection tools.

Several studies have investigated the overall performance of Wells turbine in existing shoreline installations with the aim of improving its efficiency. For example, the Wells turbine prototype installed in Islay, Scotland is investigated in (C.E.TINDALL and XU, 1996, Whittaker et al., 1997). The Vizhinjam OWC was installed in Trivandrum, India in 1991 and is investigated in (Jayashankar et al., 2000). Numerical simulation of

(Jayashankar et al., 2000) shows an increase of turbine output power for a numerical module with control mechanism (by varying the rotor resistance of the induction machine) as compared to an uncontrolled one, for the same variation of differential pressure (aerodynamic input, N/m^2). The performance of the contra-rotating Wells turbine installed in the LIMPET is compared to the predicted performance from theoretical analysis and model tests in (Folley et al., 2006). It is found that a contra-rotating Wells turbine has a lower efficiency than a biplane or monoplane Wells turbine with guide vanes. In addition, a contra-rotating Wells turbine requires an additional generator, or a gearbox.

Table 1.2 Summary of the existing Wells turbine projects

Devices	Location	Building	Output	No. of turbines	Diameter	Type of turbine
Sanze shoreline gully	Gully ,Japan	1984	40 kW	2	-NA-	-NA-
Kvaerner-Brug, Norwegian OWC	Toftestallen, Norway	1985	500 kW	1	-NA-	-NA-
Sakata, Japan	Sakata, Japan	1989	60 kW	1	1.337 m	Monoplane with guide vanes
Prototype OWC device (Raghunathan S. et al., 1995)	Islay, Scotland	1991	75 kW	2	1.2 m	Biplane
Vizhinjam OWC	Trivandrum, India	1991	150 kW	1	2 m	Monoplane
OSPREY	Dounreay, Scotland	1995	2 MW	4	3 m	Contra-rotating
Mighty Whale	Japan	1998	120 kW	1	1.7 m	Monoplane with guide vanes
The Pico Power Plant	Azores, Portugal	1999	400 kW	1	2.3 m	Monoplane with guide vanes
LIMPET	Islay, Scotland	2000	500 kW	2	2.6 m	Contra-rotating
Shanwei, Guangdong, China	Shanwei, China	2001	100 kW	1	-NA-	-NA-
Mutriku Wave Energy Plant (TV, 2007, Torre-Enciso et al., 2009)	Spain	2009	296 kW	16	1.25 m	Biplane

1.5 Motivations behind this work

Recent studies proved that entropy generation within various wave energy extracting systems plays a significant role in determining the overall efficiency of the system(Miguel and Aydin, 2011, Vosough and Sadegh, 2011). Thus, researchers must take into account the entropy analysis for the Wells turbine while investigating the wave energy extracting performance. The concept is to keep the entropy generation rate as low as possible in order to maximize the second law of thermodynamics efficiency of the system. The wave motion would be presented as a sinusoidal wave, which has accelerating and decelerating flows that creates the compression and suction cycles. The generated entropy value around Wells turbine varies according to the design of the turbine blade. Therefore, the entropy generation around Wells turbine aerofoil section must be studied using a flow analysis method. To the best of this author's knowledge, no study exists which analyse the entropy generation under sinusoidal flow around the aerofoil section (Chapter 5)

The entropy generation around the aerofoil section is always increasing with respect to time, however the increasing rate differs for different designs and operating parameters. Therefore, investigating Wells turbine performance must take into account the first as well as the second law of thermodynamics for different designs and operating conditions using flow analysis software (Chapter 5 and Chapter 6).

Many efforts have been made to improve the Wells turbine performance especially at the stall regime. On the other hand, one of the most popular methods that has been used to decrease flow separation around the aerofoil section and delay the stall is the flow control method. Current researchers are only investigating the aerofoil with the passive flow control methods, such as the suction and blowing slot under steady (non-sinusoidal) flow. It is important to investigate the passive flow control methods (e.g. the suction and blowing slot) which affect the entropy generation behaviour under sinusoidal flow. To the best of this author's knowledge, to date no specific unsteady CFD study of the slot

effect with sinusoidal flow on the entropy generation rate has been performed for Wells turbine (Chapter 6).

While improving the generated torque coefficient on the aerofoil section with the attached slot, it is equally important to accurately model the effect on the entropy generation and the second law efficiency. Therefore, it is essential that to investigate and define the optimum parameters (e.g. slots number, locations, and angle) for single and multi-slots based on the first and second law analysis. To the best of this author's knowledge, to date no study exists which define the optimum location, diameter and angle for single slot, in addition the optimum location and number for multi-slots attached to the aerofoil under sinusoidal flow inlet velocity based on the first and second law analysis (Chapter 6).

Wells turbine as wave energy extractor does not require high amount of crossing flow to operate at the maximum performance. The sea wave speed in Egypt is relatively low but stable, therefore Egyptian coastal sites are very suitable locations to extract wave energy via Wells turbine. The different sinusoidal wave frequencies are used to simulate the different real wave frequencies according to the summer and winter seasons. To the best of this author's knowledge, to date no specific study about the wave energy at Egyptian coastal via Wells turbine using the first and second law analysis has been performed (Chapter 3, Chapter 5 and Chapter 6).

1.6 Objectives and scope of thesis

As it is noted above, Wells turbine consists of a number of blades that have symmetrical aerofoil section. This aerofoil section under different conditions with various geometric parameters was investigated by other researchers to improve the overall system performance. Different methods were used to achieve this purpose, such as experimental, analytical and numerical simulation. CFD analysis is often used to investigate and analyse the flow around the aerofoil section which refers to the turbine blade. The force coefficients, such as torque coefficient and the entropy generation

value, are calculated and compared under different conditions with various design parameters by analysing the flow around the aerofoil section using CFD software, where the force coefficients are referring to the first law analysis and the entropy generation value is referring to the second law analysis. Therefore, in this work, CFD technique is used to study and link the first and second law analyses.

Most of the researchers investigated the performance of different aerofoil designs and different operational conditions where analysing the problem is based only on the parameters of first law of thermodynamics. It is essential to investigate at the second law of thermodynamics to form a deeper understanding. In this study, the entropy generation, due to viscous dissipation, around Wells turbine aerofoil sections under unsteady flow configurations was investigated.

The aim of this thesis is to analyse the entropy generation due to viscous dissipation around Wells turbine blade and to study the turbine performance for different operating conditions (the flow Reynolds number and the aerofoil angle of attack), blade designs (different aerofoils), and flow directions (sinusoidal wave cycle). Furthermore, this study also aims to minimize the entropy generation rate while increasing the torque output by means of several passive flow control methods.

The performance of Wells turbine at stall and near-stall conditions can be radically improved by using passive flow control methods, such as blowing or suction slots. This was achieved by conducting CFD based first and second law analyses for the Wells turbine aerofoil, without and with suction slots, under oscillating and non-oscillating flow conditions. Single-slot and multi- slots aerofoil geometries were created normal to the chord. These added slots take advantage of the pressure difference between the top and bottom surfaces and create suction and blowing effect, which delays the stall. Therefore, there is no need to generate any specific active suction or blowing within the aerofoil or the slots. Along with this design, there are two new aspects here: 1) improving the performance of Wells turbine in near-stall conditions, 2) applying the entropy generation minimization method to conduct the second-law analysis. An

investigation on the entropy generation, due to viscous dissipation, around turbine aerofoils for unsteady flow configurations was carried out. Apart from that, the effect of slots with different design parameters in oscillating (i.e. sinusoidal) flow is investigated, which is new compared to the unidirectional flow as in aerodynamics applications. Finally, the real data from the Egyptian coasts was used as a case study via investigating the first law analysis (torque coefficient) and second law analysis (global entropy generation rate) for different turbine aerofoils.

The objectives are summarized as follows:

1. Using the entropy analysis for Wells turbine blade as a performance indicator for different operating conditions, blade designs and flow directions.
2. Improving the performance and minimizing the entropy generation of Wells turbine in near-stall conditions using passive flow control methods, such as suction and blowing slots.
3. Studying the effect of the slots in the entropy generation under oscillating flow.
4. Optimizing the location and diameter for single and multi- slots as wells as slot angle, based on the entropy generation analysis.
5. Investigating the possibility of extracting wave energy from the Egyptian coasts (as a case study) using the oscillating water system based on the real data from the site.

1.7 Thesis Structure

This thesis has four parts, PART I provides a brief introduction to wave energy conversion and Wells turbine system through Chapter 1. It also provides the literature review in Chapter 2, which is concerned with the research directions and methodologies which aim at enhancing the performance and efficiency of Wells turbine. This chapter also provides a thorough discussion of the use of computational fluid dynamics (CFD) for performance modelling and design optimization of Wells turbine.

PART II includes the mathematical formulations, numerical methodology and the CFD verification and validation results that are used in this thesis. Both mathematical and

numerical methods used in this thesis are described in Chapter 3. Chapter 3 also contains force analysis, a discussion of the basic physical models for flows, a description of the turbulence modes used for the study. The starting and running characteristics were also investigated using the analytical analysis in this chapter. The CFD verification and validation are described in Chapter 4. This chapter includes the computational model and boundary conditions, grid sensitivity test and the validation of the numerical schemes results.

PART III of this thesis contains different case studies and results. The entropy generations, due to viscous dissipation, around Wells turbine aerofoils with unsteady flow configuration are carried out in Chapter 5. In this chapter, the entropy analysis for Wells turbine blade was studied with different terms such as operating condition, blade design and flow direction. In addition, the entropy generation minimization method was applied on the northern coast of Egypt, as a case study. In Chapter 6, the Wells turbine with passive flow control is presented. The entropy generation and the torque coefficient behaviour under the passive flow control method are shown. Also, the optimized location and diameter for single and multi-slots, in addition slot angle based on the entropy generation, are also presented.

Finally in PART IV, all the results from this thesis are presented in brief, and some conclusive recommendations are made for further extension of this research work. The references used in present studies are also provided at the end of this thesis.

1.8 Summary

The general perspectives, objectives and the structure of this thesis have all been presented in this chapter.

Chapter 2 Literature Review

2.1 Introduction

The objective of this chapter is to present a review of the various flow control such as (suction and blowing) and entropy analysis for conversion systems. This chapter also provides an updated and a comprehensive account of the state of the art research on Wells turbine. In particular, this chapter is concerned with the research directions and methodologies which aim at enhancing the performance and efficiency of Wells turbine. This chapter also provides a thorough discussion of the use of computational fluid dynamics (CFD) for performance modelling and design optimization of Wells turbine. Since this work is related to three aspects, flow control for aerofoil; entropy analysis for conversion systems and Wells turbine, the following sections are going to review them separately.

2.2 Flow control for aerofoil

Flow control can be defined as a process used to alter a natural flow state or development path (transient between states) into a more desired state (or development path; e.g. laminar, smoother, faster transients) (Collis et al., 2004). It could be more precisely defined as modifying the flow field around the aerofoil to increase lift and decrease drag. This could be achieved by using different flow control techniques such as blowing and suction, morphing wing, plasma actuators, and changing the shape of the aerofoil (Katam, 2005). All the techniques essentially do the same job, i.e. reduce flow separation so that the flow is attached to the aerofoil and thus reduce drag and increase lift. Flow control techniques can be broadly classified as active and passive flow control which can further be classified into more specific techniques (Gad-el-Hak et al., 1998). The terms “active” or “passive” do not have any clearly accepted definitions, but nonetheless are frequently used. Typically, the classification is based either on energy

addition, on whether there are parameters that can be modified after the system is built, or on whether the control system is steady or unsteady.

The science of effective flow control originated with Prandtl (1904), who introduced boundary layer theory, explained the physics of separation phenomena, and described several experiments in which the boundary layer was controlled. Prandtl also pioneered the modern use of flow control (Prandtl, 1904)- he introduced the idea of self-similarity, explained the mechanics of steady two-dimensional separation, and opened the way for understanding the motion of real fluids. Subsequently in the late 1950's, (Thwaites, 1949), (Stratford, 1959) and (Curle and S., 1957) defined the various methods for predicting laminar and turbulent boundary layers, which broadened the 'way' that was opened by Prandtl.

2.2.1 Passive flow control

Passive flow control is a flow control technique which does not require auxiliary power or energy to be added to the flow. Most common forms of passive flow control are modifying the wing geometry, aerofoil section for blade turbine, flaps on aircraft wings, and similar shape modifications, all to reduce drag and increase lift. The fundamental principle of this technique is boundary layer control, which most commonly involves suppression or delay of separation. Apart from the common forms and techniques, many other passive techniques have been successful in reducing skin friction in a turbulent flow, such as polymers, particles, and vortex generators which appear to act indirectly through local interaction with discrete turbulent structures; particularly small scale 5 eddies within the flow. Common characteristics of all of these passive methods are increased losses in the near-wall region, thickening of the buffer layer, and lowered production of Reynolds shear stress (Gad-el-Hak, 2001). Boundary layer control is divided into laminar separation control and turbulent separation control. With the advent of new technologies emphasis has been on reducing separation, thereby considerably increasing the lift to drag ratio. Numerous researchers have done extensive research in the field of turbulent separation control as the aerofoils in this region are used in the

general aviation industry. The main goal of laminar flow control is to increase lift and reduce drag by controlling separation or controlling the point of reattachment, or delaying the transition. There are many interdependencies in these control objectives as depicted by (Gad-el-Hak, 2000).

The criterion for transition to turbulence was studied by several researchers such as (Crabtree, 1958). Since turbulence was not fully understood, many approximate methods, based on semi-empirical theories for the criteria of turbulence separation, had been devised, such as the methods by (Thwaites, 1949) and (Maskell, 1958). The effects of compressibility on separation were also studied and tested by (Reshotko and Tucker, 1957), (Allen and Gerald, 1947) and (Stack, 1944). But all the analytical studies were limited to simple conditions and assumptions; hence the predictions did not agree with the experiments in most cases. Streamlining considerably reduces the separation by reducing the pressure rise. (McCullough and Gault, 1951) conducted their experiments on three different aerofoil sections NACA 63_3-018, NACA 63-009, and NACA 64A006 which have different thickness values and different leading edge radii. NACA 633-018 showed maximum lift when plotted with angle of incidence at Re = 5.8×10^6 when compared to other aerofoil sections. The maximum thickness and leading edge radius of NACA 63_3-018 were large when compared to the other two aerofoils and this made the transition to take place at minimum pressure point thereby increasing the lift. Laminar separation bubbles were seen in the other two aerofoil sections thereby decreasing the lift values when plotted with respect to the angle of incidence.

Experiments of (Meuller, 1982) also showed increase in the lift values for Eppler-61 aerofoil which has almost the same thickness as NACA 64A006 but is highly cambered. (Sunada et al., 1997) was performed research on the different aerofoil section characteristics by changing the parameters such as camber, thickness and roughness at a Reynolds number of 4×10^3. They deduced that low Reynolds number aerofoils have less thickness when compared to aerofoils with sharp leading edge at high Reynolds numbers. Optimal aerofoils at this low Reynolds numbers have a camber of about 5%

and maximum camber occurs at mid-chord. They also found that leading edge vortices play a major role in deciding the characteristics of these aerofoils.

It can be concluded that the streamlining greatly increases lift by reducing the steepness of the pressure rise and thickness is also one of the major factors effecting the separation. Furthermore, other passive approaches were tried, such as passive suction and passive vortex generators. The idea of passive suction is to use a passive porous surface (L. Bahi and Nagamatsu, 1983) (Savu and Trifu, 1984) to mitigate the local pressure gradients and obviate separation to reduce drag. The vortex generators (Taylor, 1948) use passive momentum adding to the near wall boundary to conquer the adverse pressure gradient, and this approach was widely used for aerofoil flow control (Pearcey, 1961) (Nickerson, 1986) (Bragg and Gregorek, 1987).

2.2.2 Active flow control

Active flow control is a scheme which involves energy expenditure and a control loop. Active technique is a special form of flow control technique which uses dynamic data during the control process and regulates the input parameters. While passive methods have played an important role in the early years of flow control and will continue to do so, these methods are usually limited to certain working conditions and are not always the best way of controlling the flow field. This calls for more advanced methods of flow control, i.e. active flow control, where the control parameters change dynamically with the change in flow field to augment favourable flow control. Suction, blowing, and synthetic jets are among the most common methods of active flow control techniques for high Re and for commercial and military aircraft. Morphing wings on the other hand are more common for low Re regimes.

(Gu et al., 1993) used leading edge suction on a delta wing to control the vortices. Experimental investigation of flow past a half delta wing at high angle of attack was performed using steady suction, steady blowing and alternate suction and blowing in the tangential direction along the leading edge of the wing. It was shown that this substantially retards the onset of vortex breakdown and stall. As a result of this type of

control, the vortex structure in the cross-flow plane is modified from a fully stalled condition to a highly coherent leading-edge vortex.

(Saeed and Selig, 1996) presented a generalized multipoint method for the inverse design of aerofoils with slot suction in incompressible potential flow. The design tool was validated against experimental data and was used interactively to perform rapid trade studies to examine the potential payoff for boundary-layer control as applied to the advanced-concept wings. Design changes in the aerofoil were proposed as a result of slot injection.

(Wright and Nelson, 2001) was conducted wind tunnel experiments to optimize distributed suction for laminar flow control. The experiments involved reducing the energy consumption to perform suction, without compromising on drag reduction. A large (2 m chord length and 1.6 m span) aerofoil model was tested at various angles of attack. The effect of pressure gradient on the efficiency of suction was observed, and a relationship between transition and drag was also presented.

(Wong and Konstantinos, 2006) performed experimental investigation of span-wise blowing at different positions (0%, 25% and 100% of chord length) on a NACA 0012 aerofoil. Lift, drag and pitching moment were measured for a range of angles of attack (from -20 degrees to +20 degrees) and at Re 1.25×10^5. It was experimentally proved that lift was considerably improved as a result of blowing at 0.25c as compared to the baseline (no blowing) case.

(Greenblatt and Wygnanski, 2000) provide an excellent review of the various periodic excitation methods, mainly steady suction and blowing. This review gives a detailed discussion of the mechanism and also the recent developments in the field. Previous reviews that provide a detailed discussion of the subject include (Bushnell and McGinley, 1989), (Fiedler and Fernholz, 1990), (Gad-el-Hak and Bushnell, 1991), (Moin and Bewley, 1994), and (Gad-el-Hak, 1994).

Synthetic jets, in general, consist of an enclosed cavity with one side of the cavity having an opening or openings to the free-stream flow (Glezer et al., 1998). A synthetic, or zero-mass, jet derives its name from the total mass flow into and out of the cavity. During the first phase of the jet's operation, entrained fluid is drawn into the enclosed cavity. This same fluid is then expelled through the opening back into the free-stream flow. Therefore, the net mass through the cavity opening is zero. However the net momentum transferred into the fluid is non-zero which enables flow control. Candidate designs of synthetic jets include piezoelectric ceramics (Smith and Glezer, 1998), fluidics (Glezer, 1999), and linear and rotary electromechanical motors (McCormick et al., 2001). Experimental studies (Gilarranz and Rediniotis, 2001), (Gilarranz et al., 1998) and designs are actively carried by the Georgia Institute of Technology and Texas A&M University.

Synthetic jets have been actively applied to separation control to generate virtual shapes on solid walls. They can efficiently provide periodic forcing for dynamic separation control and completely suppress the separation by sufficient momentum injection when oscillating at higher levels. The applications of synthetic jets are numerous, such as shear flow control using fluidic actuator technology and aerodynamic flow control of bluff bodies using synthetic jet actuators. The abilities of synthetic jets are so versatile that they also apply to other areas such as the mixing enhancement in combustion (Liang, 2004).

Perhaps the most influential work in synthetic jets has been performed at Georgia Tech by Glezer and colleagues. Their work was the first to characterize the basic performance of the synthetic jets and their ability to affect the flow over aerodynamic surfaces. Several papers (Coe et al., 1995), (Smith and Glezer, 1997), (Amitay et al., 1997) written by this group experimentally characterize the small-scale effects of synthetic jets. During their efforts, this group has employed several methods of experimentally measuring the flow field including phase-locked Schlieren imaging, hot-wire anemometry, and smoke visualization (Kiddy et al., 2000). In addition to characterizing the performance of a single synthetic jet, Smith and Glezer investigate the performance

of two adjacent synthetic jets (Smith and Glezer, 1997). Interestingly, they note that by phasing the timing of the jet actuation the direction of the resulting jet can be modified.

Morphing wing studies have been performed by various researchers in the past few years. This technique is most commonly used in regimes of low Reynolds number flights, such as the Micro Aerial Vehicles. Munday and Jacob (2002) experimentally investigated a wing with a conformal camber. The wing used an adaptive actuator mounted internally to alter the shape of the suction surface which resulted in a change in the effective camber by increasing the maximum thickness and moving the location of maximum thickness aft. They tested various oscillation frequencies at Reynolds numbers of 25,000 and 50,000 and several angles of attack. These oscillating modes showed a pronounced reduction in separation, hence the drag (Munday and Jacob, 2002).

(Kota et al., 2003) applied the morphing wing technology in designing morphing aircraft structures. Here, simple inputs are provided using actuators and the structures are deformed according to the input. In addition, these synthesis methods seek to optimize the stiffness of the structure to minimize actuator effort and maximize the stiffness with respect to the environment (external loading). (Martin et al., 2005) were performed experimental investigation of the technique. Using Combined Proper Orthogonal Decomposition and Linear Stochastic Estimation technique, they developed flow induced vibrations on the wing of the micro aerial vehicle.

2.3 Exergy and entropy analysis for energy conversion systems

Various thermal systems were assessed using advanced exergy analysis methods of this time. (Morosuk and Tsatsaronis, 2008) presented advanced exergy methodology and applied it to an absorption refrigeration machine. The concept of the advanced exergy analysis was explained, and the fundamental exergy terms were defined in this research. (Kelly et al., 2009) gave five different approaches to split exergy destruction into parts: approach based on thermodynamic cycles, engineering approach, exergy balance

method, equivalent component method and structural theory and malfunction/dysfunction analysis. In this text, a vapour compression refrigeration machine and an open cycle gas turbine system were evaluated by using the approach based on the thermodynamic cycles and the engineering approach. Two approaches were compared on the basis of the results obtained from a vapour compression refrigeration machine analysis. The approach based on thermodynamic cycles was concluded to be beneficial from the point of convenience and led to the best results for systems, which could be defined by thermodynamic cycles. The significance of the advanced exergy terms were highlighted in (Kelly et al., 2009), and the advanced exergy analysis of refrigeration machines using different working fluids was introduced. Also, the structural theory and malfunction/dysfunction analysis, which were described in detail by (Lozano, 1994), were categorized as limited to calculate endogenous and exogenous parts of the exergy destruction. In the end of the paper, for the improvement of the refrigeration machines, the evaporator and the compressor are emphasized for consideration.

An approach to splitting exergy destruction within an electricity generation and LNG (liquefied natural gas) system into parts was discussed in another work (Tsatsaronis and Morosuk, 2010). The paper covered splitting the exergy destruction within each component into its unavoidable, avoidable, endogenous and exogenous parts as well as a detailed splitting of the avoidable exogenous exergy destruction. As a result of the study, some suggestions for improvement of the examined system were proposed. LNG refrigeration system was evaluated in terms of the advanced exergy methodology (Tsatsaronis G. and T., 2010). In the paper, a more efficient operation of a three-cascade refrigeration system for LNG purposes was explained from the viewpoint of thermodynamic principles. Thus, locations of the irreversibility within the system were revealed by splitting exergy destruction into endogenous/exogenous and avoidable/unavoidable parts. (Morosuk and Tsatsaronis, 2011) dealt with exergy destruction within a gas turbine-based LNG regasification and electricity generation facility. The advantages of the advanced exergy analysis were stated while the

interactions among components and splitting exergy destruction within system components into parts were demonstrated in the paper.

The advanced exergy-based evaluation of the same system was presented in (Morosuk T., 2012). The performance, economic and environmental aspects of the system were proven based upon avoidable and unavoidable exergy destruction parts. Within this scope, the potential for improving the thermodynamic efficiency and reducing the overall cost and the overall environmental impact were determined. (Petrakopoulou et al., 2012b) applied the advanced exergy theory to a combined cycle power plant to present exergy destruction partition within the system. Most of the exergy destructions in the system components were found to be unavoidable, and it was identified with the internal technological limitations of the components. A refrigeration machine using a Voorhees' compression process was evaluated by (Morosuk et al., 2012) with the aid of advanced exergy methods. The detailed exergy destruction analysis of the Voorhees' compression process, which was commonly analysed on the basis of the first law of thermodynamics, was discussed in this paper. In this way, the limitations of the energetic analysis for such a complex process were demonstrated. In (Petrakopoulou et al., 2012a), the environmental analysis of a near-zero emission power plant was performed based upon results obtained from the advanced exergy analysis. The environmental impacts of each component of the system were split into avoidable/unavoidable and endogenous/exogenous parts. With the purpose of minimizing the environmental impact of the plant operation, the avoidable part of the impact was aimed to decrease. The environmental impact was related to the unavoidable and endogenous exergy destructions of individual components as a result of the study. (Tsatsaronis et al., 2013) brought a new perspective to the thermodynamic inefficiencies in combustion processes by benefiting from the methodology of splitting the exergy destructions. Estimating the thermodynamic inefficiencies caused by each of the chemical reaction, heat transfer, friction and mixing parameters was discussed while addressing the benefits of the advanced exergy-based evaluation methods for the energy systems with combustion processes in the paper. Further applications of the advanced

exergy based analysis on various energy conversion systems can be found in (Mosaffa et al., 2014, Erbay and Hepbasli, 2014, Açıkkalp et al., 2014b, Vučković et al., 2014, Keçebaş and Hepbasli, 2014, Tan and Keçebaş, 2014, Açıkkalp et al., 2014a, Gong and Goni Boulama, 2014).

Entropy-based design and exergy analysis have been shown to identify the maximum theoretical capability of energy system performance in various applications. For example, it can provide component-level energy management to improve diffuser performance (Adeyinka O., 2005) and reduce voltage losses within a fuel cell (Naterer, 2006). Exergy analysis has been used to diagnose inefficiencies of power plants (Uche, 2006) and minimize the carryover leakage irreversibilities in a power plant regenerative air heater (Jassim, 2004) and many other power plant associated applications. These studies have shown exergy analysis to be very useful for improving a wide range of thermo fluid systems. Exergy analysis also provides a design tool for increased accuracy and a more efficient performance.

Thermodynamic aspects of renewables were investigated for sustainable development by Dincer and Rosen, and they explained relations between exergy and sustainable development (Dincer and Rosen, 2005). Arrangements to improve energy efficiency may reduce environmental impacts by reducing energy losses. Such activities have led to an increase in exergetic efficiency and a reduction in exergy losses. The most appropriate link between the second law and the environmental impact has been suggested to be exergy, in part because it is a measure of the deviation between the state of the system and that of the environment. The magnitude of exergy of the system depends on the states of both the system and the environment. This deviation is zero only when the system is in equilibrium with its environment (Rosen, 2002).

On the other hand, several recent studies have reported its crucial significance to the exergy and entropy analysis in the design and optimization of wind turbines. Baskut,O. (Baskut et al., 2011) have used the entropy and exergy analysis on wind turbine power plants and emphasized that it is a more efficient tool than energy analysis (i.e. first law)

for system performance assessment and improvement since it allows true magnitudes of the losses to be determined qualitatively. (Redha et al., 2011) have studied the performance of wind energy system and it was concluded that second law efficiency is more precise to describe the losses in the system. (Pope et al., 2010) used entropy analysis to compare the performance of a variety of wind power systems and concluded that exergy analysis was shown to allow a diverse range of geometric and operating designs to be compared with a common metric.

Through an energy and exergy analysis of the characteristics of wind energy, it was found that differences between energy and exergy efficiencies are approximately 20-24% at low wind speeds and approximately 10-15% at high wind speeds (Sahin et al., 2006a). Sahin and his co-authors (Sahin et al., 2006b) developed a useful exergetic analysis technique for determining the exergetic efficiency of a wind turbine. The technique utilizes the wind chill temperature associated with wind velocity to predict the entropy generation of the process. Better turbine design and location selection can be achieved with the aid of such exergy analysis.

Koroneos and his team (Christopher Koroneos et al., 2003) applied exergy analysis to renewable energy sources including wind power. But in this research only the electricity generation of wind turbines is taken into account. They concluded that while the wind speed changes between 5 m/s and 9 m/s, exergy efficiency changes between 35% and 45%. Exergy lost in rotor mostly. The (Xydis et al., 2009) implemented the exergy analysis methodology as a wind farm sitting tool. Rosen and his co-authors (Rosen et al., 2008) studied a new sustainability index as a measure of how exergy efficiency affects sustainable development. They took the role of exergy in increasing efficiency and sustainability and reducing environmental impact as subject, and they reached result: Exergy can identify better than energy the environmental benefits and economics of energy technologies. The results suggest that exergy should be utilized by engineers and scientists, as well as decision and policy makers, involved in green energy and technologies in tandem with other objectives and constraints. Ozgener and his team (Ozgener, 2006, Ozgener and Ozgener, 2007, Ozgener et al., 2009) performed a case

study on the exergy analysis of a wind turbine system (1.5 kW) located in Solar Energy Institute of Ege University (latitude 38.24^{o}N, longitude 27.50^{o}E), Izmir, Turkey. They reported that the exergy efficiency changed between 0% and 48.7% at different wind speeds according to a dead state temperature of 25^{o} C and an atmospheric pressure of 101.325 kPa considering pressure differences between state points. Considering temperature differences between state points exergy efficiencies were calculated to be 0-89%. (Ahmadi and Ehyaei, 2009) have studied exergy analysis recently on a wind turbine. Modelling entropy production, they concluded that entropy production is directly opposite to the energy production, also they revealed that exergy analysis is more powerful than energy analysis for energy systems.

The exergy and entropy analysis for Wells turbine has not been investigated yet, except (Shaaban, 2012), where exergy analysis is performed using the numerical simulation for steady state biplane Wells turbines. The upstream rotor has a design second law efficiency of 82.3%, although compared to the downstream rotor second law efficiency of 60.7% for the same system. Furthermore, a comparison of total entropy generation, due to viscous dissipation, between a suggested design (variable chord) and a constant chord Wells turbine is presented in (Soltanmohamadi and Lakzian, 2015). The detailed results demonstrate an increase in static pressure difference around new blade and a 26.02 % average decrease in total entropy generation throughout the full operating range. The authors in previous research are based on these thesis publications.

2.4 Performance parameters of Wells turbine

There are several factors that influence the design, hence performance, of Wells turbine (Falcão, 2010, Raghunathan, 1995b, Raghunathan, 1995a). The optimization and improvement of such parameters aim mainly at overcoming the existing disadvantages of the system. Typical Wells turbine systems show several well-known drawbacks: low tangential force, leading to low power output from the turbine; high undesired axial force; a relatively low aerodynamic efficiency; and a limited range of operation due to

stall. This section of the thesis aims at reviewing the efforts done to overcome such disadvantages and improve the performance by controlling the design parameters.

2.4.1 Guide vane

In a number of previous studies, it was concluded that the delay of stall onset contributes to improving Wells turbine performance. This delay can be achieved by setting guide vanes on the rotor's hub as illustrated in Figure 2.1.

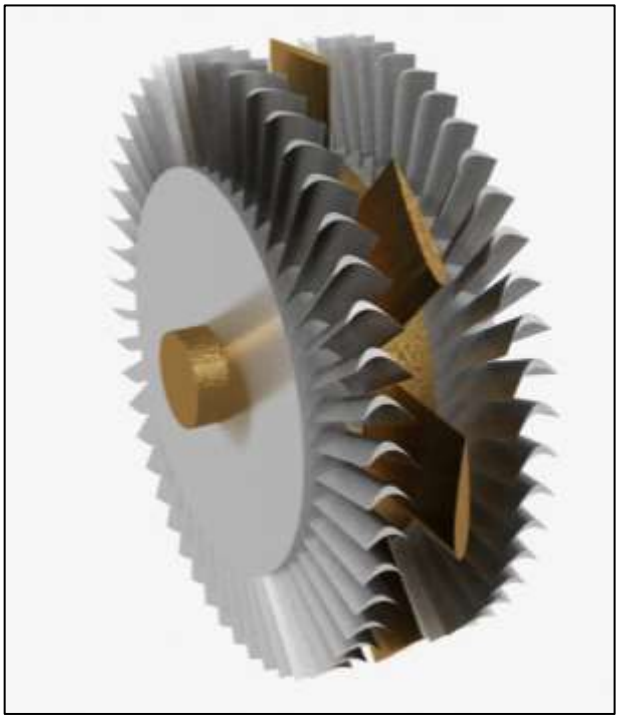

Figure 2.1 Illustration of guide vanes installed with Wells turbine rotor

The variables that affect the aerodynamic performance of a Wells turbine are discussed in (Raghunathan, 1995b, Raghunathan, 1995a), and it was found that the swirl losses at the turbine exit can be reduced by the use of guide vanes. Also, a multi-plane turbine without guide vanes was less efficient (approximately 20%) than the one with guide vanes. By testing a Wells turbine model under steady flow conditions, and using the computer simulation (quasi-steady analysis), a comparison between Wells turbines having 2D guide vanes and 3D guide vanes is conducted (Setoguchi et al., 2001, Takao et al., 2001). It showed that the 3D case has superior characteristics in the running and

starting conditions. The results of mathematical simulations considering several aerodynamic designs of the Wells turbine are shown in Table 2.1 (Brito-Melo et al., 2002). Different guide vanes designs were compared and investigated analytically (Masami Suzuki and Arakawa, 2002), taking into account the turbine starting characteristics and efficiency in irregular wave conditions. Table 2.2 shows the best two designs, but for the total performance, G15N11S40 is recommended. R7N08N65 has rectangular blades, a solidity of 0.7, normal blades, 8 blades, and a TC (the gap between the casing and blade tip) of 0.65mm. The G15N11S40 has 1.5 solidity, 11 blades, and the axial spacing between rotor and guide vane =40mm.

Table 2.1 A summary of the performance data for the different turbines, (Brito-Melo et al., 2002)

	NACA0015		HSIM 15-262123-1576 (Gato, 1996)	
Max. Efficiency	Without guide vanes	with guide vanes	Without guide vanes	with guide vanes
	58%	71%	55%	67%

Table 2.2 Maximum efficiency with minimum torque and starting torque coefficients (Masami Suzuki and Arakawa, 2002)

Turbine Profile	Maximum efficiency	minimum torque coefficient	starting torque coefficient
R7N08N65 G15N11S40	44.8%	0.41	0.49
R7N08F65 G15N21S31	47.4%	0.08	0.33

2.4.2 Hysteretic behaviour

As shown in Figure 2.2, due to the reciprocating flow, the performance of the Wells turbine has a hysteretic loop in which the values of C_A and C_T in the accelerating flow are smaller than those in the decelerating flow. Hysteresis characteristics are produced

by the pressure difference induced by the different behaviour of wakes between an accelerating flow and a decelerating flow in the same angle of attack, as illustrated in Figure 2.2.

A considerable number of parametric studies, using experimental and numerical approaches, are presented in (Raghunathan, 1995b). It is found that the hysteresis effects are caused by asymmetry in the boundary-layer development on the blade surface and oscillating motion of the wake, the extent of which can be appreciable at low Reynolds numbers. Hysteresis effects are found to be directly proportional to the turbine solidity (Raghunathan, 1995b) and blade thickness (Setoguchi T, 1998) and insensitive to blade AR and surface roughness (Setoguchi T, 1998). These effects can be smaller on large-scale turbines, where the boundary layer on the blades is turbulent and relatively thin. A CFD model of Wells turbine is used to investigate the hysteretic behaviour in (Tae-Hun Kim et al., 2002).

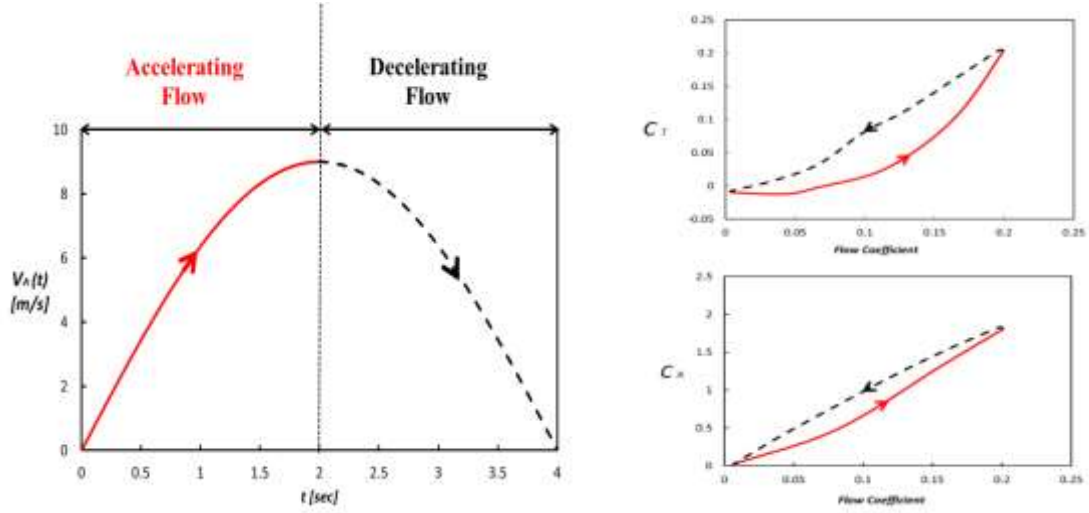

Figure 2.2 Typical Hysteresis loop obtained in the Wells turbine for one-half cycle of the sinusoidal flow in the unstalled condition. Graph reproduced after (Mamun, 2006)

The blade angle of attack is also found to be directly proportional to the hysteretic effects. In order to investigate the mechanism of the hysteretic behaviour of Wells turbine and also the effect of solidity, setting angles and blade thickness on the hysteretic behaviour of Wells turbine (where the setting angle is defined as an angle between the

blade chord line and the rotational direction of rotor, ωR_m), CFD simulations are conducted for the flow field around a blade of a Wells turbine by (Kim et al., 2002b, Setoguchi et al., 2003a). It is found that the mechanism to change the vortex intensity in the wake can be explained according to the vortex theorem. The vortex is intensified by the clockwise trailing shed vortices in the accelerating flow process, while it is suppressed by the counter clockwise vortices in the decelerating flow process. The hysteretic characteristics in sinusoidal flow are experimentally assessed in four kinds of turbines (NACA0020; NACA0015; CA9; and HSIM 15-262123-1576) in (Kinoue et al., 2003b, Setoguchi et al., 2003c). It is found that all turbines have similar hysteretic loops; however, the hysteresis characteristics of the Wells turbine are less sensitive to the blade profile than to solidity, setting angles and blade thickness.

Numerical simulations are conducted for the hysteretic behaviour of monoplane and biplane Wells turbines in (Kinoue et al., 2003a, Kinoue et al., 2004, Mamun et al., 2004). It is found that for the monoplane Wells turbine, the hysteretic loop is opposite to the well-known dynamic stall (Ericsson, 1987, CRIMI, 1972, McCroskey, 1980b, McCroskey, 1980a, Shida, 1987, Carr, 1988) of an aerofoil. The hysteretic behaviour is associated with a stream wise vertical flow appearing near the suction surface. For the biplane Wells turbine, the hysteretic behaviour is similar to that of the monoplane at lower attack angles. However, the hysteretic loop similar to the dynamic stall is observed at higher attack angles, which is attributed to unsteady flow separation near the hub and the trailing edge of the suction surface of the upstream blade. The magnitude of hysteretic loop is further decreased in the biplane turbine with staggered blades than in the one without stagger.

The effects of blade profile and rotor solidity on hysteretic behaviour of Wells turbine operating under bi-directional airflow have been experimentally studied in (Thakker and Abdulhadi, 2007, Thakker and Abdulhadi, 2008). It is shown that the size of hysteretic loop of pressure coefficient greatly decreases with the reduction in rotor solidity. Such characteristics are less sensitive to blade profile, as shown in (Kinoue et al., 2003b, Setoguchi et al., 2003c). However, the effects of the TC region cause a reduction of the

maximum torque coefficient and a decrease of the hysteretic behaviour (TORRESI et al., 2004). The effects of unsteady flow conditions on the performance of a monoplane Wells turbine without guide vanes during a field experiment on a OWC device are described in (Camporeale et al., 2011, Camporeale and Filianoti, 2009). The torque coefficient shows a hysteretic mechanism characterized by a counter-clock-wise loop that appears with high frequency oscillations. A dynamic stall phenomenon appears with oscillations of very large amplitude, independently from the frequency.

2.4.3 Multi-plane Wells turbine

For Wells turbine systems that operate at high pressure values, a multi-plane (usually tow stage) turbine configuration can be used. Such a concept avoids the use of guide vanes, and therefore the turbine would require less maintenance and repairs (Raghunathan, 1995b). The biplane Wells turbine, see Figure 2.3 (a) and the contra-rotating Wells turbine see, Figure 2.3 (b) are investigated to achieve this purpose.

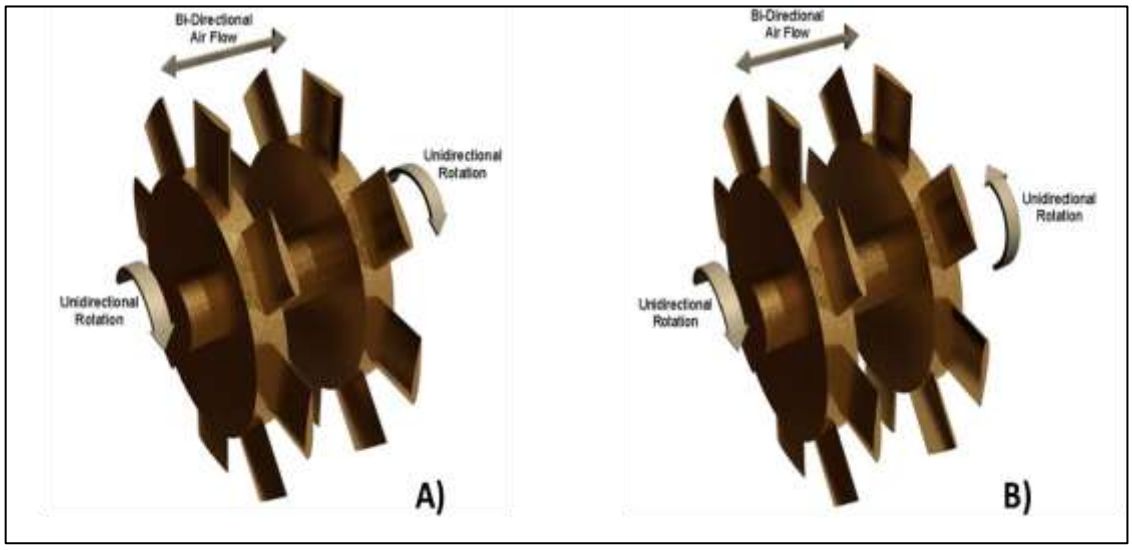

Figure 2.3 Multi plane Wells turbine (a) bi-planes Wells turbine (b) contra-rotating Wells turbine

The performance of a biplane Wells turbine is dependent on the gap between the planes, as shown in (Raghunathan, 1995b). A gap-to-chord ratio between the planes of 1.0 is recommended for the design of biplane Wells turbine in order to achieve high efficiency

in a limited space. A multi-plane turbine without guide vanes is less efficient than that with guide vanes but is relatively simple to design. A high solidity mono plane or a biplane Wells turbine is a simple configuration but has large kinetic energy losses due to swirl at the exit. Experimental results in (Gato and Curran, 1996) show that the use of two twin rotors rotating in the opposite direction to each other is an efficient means of recovering the swirl kinetic energy without the use of guide vanes.

The overall performance of several types of Wells turbine design has been studied in (Raghunathan and Beattie, 1996) and by using a semi-empirical method for predicting the performance in (Curran et al., 1998). Similar comparisons are undertaken using experimental measurements in (Gato and Curran, 1997). Monoplane, biplane, monoplane with guide vane and contra-rotating turbines viscous losses on the turbine rotors constitute the largest part of the losses. Therefore, the recovery methods have specific operational ranges. The contra-rotating turbine has an operational range that is similar to that of the monoplane turbine with guide vanes and achieves similar peak efficiency. However, the flow performs better than later in the post-stall region. The value of peak efficiency of contra-rotating turbine is higher than that of monoplane turbine without guide vane by 12% and by 9% for biplane turbine. It is also evident in (Gato and Curran, 1997) that the swirl component determines which rotor of a multi-plane turbine will stall first. On quite the contrary, investigated in (Folley et al., 2006) are use theoretical analysis and model tests to the predicted performance of the contra-rotating Wells turbine installed in the LIMPET, and it is found that a contra-rotating Wells turbine has a lower efficiency than that of a biplane or monoplane Wells turbine with guide vanes. In addition, a contra-rotating Wells turbine requires an additional generator, or a gearbox, to reverse the direction of rotation of one rotor.

Two-stage Wells turbines with symmetric and non-symmetric aerofoils have been investigated in (Mohamed et al., 2008). Numerical optimization procedure has been carried out to optimize the performance of the turbine as a function of the non-dimensional gap between the two rotors. It leads to an optimal value of the non-dimensional gap near 0.85 when simultaneously considering the request of maximum

tangential force coefficient, of maximum efficiency for the prescribed operating range (angle of incidence = 8 to 14 degree) and the needed size of the system.

2.4.4 Flow through Wells turbine

It is important to design a turbine that has as high operating aerodynamic efficiency as possible and is matched with the OWC system for pressure drop and flow rate over a wide range of sea conditions. For this purpose, many studies have investigated the flow through the turbine, see (Figure 2.4).

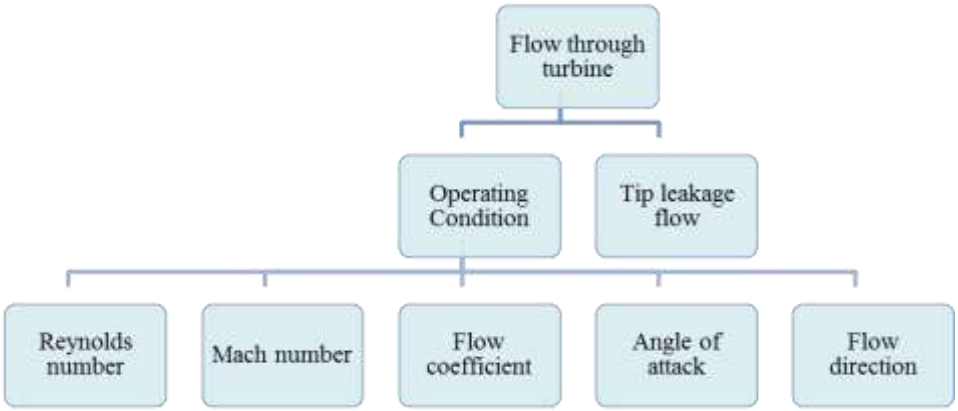

Figure 2.4 Flow over turbine parts and operating condition parameter

The basic principles and procedures for designing a Wells turbine for a wave energy power station are described in (Raghunathan, 1995a). The aerodynamic efficiency increases with flow ratio up to a certain critical value, after which it decreases. In order to avoid transonic effects, the maximum Mach number on the blades should be less than the critical Mach number. However, the critical Mach number decreases with an increase in incidence or solidity. Finally, the turbine maximum efficiency increases with an increase in Reynolds number.

The prediction methods and the variables that affect the aerodynamic performance of a Wells turbine are reviewed in (Raghunathan, 1995b). It shows that Wells turbine is less sensitive to inlet turbulence compared to conventional turbo-machines. The performance of a turbine in sinusoidal flow is better than that in a random air flow.

A computational model has been used in (Dhanasekaran and Govardhan, 2005) to study the performance and aerodynamics of the turbine, quantitatively and qualitatively. In addition, it is used to study the flow coefficient, turbine stalls and the appropriate inlet velocity profile. It is found from the computed results that the wakes behind the turbine blades (NACA0021) merge rigorously in the portion of Radius ratio =0.45:1.0, which leads the turbine to stall. The TC leakage flow is considerably higher in the trailing edge portion. However, as the flow coefficient increases, leakage flow region advances towards the leading edge, causing a large mass flow of air to leak through the gap.

The flow-field through a high solidity (σ = 0.6366) Wells turbine using blades with constant chord NACA0015 profiles is described in details in (Torresi et al., 2008). Separation at the outer radii has been detected for high values of the flow rate, which turns out to be induced by a radical shift of the mass flow through the turbine, mainly due to the cascade effect (Raghunathan et al., 1981b).

Numerical simulations have been performed to examine the flow-field through the turbine blades at different flow-rates in (Torresi et al., 2009). It is found that the flow separation at the tip is detectable by the presence of the pressure plateau along the suction side at coefficient = 0.238 and, more importantly, at coefficient = 0.257.
An analysis, based on the actuator disk theory (S. Raghunathan, 1987, L. M. C. Gato, 1984, Horlock, 1978), is presented, and results are compared with corresponding CFD simulations in (Torresi et al., 2011). It is illustrated that for low values of flow coefficient, flow separation occurs near the rotor hub rather than at the blade tip, consequently improving the global turbine performance.

Numerical simulations are performed in (Carija et al., 2012) to indicate that pressure and torque coefficients increase when the flow rate coefficient increases. Highest calculated efficiency of the Wells turbine in (Carija et al., 2012) is calculated to be around 60% for non-dimensional flow coefficient = 0.155. Operation of one OWC plant would produce 1850 kWh of energy per year for the assumed average sea regime data in the Adriatic Sea(Zorović et al., 2003). Experimental characterization of Wells turbine with

NACA0015 profiles submitted to a bi-directional flow is carried out, and the results are presented and analysed in (Paderi and Puddu, 2013). For several test conditions, the maximum efficiency (approximately from 0.3 to 0.43 for different test) of the turbine is always obtained for values of the flow coefficient between 0.19 and 0.21.

2.4.5 Design optimization

This subsection reviews different methods to optimize the design of Wells turbine in order to improve its overall performance: by changing in blade dimension or position, by adding plate on the blade or finally by creating a new blade shape, see (Figure 2.5).

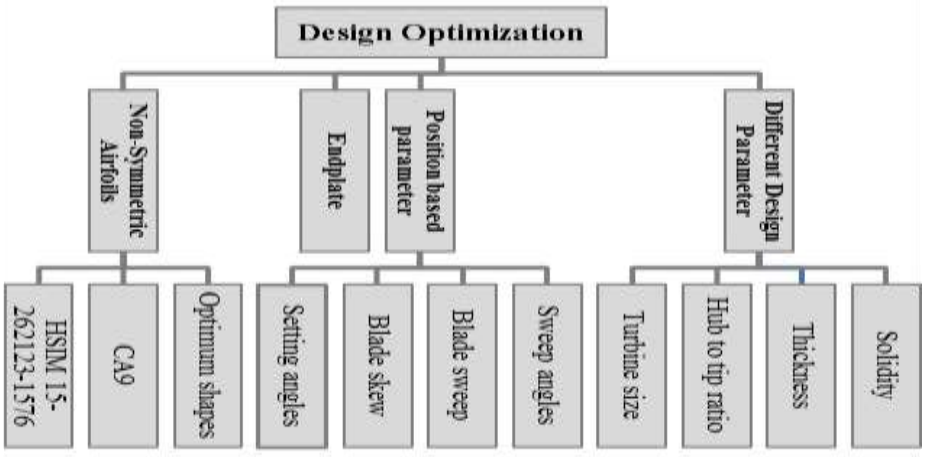

Figure 2.5 Design optimization parameter and sub parameter

2.4.5.1 Different design parameter for turbine

Various wind tunnel tests on NACA four-digit aerofoils in a tandem cascade with the angles of incidence ranging from 0 to 90 degree are described in (Raghunathan et al., 1981b). The increase in the blade thickness results in larger negative values of torque coefficient and has a favourable effect on starting.

The prediction methods and the variables that affect the aerodynamic performance of a Wells turbine are discussed in (Raghunathan, 1995b, Raghunathan, 1995a). A large solidity is needed for the turbine to be self-starting. It is advisable to choose a thicker

profile for small-scale turbines and a thinner profile for a large-scale turbine. Values of hub-to-tip ratio approximately equal to 0.6 are recommended for design. The ability of a 3-D CFD method to predict the effect of solidity on the performance of a monoplane Wells turbine has been tested by (Watterson et al., 1997). Calculations of the effect of solidity on turbine performance are predicted both qualitatively and quantitatively, and the effect of clearance is qualitatively correct. The operational matching of the performance of the turbine is used as the premise in achieving an optimal design configuration and sizing. The range and frequency of power bands presented to the turbine over long periods of time are in (Curran, 2008), which results in a 5% improvement in power output with the optimal size of the turbine required to be slightly larger than the average pneumatic power rating would suggest.

2.4.5.2 Position based parameter

The change in the position of blade according to the hub centreline through different parameters (sweep angle, blade sweep, blade skew and setting angles) has a direct effect on the performance of turbine.

2.4.5.2.1 Sweep angle, blade sweep and blade skew

An experimental work is presented to investigate and compare the aerodynamic performance of the backward swept, see Figure 2.6, and unswept angle blades for different rotor solidities (0.64 and 0.32) for 0 degree and 20 degree setting pitch angles in (Gato and Webster, 2001). Results for the 0 degree setting pitch angles have shown that the swept back angle blade produces a more positive value of efficiency and torque than that of the standard unswept blades but at the expense of peak efficiency. The experimental results show that this sweeping back angle has to be minimized in order to reduce its detrimental effect on the overall turbine efficiency.

The calculations of the blade sweeps for the Wells turbine, see Figure 2.7, with a numerical code by (Kim et al., 2002a) and experimentally with quasi-steady analysis in (Setoguchi et al., 2003c). As a result, it is found that the performance of the Wells

turbines is influenced by the blade sweep, and a suitable choice for the sweep ratio is 35%.

Figure 2.6 Backward sweep angle

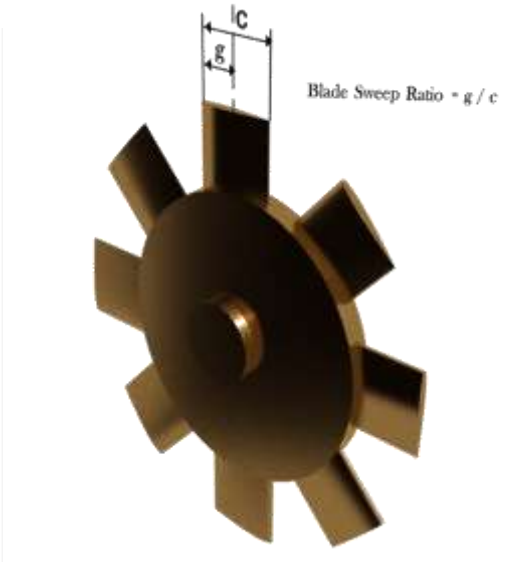

Figure 2.7 Blade sweep ratio

The effect of blade skew, see Figure 2.8, on the aerodynamic performance and associated aerodynamic noise is assessed in (Starzmann and Carolus, 2013a) by using both numerical simulations and experiments to develop an analytical blade design tool for Wells turbines, incorporating blade skew. Inception of stall inevitably causes an increase of specific sound power level by up to 20 db. The backward/forward blade skew delays the onset of stall and extends the turbine's range of stall-free operation by 106% of the baseline. The flow generated sound in unstalled operation was decreased up to 3 db by optimal backward / forward blade skew.

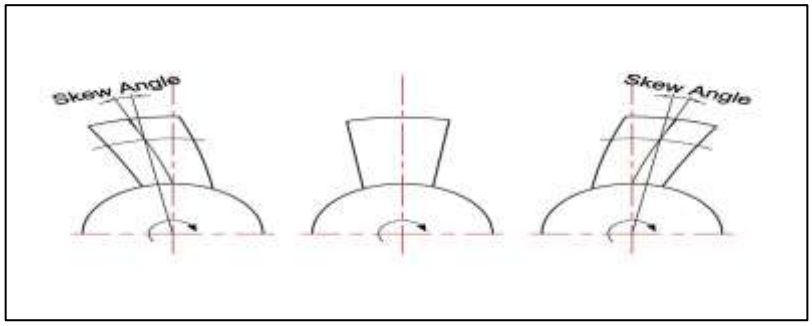

Figure 2.8 Blade Skew: left: backward skewed blade; middle: straight blade; right: forward skewed blade (Starzmann and Carolus, 2013a)

2.4.5.2.2 Setting pitch angles for blade

Setting the blades at their optimum pitch angle during compression and suction is expected to substantially improve Wells turbine efficiency (Inoue, 1989, Salter, 1993, Sarmento AJNA, 1987, Setoguchi, 1997, Takao, 1997a, Takao, 1997b, Vakalis IS, 2000, Thakker T, 2001). This is achieved by the turbine manufacturer in such a way to allow the turbine blades to rotate around their axis with an angle that equals ± optimum blade setting pitch angle.

The performance of Wells turbine using self-pitch-controlled blades taking real air flows to the turbine into account is clarified by (M. Takao and Lee, 2002). Experimental investigations and computer simulations using a quasi-steady analysis are performed on the optimum setting angle during suction, and it is found to be 6 degrees while the one during compression is found to be 10 degrees. A modified Wells turbine with setting angle has been investigated by model testing and numerical simulation in (Setoguchi et al., 2003b). It is found that the new turbine using rotor blades with a fixed setting angle is superior to the conventional Wells turbine, and that the optimum setting angle was 2 degrees for compression velocity amplitude to suction velocity ratios 0.8 and 0.6, in both with guide vanes and without guide vanes configurations.

A 400 kW variable-pitch Wells turbine is built to be tested in the Pico plant, Azores, Portugal alongside a fixed pitch Wells turbine of a similar rating (Taylor and Caldwell, 1998). It is hoped that the variable-pitch Wells turbine will demonstrate increased net

energy productivity. Therefore, the variable-pitch turbine should be able to demonstrate increased energy productivity compared to that of fixed-pitch machines. Moreover, the eddy-current pitch actuation system should provide responsive and energy efficient pitching, but it was never installed. The relatively modest efficiency of the Wells turbine, especially when operating in the compressor mode, severely limits the gains from reactive control.

A numerical optimization algorithm based on CFD simulation is implemented in order to optimize the blade pitch angle in (Mohamed and Shaaban, 2014). The standard NACA 0021 and AOP are numerically investigated. The present CFD optimization results show that the optimum blade pitch angle for NACA 0021 is +0.3 degree while that of the AOP equals +0.6 degree. The present aerofoils with the optimized pitch angle show an average efficiency improvement of 3.4% for standard NACA 0021 and 4.3% for the AOP.

A numerical optimization algorithm is implemented in this paper (Mohamed and Shaaban, 2013). The CFD optimization results show that the optimum blade pitch angle for NACA 0021 is 0.3 degree while that of the optimized blade equals 0.6 degree. Up to 2.3% improvement in NACA 0021 turbine efficiency and 6.2% improvement in AOP efficiency are achieved.

2.4.5.3 Endplate

In order to improve the performance of the Wells turbine, the effect of end plate, see Figure 2.9, on the turbine characteristics has been examined in (Mamun et al., 2006, Takao et al., 2007). Using an experimental model and a CFD method shows that the optimum plate position was a forward type. Also, the peak efficiency increases approximately 4% as compared to the Wells turbine without an endplate.

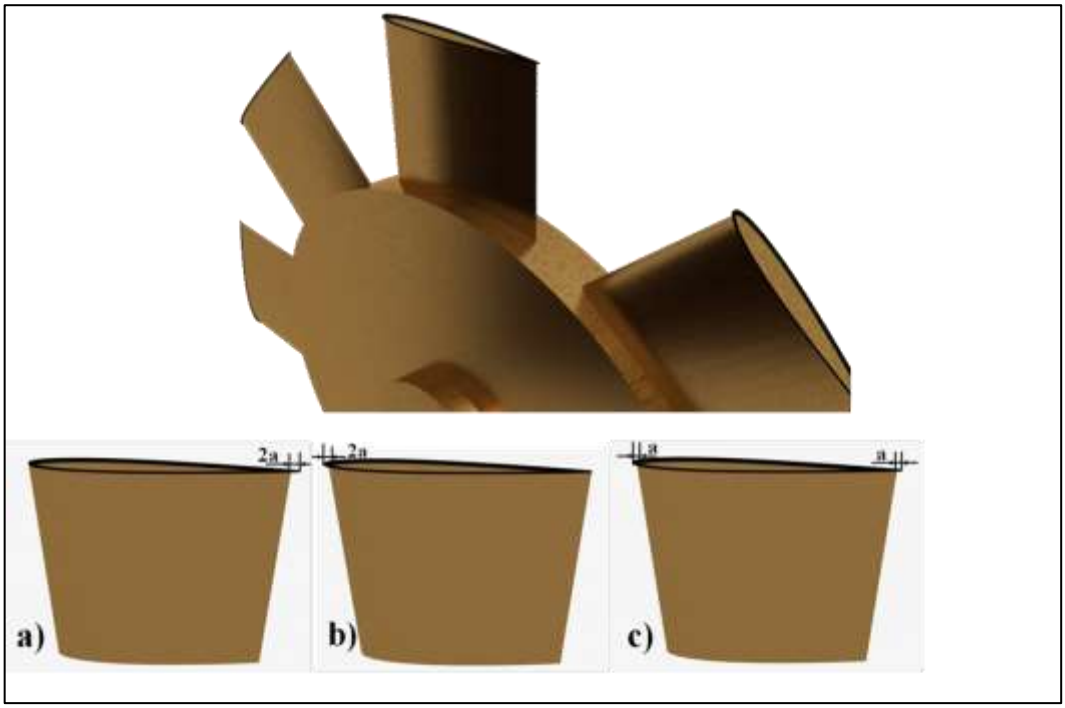

Figure 2.9 Rotor blade with end plate a) backward type; ; b) forward type c) middle type

2.4.5.4 Non-Symmetric aerofoils

A methodology for numerical simulation of a CA9 rotor Wells turbine is presented in (Thakker et al., 2001). Researchers have stressed the use of traditional symmetrical NACA series blades until they developed an optimized profiles: CA9, which has the same thickness as NACA0015 and is optimized in terms of the leading edge radius, maximum thickness position and trailing edge slope (Thakker et al., 2000a, THAKKER et al., 2000b). It shows superiority over a standard NACA0015. A maximum efficiency of 70% is obtained, and the overall computed performance related to reasonable qualitative agreement with experimental one. The calculations of the blade sweeps for the Wells turbine with the NACA0020 and the CA9 blades are carried out to clarify the performance with a numerical code by (Kim et al., 2002a). The overall performances for the NACA0020 blade are better than those for the CA9 blade. Generally, the blade thickness is thinner on NACA four digit series, while the maximum efficiency is higher and the stall margin deteriorates. However, both the maximum efficiency and the stall

margin for the NACA0020 blade in this calculation are better related to those for the CA9 blade.

Four kinds of blade profile are selected with regard to the blade profile of the Wells turbine in (Kinoue et al., 2003b, Setoguchi et al., 2003c, Takao et al., 2006). The types of blade profiles are as follows: NACA0020, NACA0015, CA9, and HSIM 15-262123-1576. The experimental investigations have been performed for two solidities (0.48 and 0.64) by experimental testing (steady flow conditions) and numerical simulation using a quasi-steady analysis (running and starting characteristics under sinusoidal flow). As a conclusion, NACA0020 is superior to other turbines (NACA0020; NACA0015; CA9; and HSIM 15-262123-1576) in the small scale model testing. For a large-scale Wells turbine operated at high Reynolds number, a suitable choice is the blade profile of NACA0015. However, the experimental investigations operating under sinusoidal and real sea conditions in (Thakker and Abdulhadi, 2007, Thakker and Abdulhadi, 2008) conclude that the preferred rotor geometry is CA9 blade profile, with rotor solidity 0.64.

Two-stage Wells turbines with symmetric and non-symmetric aerofoils have been investigated in (Mohamed et al., 2008), and the numerical algorithms are used to estimate the optimum shape with an increase of efficiency (by 2.1%) and of tangential force coefficient (by 6%), compared to the standard NACA 2421. An optimization process is employed in order to increase the tangential force induced by a monoplane Wells turbine in (Mohamed et al., 2011). A relative increase of the tangential force coefficient exceeding 8.8% (as a mean, 11.3%) is obtained for the full operating range. At the same time, the efficiency improves also by at least 0.2% and up to 3.2% (as a mean, 1%) compared to the standard NACA 0021.

2.4.6 Tip clearance

The gap between the casing and blade tip is a very effective parameter on the turbine behaviour. The effect of the flow around the tip is more significant in the process of turbine stall than that around the hub (Inoue, 1987, Raghunathan, 1991, Tagori, 1987).

The prediction methods and the variables that affect the aerodynamic performance of a Wells turbine are discussed in (Raghunathan, 1995a, Raghunathan, 1995b). The Wells turbine is very sensitive to TC when compared to conventional turbines. Therefore, values of a TC ratio less than 0.02 are recommended for design. The ability of a 3-D CFD method to predict the effect of TC on the performance of a monoplane Wells turbine has been tested in (Watterson et al., 1997). It is shown that as the TC increases, the performance of the turbine drops.

In order to examine the effect of the extent of the TC on the steady performance of the turbine, the results of numerical computations performed with different TC (1%, 5% and 10% of the chord length) and different flow conditions (0.15, 0.225, and 0.275) are illustrated in (Torresi et al., 2008). The stagnation pressure drop coefficient decreases when increasing the TC. On the other hand, the torque coefficient decreases when increasing the TC. In fact, the gap must be neither too small in order to avoid flow separation already existing at low values of the flow coefficient nor too large in order to avoid too small performance caused by small pressure drop through the turbine and large tip leakage flow. A comparison between numerical and experimental investigations is conducted in (Taha et al., 2010) for studying uniform TC ratio. Regarding turbine efficiency, it is found that the peak efficiency of the turbine decreases, and shifts towards a higher flow coefficient as the TC to chord length ratio increases, while the stall margin becomes wider.

The performance of a Wells turbine with various non-uniform TC is examined using CFD by (Taha et al., 2011). The performance of turbines with uniform and non-uniform TC is compared. It is shown that the turbine with non-uniform TC seems to have a preferable overall performance. CFD models based on the LIMPET OWC turbo generation section are studied in (Ahmed and Mueller, 2013) to investigate how airflow impingement created by a rotating turbine directly upstream increases the heat transfer away from an electrical generator, and also how this could be increased by adjusting the clearance between the turbine tips and shroud. As the clearance between the turbine tip

and shroud is reduced, the performance of the turbine in terms of torque and efficiency rises as does the heat transfer from the generator.

2.5 CFD models of Wells turbine

2.5.1 General description of the flow around Wells turbine

To the best of the author's knowledge, there are no published studies about the physics of oscillating flow around Wells turbine using laser techniques. It is difficult, therefore, to correlate the published CFD models of such flow physics in order to induce a universally valid description of all flow phenomena. However, there are some phenomena that do exist due to the nature of the oscillating flow behaviour as well as to the operational structure of the turbine. There are numerous experimental studies that were conducted using high-resolution measurement techniques, which studied oscillating flow (i.e. oscillating angle of attack) around stationary and moving aerofoil for aeronautic applications. Such a flow is similar to the oscillating flow around Wells turbine in the sense of the relationship between oscillating flow interaction with aerofoil wall. For a NACA-0012 aerofoil subjected to an oscillating flow of frequency 1.67 Hz at an average Reynolds number of $12x10^3$, it is found that the flow exhibits manifested vertical flow patterns (Koochesfahani, 1989). Such a study is conducted using Laser Doppler Velocimetry (LDV) and reports the presence of axial flow along the core of the vortices pattern, which complicates the vorticity field. Similar flow patterns for the same aerofoil are reported for a higher range of Reynolds number ($Re = 1\times10^5 \sim 2\times10^5$) and a lower frequency (0.188 Hz) (Berton et al., 2002). Hribernik et al. (Hribernik et al., 2012) demonstrated by PIV measurements that the separation region (i.e. bubble) generated on a generic aerofoil exhibits oscillations under oscillating angle of attack flow. They reported that the separation bubble oscillated around its mean position at an interval of 10% of the chord length. A similar oscillating behaviour of the separation bubble was reported using LDV measurements, and correlated to dynamic stall conditions of a NACA0012 oscillating aerofoil (Chandrasekhara and Ahmad, 1991). It was also reported that the flow near the leading edge wall, due to the oscillation of the separation

bubble, changes from a jet-like flow to a wake flow. These results were recently confirmed in (Sharma and Poddar, 2013) using PIV measurements of the flow around oscillating NACA0015 aerofoil for Reynolds number of $2x10^5$ and frequency of up to 0.5 Hz.

It is clear that the oscillating flow around Wells turbine is complex. The presence of strong vorticity field, as well as the dynamic behaviour of separation regions, can be easily confirmed by induction of similar flow phenomena in the absence of laser measurements of such flows in the time being. Streamline curvature around Wells turbine was also reported by means of numerical simulations (Gato and Falcao, 1988). These flow features impose certain critical limitations on the CFD models of Wells turbine, especially in terms of modelled boundary conditions and turbulence models.

2.5.2 CFD modelling goals of Wells turbine

Given the general operating conditions, air flow around and through Wells turbine can generally be considered an incompressible flow, where the mass conservation equation is given by:

$$\frac{\partial \rho}{\partial t} + \frac{\partial \rho \overline{u}_i}{\partial x_i} = 0 \qquad (2.1)$$

The Navier-Stokes equation, in conservation form, can be written as:

$$\rho \frac{\partial u_i}{\partial t} + \rho \frac{\partial}{\partial x_j}\left(u_j u_i\right) = -\frac{\partial p}{\partial x_i} + \frac{\partial}{\partial x_j}\left(2\mu s_{ji}\right) \qquad (2.2)$$

Where the strain rate tensor is $S_{ji} = \frac{1}{2}\left(\frac{\partial u_i}{\partial x_j} + \frac{\partial u_j}{\partial x_i}\right)$.

The modelling of turbulent flow through Wells turbine can be done by solving equation (2.2) directly on a computational grid with a number of cells in the order of $Re^{\frac{9}{4}}$ (Wilcox, 1998), which is computationally expensive if one considers rotor optimization

simulations. The other two approaches, which are computationally efficient, are either by solving the Reynolds Averaged Navier Stokes (RANS) using a Reynolds stress closure or by solving a filtered Navier-Stokes equation, or by using a hybrid approach that combines the previous two.

In fact, it is always difficult to decide which turbulence modelling approach to follow in CFD models. However, the consideration of the model essential objectives can be an excellent guideline to make such a decision. The ideal Wells turbine CFD model objectives can be summarized as follows:

1. To provide good prediction of the flow around the turbine so that the performance parameters such as forces, torque, efficiency, etc. can be computed.
2. To respond effectively to the changes in the design i.e. flow geometry so that different designs can be simulated for optimization purposes.

When these objectives are considered, the first issue to be discussed is model temporality. A large number of Wells turbine CFD models relied on solutions of the steady averaged Navier-Stokes equation (Torresi et al., 2008, Taha et al., 2011, Taha et al., 2010, Kim et al., 2002a). However, such models are only capable of providing average estimations of the turbine cycle relative to OWC. Models based on the unsteady solution of Navier-Stokes equation are numerous as well, mainly adopting uniform (i.e. sinusoidal) wave form on the boundary as an approximation of the irregular wave forms that exist in nature (Nunes et al., 2011, Thakker and Abdulhadi, 2008, Sefoguchi et al., 2004). Models based on irregular wave forms are relatively scarce in literature records (Maeda et al., 2001, Takao and Setoguchi, 2012), perhaps due to the complexity that irregular boundary conditions impose on the model solution convergence. The use of steady models can be acceptable for preliminary achievement of the first modelling objective. However, given the numerous design details, as shown in section 2.4, and their impact on the flow structure, the use of unsteady models is necessary to complete the first objective, and also the second one. Conservative sinusoidal approximation of irregular wave forms can be accepted for comparing design modifications or different

components between two systems. Conservativeness in this context refers to precautions related to the averaging of the frequencies, not just the amplitudes, of the complete irregular wave spectrum. However, to use CFD as a tool for econometric analysis of Wells energy systems, models based on irregular wave forms which emulate the actual wave properties in the potential installation sites should be considered.

2.5.3 Turbulence modelling considerations

The solution of equation (2.2) in turbulent flow regime requires an approach for modelling the viscous term of the equation. The adoption of Reynolds averaging, which yields the RANS equation, is the most common approach for such purpose. The RANS equation is:

$$\rho \frac{\partial U_i}{\partial t} + \rho U_j \frac{\partial U_i}{\partial x_j} = -\frac{\partial P}{\partial x_i} + \frac{\partial}{\partial x_j}\left(2\mu S_{ji} - \rho \overline{u'_j u'_i}\right) \tag{2.3}$$

The last term on the RANS of equation (2.3) is called the Reynolds stress term, often denoted as τ_{ji}. This term couples the turbulent fluctuations to the mean flow by assuming that such fluctuations generate additional stresses or produce momentum transport (Davidson, 2004). This term is the major problem of turbulence modelling since it requires to be solved in order to compute the mean flow field variables. However, to compute this term, additional equations are required. There are two major methods to provide closure for the Reynolds stress terms in the Navier-Stokes equation, as fully described in (Wilcox, 1994) and (Davidson, 2004). The first method is by taking the moments of the Navier-Stokes equation. This is achieved by multiplying the equation by a fluctuating property and performing time averaging for the resulting equation (Wilcox, 1994). This method leads to the development of second order closures, which include transport equations for all the components of the Reynolds stress term. This is called *Reynolds Stress Model*. The most common and well-tested form of such a model is the LRR (Launder, Reece and Rodi) model that was proposed in (Launder et al., 1975). The model is composed of one transport equation for τ_{ji},

dissipation rate and pressure-strain correlations, auxiliary relation for the production of τ_{ji} as well as model coefficients (Wilcox, 2006a). Although such a model predicts the anisotropic flow field by calculating the components of τ_{ji}, its numerical implementation always faces numerous challenges that make the results of such a model not as accurate as they are theoretically expected. These challenges are thoroughly discussed in (Piquet, 2013).

The second method of closure for the Reynolds stress term is the eddy viscosity concept. This concept is based on the work of Boussinesq, who postulated that the momentum transfer caused by turbulent eddies is analogous to the momentum transfer caused by the random motion of molecules (Boussinesq, 1877). A detailed explanation of the Boussinesq hypothesis is given in (Wilcox, 1994) and in a recent historical discussion presented in (Schmitt, 2007). The Boussinesq hypothesis dictates that the Reynolds stress is proportional to the mean strain-rate tensor and the constant of proportionality is the *turbulence* or *eddy viscosity* a scalar quantity often denoted as μ_t. According to such a hypothesis, the Reynolds stress term is given by:

$$-\rho\overline{u_i'u_j'} = \mu_t\left(\frac{\partial\overline{u}_i}{\partial x_j}+\frac{\partial\overline{u}_j}{\partial x_i}\right)-\frac{2}{3}\delta_{ij}\left(\rho k+\mu_t\frac{\partial\overline{u}_k}{\partial x_k}\right) \tag{2.4}$$

The most common turbulence models for engineering applications are based on the eddy viscosity concept. The eddy viscosity models are the most common class of turbulence models used in modelling Wells turbine. The following section explains some details about these models and their inherited physical assumptions.

2.5.3.1 Turbulent viscosity models

In order to solve equations (2.3) and (2.4), additional transport equations for calculating the turbulence scalars (i.e. turbulence kinetic energy, turbulence dissipation rate, etc.) must be solved. There are numerous models for different classes of turbulence flow that solve transport equations for such scalars. Each of these models has inherited physical assumptions that postulate limitations and restrictions on its implementation. The most

commonly used turbulence models in the CFD models of Wells turbine are the $k-\varepsilon$ models and $k-\omega$ models. The transport equations for such models can be found in (Wilcox, 2006a). Each class of these models computes turbulent viscosity via a specific scalar correlation. The following table (Table 2.3) shows different correlations for the most used eddy viscosity and the variables of each correlation.

Turbulent viscosity models are based on the assumption of isotropic turbulence, which means that these models inherently assume that the components of Reynolds stress tensor equally affect the mean flow in space. This assumption is coherent with Kolmogorov (1941) theory of turbulence (Frisch and Kolmogorov, 1995, Birnir, 2013). Hence, although the isotropy assumption might lead to an intuition that turbulence viscosity predictions should not be accurate, extensive numerical investigations utilizing these models have yielded successful predictions of complex flows. Examples on the success of eddy viscosity models in predicting different types of vorticity-dominated flow and flow with streamline curvature can be found in (Secchiaroli et al., 2009, Ridluan et al., 2007, Eiamsa-ard and Promvonge, 2007, Jochmann et al., 2006, Al-Ajmi et al., 1998, Zhang and Nieh, 1997, Sampath and Ganesan, 1982, Przekwas et al., 1983, Saqr and Wahid, 2014, Radwan et al., 2014, Saqr et al., 2012, Saqr et al., 2010).

Table 2.3 Eddy viscosity correlation for the most used turbulence models in the Wells turbine CFD models

Eddy viscosity correlation	Turbulence model	Notes
$\mu_t = \rho C_\mu \frac{k^2}{\varepsilon}$	Standard (Launder and Sharma, 1974) and RNG (Yakhot et al., 1992) $k-\varepsilon$	C_μ is an empirical constant, k and ε are the turbulence kinetic energy and its dissipation rate. C_μ values are 0.09 and 0.0845 for the standard and RNG models, respectively.
	Realizable $k-\varepsilon$ (Shih et al., 1995)	Where C_μ is not constant and given by: $C_\mu = \frac{1}{A_0 + A_s U^* \frac{k}{\varepsilon}}$, where A_0 =4.0; $U^* = \sqrt{S_{ij}S_{ij} + \Omega_{ij}\Omega_{ij}}$, $A_s = \sqrt{6}\cos\left(\frac{1}{3}\arccos\left(\sqrt{6}W\right)\right)$, $W = \frac{\sqrt{8}S_{ij}S_{jk}S_{ki}}{S^3}$, and the vorticity tensor is given by $\Omega_{ij} = \frac{1}{2}\left(\frac{\partial \overline{u}_i}{\partial x_j} - \frac{\partial \overline{u}_j}{\partial x_i}\right)$
$\mu_T = \rho \frac{k}{\omega}$	Wilcox original (Wilcox, 1988) and modified (Wilcox, 2006a)$k-\omega$	ω is the specific dissipation rate of turbulence kinetic energy

LES (Large Eddy Simulation) (Sagaut, 2005) provides an alternative approach in which the large eddies are computed in a time-dependent simulation that uses a set of filtered equations. Filtering is essentially a manipulation of the exact Navier-Stokes equations to remove only the eddies that are smaller than the size of the filter, which is usually taken as the mesh size. Like Reynolds averaging, the filtering process creates additional unknown terms that must be modelled in order to achieve closure. Statistics of the mean flow quantities, which are generally of most engineering interest, are gathered during the

time-dependent simulation. The attraction of LES is that: by modelling less of the turbulence (and solving more), the error induced by the turbulence model will be reduced (LESIEUR, 2008).

It is theoretically possible to directly resolve the whole spectrum of turbulent scales using an approach known as direct numerical simulation (DNS) (Tsinober, 2009). Basically, in LES, large eddies are resolved directly while small eddies are modelled. Solving only for the large eddies and modelling the smaller scales results in mesh resolution requirements that are much less restrictive than with DNS. Typically, mesh sizes can be at least one order of magnitude smaller than with DNS (Pozrikidis, 2009). Furthermore, the time step sizes will be proportional to the eddy-turnover time, which is much less restrictive than with DNS. In practical terms, however, extremely fine meshes are still required. It is only due to the explosive increase in computer powers that LES can be considered as a possibility for engineering calculations (Hoffmann and Chiang, 2000a, Hoffmann and Chiang, 2000b). However, the use of different turbulence models in Wells turbine models requires certain considerations to be made. Some of these considerations are related to the empirical coefficients in the eddy viscosity and turbulence transport equations (Speziale et al., 1992, Ekaterinaris and Menter, 1994). Other considerations are related to the suitability of each model to different flow regimes and configurations (Wilcox, 1993, Menter, 1994).

Due to the difficulty and the high cost of other methods, such as the experimental method, to make bidirectional flow with different operating conditions to study the flow of the hysteretic or of very sensitive and accurate areas such as tip area, the CFD method plays an essential role as evidenced in the research. A detailed summary of CFD studies of Wells turbine is given in Table 2.4.

Table 2.4 Detailed summaries of CFD studies of Wells turbine

Ref.	Turbulence model	Reynolds number	No. of Elements	Blade profile	Boundary Condition
(Watterson and Raghunathan, 1996)	*K-Epsilon* model together with a modified low Reynolds number model	$8\ 10^5$	449,736	NACA0015	3D-Unsteady
(Watterson et al., 1997)	*K-Epsilon* model together with a modified low Reynolds number model	$8\ 10^5$	436,000	NACA0015	3D-Unsteady
(Thakker et al., 2001)	RNG *K-Epsilon* model	$5\ 10^5$	80000	CA9	3D-Steady
(Tae-Hun Kim et al., 2002)	*K-Epsilon* model	-NA-	400,000	NACA0012, NACA0015, NACA0021	3D-Unsteady-(Time step = 0.001 sec- sinusoidal wave)
(Kim et al., 2002a)	*K-Epsilon* model with a modification model	Low Reynolds number	70,000 nodes	NACA0020, CA9	3D-Steady
(Kim et al., 2002b)	RNG-SGS model	$2.4\ 10^5$	560,000	NACA0015, NACA0020	3D-Unsteady-($f = 0.167$ - one-half period of the sinusoidal wave)
(Kinoue et al., 2003a)	RNG-SGS	$2.4\ 10^5$	560,000	NACA0020	3D-Unsteady-($f = 0.167$ - one-half period of the sinusoidal wave)
(Setoguchi et al., 2003a)	RNG-SGS model	$2.4\ 10^5$	560,000	NACA0020, NACA0015	3D-Unsteady ($f = 0.167$- sinusoidal wave)
(Kinoue et al., 2004)	large eddy simulation- RNG-SGS model	$2.4\ 10^5$	560,000 (monoplane)- 720,000 (biplane)	NACA0020	3D-Unsteady-($f = 0.167$ - half period of the sinusoidal wave)
(Mamun et al., 2004)	LES - RNG-SGS model	$2.4\ 10^5$	560,000 (monoplane)- 720,000 (biplane)	NACA0020	3D-Unsteady-(one-half period of the sinusoidal-)
(TORRESI et al., 2004)	K-Omega SST	539233	163840	NACA0015	3D-steady (Two sinusoidal wave-0.8 and 1.2 m wave height-2.275 and3.413 m/s axial velocity)
(Dhanasekaran and Govardhan, 2005)	*K-Epsilon* model	-NA-	620,000	NACA 0021	3D-steady

Table 2.4 (Continued)

Ref.	Turbulence model	Reynolds number	No. of Elements	Blade profile	Boundary Condition
(Mamun et al., 2006)	*K-Epsilon* model	From 1.0 10^5 to 3.8 10^5	560,000 and 580,000	NACA0020 with endplate	3D-Steady
(Takao et al., 2007)	RNG- *K-Epsilon* model	2.5 10^5	570,000	NACA0020 with endplate	3D-Steady
(Mohamed et al., 2008)	SST model	2.4 10^5	25600	(AOP) based on NACA 2421	2D-Steady
(Torresi et al., 2008)	Spalart Allmaras	-NA-	1 092 352	NACA0015	3D-Steady
(Torresi et al., 2009)	Spalart Allmaras, K-Omega SST	2 10^5	2 10^6, 2.4 $10^6$and 4.1 10^6	NACA0015	3D-Steady
(Taha et al., 2010)	Realizable *K-Epsilon*	From 0.74 10^5 to 4.41 10^5	295,500	NACA0020	3D-Steady
(Torresi et al., 2011)	k-SST model	From 34833 to 42199	4 10^6	NACA0015	3D-Steady
(Mohamed et al., 2011)	Realizable *K-Epsilon*	2.4 10^5	between 60,000 and 80,000	NACA 0021, (AOP)	2D-Steady
(Taha et al., 2011)	Realizable *K-Epsilon*	From 0.68 10^5 to 4.41 10^5	295,500	NACA0020	3D-Steady
(Carija et al., 2012)	Realizable *K-Epsilon*	-NA-	424686	NACA0021	3D-Steady
(N. Rostamzadeh, 2012)	SST transitional model	120000	3.5 10^6 (nodes)	NACA0021	3D-Unsteady (time-step = 5 10^{-5})
(Shaaban, 2012)	Realizable *K-Epsilon* model	-NA-	1,236,576	NACA0015	3D-Steady

Table 2.4 (Continued)

Ref.	Turbulence model	Reynolds number	No. of Elements	Blade profile	Boundary Condition
(Shaaban and Abdel Hafiz, 2012)	Realizable *K-Epsilon* model	-NA-	1,131,540	NACA0015	3D-Steady
(Ahmed and Mueller, 2013)	K-Omega SST	$1.4\ 10^5$- $2.8\ 10^5$	-NA-	NACA0020	3D-Steady
(Mohamed and Shaaban, 2013)	Realizable *K-Epsilon* turbulence model	$2.\ 10^4$	2D- 60,000, 80,000/3D-1,348,760/(AOP) 1,404,690	NACA0021, AOP	3D-2D-Steady
(Starzmann and Carolus, 2013a)	Standard fully turbulent shear-stress transport turbulence model	$5.0\ 10^5$	$1.8\ 10^6$	Hub: NACA0018-63/Midspan: NACA0015-63/Tip: NACA0012-63	3D- Steady
(Starzmann and Carolus, 2013b)	SST-turbulence model	$5.4\ 10^5$	1.8 million	Hub: NACA0021-63/Mid: NACA0018-63/Tip: NACA0015-63	3D- Steady
(Mohamed and Shaaban, 2014)	Realizable *K-Epsilon* turbulence model	$2.4\ 10^5$	60000–80000	NACA0021, (AOP)	2D-Steady
(Shehata et al., 2014)	Realizable *K-Epsilon* model	$6\ 10^4$- $4\ 10^5$	312951	NACA0012, NACA0015, NACA0020 and NACA0021	2D-Steady
(Soltanmohamadi and Lakzian, 2015)	RNG- *K-Epsilon* model	-NA-	238,876 - 207,638	NACA0020 and variable chord aerofoil	3D- Steady
(Halder et al., 2015)	K-Omega SST	-NA-	1,424,016	NACA0015	3D- Steady
(Halder and Samad, 2015b)	K-Omega SST	-NA-	-NA-	Modified blade	3D- Steady
(Ghisu et al., 2015)	Transition SST model	$0.8\ 10^5$ - $1.5\ 10^5$	-NA-	NACA 0015	3D-Unsteady-T= 9 sec
(Halder and Samad, 2015a)	K-Omega SST	1,368,000	1,424,016	NACA 0015	3D- Steady
(Shehata et al., 2016)	Realizable *K-Epsilon* model	$6\ 10^4$- $4\ 10^5$	312951	NACA0012, NACA0015, NACA0020 and NACA0021	2D-Unsteady-T= 6.7 sec

2.6 Summary

In this chapter we discussed the previous work related to flow control, techniques of flow control, exergy and entropy analysis for energy conversion systems. Furthermore, a comprehensive review for the Wells turbine research is presented also in this chapter. The literature references are categorized according to the research approaches to different Wells turbine components and according to the research methods investigating Wells turbine. Since CFD is a widely used approach in Wells turbine research, an independent section of the review is devoted to comparatively discuss its methods and techniques. The following remarks can be concluded from this chapter:

- The passive flow control using the suction or blowing slot has not been investigated yet for the aerofoil section under sinusoidal inlet velocity flow.
- The exergy and entropy analysis for Wells turbine has not been reported yet.
- No specific study of the suction and blowing slot effect with sinusoidal flow on the entropy generation value has been performed
- Guide vanes and multi stage of Wells turbine that have the same direction of rotation are used to increase the efficiency; in addition, the increase in Reynolds number, Mach number, flow coefficient and angle of attack leads to an increase in the efficiency of Wells turbine, until a certain critical value.
- Determining the optimum position of endplate and the optimum value of blade sweep ratio, tip clearance, blade skew and setting pitch angle increases the efficiency of Wells turbine. However, the numerical optimization process is used to create optimum non-symmetric aerofoil.

The output publication from this chapter is “Wells turbine for wave energy conversion: a review” (International Journal of Energy Research, 41 (2017) 6-38)

PART II Mathematical and Numerical Modelling Methods

Chapter 3 Mathematical Formulations and Numerical Methodology

3.1 Introduction

Both first and second law analysis methods are described in this chapter. It also contains a discussion and a description of the turbulence models used for this study. The turbine efficiency calculations were also highlighted using the analytical analysis.

3.2 Mathematical method and its approach

3.2.1 First law of Thermodynamics

As seen in Chapter 1, the tangential force in terms of lift and drag components are given by equation (1.3), and consequently the aerodynamic driving torque becomes:

$$Torque = F_t \ R_m \tag{3.1}$$

Expressing lift and drag forces in terms of air density, incident velocity, blade area and appropriate aerodynamic coefficients, the tangential force and its driving torque become:

$$F_t = \frac{1}{2}\rho V_r^2 \, AC_L \ sin\,\alpha - \frac{1}{2}\rho V_r^2 \, AC_D \ cos\,\alpha \tag{3.2}$$

$$Torque = \frac{1}{2}\rho V_r^2 \, A \, R_m (C_L \ sin\,\alpha - C_D \ cos\,\alpha) \tag{3.3}$$

where lift and drag coefficients C_L and C_D are given by:

$$C_L = \frac{L}{\frac{1}{2}\rho (V_r)^2 \, A} \tag{3.4}$$

$$C_D = \frac{D}{\frac{1}{2}\rho (V_r)^2 A} \tag{3.5}$$

The resultant velocity V_r is given by:

$$V_r = \sqrt{V_A^2(t) + \omega^2(t) R_m^2} \tag{3.6}$$

$$\alpha = tan^{-1} \frac{V_A}{\omega R_m} \quad (3.7)$$

The torque coefficient can then be expressed as:

$$C_T = (C_L \sin\alpha - C_D \cos\alpha) \quad (3.8)$$

Equation (3.3) can be rewritten as:

$$Torque = \frac{1}{2}\rho V_r^2 A R_m C_T \quad (3.9)$$

The C_T is an important parameter, as it is a function of both α and Reynolds number . When the value of C_T is positive, it means that the tangential force direction is with the rotation direction. In case of negative values, it resists the turbine rotation.

Using equation (3.6), the driving torque in equation (3.9) can be written as:

$$Torque = \frac{1}{2}\rho\left(V_A{}^2 + (\omega R_m)^2\right) A R_m C_T \quad (3.10)$$

The pressure difference Δp across the rotor is calculated from:

$$\Delta p = \frac{\mathrm{F_A}}{\mathrm{Area}} \quad (3.11)$$

where F_A is the axial force given by:

$$F_A = \frac{1}{2}\rho V_r^2 A(C_L \cos\alpha + C_D \sin\alpha) = \frac{1}{2}\rho V_r^2 A C_A \quad (3.12)$$

where C_A axial force coefficient is given by:

$$C_A = C_L \cos\alpha + C_D \sin\alpha \quad (3.13)$$

$$\Delta p = \frac{\frac{1}{2}\rho (zcb)\left[V_A^2 + (\omega R_m)^2\right] C_A}{\pi R_m^2} \quad (3.14)$$

When the turbine is in the running condition, the parameters of the turbine performance, such as T_L, ω, Q, Δps etc, vary periodically. In this case, turbine performance is indicated by their mean values.

The mean output power is expressed as:

$$Output\ Power = T_L \omega_{avr} \quad (3.15)$$

where ω_{avr} is the average velocity during a complete cycle given by:

$$\omega_{avr} = \frac{1}{T}\int_0^T \omega(t)dt \tag{3.16}$$

The load torque can be expressed in a non-dimensional form as:

$$X_L = \frac{T_L}{\rho\pi R_m^3 V_a^2} \tag{3.17}$$

Hence, the output is:

$$Output\ Power\ = X_L \pi \rho {V_{Am}}^2 {R_m}^3 \omega_{avr} \tag{3.18}$$

The output power is given in a non-dimensional form (power coefficient) as:

$$\mathrm{W}^* = \frac{\text{Output Power}}{\rho\ \ \omega^3 \mathrm{D}_\mathrm{m}^5} \tag{3.19}$$

$$\text{Input power } = \frac{1}{T}\int_0^T \Delta P\ \ Q\ dt \tag{3.20}$$

where Q is the volume flow rate passing throgh the rotor area to the turbine and given by:

$$Q = V_A\ A_r \tag{3.21}$$

The mean turbine efficiency is

$$\eta_F = mean\ value\ of\ \frac{Output\ Power}{Input\ Power} = \frac{\frac{1}{T}\int_0^T T_L \omega(t)\ dt}{\frac{1}{T}\int_0^T \Delta PQ\ \ dt} \tag{3.22}$$

The flow coefficint ϕ relating tangential and axial velocties of the rotor is difined as:

$$\phi = \frac{V_{Am}}{\omega_{avr} R_m} \tag{3.23}$$

The tip speed ratio is defined as:

$$TSR = \frac{\omega_{avr} R_m}{V_{Am}} \quad (3.24)$$

and the solidity (a measure of the blockage offered by the blades to the flow of air)

$$\sigma = \frac{\mathrm{Z\,C}}{2\,\pi\,\mathrm{R_m}} \quad (3.25)$$

And finally the Reynolds number is difined as:

$$\mathrm{Re} = \frac{V_r C \rho}{\mu} \quad (3.26)$$

For the first law of thermodynamics, the lift and drag coefficient C_L and C_D are computed from the post processing software. Then, the torque coefficient can then be calculated from equation (3.8) (Sheldahl and Klimas, 1981).

3.2.2 Turbine efficiency calculation

The efficiency calculations for the Wells turbine under sinusoidal-flow conditions have been studied using an analytical mathematical model. The net torque that drives the Wells turbine is a resultant of the summation of all torques exerted on the turbine as follows:

$$\sum Torque = T_{aerodynamic} - T_{Load} - T_{Loss} \quad (3.27)$$

$$\Sigma\, Torque = \frac{1}{2}\rho\left(V_a{}^2 + (\omega\, R_m)^2\right) A\, R_m C_T - T_L - T_{Loss} \quad (3.28)$$

where T_L is the load torque.

Applying the angular moment equation of motion along turbine axis, we get

$$I\frac{d\omega}{dt} = \sum Torque \quad (3.29)$$

where I is the rotor mass moment of inertia and ω is the angular velocity of the rotor varying with time. Neglecting the torque losses and substituting from eq. (3.28) into (3.29) we get:

$$I\frac{d\omega}{dt} = \frac{1}{2}\rho\left(V_a{}^2 + (\omega\, R_m)^2\right) z\, c\, b\, R_m C_T - T_L \quad (3.30)$$

Hence, the rotor equation of motion is

$$I\frac{d\omega}{dt} = \frac{1}{2}\rho\left(V_a{}^2 + (\omega\, R_m)^2\right) z\, c\, b\, R_m C_T - X_L \rho\pi R_m^3 V_a^2 \quad (3.31)$$

$$\frac{d\omega}{dt} = \frac{\frac{1}{2}\rho\left(V_a{}^2 + (\omega\, R_m)^2\right) z\, c\, b\, R_m C_T - X_L \rho\pi R_m^3 V_a^2}{I} \quad (3.32)$$

$$\int d\omega = \int \frac{\frac{1}{2}\rho\left(V_a{}^2 + (\omega\, R_m)^2\right) z\, c\, b\, R_m C_T - X_L \rho\pi R_m^3 V_a^2}{I}\ dt \quad (3.33)$$

$$\omega_2 - \omega_1 = \frac{\frac{1}{2}\rho\left(V_a{}^2 + (\omega\, R_m)^2\right) z\, c\, b\, R_m C_T - X_L \rho\pi R_m^3 V_a^2}{I}\ t_2 - t_1 \quad (3.34)$$

Figure 3.1 shows the flow chart that displays the main steps that implement the mathematical model using the MATLAB software. These steps are based on the equations that are derived earlier, starting from setting the initial angular velocity that causes the initial motion and certain operational conditions (Ayat, 2013) to calculate the generated force on the blade and to get the instantaneous angular velocity, the output power and efficiency. In this section, the rotor geometry data from existing Wells turbine projects (the OSPREY) (Thorpe, 1995) are used as inlet parameters for the mathematical model.

3.2.2.1 Analytical analysis

The experimental data from (Thakker and Abdulhadi, 2007, Thakker and Abdulhadi, 2008) for an unsteady flow was used to validate our analytical mathematical model. The experimental data from a test rig was used by Wave Energy Research Team, University of Limerick. It consisted of a bell mouth entry, test section, drive and transmission section, a plenum chamber with honeycomb section, a calibrated nozzle, and a centrifugal fan. The turbine test section had an internal diameter of 600 mm and a fabricated rotor of a 598 mm diameter, leaving a tip clearance of 1 mm. The hub

diameter is 358.8 mm, providing a hub to tip ratio of 0.6 and chord length of 120 mm. The turbine was mounted on a shaft in a cylindrical annular duct. The shaft was coupled to motor/generator via a torque meter. The turbine blades (8 blades for solidity = 0.64 and 6 blades for solidity = 0.48) were set on the hub at a 90◦ angle of stagger along the y-axis.

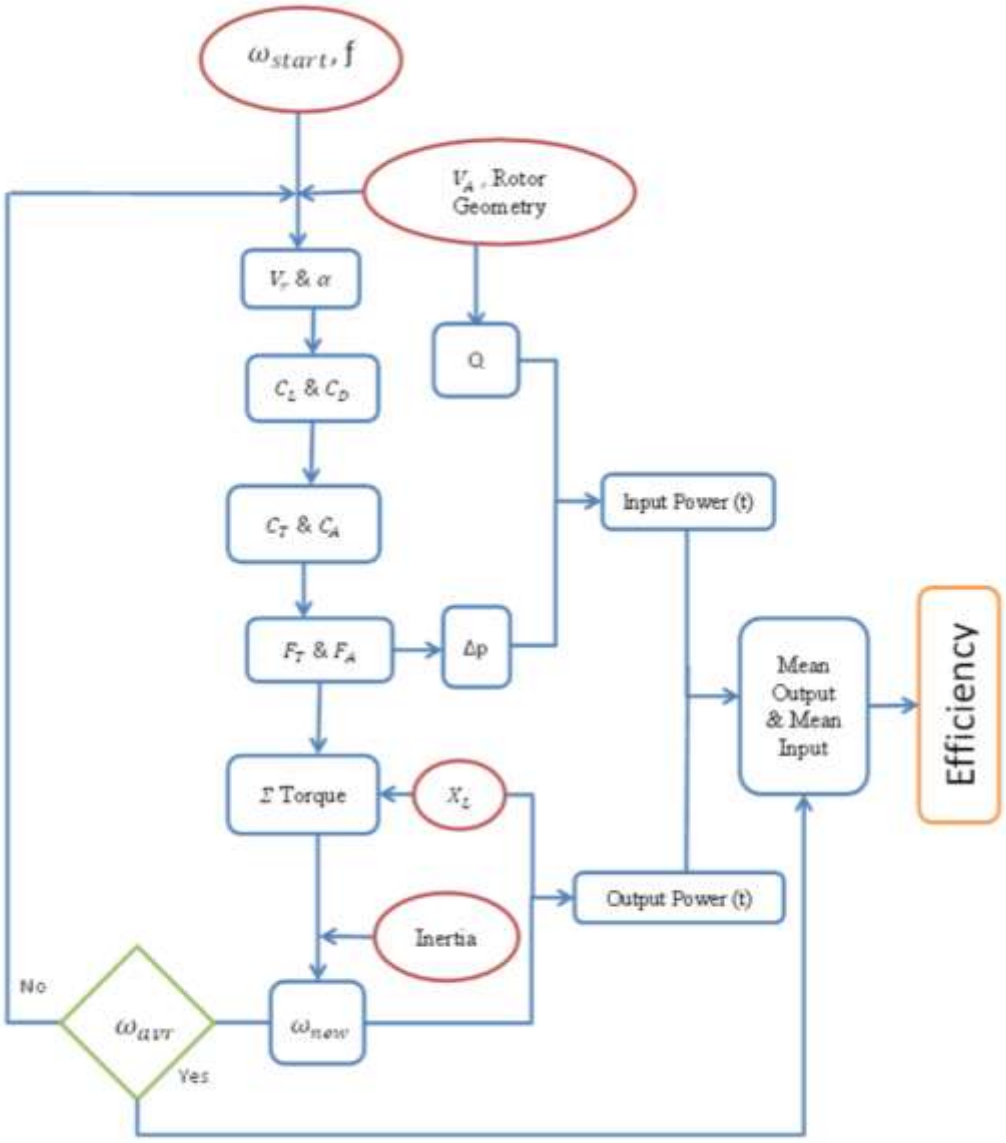

Figure 3.1 Flow chart of implementing analytical mathematical model on Wells turbine performance

Figure 3.2 shows a good agreement between the mean efficiency from reference (Thakker and Abdulhadi, 2007, Thakker and Abdulhadi, 2008) with t_{sin} equal to 9.2 sec and predicted mean efficiency from the mathematical code at same t_{sin}.

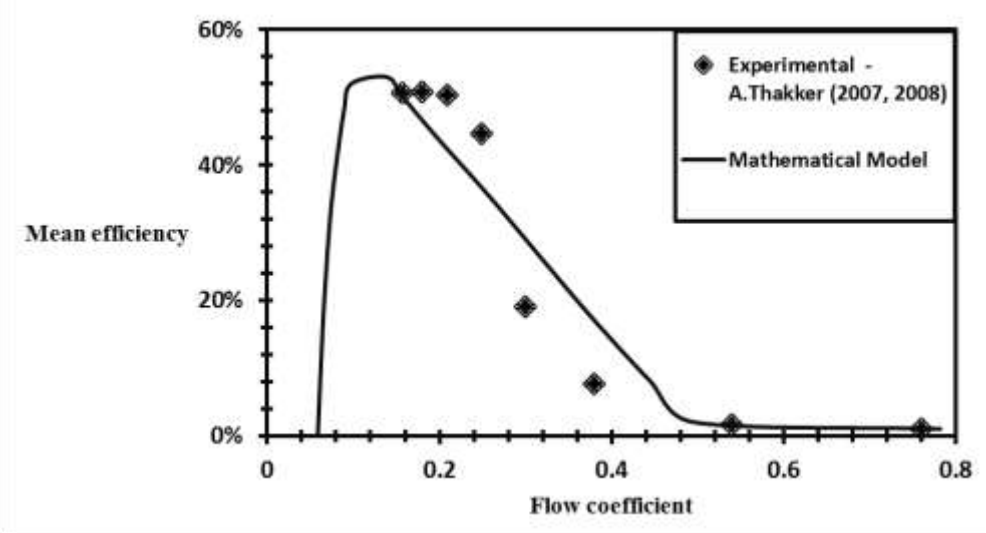

Figure 3.2 Mean efficiency of NACA0015 under sinusoidal flow conditions with solidity = 0.64

To examine the effect of wave time period (operating parameter), as well as solidity and aerofoil section (design parameters) on the starting and running characteristics, a mathematical analysis was used. It was also used to estimate the turbine efficiency and the output power. The mathematical model gives the relationship of rotor angular velocity with time as a curve in Figure 3.3, where the Figure shows the NACA0012 aerofoil at a time period equal to 6 sec with solidity equal to 0.64 in free running condition and with different loading torque coefficients. Furthermore, it can be noted that the rotor angular velocity was oscillating around a certain average value due to the oscillating inlet velocity.

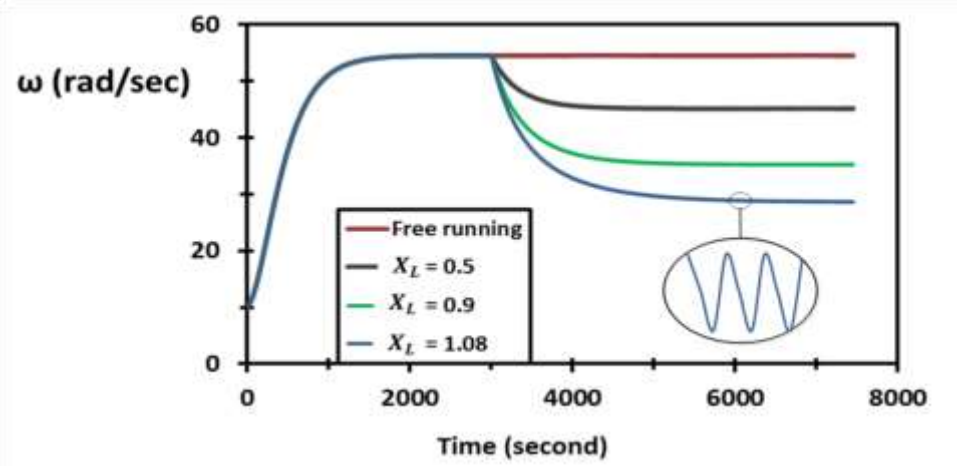

Figure 3.3 Angular velocity variations with time for different loading torque coefficient

Figure 3.4 represents starting and running characteristics by changing specific parameters, such as time period, solidity and aerofoil section. It can be noted that the crawling condition appears at the starting period for the sinusoidal wave cycle with t_{sin} equal to 4 sec. However, the three different time periods give the same average velocity (51.6 rad/s) after the starting period. According to Figure 3.4 B) the change in solidity from 0.64 to 0.8 does not have an effect (approximately) on the starting and running characteristics. On the other hand, the NACA0015 aerofoil section has the same starting characteristics of NACA0012 but lower rotor average velocity (45.9 rad/s) than NACA0012, see Figure 3.4 C).

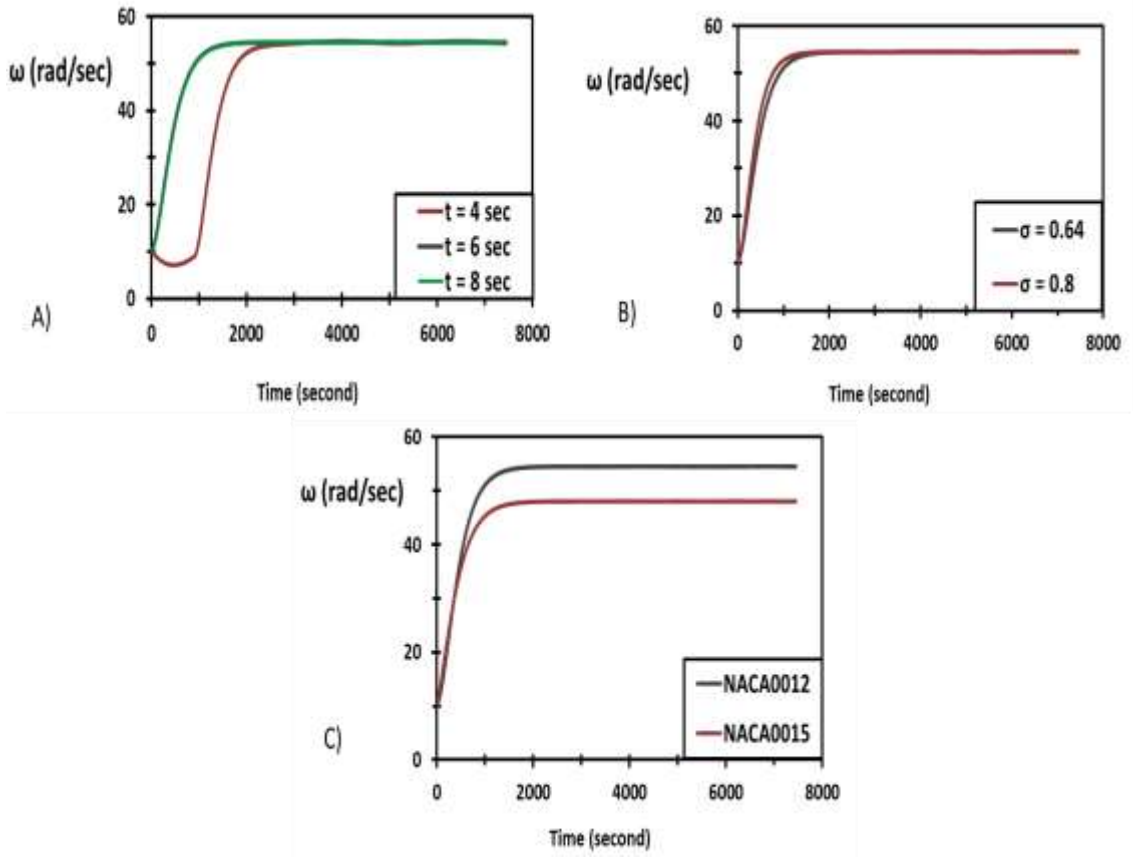

Figure 3.4 Angular velocity variation with time in free running condition, A) Time period ($\boldsymbol{t_{sin}}$ = 4, 6 and 8 sec), B) Solidity (0.64 and 0.8) and C) Aerofoils section (NACA0012 and NACA0015)

The mean turbine efficiency under sinusoidal flow conditions with different operating and design parameters was shown in Figure 3.5. It can be noted that the peak efficiency for the turbine which has sinusoidal wave with t_{sin} equal to 4 sec higher than that with 6 sec and 8 sec by 8%, see Figure 3.5 A). It can also be noted that the turbine which has sinusoidal wave with t_{sin} equal to 4 sec works with a higher flow coefficient than that with 6 sec and 8 sec by 17%. Figure 3.5 B) shows that the increase in turbine solidity from 0.64 to 0.8 decreases the peak efficiency by 1% and does not have an effect on the flow coefficient. On the other hand, the change in the aerofoil section of a turbine from NACA0012 to NACA0015 does not have an effect on the peak efficiency. However, the turbine with NACA0015 aerofoil section works with a higher flow coefficient by 15% than that with NACA0012 aerofoil section.

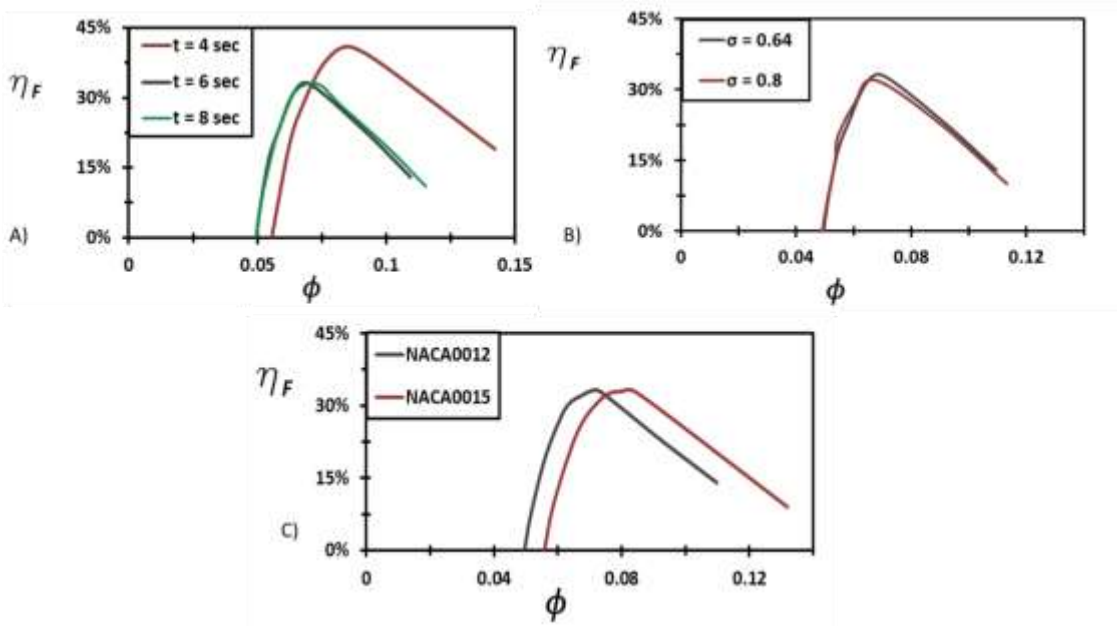

Figure 3.5 The mean efficiency of turbine under sinusoidal flow conditions, A) Time periods (t_{sin} = 4, 6 and 8 sec), B) Solidity (0.64 and 0.8) and C) Aerofoils section (NACA0012 and NACA0015)

Figure 3.6 presents the net output power for the Wells turbine under different operating and design parameters based on the real data from the Egyptian northern coast. It can be concluded that the operating condition inlet flow with 6 sec time period gives a maximum output power that is higher than 4 sec by 19%, and 8 sec by 1%, see Figure 3.6 A). In addition, the change in the design parameters had an effect on the output power value. So, the increase in solidity from 0.64 to 0.8 came with an increase in the net output power by 18% (Figure 3.6 B). Moreover, Figure 3.6 C) shows that the Wells turbine with NACA0012 aerofoil section has a higher net output power than that with NACA0015 aerofoil section by 31%. These values were generated from one turbine without any attached guide vans or other enhanced performances, but in the real station, the number of turbine reached two turbines such as the Prototype OWC device (biplane) (Raghunathan S. et al., 1995) and LIMPET (Boake et al., 2002, Whittaker, 1993b, Heath, 2002, Wavegen, 2002, Heath, 2000, Belfast, 2002) (contra-rotating) in Scotland. Furthermore, the number of turbines can reach four as in the OSPREY (Thorpe, 1995) used in Scotland or sixteen turbines such as in Mutriku Wave Energy Plant (TV, 2007,

Torre-Enciso et al., 2009) in Spain. In addition, the guide vans can be attached to increase the turbine performance, such as Mighty Whale (Y. Washio et al., 2000) in Japan and The Pico Power Plant (Falcao, 1995, Falcao, 2000, Falcao, 1999, Falcao, 2003, Falcao, 2004, Falcao, 2002) in Portugal.

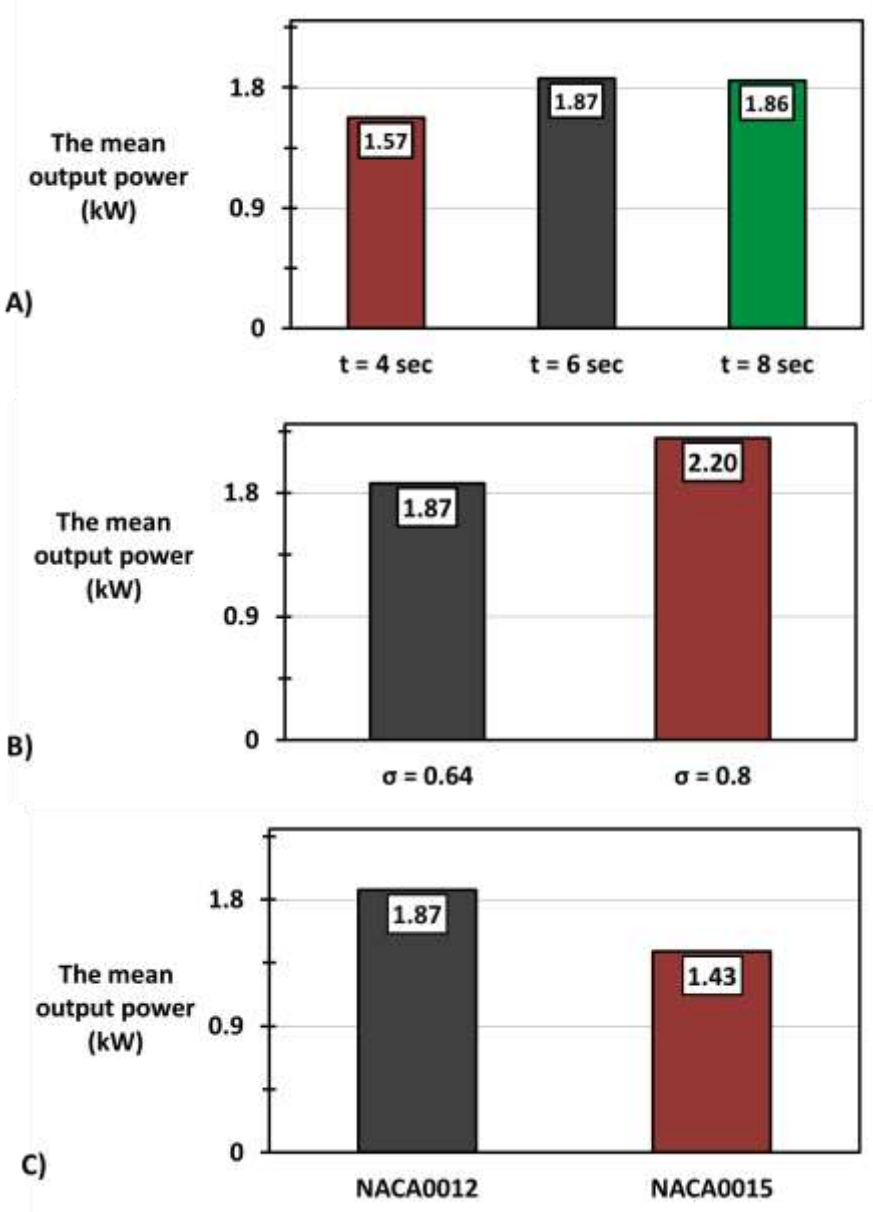

Figure 3.6 The value of output power for the turbine under sinusoidal flow conditions, A) Time periods (t_{sin} = 4, 6 and 8 sec), B) Solidity (0.64 and 0.8) and C) Aerofoils section (NACA0012 and NACA0015)

3.2.3 Second law of Thermodynamics

For a system that operates in the unsteady state, assume its instantaneous inventories of mass, energy, and entropy are M, E, and S. The system experiences the net-work transfer rate $\dot{W}$, heat transfer rates ($\dot{Q}_0$, $\dot{Q}_1$,..., $\dot{Q}_n$) with n+1 temperature reservoirs (T_0 ,T_1 ,...,T_n), and mass flow rates $\dot{m}_{in}$, $\dot{m}_{out}$ through any number of inlet and outlet ports and h° is shorthand for the sum of specific enthalpy, kinetic energy, and potential energy of a particular stream at the boundary. The first law of thermodynamics for this system can expressed as (Bejan, 1988):

$$\frac{dE}{dt} = \sum_{i=0}^{n} \dot{Q}_i - \dot{W} + \sum_{in} \dot{m}\, h^o \sum_{out} \dot{m}\, h^o \qquad (3.35)$$

And the second law of thermodynamics as:

$$S_{\text{gen}} = \frac{dS}{dt} - \sum_{i=0}^{n} \frac{\dot{Q}_i}{T_i} - \sum_{in} \dot{m}\, S + \sum_{out} \dot{m}\, S \qquad (3.36)$$

Where, the total entropy generation rate S_{gen} is simply a definition (notation) for the entire quantity on the left-hand side of the inequality sign. By eliminating $\dot{Q}_0$, the work transfer rate could be written as (Hirsch, 2007):

$$\dot{W} = -\frac{d}{dt}(E - T_o S) + \sum_{i=0}^{n} \left(1 - \frac{T_o}{T_i}\right) \dot{Q}_i + \sum_{in} \dot{m}\, (h^o - T_o S) - \sum_{out} \dot{m}\, (h^o - T_o S) - T_o\, S_{\text{gen}} \qquad (3.37)$$

The work transfer rate for a reversible process ($S_{\text{gen}} = 0$) could be written as:

$$\dot{W}_{rev} = -\frac{d}{dt}(E - T_o S) + \sum_{i=0}^{n} \left(1 - \frac{T_o}{T_i}\right) \dot{Q}_i + \sum_{in} \dot{m}\, (h^o - T_o S) - \sum_{out} \dot{m}\, (h^o - T_o S) \qquad (3.38)$$

Therefore, it can be concluded that the second law of thermodynamic defines the net-work transfer rate $\dot{W}$ as (Bejan, 1996):

$$\dot{W}_{rev} - \dot{W} = T_o S_{gen} \qquad (3.39)$$

Which has been known for most of this century in engineering as the Gouy–Stodola theorem (A. Stodola, 1910).

It is possible to express the irreversible entropy generation in terms of the derivatives of local flow quantities in the absence of phase changes and chemical reactions. The two dissipative mechanisms in viscous flow are the strain-originated dissipation and the thermal dissipation, which correspond to a viscous and a thermal entropy generation, respectively (Iandoli, 2005). Thus, it can be written,

$$S_{gen} = S_V + S_{th} \tag{3.40}$$

In incompressible isothermal flow, such as the case in hand, the thermal dissipation term vanishes. The local viscous irreversibilities therefore can be expressed as:

$$S_V = \frac{\mu}{T_o}\dot{\phi} \tag{3.41}$$

Where $\dot{\phi}$ is the viscous dissipation term that is expressed in two dimensional Cartesian coordinates as (Iandoli, 2005):

$$\dot{\phi} = 2\left[\left(\frac{\partial u}{\partial x}\right)^2 + \left(\frac{\partial v}{\partial y}\right)^2\right] + \left(\frac{\partial u}{\partial y} + \frac{\partial v}{\partial x}\right)^2 \tag{3.42}$$

Equations 3.41 and 3.42 were used to create the UDF file, which is used to calculate the local entropy from the FLUENT software. Then, the global entropy generation rate is hence expressed as:

$$S_G = \iint_{xy} S_V \, dy dx \tag{3.43}$$

Which is also calculated from the FLUENT software by integral the global value,
Equation (3.44) is defining the exergy value, which can be written as:

$$Exergy = KE + S_G \tag{3.44}$$

and finely the second law efficiency is defined as (Pope et al., 2010):

$$\eta_S = \frac{KE}{Exergy} \tag{3.45}$$

Where $KE = \frac{1}{2}V^2$

From the above equations, it can be concluded that the torque coefficient indicates to the first law efficiency and the global entropy generation rate indicates to the second law and efficiency, where the increase in torque coefficient leads to an increase in the first law efficiency. On the other hand, the decrease in the global entropy generation rate leads to an increase in the second law efficiency.

3.3 Modelling equations

3.3.1 RANS

The mathematical model consists of the governing equations of turbulent incompressible unsteady flow in two-dimensional generalized coordinates, which can be written in vector notations as (Launder and Spalding, 1974):

Continuity: $\frac{\partial \rho}{\partial t} + \frac{\partial \rho \bar{u}_i}{\partial x_i} = 0$ (3.46)

The Navier–Stokes equations are based on the assumption that the fluid, at the scale of interest, is a continuum, in other words is not made up of discrete particles but rather a continuous substance. Another necessary assumption is that all the fields of interest like pressure, flow velocity, density, and temperature are differentiable, weakly at least. The equations are derived from the basic principles of continuity of mass, momentum, and energy. For that matter, sometimes it is necessary to consider a finite arbitrary volume, called a control volume, over which these principles can be applied.

RANS: $$\rho \frac{\partial \overline{u_i}}{\partial t} + \frac{\partial}{\partial x_i}\left(\rho \bar{u}_i \bar{u}_j\right) = -\frac{\partial p}{\partial x_j} + \frac{\partial}{\partial x_j}\left[\mu\left(\frac{\partial \bar{u}_i}{\partial x_j} + \frac{\partial \bar{u}_j}{\partial x_i} - \frac{2}{3}\delta_{ij}\frac{\partial \bar{u}_j}{\partial x_i}\right)\right] + \frac{\partial}{\partial x_j}\left(-\overline{\rho u_i' u_j'}\right)$$ (3.47)

See section (2.4.3.), the turbulent flow is modelled using the Realizable k-ε model, Transport equation of turbulent kinetic energy (k)

$$\frac{\partial}{\partial t}(\rho k) + \rho \frac{\partial}{\partial x_i}(U_i k) = \frac{\partial}{\partial x_j}\left[\left(\mu + \frac{\mu_T}{\sigma_k}\right)\frac{\partial}{\partial x_j} k\right] + \mu_T S^2 - \rho\,\varepsilon \qquad (3.48)$$

Specific dissipation rate equation is:

$$\frac{\partial}{\partial t}(\rho \varepsilon) + \rho \frac{\partial}{\partial x_i}(U_i \varepsilon) = \frac{\partial}{\partial x_j}\left[\left(\mu + \frac{\mu_T}{\sigma_\varepsilon}\right)\frac{\partial}{\partial x_j} \varepsilon\right] + C_1 \rho S_\varepsilon - C_2 \rho \frac{\varepsilon^2}{k + \sqrt{\nu\varepsilon}} \qquad (3.49)$$

Where $C_1 = max\left(0.43, \frac{\eta}{\eta + 5}\right)$, $C_2 = 1.9$

$$C_\mu = \frac{1}{A_0 + A_s U^* \frac{k}{\varepsilon}} \qquad (3.50)$$

Where

$A_0 = 4.0$, $U^* = \sqrt{S_{ij} S_{ij} + \Omega_{ij} \Omega_{ij}}$, $A_s = \sqrt{6}\cos\left(\frac{1}{3} arccos\left(\sqrt{6}W\right)\right)$, $W = \frac{\sqrt{8}\, S_{ij} S_{jk} S_{ki}}{S^3}$

and the vorticity tensor $\Omega_{ij} = \frac{1}{2}\left(\frac{\partial \overline{u_i}}{\partial x_j} - \frac{\partial \overline{u_j}}{\partial x_i}\right)$

Where $\bar{u}$ is the Reynolds averaged velocity vector. The present study adopts one and two-equation turbulence models to close the Reynolds stress term $\left(-\overline{\rho u_i' u_j'}\right)$ of the RANS equation (Wilcox, 2006b) as shown in the following section. The transport equations of such models can be found in turbulence modelling texts, such as (Hirsch, 2007).

3.3.2 LES

The governing equations employed for Large Eddy Simulation (LES) are obtained by filtering the time-dependent Navier-Stokes equations. The filtering process effectively filters out eddies whose scales are smaller than the filter width or grid spacing used in the computations. The resulting equations thus govern the dynamics of large eddies. A filtered variable (denoted by an over-bar) is defined by (SB., 2000):

$$\overline{\phi}\,(x) = \int_{FD} \phi(x')G(x,x')dx' \qquad (3.51)$$

Where FD is the fluid domain, and G is the filter function that determines the scale of the resolved eddies. In FLUENT, the finite-volume discretization itself implicitly provides the filtering operation(Mamun, 2006):

$$\overline{\phi}\,(x) = \frac{1}{V}\int_V \phi(x')dx',\ \ x' \in V \qquad (3.52)$$

Where V is the volume of a computational cell. The filter function, G (x, x'), implied here is then

$$G\,(x,\ x') = \begin{cases} 1/V & for\ \ x' \in V \\ 0 & otherwise \end{cases} \qquad (3.53)$$

The LES model will be applied to essentially incompressible flows. Filtering the incompressible Navier-Stokes equations, one obtains (DAHLSTROM, 2003)

$$\frac{\partial \rho}{\partial t} + \frac{\partial \rho \overline{u}_i}{\partial x_i} = 0 \qquad (3.54)$$

$$\frac{\partial \overline{u}_i}{\partial t} + \frac{\partial \overline{u}_i}{\partial x_j}\left(\overline{u}_j\right) = \frac{\partial}{\partial x_j}\left(\mu \frac{\partial \overline{u}_i}{\partial x_j}\right) - \frac{\partial \overline{\rho}}{\rho\, \partial x_i} + \frac{\partial \tau_{ij}}{\rho\, \partial x_j} \qquad (3.55)$$

Where τ_{ij} is the sub-grid-scale stress defined by

$$\tau_{ij} = \rho\overline{u_i u_j} - \rho\overline{u_i}\ \overline{u_j} \qquad (3.56)$$

The sub-grid-scale stresses resulting from the filtering operation are unknown and require modelling. The majority of sub-grid-scale models are eddy viscosity models of the following from (Moin P, 1991):

$$\tau_{ij} - \frac{1}{3}\,\tau_{kk}\sigma_{ij} = -2\mu_t \overline{S}_{ij} \qquad (3.57)$$

Where $\overline{S}_{ij}$ is the rate-of-strain tensor for the resolved scale defined by:

$$\overline{S}_{ij} = \frac{1}{2}\left(\frac{\partial \overline{u}_i}{\partial x_j} + \frac{\partial \overline{u}_j}{\partial x_i}\right) \qquad (3.58)$$

and μ_t is the sub-grid-scale turbulent viscosity, which the Smagorinsky-Lilly model is used for it (DK., 1992). The most basic of sub-grid-scale models for "Smagorinsky-Lilly model" was proposed by Smagorinsky (Hinze, 1975) and further developed by Lilly (Launder and Spalding, 1972). In the Smagorinsky-Lilly model, the eddy viscosity is modelled by:

$$\mu_t = \rho L_s^2 \left|\overline{S}\right| \quad (3.59)$$

Where L_s is the mixing length for sub-grid-scale models and $\left|\overline{S}\right| = \sqrt{2\overline{S}_{ij}\overline{S}_{ij}}$. The $L_s$is computed using:

$$L_s = \min(kd, C_s V^{1/3}) \quad (3.60)$$

Where C_s is the Smagorinsky constant, $k = 0.42$, d is the distance to the closest wall, and V is the volume of the computational cell. Lilly derived a value of 0.23 for C_s from homogeneous isotropic turbulence. However, this value was found to cause excessive damping of large-scale fluctuations in the presence of mean shear or in transitional flows. A dynamic SGS model was not particularly necessary in the LES models due to the turbulence flow at all domain, therefore, C_s= 0.1 has been found to yield the best results for a wide range of flows (Mamun, 2006) (Mamun et al., 2004) (Kinoue et al., 2004).

3.4 Summary

In this chapter, the first law analysis and the entropy analysis were introduced. The operation cycle and efficiency curve have been also applied successfully to Wells turbine with real data in this chapter. In addition the numerical modelling methodology was presented. The needed methodology for these methods is described in the next chapters.

The output publication from this chapter is: "Comparative analysis of different wave turbine designs based on conditions relevant to northern coast of Egypt" (Energy (2016)-

In Press). Furthermore, the mathematical formulations and numerical methodology from this chapter were used in all the output publications from this thesis.

Chapter 4 CFD Verification and Validation Result

4.1 Introduction

The two main principles that are necessary for establishing credibility are verification and validation. Verification is the process of determining that a model implementation accurately represents the developer's conceptual description of the model and the solution to the model. Validation is defined as the process of determining the degree to which a model is an accurate representation of the real world from the perspective of the intended users of the model. The CFD verification and validation result for such models used in this work is presented in this chapter. Also, this chapter contains a description of the turbulence models used in stall condition, an expression of the discretization methods employed and the boundary conditions for this work.

4.2 Computational model and boundary conditions

Two-dimensional numerical models for NACA0015 aerofoils were built and validated against experimental measurements under unsteady flow conditions with non-oscillating velocity and under unsteady flow with sinusoidal inlet velocity. The computational domain is discretized to Cartesian structured finite volume cells using GAMBIT code. The application of such boundary condition types (Starzmann and Carolus, 2013b, Mohamed and Shaaban, 2013, Torresi et al., 2009, Mamun et al., 2004) matches the Green-Gauss cell based evaluation method for the gradient terms used in the solver (ANSYS FLUENT). Numerous tests accounting for different interpolation schemes were used to compute cell face values of the flow field variables, the variables of governing equation which are velocity and pressure; in addition, convergence tests have been undertaken. The second order upwind (Smagorinsky, 1963) interpolation scheme was used in this work, where it yields results that were approximately similar to such

yielded by third order MUSCL scheme in the present situation. In addition, in some cases, the third order MUSCL scheme was given high oscillatory residual during the solution. The Quad-Pave meshing scheme (Structured Grid) is used in this work. It was also found that the solution reaches convergence when the scaled residuals approaches 1×10^{-5}. At such limit, the flow field variables holds constant values with the application of consecutive iterations. Figure 4.1 shows the dimensions of whole computational domain and location of aerofoil. Figure 4.2 shows the grid distribution near the wall of the aerofoil.

The axial flow of Wells turbine was modelled as a non-oscillating velocity and a sinusoidal wave in this simulation. Therefore, inlet boundary conditions were set to change as time. In order to apply the inlet sinusoidal wave boundary condition, inlet velocity with periodic function is generated as follows According to the literature the researchers are use this equation for sinusoidal wave inlet velocity with nonzero mean velocity over aerofoil and other object, please see references (Tae-Hun Kim et al., 2002, Nomura et al., 2003).

$$V_a = V_o + V_{am}\ sin\ (\sin 2\pi f t_{sin}) \qquad (4.1)$$

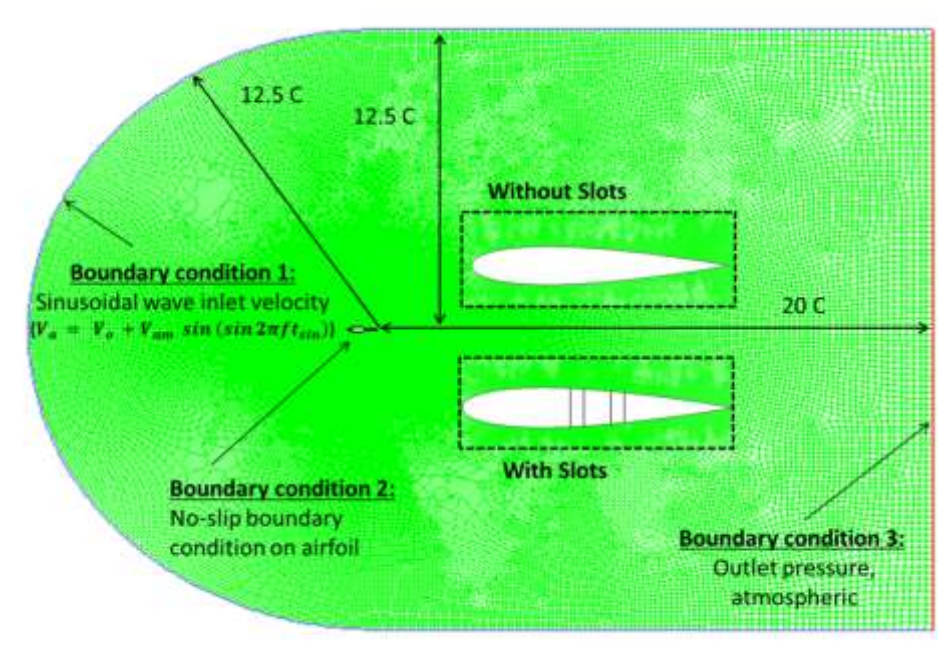

Figure 4.1 The dimensions of whole computational domain and location of aerofoil

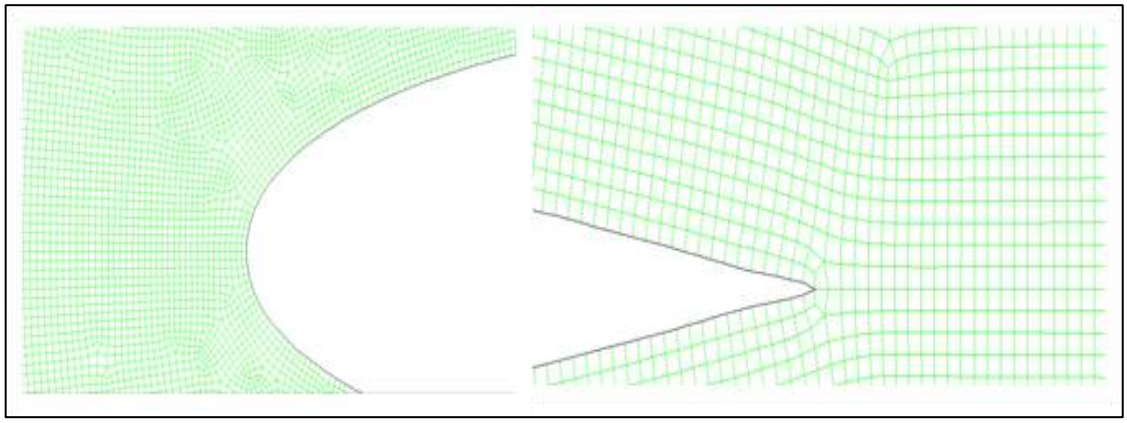

Figure 4.2 Computational grid near the wall of the aerofoil

4.3 Grid sensitivity test (Verification)

In order to ensure that the numerical model is free from numerical diffusion and artificial viscosity errors, several grid numbers were tested to estimate the number of grid cells required to establish a grid-independent solution. Table 4.1 shows the specifications of different grids used in unsteady flow with non-oscillating velocity. Figure 4.3 shows the pressure coefficient distribution on the upper and lower surfaces of the NACA0012 aerofoil as computed by the four grids. Grid D required more time than grid C, yielding similar results. Therefore, grid C was chosen to conduct the analysis presented hereafter.

Table 4.1 Specification of grids

Grid	No. of Cells	First cell	Growth rate	Aspect ratio	Equi-Angle skew
A	112603	1×10^{-4}	1.02	1.996	0.429
B	200017	1×10^{-5}	1.015	2.5	0.475
C	312951	1×10^{-5}	1.012	2.38	0.514
D	446889	1×10^{-6}	1.01	2.55	0.513

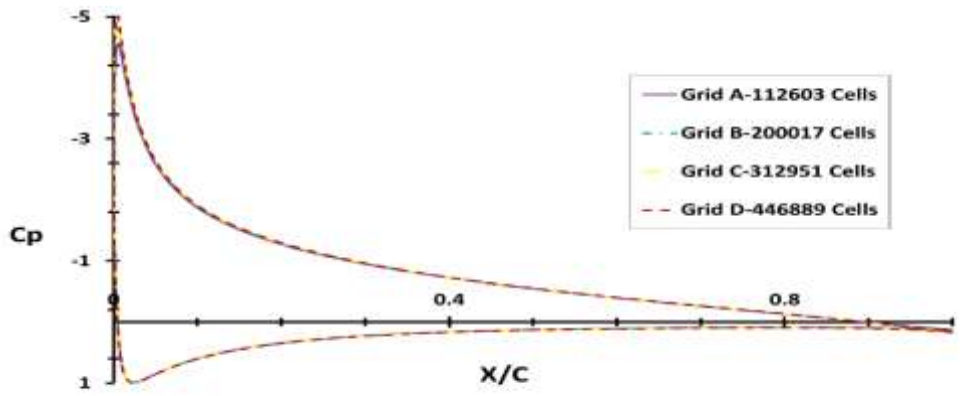

Figure 4.3 Pressure coefficient plotted on the normalized aerofoil cord at different grid resolutions

4.4 LES resolution quality assessment

In the most common practice, in LES, the filter length depends on the resolution of spatial discretization (i.e. grid) in a specified problem. The implication of the filtering technique, which is the backbone of LES, is the question about the resolution of the resolved scales in comparison with the total turbulence spectrum in the flow. An assortment of several attempts were made to propose and index of LES quality (Celik et al., 2005). The most established index of LES quality was proposed by Pope (Pope, 2004). Such quality index can be expressed mathematically as a function $M(x,t)$ of space and time as:

$$M(x,t) = \frac{K_{Res}}{K_{Res}+K_{SGS}} \qquad (4.2)$$

where K_{Res} and K_{SGS} are the resolved and subgrid modeled turbulent kinetic energy scalars, respectively. In the present work, K_{Res} can be calculated as: $K_{Res} = \frac{1}{2}(\tilde{u}^2 + \tilde{v}^2)$ and K_{SGS} can be calculated as $K_{SGS} = \frac{\nu_t^2}{(C\Delta)^2}$ where ν_t is the subgrid modeled turbulent kinematic viscosity as calculated in the Smagorinsky model as: $\nu_t = L_s^2|\bar{S}|$, where L_S is the mixing length for subgrid scales as calculated in equation (3.60) and Δ is the filter length. Pope (Pope, 2004) has evidently shown that when $M(x,t) \geq 80\%$ the LES is

sufficiently resolved and the flow field is properly resolved. Literature records support Pope's proposition in numerous and variant flows as reported in (Mazzei et al., 2016, Fureby, 2017, Georgiadis et al., 2010). In the present work, the quality index $M(x,t)$ was calculated for the computational domain and plotted against LES filter length as in Figure 4.4 A. It is shown that $M(x,t) \geq 80\%$ for filter lengths in the range $\Delta \geq 0.01$. In Figure 4.4 B a histogram of the filter length shows that approximately 98% of the grid has values of $M(x,t)$ larger than 90% which satisfies Pope's criteria for fully resolved LES.

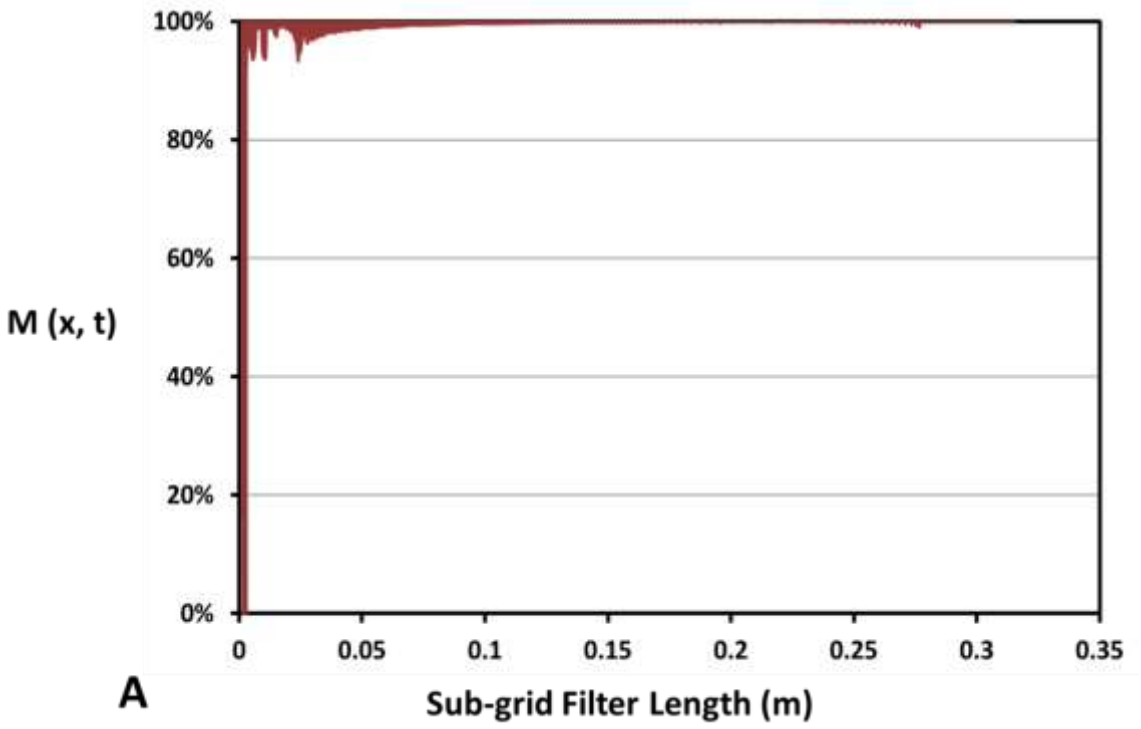

A

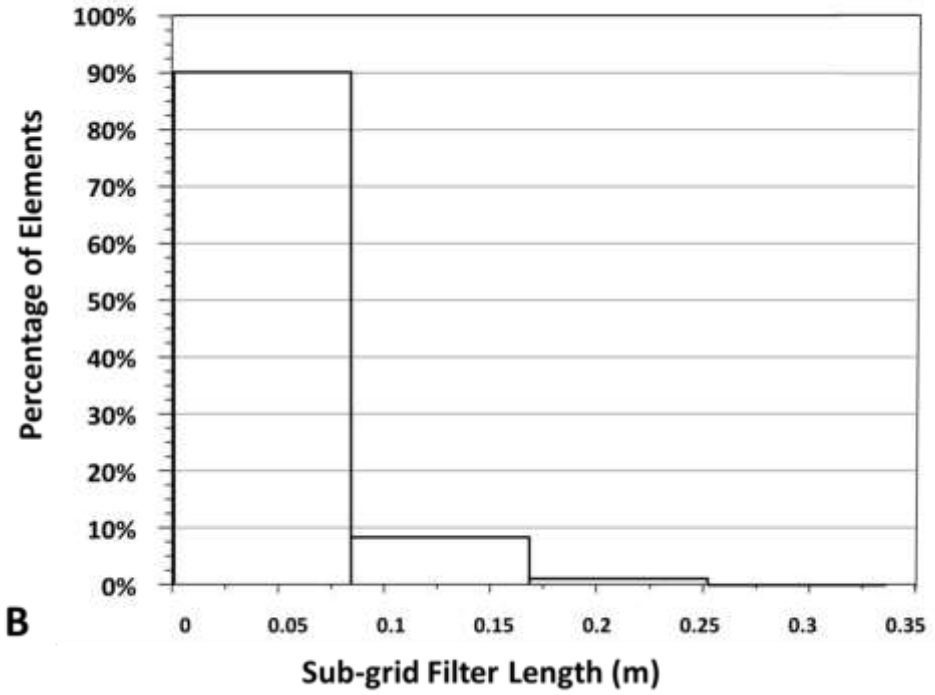

Figure 4.4 LES quality A) A histogram of Number of Elements for the Sub-grid Filter Length B) The measure of LES quality by M (x, t) with the Sub-grid Filter Length

4.5 Validation of the CFD model

4.5.1 RANS

Four turbulence models were used to model the steady flow around two dimensional NACA0012 aerofoils in order to determine the model which gives the best agreement with experimental data adopted from (Gregory and O'reilly, 1970). All models performed quite well in the simulation yielding predictions which are in excellent agreement with measurements, as shown in Figure 4.5. The S-A and V^2F models, however, showed slight under-predictions near to the blade leading edge in comparison with the other two models. The $k-\omega$ SST model required more time than the Realizable $k-\varepsilon$ model, yielding similar results.

The experimental data from reference (Nomura et al., 2003) are adopted to simulate and validate the unsteady sinusoidal wave inlet velocity. Details of the second validation case, where experimental data for unsteady forces (F_D) acting on a square cylinder in oscillating flow with nonzero mean velocity, are measured. The oscillating air flows are generated by a unique AC servomotor wind tunnel. The generated velocity histories are almost exact sinusoidal waves.

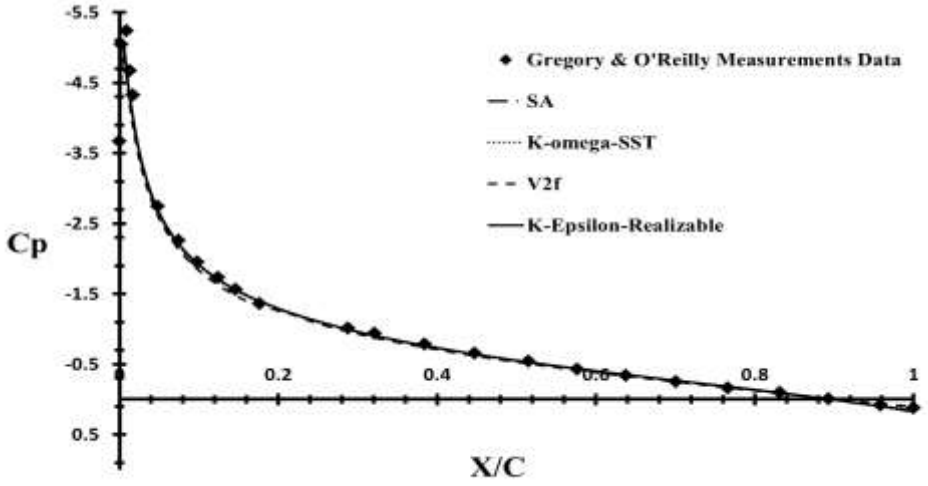

Figure 4.5 Pressure coefficients with the cord length of blade for different viscous model

Time step was set as 0.056 second in order to satisfy CFL (Courant Friedrichs Lewy) (DE Moura, 2013) condition equal to 1. Figures 4.6 and 4.7 show an excellent agreement between measured drag force from reference (Nomura et al., 2003) and calculated drag force from CFD models under sinusoidal flow boundary conditions based on RANS- $k-\varepsilon$ Realizable model at two different frequencies (2 Hz and 1 Hz).

4.5.2 LES

The unsteady RANS equations have been widely used to compute dynamic stall flow, but the results are far from being totally reliable for predicting the dynamic stall

behaviour of aerofoils (Szydlowski and Costes, 2004); moreover, they have a large computational cost. In this context, some researchers have chosen to start from scratch by considering static stall. They have proven that the solution shows grid and turbulent model dependency (Gleize et al., 2004). Furthermore, the simpler case of static stall, RANS simulation does not correctly predict the stall angle of attack. Other studies (Sankar et al., 2002, Wilder et al., 1993) have shown that this phenomenon is very sensitive to the transition of the boundary layer at the leading and trailing edge. This may be one of the reasons why the RANS approach, which has not been developed to treat transition, fails to predict stall occurrence. As large-eddy simulation (LES) provides an effective tool for tackling such flow condition.

One of the work objectives is to study the stall regime; therefore, an accurate simulation for the stall must be done. Figure 4.8 show that a comparison between different models to simulate two dimensional NACA0015 in unsteady flow with stall angle (13.6 degrees) with Reynolds number equal to 2×10^5 from experimental data (Torresi, 2007) was presented. The comparison use only the stall angle to identify which model can present it. The Large Eddy Simulation model (LES) give good result for the torque coefficient value, while, other models cannot predict the stall angle. The LES model was shown high disturbance for the path line of the flow stream and the pressure distribution at the upper surface, which it leads to the stall condition. The larger turbulent separated zone of the LES may be a reason for the lower value of the lift force (Richez et al., 2007). The LES was shown that some vortexes were formed and caused to appear a fluctuation behaviour of pressure distribution on the upper surface of the aerofoil, whereas other models were not able to predict it (Rezaei et al., 2013). On the other hand, the unsteady RANS turbulence modelling has shown a quite dissipative character that attenuates the instabilities and the vortex structures related to the dynamic stall (Martinat et al., 2008). Therefore, the LES model will be used in this work when the stall behaviour is investigated in Chapter 6. Otherwise, the Realizable $k-\varepsilon$ model will be used in Chapter 5.

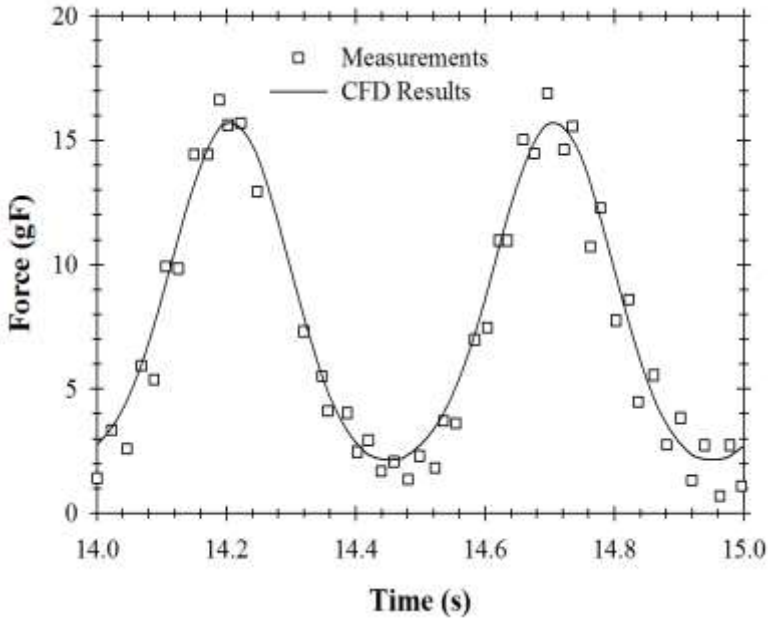

Figure 4.6 Measured unsteady in-line force F_D (angle of attack= 0 degree) and F_D calculated from CFD for frequency 2 Hz

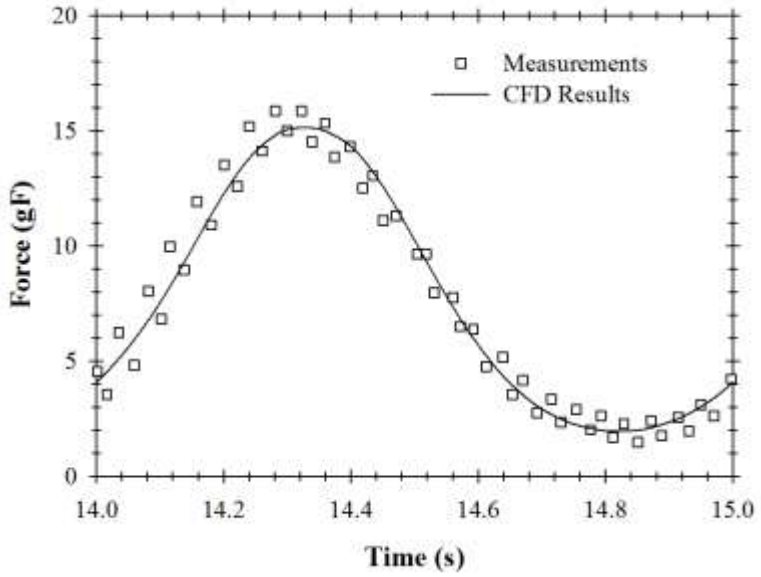

Figure 4.7 Measured unsteady in-line force F_D (angle of attack= 0 degree) and F_D calculated from CFD for frequency 1 Hz

LES model was used to model the flow around NACA0015 aerofoil in order to give the best agreement with experimental data adopted from (Torresi et al., 2009) and square cylinder from (Nomura et al., 2003). Large Eddy Simulation model gives an excellent result when they are used to simulate the aerofoil in stall condition, according to literature survey (Kawai and Asada, 2013, Richez et al., 2007, Alferez et al., 2013, Kim et al., 2015, AlMutairi et al., 2015, Armenio et al., 2010, Hitiwadi et al., 2013, Bromby, 2012, DAHLSTROM, 2003).

Although LES is a 3D model by definition, there have been numerous successful attempts to use it in 2D applications, such as flow over obstacles(SKYLLINGSTAD and WIJESEKERA, 2004), hump(Avdis et al., 2009), block(Cheng and Porté-Agel, 2013), aerofoils(Hitiwadi et al., 2013, Christian Tenaud and Phuoc, 1997) and Hills(Ashvinkumar Chaudhari et al., 2012). Other two-dimensional model applications include the problems dealing with dam-break (Özgökmen et al., 2007), mechanism of pollutant(Michioka et al., 2010, Chung and Liu, 2013), heat transfer(Andrej Horvata, 2001, Matos et al., 1999), turbulent Convection (Chen and Glatzmaier, 2005) and Parallel Blade Vortex (Liu et al., 2012). The flow under investigation occurs due to sinusoidal velocity signal in the XY plane, with no other velocity signals in other domains. Hence, all the main flow phenomena of interest occurs in the XY plane except for the vortex stretching and secondary shedding which occur in the XZ and YZ planes. The author has reviewed the 2D assumption of the flow under consideration in their recent extensive review paper (Shehata et al., 2017) and concluded that the 2D assumptions are not influential in the flow structure nor the aerodynamic performance of the aerofoil under oscillating flow. Hence, the governing equations were reduced to two dimensional form, and solved accordingly. Consequently, and given the fact that this reduction is physically valid, the method of solution of the governing equation (i.e. LES) must follow the coordinate formalism of the governing equations, hence it was solved as two-dimensional problem.

In this section, two sets of experimental data were used to validate the numerical model from references. First, experimental data from references (Torresi et al., 2009, Torresi et al., 2007b, Torresi et al., 2007a) are used to simulate and validate the stall condition. Details of the first validation case are given, where Wells turbine prototype under investigation is characterized by the following parameters: hub radius, is equal to101 mm; tip radius, equal to 155 mm; NACA0015 blade profile with constant chord length, equal to 74 mm; and number of blades, equal to 7. Therefore, the hub-to-tip ratio and the solidity are equal to 0.65 and 0.64, respectively. The uncertainty in the measurements is 5%. The blades have been produced with composite material reinforced by carbon fiber with suited attachment. Second, experimental data from reference (Nomura et al., 2003) are adopted to simulate and validate the unsteady sinusoidal wave inlet velocity, where experimental data for unsteady forces (F_D) acting on a square cylinder in oscillating flow with nonzero mean velocity are measured.

For unsteady flow with non-oscillating velocity, Figure 4.9 shows a very good agreement between measured torque coefficient from reference (Torresi et al., 2009) and calculated torque coefficient from CFD result at Reynolds number equal to 2×10^5. Time step was set as 0.0089 second in order to satisfy CFL condition equal to 1. It can be noted from Figure 4.8 that the computational model has (approximately) the same stall condition value as the reference. The comparison between those results and the percentage of error are shown in Table 4.2.

Furthermore, for unsteady flow with sinusoidal inlet velocity, see equation 4.1. Figure 4.10 shows a very good agreement between measured drag force from reference (Nomura et al., 2003) and calculated drag force from CFD at two different frequencies (2 Hz and 1 Hz). Figure 4.10 show that the computational model has (approximately) the same behaviour of oscillating flow condition as the reference; see also the error percentage in Table 4.3 for the two frequencies.

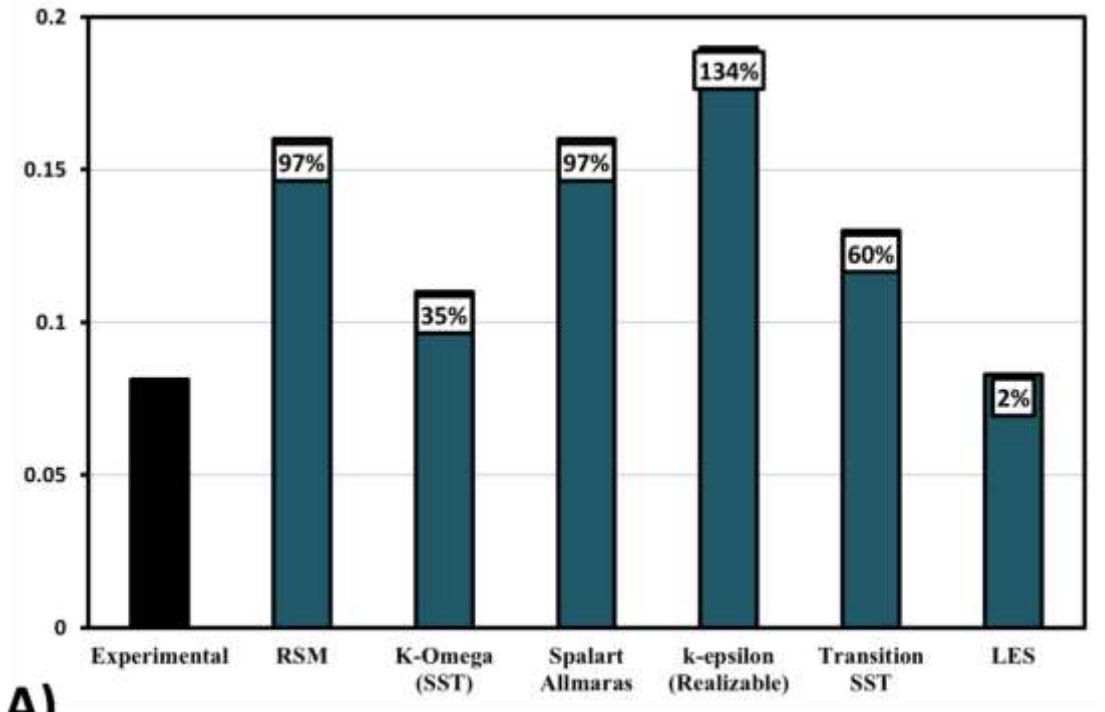
0.2
0.15
0.1
0.05
0
97%
35%
97%
134%
60%
2%
Experimental
RSM
K-Omega (SST)
Spalart Allmaras
k-epsilon (Realizable)
Transition SST
LES

A)

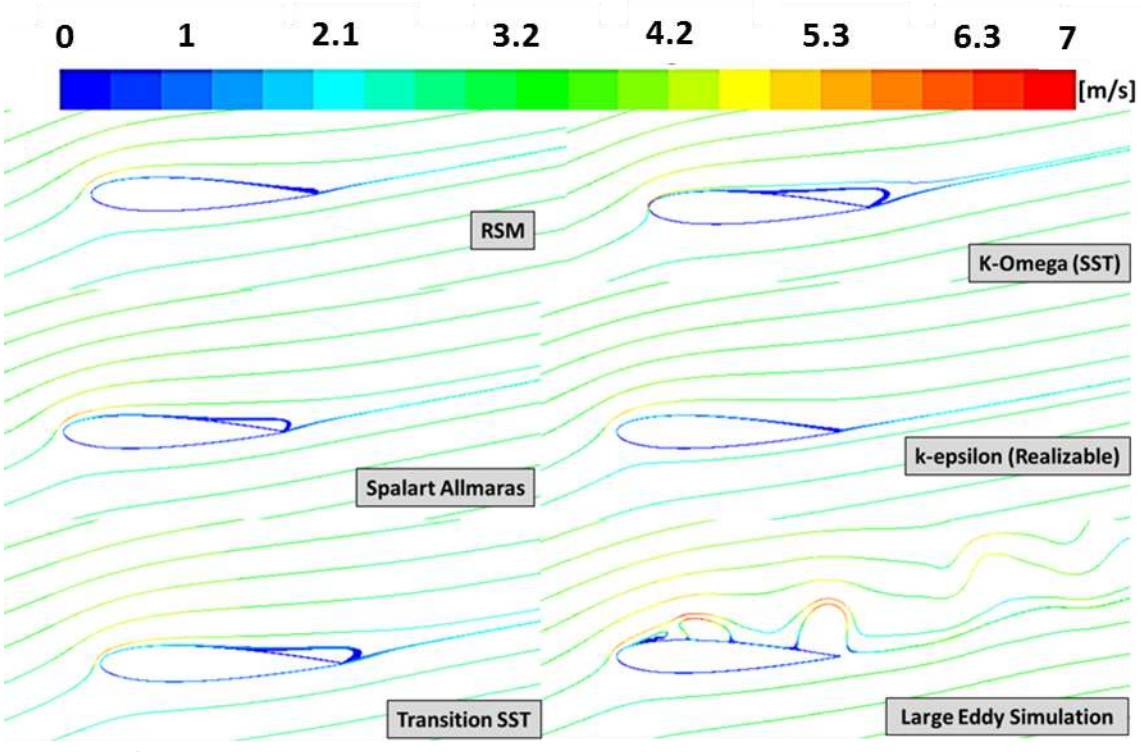
0
1
2.1
3.2
4.2
5.3
6.3
7
[m/s]
RSM
K-Omega (SST)
Spalart Allmaras
k-epsilon (Realizable)
Transition SST
Large Eddy Simulation

B)

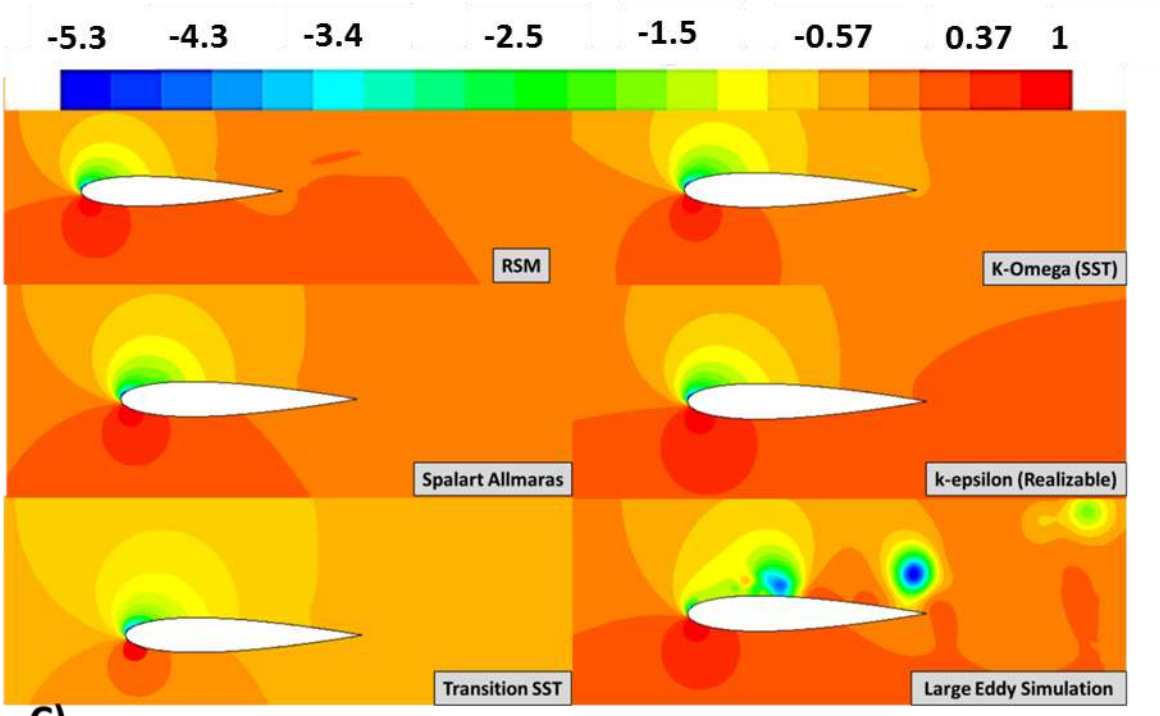
-5.3
-4.3
-3.4
-2.5
-1.5
-0.57
0.37
1
RSM
K-Omega (SST)
Spalart Allmaras
k-epsilon (Realizable)
Transition SST
Large Eddy Simulation

C)

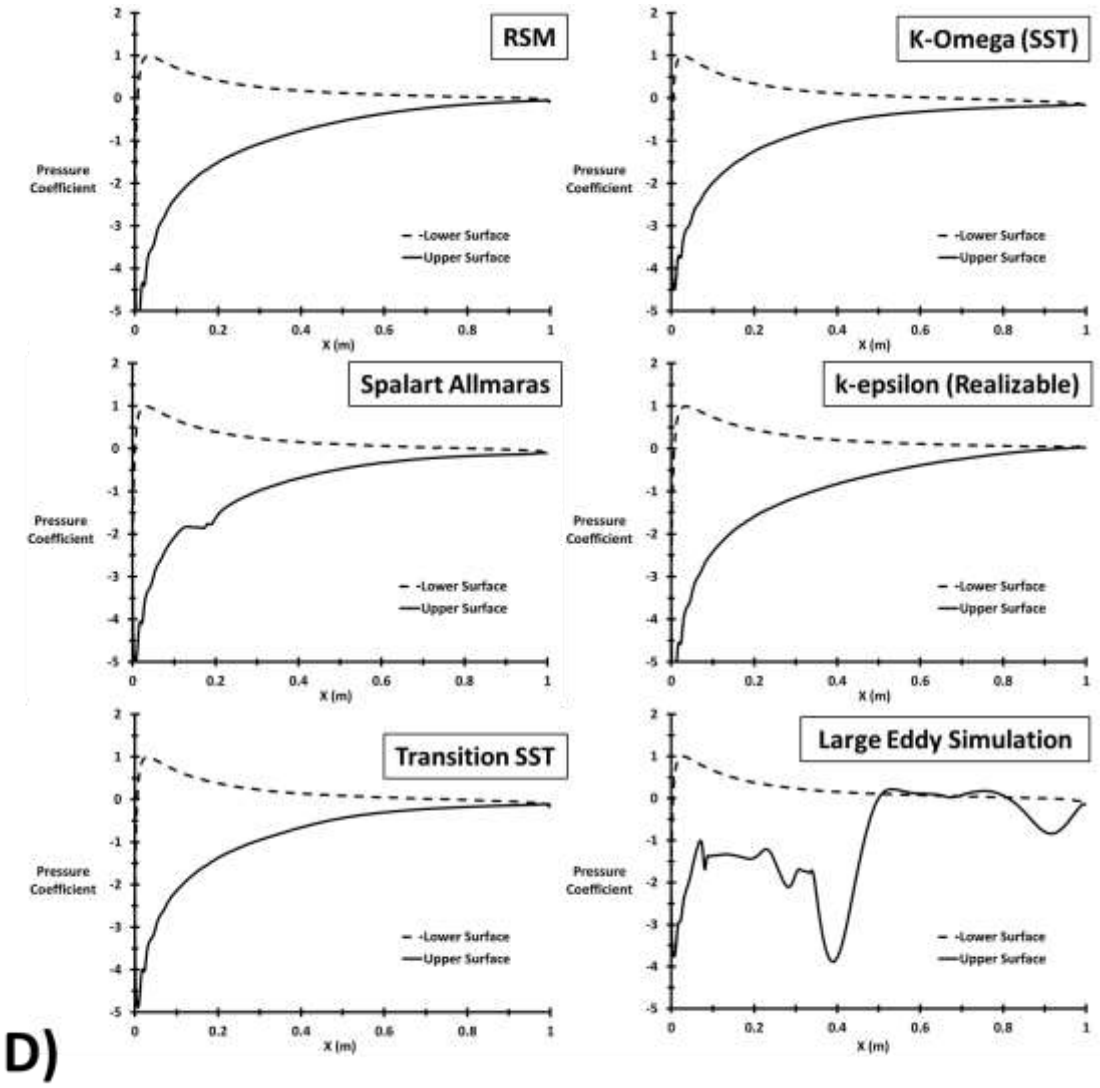

Figure 4.8 Comparison between different models to simulate the stall angle from experimental data A) Torque coefficient B) Path-line coloured by the velocity magnitude C) Contours of pressure distribution D) Pressure distribution at upper and lower surface

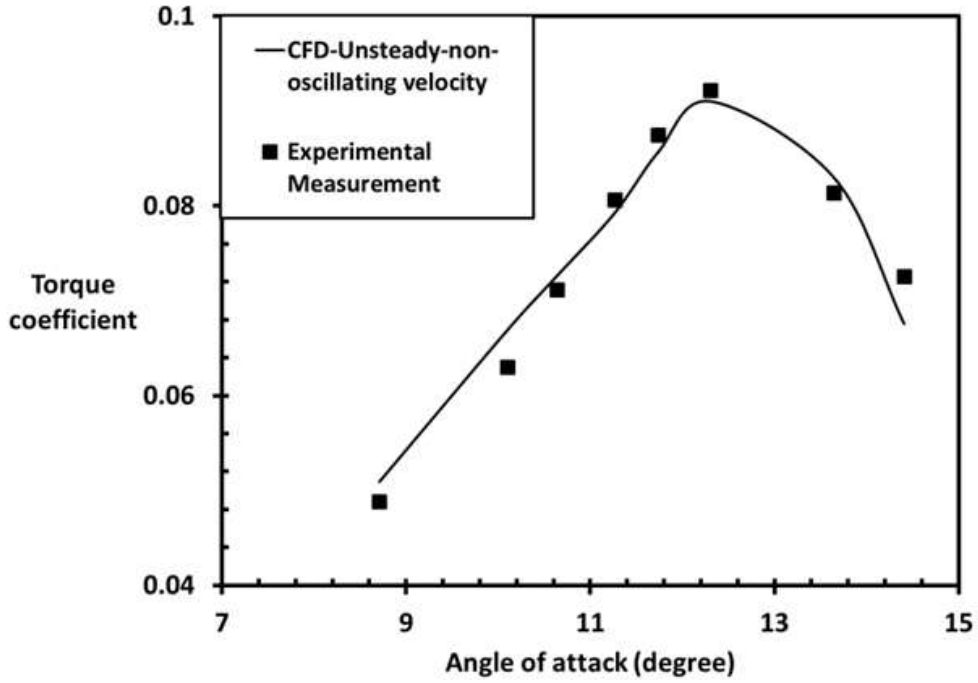

Figure 4.9 Measured torque coefficient from reference (Torresi, 2007) and calculated torque coefficient from CFD unsteady flow with non-oscillating velocity

Table 4.2 The error percentage between measured torque coefficient from reference (Torresi, 2007) and calculated torque coefficient from CFD under unsteady flow with non-oscillating velocity

Torque Coefficient	**Angle of attack (Degree)**							
	8.7	10.1	10.6	11.3	11.7	12.3	13.6	14.4
Experimental	0.0488	0.0631	0.0712	0.0807	0.0875	0.0922	0.0814	0.0725
CFD	0.0509	0.06689	0.0726	0.0793	0.0856	0.091	0.083	0.0676
Error %	4	6	2	-2	-2	-1	2	-7

Finally, from Figure 4.11 it can be noted that there is an excellent agreement between the result of computational model under sinusoidal inlet flow velocity and experimental data from (Torresi et al., 2009). The comparison of results and the percentage of error are shown in Table 4.4. The Large Eddy Simulation computational model has (approximately) the same stall condition value as the reference

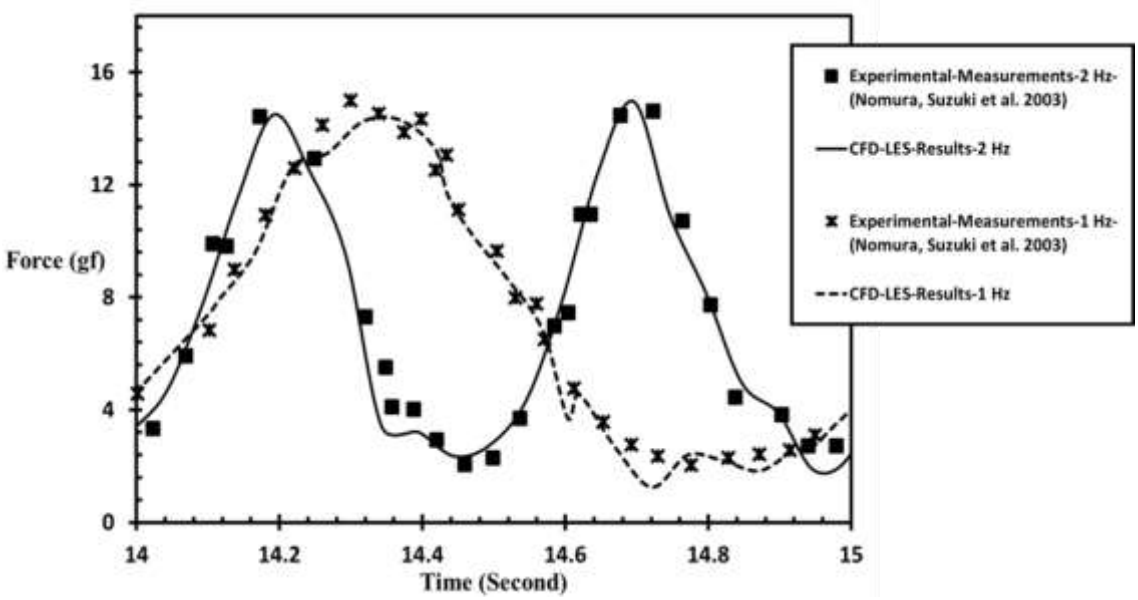

Figure 4.10 Measured unsteady in-line force F_D from reference ((Nomura, Suzuki et al. 2003) with angle of attack= 0 degree and F_D calculated from the present CFD

Table 4.3 The error percentage between measured F_D from reference ((Nomura, Suzuki et al. 2003) and calculated F_D from CFD under unsteady flow with sinusoidal inlet velocity

Frequency 2 Hz											
F_D **(gf)**	**Time (Second)**										
	14.02	14.1	14.12	14.3	14.4	14.5	14.6	14.7	14.8	14.9	15
Experimental	3.4	7.7	9.9	12.9	4.11	2.3	7.5	14.7	10.7	3.9	2.7
CFD	3.8	7.8	9.8	12.5	3.4	2.7	7.8	14.9	10.9	3.8	2.4
Error %	11	1	-1	-4	-17	17	4	1	2	-2	-11
Frequency 1 Hz											
Experimental	4.5	6.9	12.6	14.1	13	10.2	7.8	4.7	2.8	2.3	3
CFD	4.6	7.2	12.6	13.1	13.2	10.3	8.6	4.5	2.7	2.2	3.3
Error %	2	4	0	-7	1	1	10	-4	1	-4	10

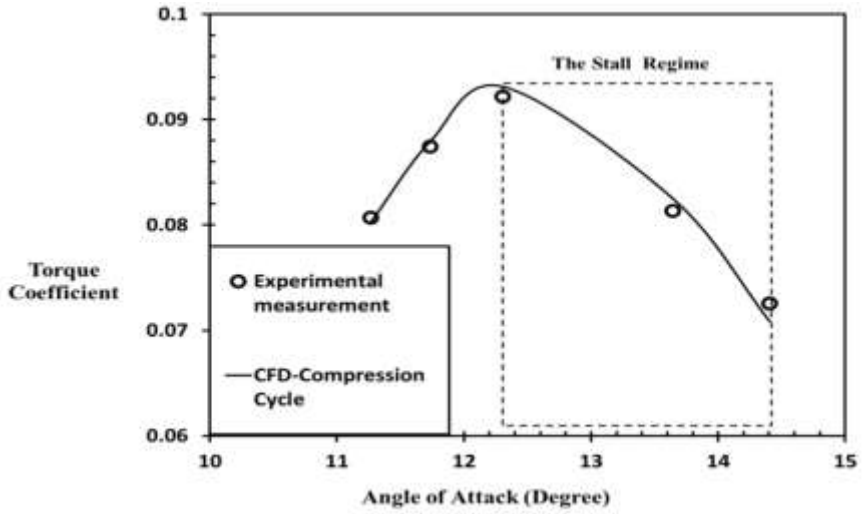

Figure 4.11 Measured torque coefficient from reference (Torresi, 2007) and calculated torque coefficient from CFD unsteady flow with sinusoidal inlet velocity

Table 4.4 The error percentage between measured torque coefficient from reference (Torresi, 2007) and calculated torque coefficient from CFD under unsteady flow with sinusoidal inlet velocity

Torque Coefficient	**Angle of attack (Degree)**				
	11.3	11.7	12.3	13.6	14.4
Experimental	0.0807	0.0875	0.0922	0.0814	0.0725
CFD	0.0803	0.0879	0.0931	0.0825	0.0709
Error %	-1	1	1	1	-2

4.5 Summary

In this chapter, the verification and validation results for CFD models were introduced. Also the computational model and boundary conditions were presented. It can be concluded that the normal operating can be simulated using the unsteady RANS equations with a Realizable k-ε model for the initializations, and then the stall condition can be clarified by using the Large Eddy Simulation for non-oscillating velocity and the sinusoidal flow. The computational models from this chapter were used as a basic model structure for the models that will be used in the next two chapters. The verification and validation result from this chapter were used in all the output publications from this thesis.

PART III Analysis and Improvement for Wells Turbine Performance with Different Cases Study

Chapter 5 Performance Analysis of Wells Turbine Blades using EGM method

5.1 Introduction

The Entropy Generation Minimization (EGM) method aims at minimizing the production of S_G in order to increase the second low of thermodynamic efficiency (see equation 3.45). This method has three steps: the first one calculates the entropy of a system at specific design, initial, boundary and operating conditions; the second one optimizes the system parameters (design, initial, boundary and operating conditions); and the last one calculates the entropy of the optimized system and checks the entropy generation and/or the second low efficiency. There is the local (detailed) EGM, which is the application of the second law on each component of the system at detailed conditions for each component to get the entropy generation due to each component of the system. The local EGM is used to optimize system design and optimize the characteristics, performance and operating conditions of each component within a system. Also, there is the global EGM, which is the application of the second law on the system as a whole at the input and output conditions, in order to get the global entropy generation rate for the system. The global EGM is used to compare different systems or the same system with different operating conditions. The last one will be used in the analysis and results, which are presented hereafter. This chapter is performed by using time-dependent CFD models of different NACA aerofoils (NACA0012, NACA0015, NACA0020, and NACA0021) under sinusoidal flow boundary conditions based on unsteady RANS-$k-\varepsilon$ Realizable model. Numerical investigations are carried out for the incompressible viscous flow around the blades to obtain the entropy generation due to viscous dissipation. Where, the V_o and V_{am} are equal to 0.04 and 2.88 m/s respectively, in addition the time period equal to 6 seconds (f equal to 0.167 Hz) is set as one period in this simulation considering to the literature survey (Kim et al., 2002b, Setoguchi et al., 2003a), see Figure 5.1. Time step is set as 0.009 second in order to satisfy CFL

condition equal to 1. The sinusoidal wave condition creates various Reynolds number up to 2.4×10^5 and this maximum value which is taken from many references such as (Kim et al., 2002b, Setoguchi et al., 2003a, Kinoue et al., 2003a, Kinoue et al., 2004, Mamun et al., 2004, Mohamed et al., 2008, Takao et al., 2007, Mohamed and Shaaban, 2014, Mohamed et al., 2011).

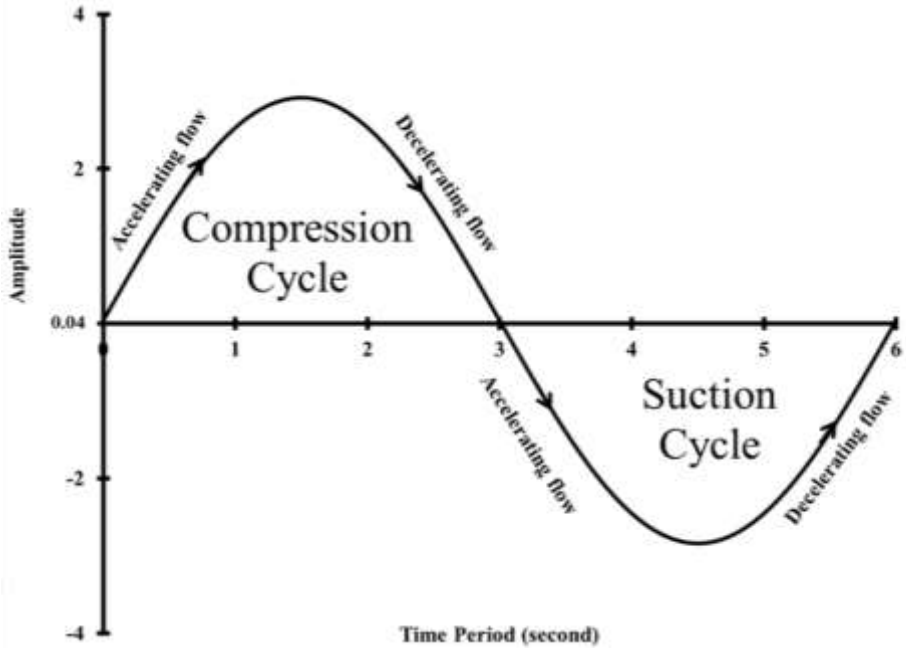

Figure 5.1 The sinusoidal wave boundary condition, which represent a regular oscillating water column

5.2 Evaluation of the second law efficiency of different NACA aerofoils

5.2.1 Steady

The numerical simulations were used to obtain local entropy viscosity predictions of the different aerofoil sections. There is a wide dispute in literature on the optimum aerofoil of the NACA standard series for Wells turbine applications. A considerable number of studies cite the results of (Raghunathan et al., 1981a) as a reference for considering NACA 0021 aerofoil to give the optimum performance for conventional Wells turbines. The present work aspires to shed light on such dispute from another perspective: second-

law analysis. Figure 5.2 shows a comparison among the global entropy generation rates for four different aerofoils. From Figure 5.2 it can be noted that the NACA0015 aerofoil section gives less value of total entropy generation.

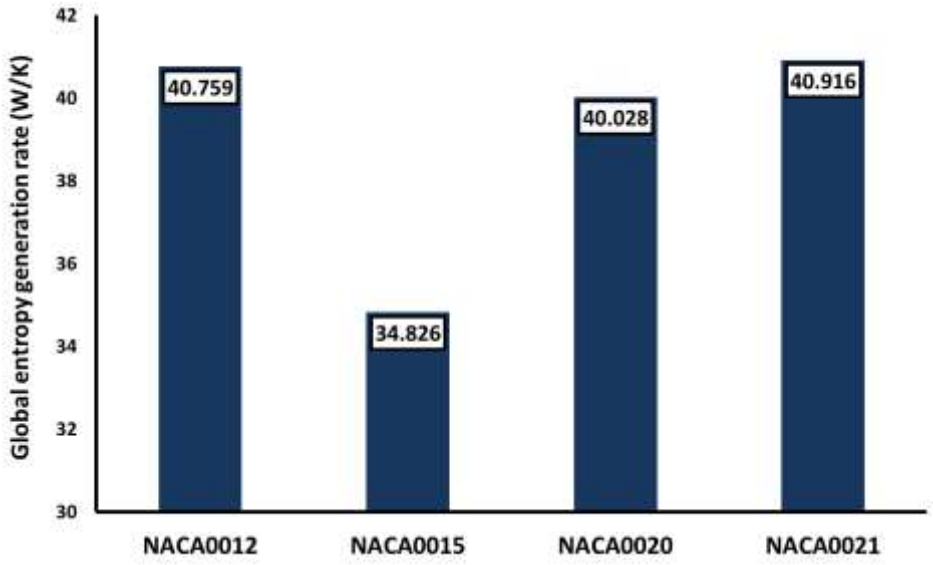

Figure 5.2 The global entropy generation rates with different aerofoil sections

To study the relationship between the Reynolds number effect and the entropy, it was simulated the flow over NACA0015 and NACA0021 aerofoils under different Reynolds number, as shown in Figure 5.3. The Reynolds number had a radical effect on the entropy generation. When the Reynolds number was increased from 6×10^4 to 1×10^5, the total entropy generation increased correspondingly higher than two folds for both aerofoils. However, when Reynolds number was increased further to 2×10^5, the total entropy generation exhibited unintuitive values ranging from 25% less to 20% higher than the corresponding value at Reynolds number equal to 1×10^5 for both aerofoils, as shown in Figure 5.3. The reason behind such phenomena can be attributed to the nonlinear complexity of the viscous dissipation term (equation 3.42), where both the square of mean rate of strain and velocity divergence contribute to the local viscous irreversibilities.

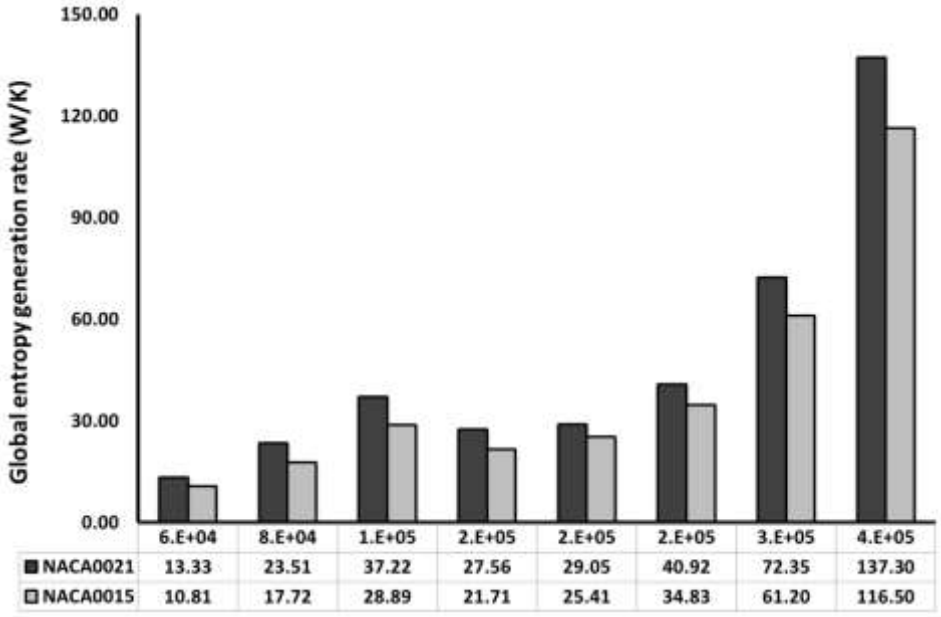

Figure 5.3 The global entropy generation rates with different Reynolds Number

5.2.2 Unsteady

The numerical simulations were used to obtain local entropy viscosity predictions of the different aerofoil sections. Figures 5.4 (a) and (b) highlight the entropy behaviour when a flow was accelerating in compression and suction cycle. Consequently, the entropy generation ratio varies with the Reynolds number at angle of attack equal to 2 degrees. The change of Reynolds number values was due to using sinusoidal wave boundary conditions. At low values of Reynolds number, the stall condition occurs at small value of angle of attack (Sheldahl and Klimas, 1981). Hence, 2 degree angle of attack was chosen to avoid the stall condition.

The Reynolds number was calculated from equation (3.26). However, the value of Reynolds number in this study can be controlled by the value of velocity, while keeping the other parameters constant.

The Reynolds number has a radical effect on the entropy generation. This was obvious in the accelerating flow in compression and suction cycle in Figures 5.4 (a) and (b), where Reynolds number increases from 6×10^4 to 1.2×10^5. As a result, the global entropy

generation rate has increased correspondingly for higher than two folds of all aerofoils. However, when Reynolds number has increased further to 1.7×10^5 (2×10^5 for NACA0012 at compression cycle) the global entropy generation rate exhibited unintuitive values ranging from 50% less to 40% lower than the corresponding value at Reynolds number equal to 1.2×10^5 for all aerofoils.

The reason behind such phenomena is also the same reason of steady condition, which can be attributed to the nonlinear complexity of the viscous dissipation term (equation 3.42) where both the square of mean rate of strain and velocity divergence contribute to the local viscous irreversibilities. This phenomenon suggests possible existence of critical Reynolds number at which viscous irreversibility takes minimum values. At high Reynolds number (greater than 2×10^5), the change in velocity value, see equation 4.1, was smaller than low Reynolds number, where at 1.2×10^5 Reynolds number the velocity becomes equal to 17.5 m/s, then increases to 24.8 m/s at 1.7×10^5 Reynolds number (41%increase rate). After that, it reaches 2×10^5 Reynolds number with velocity equal to 30.3 m/s (22%increase rate). On the other hand, at high Reynolds number (2.3×10^5), the velocity becomes equal to 33.8 m/s (10%increase rate). Then, at 2.4×10^5 Reynolds number, the velocity reaches maximum value equal to 35.04 m/s (3%increase rate), see Figure 5.1. This leads to a smaller change in flow field and entropy generation. The last one was dependent on velocity gradient see equation (3.42).

However, in Figures 5.5 (a) and (b) for decelerating flow in compression and suction cycle when Reynolds number, in Figure 5.5 (a), further decreased to 1.2×10^5, the global entropy generation rate exhibited unintuitive values ranging from 94% (NACA0021, NACA0020) less to 59% (NACA0015) and 15% for (NACA0012) higher than the corresponding value at Reynolds number equal to 1.7×10^5. For decelerating flow in suction cycle, the global entropy generation rate, at Reynolds number equal to 1.2×10^5, exhibited unintuitive values ranging from 135% (NACA0012) less to 83% (NACA0020) and 68% (NACA0021, NACA0015) which was higher than the corresponding value at Reynolds number equal to 1.7×10^5. Then, when Reynolds number further decreased to a

minimum value, the global entropy generation rate also decreased to a minimum value and not equal to zero.

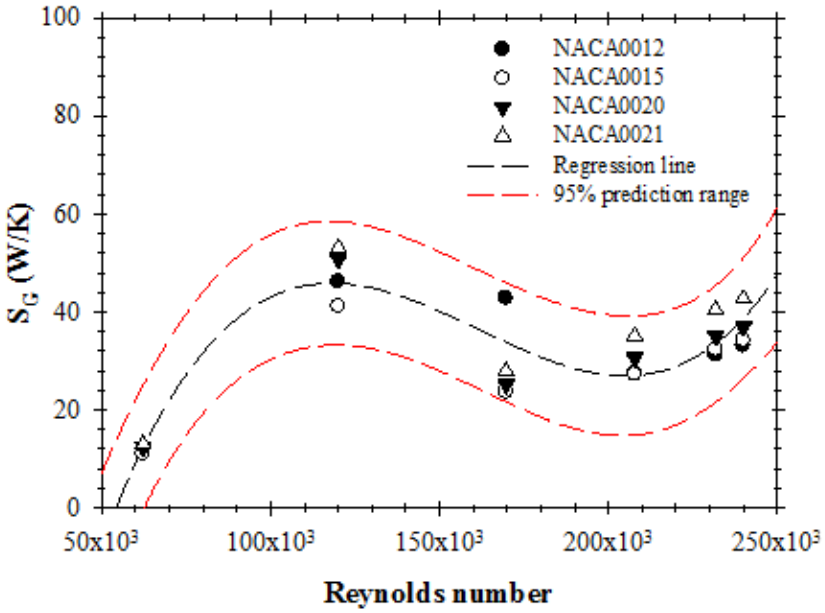

(a) Compression cycle

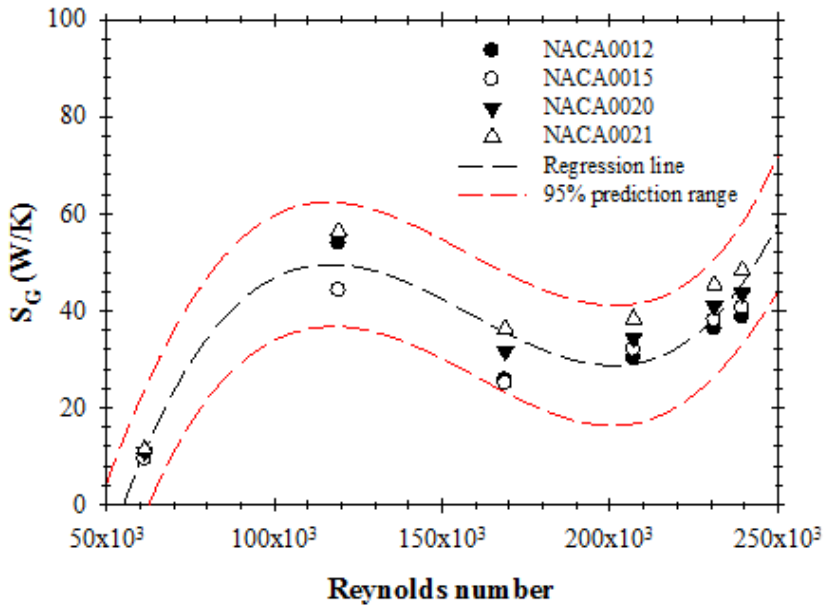

(b) Suction cycle

Figure 5.4 S_G variation with different Reynolds's number at accelerating flow (a) compression cycle for four different aerofoils (b) suction cycle for four different aerofoils

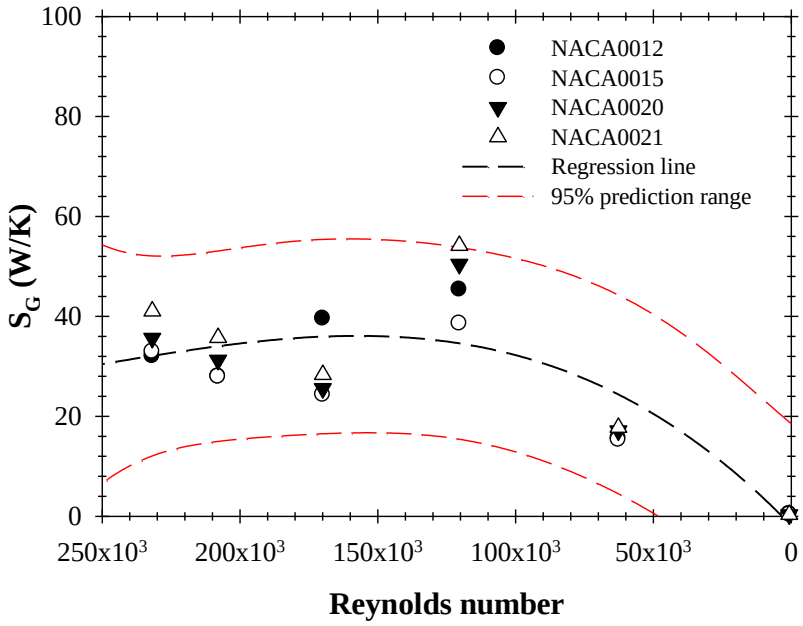

(a) Compression cycle

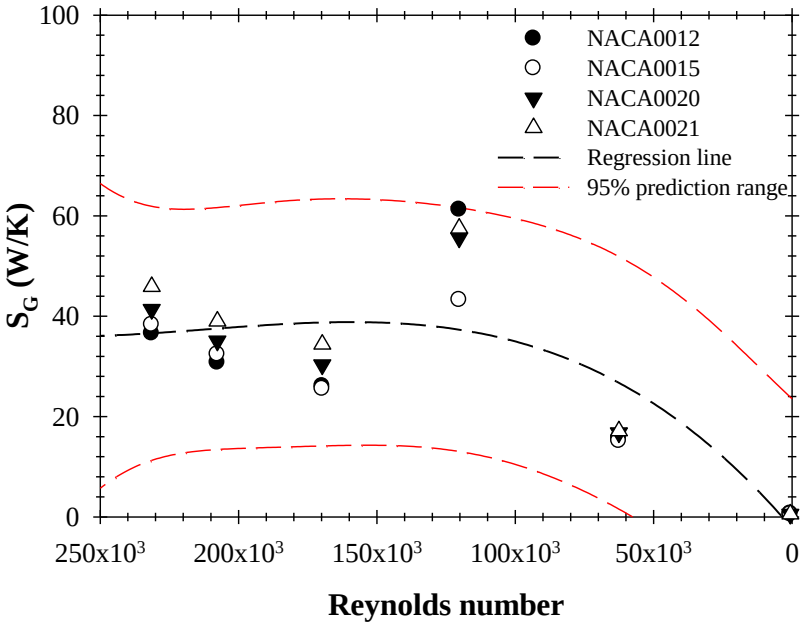

(b) Suction cycle

Figure 5.5 S_G variation with different Reynolds's number at decelerating flow (a) compression cycle for four different aerofoils (b) suction cycle for four different aerofoils

From Figures 5.4 and 5.5, at maximum Reynolds number, the NACA0012 gives a lower entropy generation rate than other aerofoil. From Figure 5.6, it can be concluded that the NACA0015 gives a lower maximum value for the global entropy generation rate than other aerofoils in both cycles. The NACA0015 aerofoil section gives less average value ranging from 20% less to 10% of the global entropy generation rate during the sinusoidal wave cycle, see Figure 5.7. To confirm these results, a comparison was conducted between the second law efficiency for four different aerofoils at compression and suction cycle (Figure 5.8) and also for the total average efficiency during the sinusoidal wave cycle (Figure 5.9), NACA0015 gives best efficiency when it was compared with other aerofoils in both compression and suction cycle and therefore in total sinusoidal wave cycle ranging from 2% less to 1%. In four different aerofoils and at certain angle of attack, the efficiency for compression cycle becomes higher than suction cycle, ranging from 1% less to 0.3%.

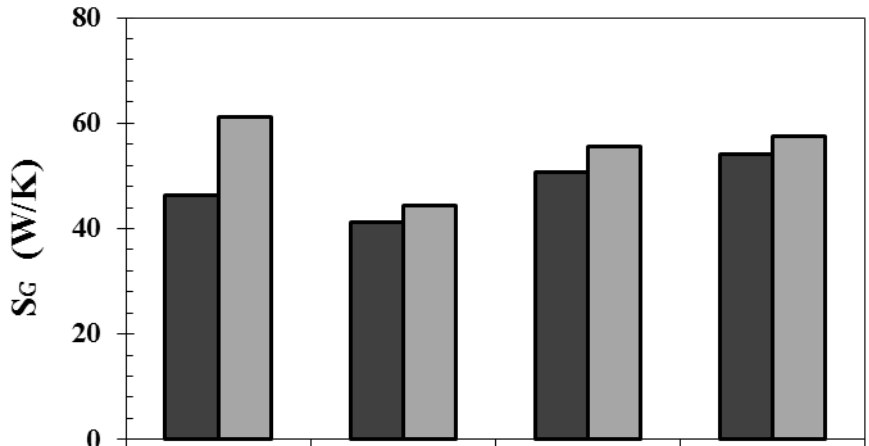

	NACA0012	NACA0015	NACA0020	NACA0021
Comp.	46.23	41.13	50.66	54.14
Suct.	61.24	44.25	55.60	57.50

Figure 5.6 The maximum value for S_G at compression and suction cycle

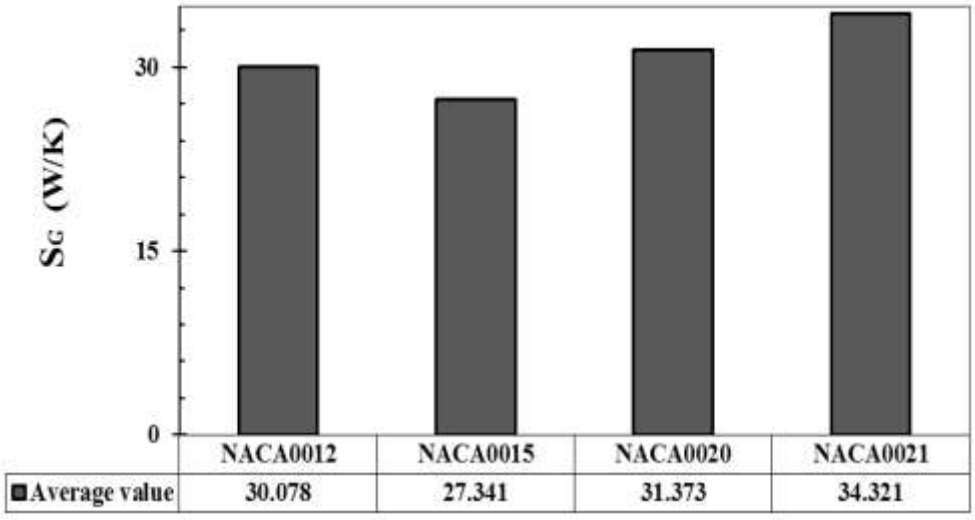

Figure 5.7 Comparisons between S_G during the sinusoidal wave cycle for four different aerofoils

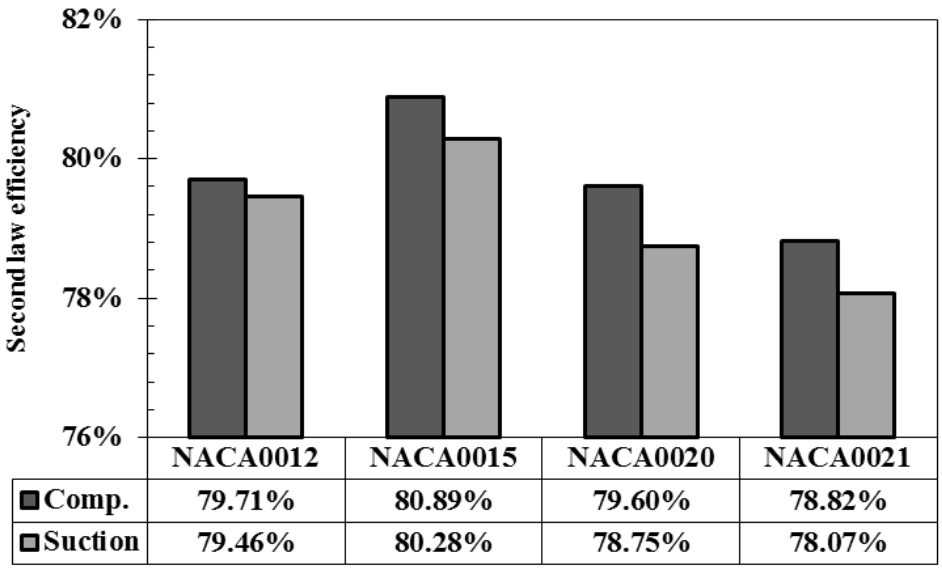

Figure 5.8 Comparisons between second law efficiency during the compression and suction wave cycle for four different aerofoils

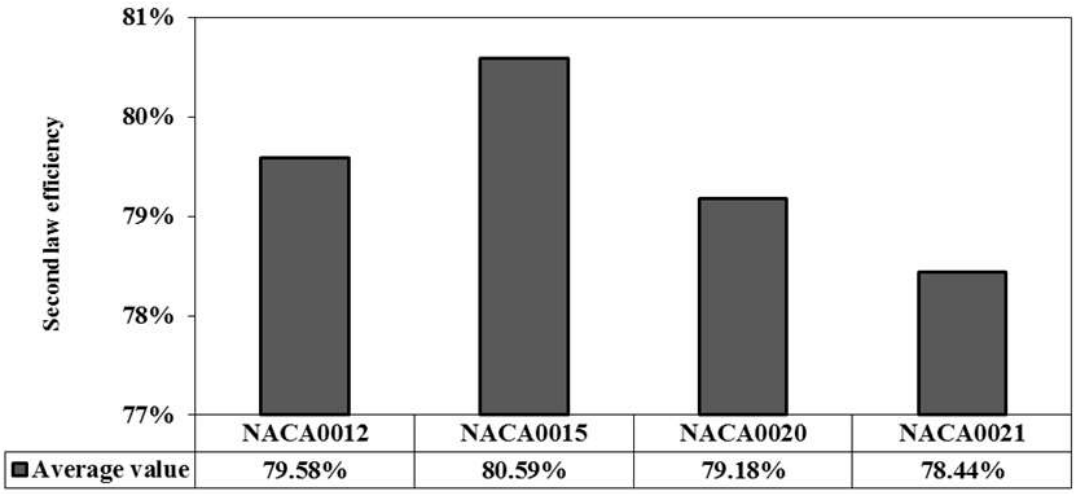

Figure 5.9 Comparisons between second law efficiency during the sinusoidal wave cycle for four different aerofoils

Contours of Exergy around the blade of NACA0015 for angle of attack 2 degree at different time and different velocity along the sinusoidal wave can be seen in Figure 5.10 that the positive value of velocity refers to compression cycle and the negative value refers to suction cycle. From this Figure, it can be observed that as the velocity increases, the value of exergy around the blade increases; However, the leading and trailing edge always has the lowest value, but at compression cycle, the area around the trailing edge has a lower value than the leading edge, and in the suction cycle, the area around the leading edge has a lower value than the trailing one.

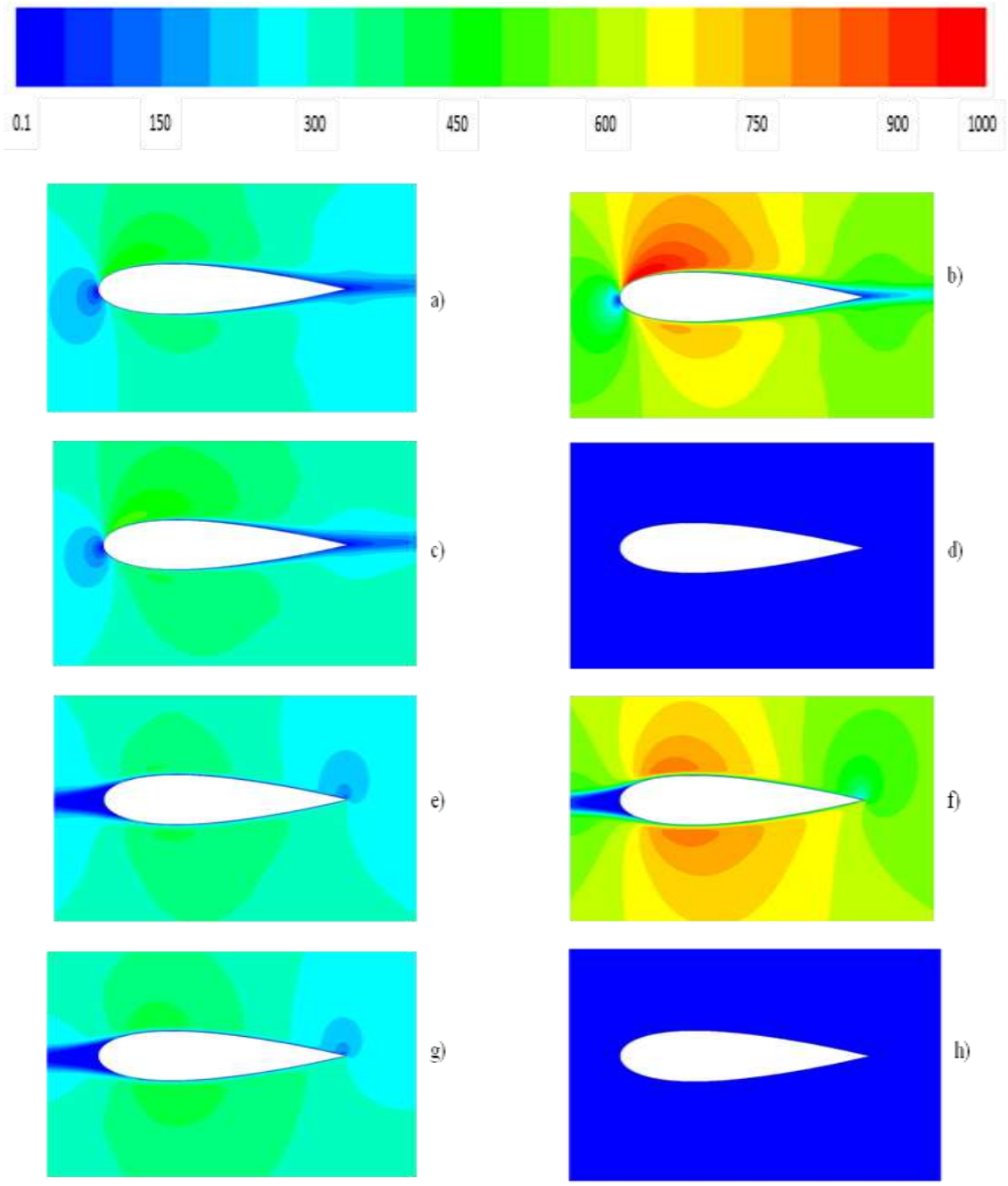

Figure 5.10 Contours of Exergy around the blade of NACA0015 with angle of attack 2 degree under sinusoidal wave, a) at t = 0.837 s b) t = 1.674 s c) t = 2.511 s d) t = 3.348 s e) t = 4.185 s f) t = 5.022 s g) t = 5.859 s h) t = 6.696 s

5.3 Effect of the angle of attack on entropy generation

5.3.1 Steady

The increase of angle of attack has a direct effect on the total entropy generation in the flow over both aerofoils, similar to the effect of Reynolds number. However, as shown in Figure 5.11, each aerofoil had a different entropy generation signature for different angle of attack. NACA0021 aerofoil yielded less entropy generation than NACA0015 at low angles ($\theta < 20^{o}$), while such a trend was reversed when higher angles were considered.

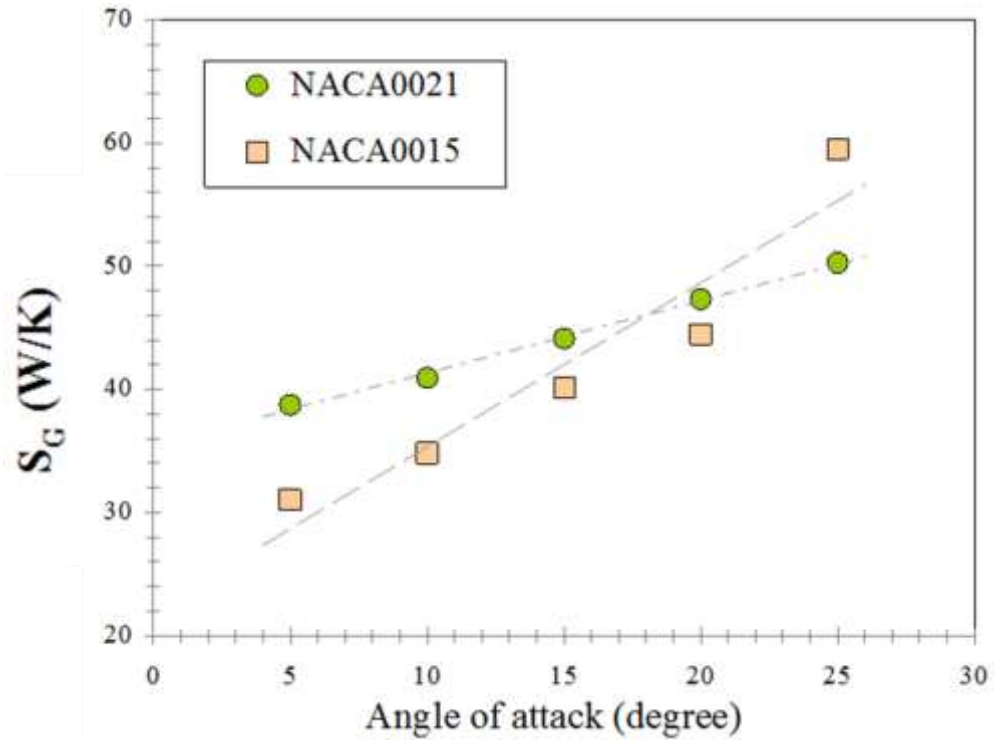

Figure 5.11 The Entropy-viscosity integral with different angle of attack

5.3.2 Unsteady

From Figures 5.12 (a) and (b), NACA0015 aerofoil has a different entropy generation values for different angles of attack listed in Table 5.1. For accelerating flow in compression cycle, Figure 5.12 (a) at Reynolds number equal to 1.2×10^{5}, the maximum

value of global entropy generation rate occurs due to 2 degree angle of attack but the minimum value of it occurs due to -15 degree angle of attack. The 17 degree angle of attack gives maximum global entropy generation rate at 1.7×10^5 Reynolds number, and the minimum value occurs due to -11 degree at the same Reynolds number. Finally, at Reynolds number equal to 2.3×10^5 and 2.4×10^5 the maximum global entropy generation rate occurs due to 17 degree and the minimum value occurs due to 5 degree.

Table 5.1 The direction for positive and negative value of angle of attack

Angle of attack	x component of velocity direction	y component of velocity direction
-15	0.966	-0.259
-11	0.982	-0.191
-5	0.996	-0.087
0	1	0
2	0.999	0.035
5	0.996	0.087
8	0.990	0.139
11	0.982	0.191
15	0.966	0.259
16	0.961	0.276
17	0.956	0.292
20	0.940	0.342
25	0.906	0.423

The trend of global entropy generation rate at suction cycle was different from the compression cycle at various angles, which can be seen in Figure 5.12 (b). For decelerating flow in suction cycle at Reynolds number equal to 1.7×10^5, the maximum global entropy generation rate occurs at 5 degree angle of attack and the minimum value occurs due to 25 degree. For Reynolds number equal to 1.2×10^5, the maximum global

entropy generation rate occurs due to 2 degree angle of attack and the minimum value due to 25 degree.

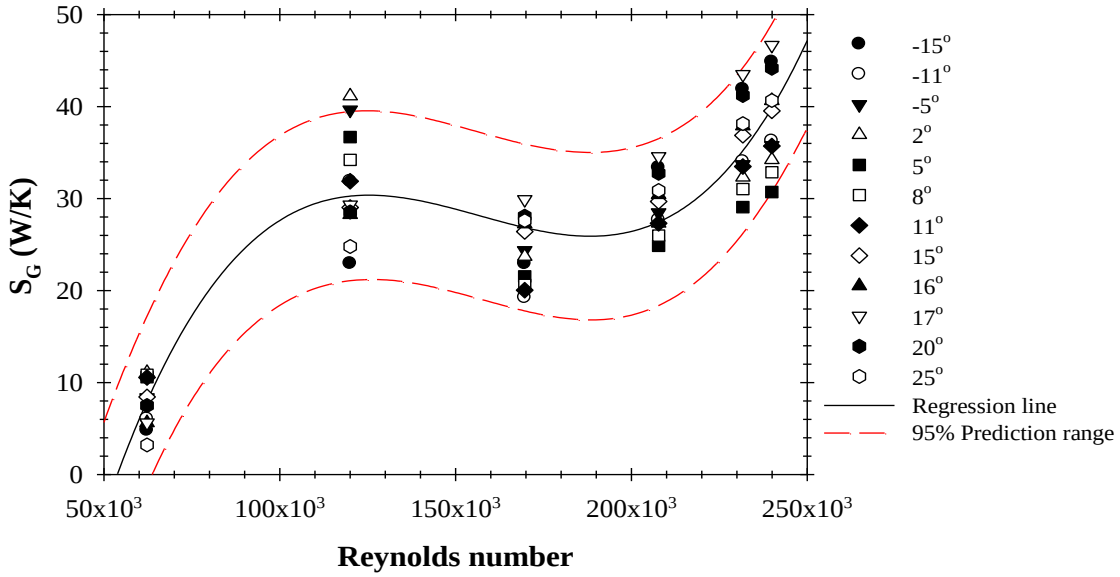

(a) Accelerating flow in compression cycle

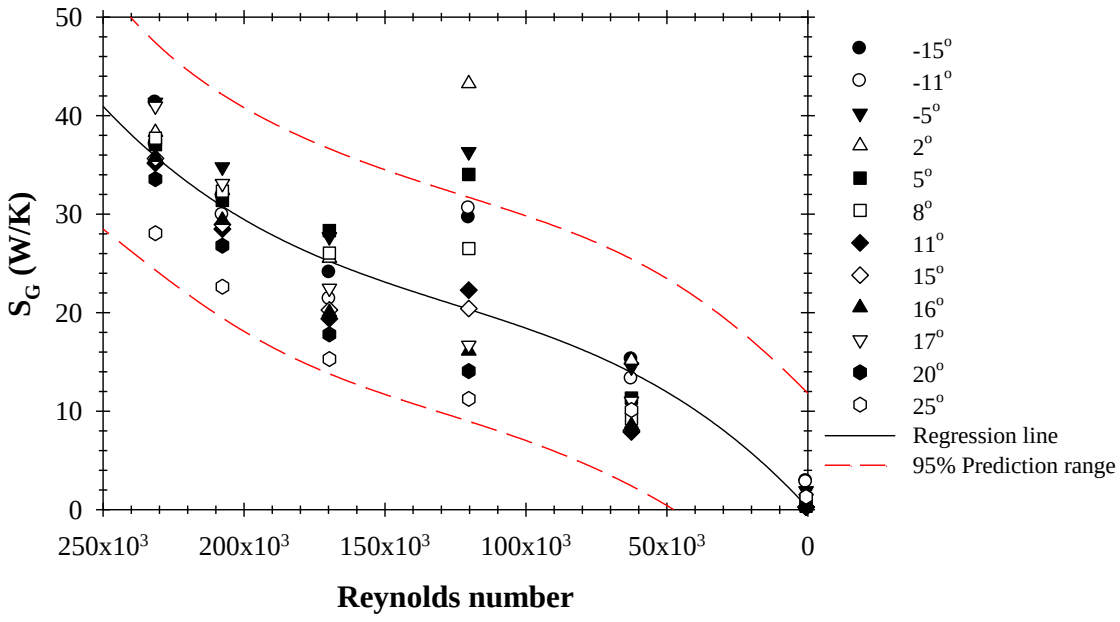

(b) Decelerating flow in suction cycle

Figure 5.12 S_G variation with different Reynolds's for NACA0015 aerofoil with different angle of attack (a) Accelerating flow in compression cycle (b) Decelerating flow in suction cycle

Low angles of attack around zero, both positive and negative direction, have a higher global entropy generation rate and lower entropy efficiency, except at 17 degree, therefore it can be noted that there is an unexpected increase in the value of global entropy generation rate accompanied by a lack of the second law efficiency, see Figures 5.13 and 5.14. As for the angle of attack from -5 to 5 degree, the entropy efficiency for compression cycle was higher than the suction cycle, but when the angle of attack increases in both directions, the efficiency for suction cycle exceeds the compression cycle, see Figure 5.15. At the same angle of attack but in a different direction, the positive direction gives higher efficiency than the negative one. For example, the second law efficiency for 5 degree was higher approximately 0.5% than -5 degree and approximately 0.1% between 11 and -11 degree and finally 0.3% between 15 and -15 degree. The minimum value for the global entropy generation rate accompanied by maximum value of the second law efficiency was happened at zero degree of angle of attack (the original position). Where, the entropy value depends on the velocity gradient (see equation 3.42). Furthermore, at different angles of attack the velocity gradient was also change which led to increase in the global entropy generation rate.

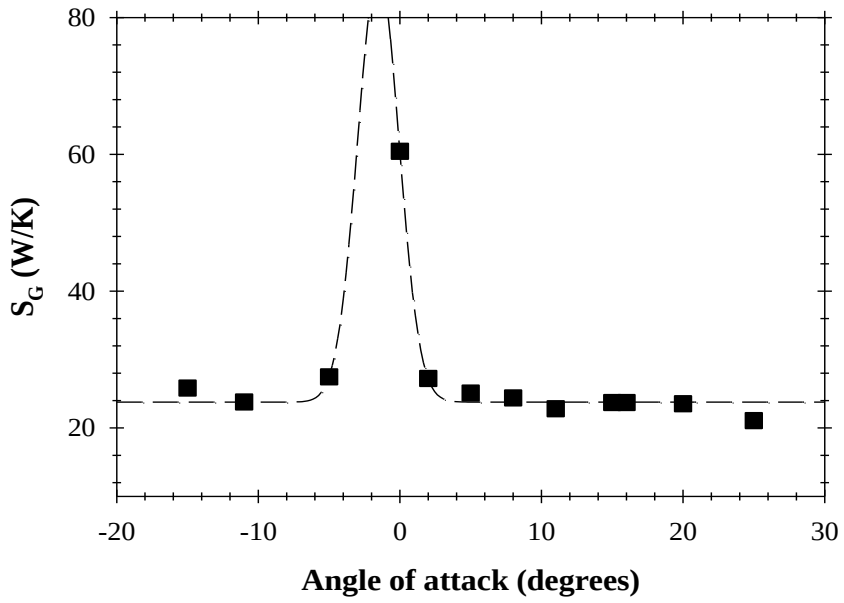

Figure 5.13 S_G during the sinusoidal wave cycle for different angle of attack. The dotted line indicates a fitting with a Gaussian distribution function

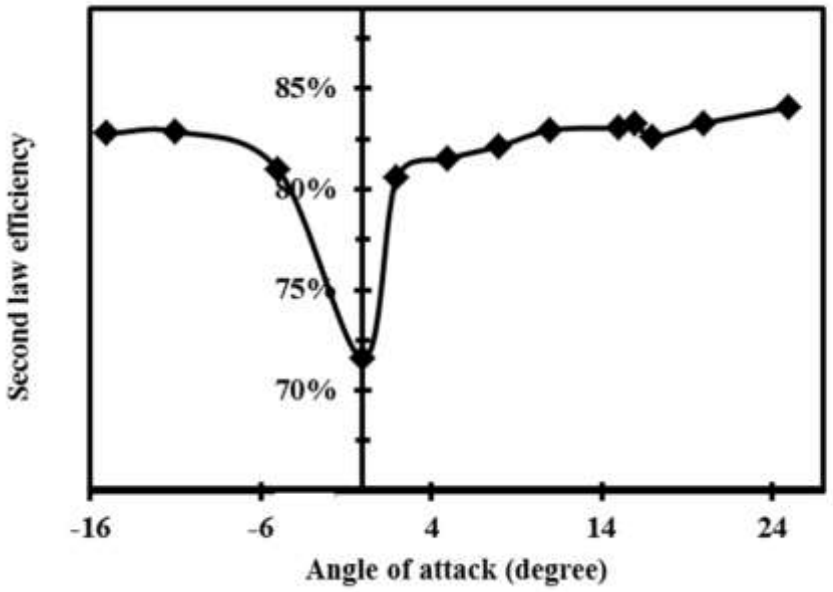

Figure 5.14 Second low efficiency during the sinusoidal wave cycle for different angle of attack

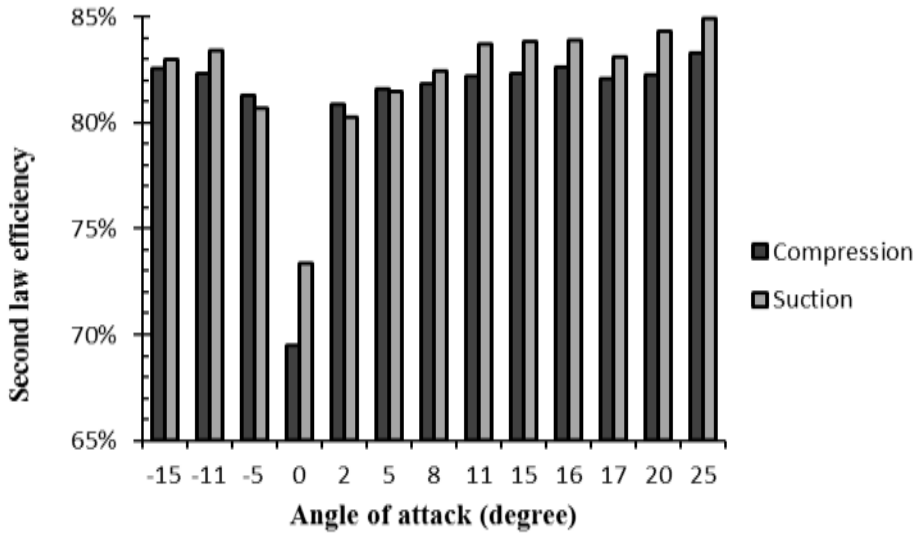

Figure 5.15 Comparisons between second law efficiency during the compression and suction wave cycle for different angle of attack

5.4 Case Study (Northern Coast of Egypt)

The most energetic coast of the Southern Mediterranean Basin is the Egyptian coast, lying between the Nile Delta and the Libyan borders with a potential of above 3.35 kW/m wave power in summer and 6.8 kW/m in winter (Mørk et al., 2010, Barstow et al., 2009) and the wave energy of about 36003 kWh/m. The most energetic sea states have significant wave heights between 1 and 4 m and wave energy periods between 4 and 8 s. The regions with increased wave energy potential are mainly the western and southern coastlines of Cyprus Island, the sea area of Lebanon and Israel, as well as the coastline of Egypt, especially around Alexandria. The significant differences between the sea in Egypt and other seas are that the sea wave in Egypt is relatively low but also stable. Hence, the potential wave energy can be revealed and exploited (Zodiatis et al., 2014). However, sea states with the wave heights greater than 5 m are not very important for the annual energy (Ayat, 2013).

The objective of this section is to carry out a study to prove that the Wells turbine could be a suitable wave energy extractor for the Egyptian coasts and breakwater via a study

on the first law analysis (torque coefficient) and second law analysis (global entropy generation rate) for different turbine aerofoils. To achieve this purpose, numerical unsteady RANS-$k-\varepsilon$ Realizable model for Wells turbine aerofoils under sinusoidal wave flow conditions were built. The results were discussed using the first law analysis in addition to the second law analysis by using the entropy generation minimization method. Where the time period is equal to 4, 6, and 8 seconds (f equal to 0.25, 0.167 and 1.25 Hz) and is set as one period in this simulation, considering the real data from the Egyptian coasts (Ayat, 2013), and V_o and V_{am} are equal to 0.04 and 2.88 m/s respectively, see Figure 5.16. The time step is set as 0.0089 second in order to satisfy CFL condition equal to 1. Furthermore, the sinusoidal wave condition creates various Reynolds number up to 2×10^5 according to the reference (Torresi et al., 2009).

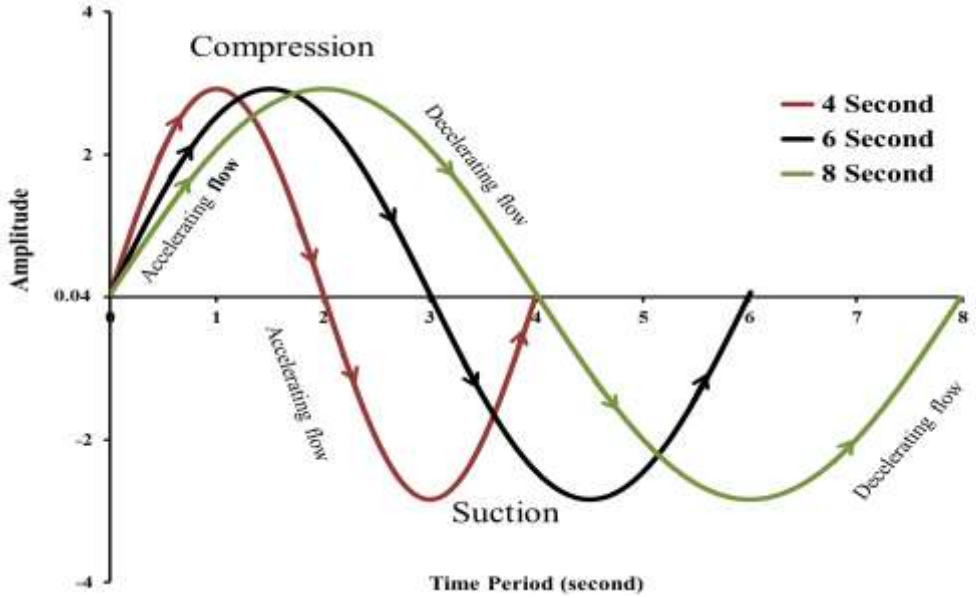

Figure 5.16 The sinusoidal wave's boundary condition, which represents a regular oscillating water column

5.4.1 First law of thermodynamics analysis

The comparison between the torque coefficient for accelerating and decelerating flow with four different aerofoils was shown in Figure 5.17. It can be noted that the sinusoidal wave with t_{sin} of 4 sec has a large torque coefficient. Moreover, the torque coefficient

value at decelerating flow is always higher than that at accelerating flow, except NACA0015 for sinusoidal wave with 6 sec. In addition, the sinusoidal wave with 8 sec has the smallest difference in torque coefficient values between accelerating and decelerating flow as show in Table 5.2.

To understand the reasons why the torque coefficient at decelerating flow is mostly higher than that at accelerating flow, the contours and path line of velocity around the blade were investigated. Figures 5.18 and 5.19 show the contours and path line of velocity magnitude around the NACA0020 aerofoil blade at the same instantaneous velocity (2.08 m/s). It can be shown that at an accelerating flow, the aerofoil has very low velocities (see Figure 5.18) and a high separation layer (see Figure 5.19) at the trailing edge area than that in a decelerating flow condition. This difference between the accelerating and the decelerating flow decreases, with an increase in t_{sin} for the sinusoidal wave.

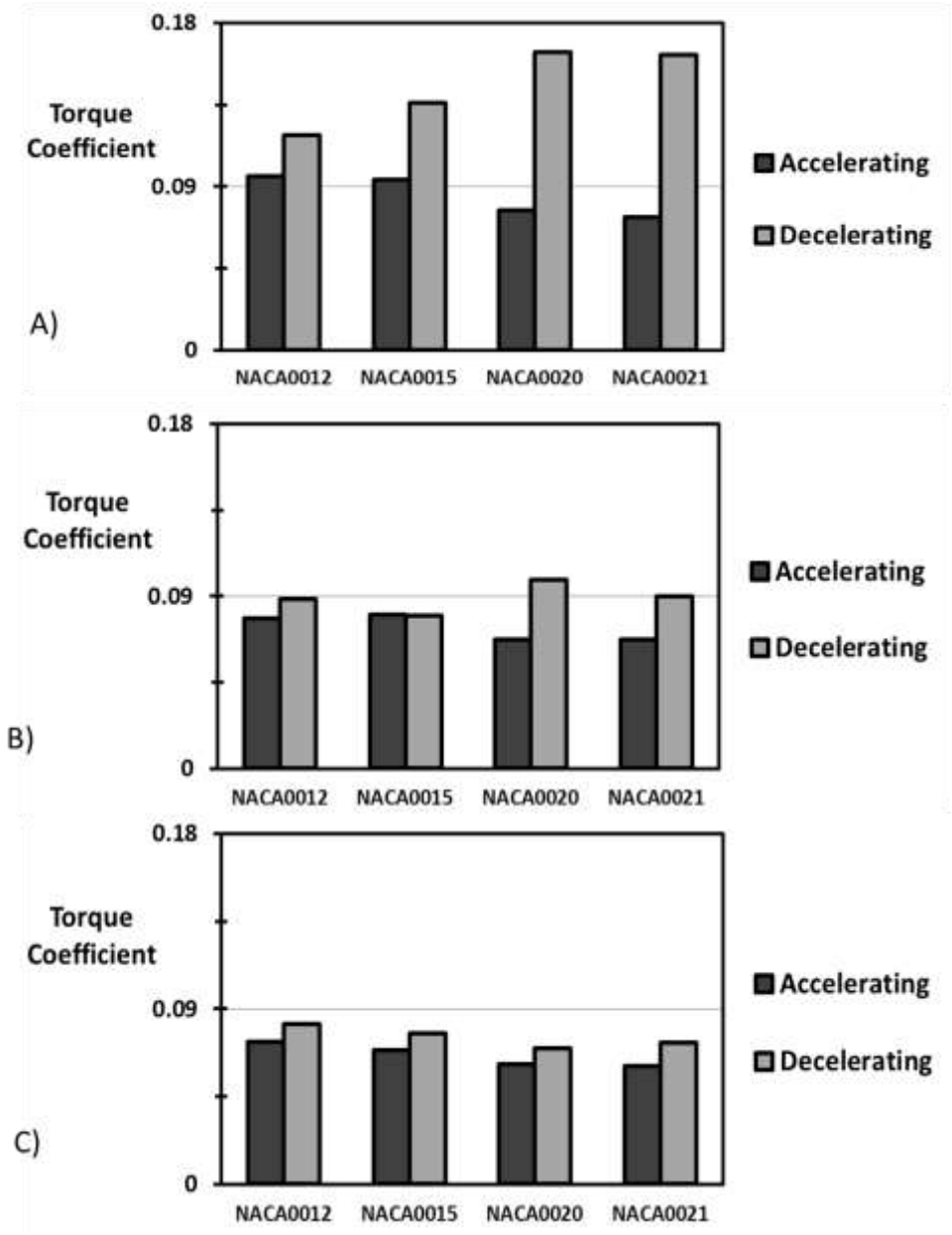

Figure 5.17 Comparisons between the torque coefficient during the accelerating and decelerating flow for four different aerofoils, A) $\boldsymbol{t_{sin}}$ = 4 sec, B) $\boldsymbol{t_{sin}}$ = 6 sec and C) $\boldsymbol{t_{sin}}$ = 8 sec

Table 5.2 The percentage of torque coefficient difference between decelerating and accelerating flow

Aerofoil section	C_T at decelerating flow is higher than that in accelerating flow by		
	For t_{sin} equal to 4 sec	For t_{sin} equal to 6 sec	For t_{sin} equal to 8 sec
NACA0012	24%	13%	12.5%
NACA0015	45%	-1%	12%
NACA0020	114%	46%	13%
NACA0021	122%	33%	20%

Figures 5.20 and 5.21 show the pressure distribution around the upper and lower surface of NACA0020, at accelerating and decelerating flow, and at velocity equal to 2.09 m/s with different time periods. The difference between the pressure value at upper and lower surface has a direct effect on the torque coefficient value, whereby, this difference at decelerating flow was lower than that at accelerating flow except t_{sin} with 8 sec. This behaviour was the same as that of the torque coefficient value. When comparing between the accelerating and decelerating flow, it can be noted that the decelerating flow has a negative pressure value. Furthermore, the increase in time period was accompanied by a decrease in pressure value at accelerating flow. On the other hand, the increase in time period was accompanied by an increase in pressure value at decelerating flow. The low-pressure area was shown around the trailing edge, and increased with the increase of time period.

The total average torque coefficient during the cycle for four different aerofoils at different time periods was shown in Figure 5.22. It can be concluded that the sinusoidal wave, with t_{sin} equal to 4 sec, has the highest torque coefficient, where, NACA0020 (with t_{sin} equal to 4 sec) gives a torque coefficient higher than NACA0012 by 13%, NACA0015 by 5% and NACA0021 by 2%. For the sinusoidal wave with t_{sin} of 6 sec, the aerofoil NACA0012 gives a torque coefficient higher than NACA0015 by 4%, but it was approximately the same as NACA0020, with an increase of only 0.6%. Also, NACA0012 gives a torque coefficient that was 6% higher than NACA0021. Finally, for

the sinusoidal wave with t_{sin} equal to 8 sec, the NACA0012 gives a torque coefficient higher than NACA0015 by 7%, NACA0020 by 18% and NACA0021 by 17%.

Figure 5.23 shows the instantaneous torque coefficient at a compression cycle for different aerofoils (NACA0012, NACA0015, NACA0020 and NACA0021) with different time periods (4 sec, 6 sec and 8 sec). It can be seen that in the first half of each cycle (accelerating flow), NACA0012 always has a higher torque coefficient. The comparison between the maximum torque coefficient values for each time period cycle was shown in Figure 5.24. The NACA0012 aerofoil section has the highest value at sinusoidal wave cycles with t_{sin} equal to 6 sec and with t_{sin} equal to 8 sec. On the other hand, the NACA0020 aerofoil section has the highest value at the sinusoidal wave cycle with t_{sin} equal to 4 sec. In addition, the NACA0020 aerofoil section (with t_{sin} equal to 4 sec) creates a torque coefficient higher than NACA0012 (with t_{sin} equal to 8 sec) by 54%, NACA0012 (with t_{sin} equal to 6 sec) by 44%, and NACA0012 (with t_{sin} equal to 4 sec) by 13%.

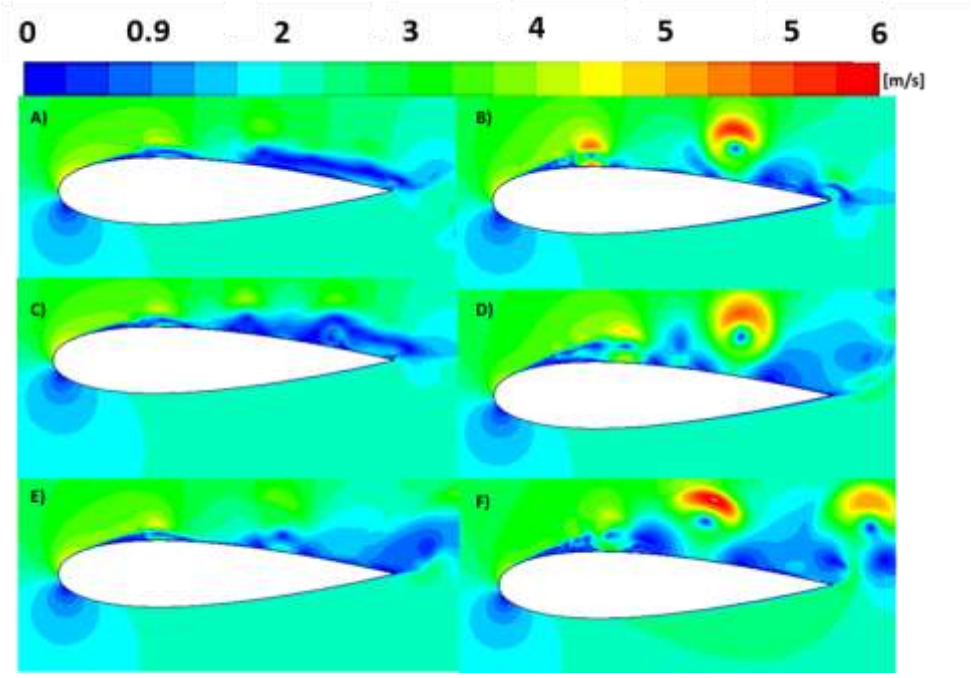

Figure 5.18 Contour of velocity magnitude for sinusoidal input flow, Accelerating flow A) $\boldsymbol{t_{sin}}$ = 4 sec, C) $\boldsymbol{t_{sin}}$= 6 sec, E) $\boldsymbol{t_{sin}}$= 8 sec and Decelerating flow B) $\boldsymbol{t_{sin}}$ = 4 sec, D) $\boldsymbol{t_{sin}}$= 6 sec, F) $\boldsymbol{t_{sin}}$= 8 sec

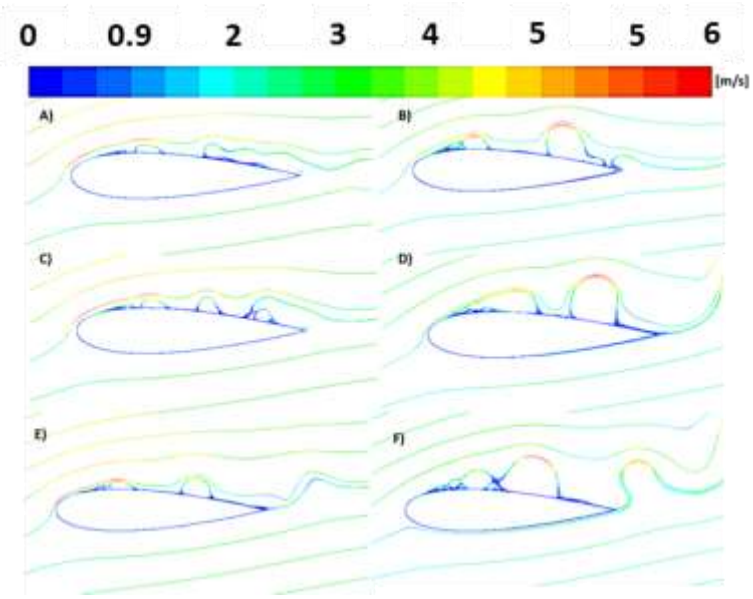

Figure 5.19 Path line of velocity magnitude for sinusoidal input flow, Accelerating flow A) t_{sin} = 4 sec, C) t_{sin}= 6 sec, E) t_{sin}= 8 sec and Decelerating flow B) t_{sin} = 4 sec, D) t_{sin}= 6 sec, , F) t_{sin}= 8 sec

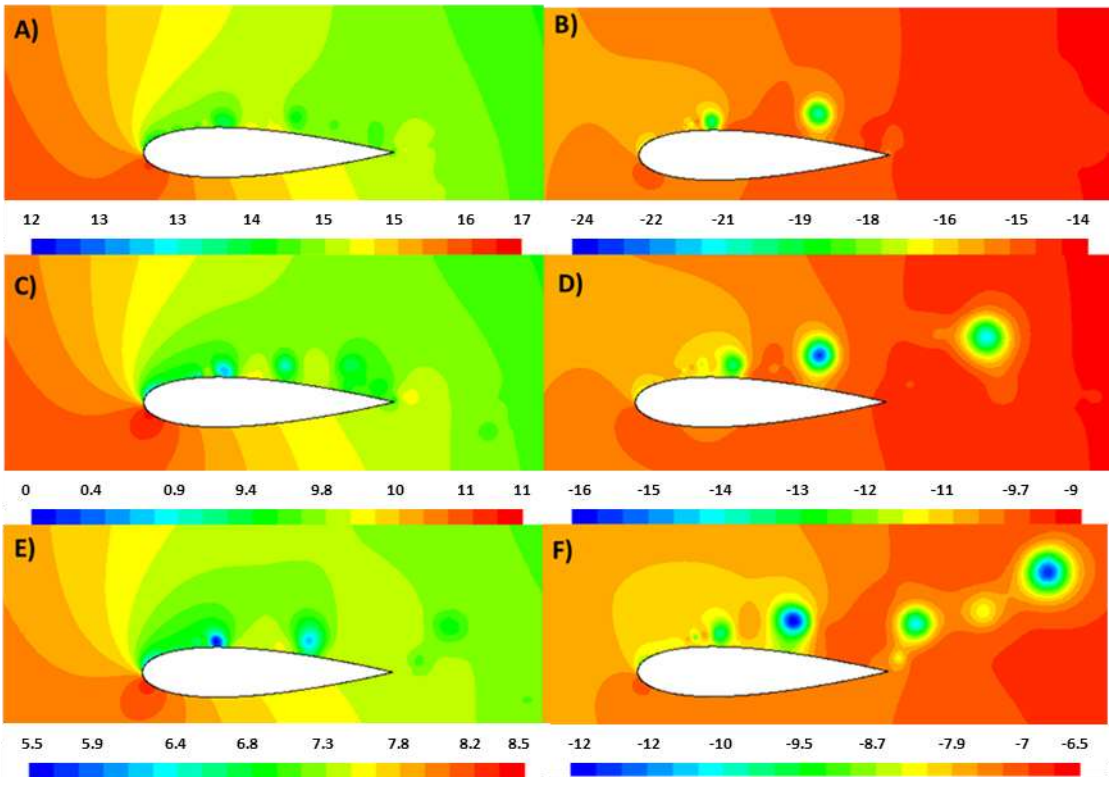

Figure 5.20 Contours of pressure coefficient around the aerofoil, Accelerating flow A) t_{sin} = 4 sec, C) t_{sin}= 6 sec, E) t_{sin}= 8 sec and Decelerating flow B) t_{sin} = 4 sec, D) t_{sin}= 6 sec, , F) t_{sin}= 8 sec

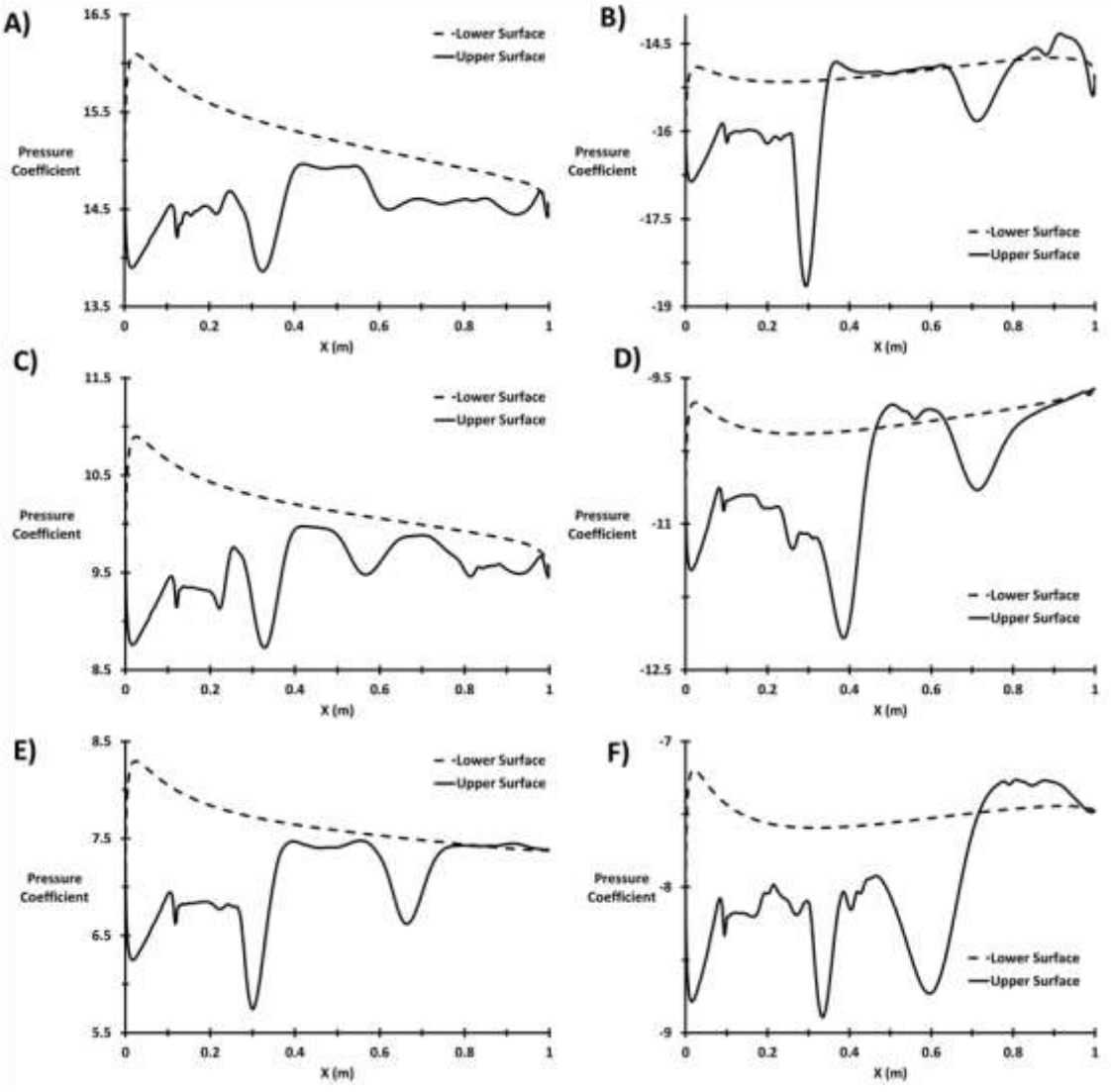

Figure 5.21 Pressure coefficient distribution on the upper and lower surface of the aerofoil, Accelerating flow A) t_{sin} = 4 sec, C) t_{sin}= 6 sec, E) t_{sin}= 8 sec and Decelerating flow B) t_{sin} = 4 sec, D) t_{sin}= 6 sec, , F) t_{sin}= 8 sec

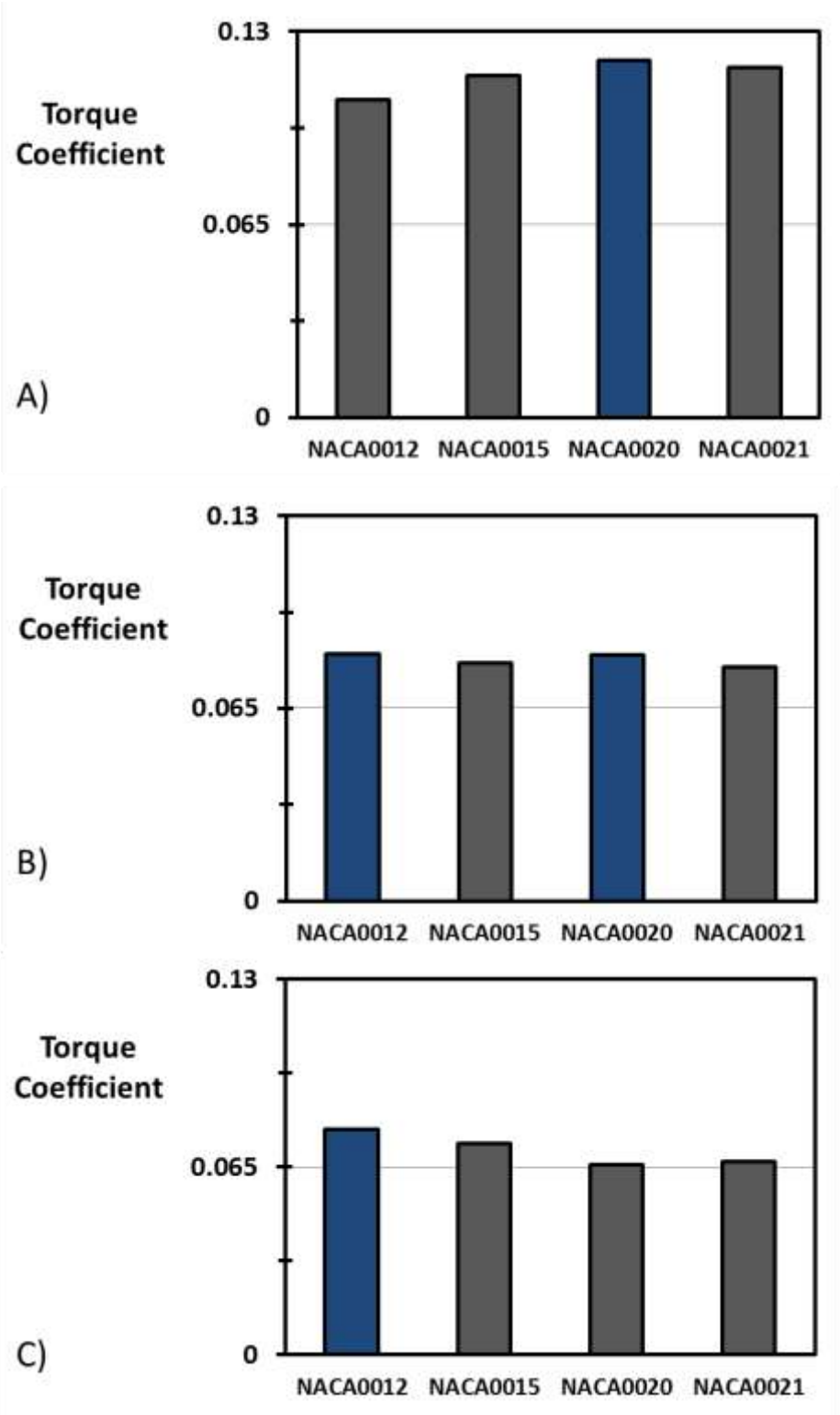

Figure 5.22 Total average values for the torque coefficient during the velocity cycle for the four different aerofoils, A) t_{sin}= 4 sec, B) t_{sin}= 6 sec and D) t_{sin}= 8 sec

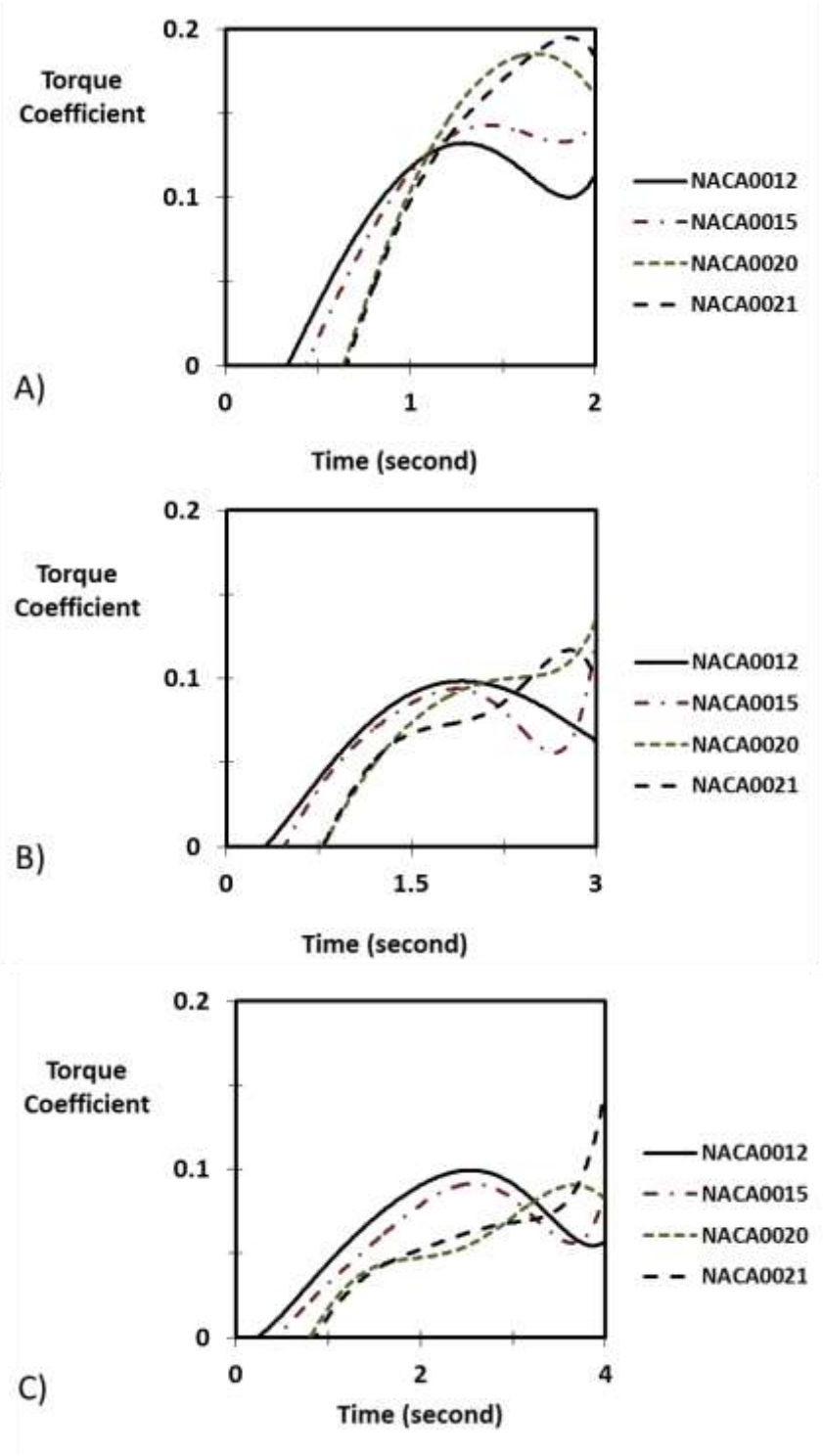

Figure 5.23 The instantaneous values for the torque coefficient during the compression cycle for four different aerofoils, A) t_{sin}= 4 sec, B) t_{sin}= 6 sec and D) t_{sin}= 8 sec

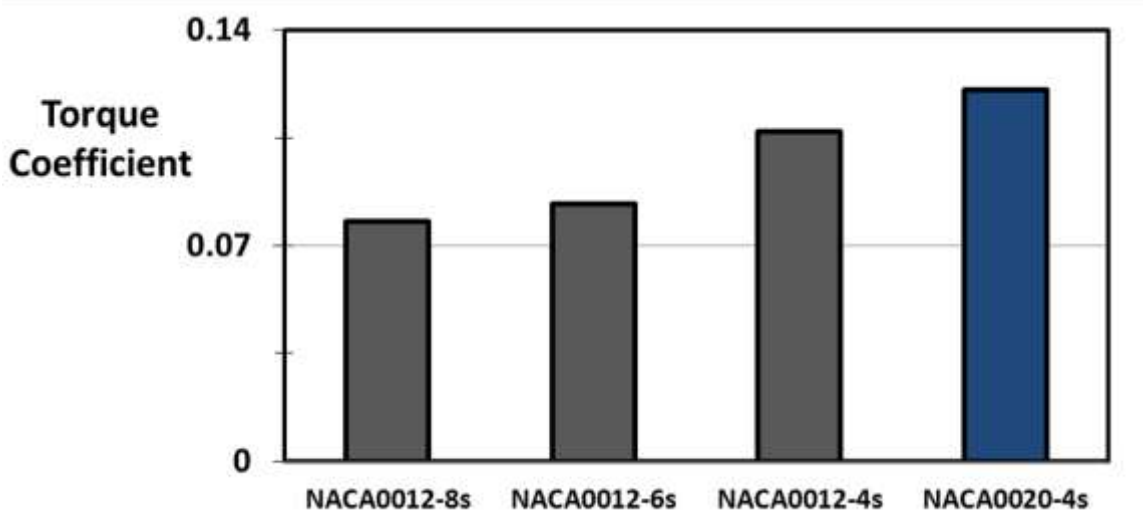

Figure 5.24 The comparison between the maximum torque coefficients for each velocity cycle

Figure 5.25 highlights the effect of the low velocity area and separation layer at trailing edge by velocity contours and path line around the NACA0012 aerofoil at a maximum velocity of 2.92 m/s. It is clear that the torque coefficient is influenced by the low velocity area and separation layer at trailing edge. When the low velocity area at trailing edge increases, the torque coefficient value decreases. Similarly, as the separation layer at trailing edge increases, the torque coefficient value also decreases. The pressure distribution around the upper and lower surface of aerofoil at accelerating and decelerating flow was shown in Figure 5.26 at a maximum velocity of (2.92 m/s), with different time periods (4, 6 and 8 sec). The higher disturbances occurring in separation layers at the upper surface than those occurring at the lower surface (Figure 5.25) is due to the irregular values of pressure at the upper surface. The low pressure areas around the trailing edge increase the separation layer at the trailing edge; therefore, the separation layers at a 4 second time period have lowest disturbances and lowest low-pressure areas around the trailing edge. Table 5.3 summarizes the torque coefficient at different time periods (t_{sin} equal to 4 sec, 6 sec and 8 sec) for the four aerofoils (NACA0012, NACA0015, NACA0020 and NACA0021).

5.4.2 Second law of thermodynamics analysis

Figure 5.27 highlights the comparison between the global entropy generation rate for accelerating and decelerating flows for the four different aerofoils. All aerofoils in the accelerating flow create a global entropy generation rate lower than that created in the decelerating flow. The difference in the global entropy generation rate between the accelerating and decelerating flows is not influenced by the change in time period (see Table 5.4). As an average for all aerofoils, the sinusoidal wave cycle with t_{sin} of 8 sec has the lowest difference in S_G between accelerating and decelerating flows for the four different aerofoils.

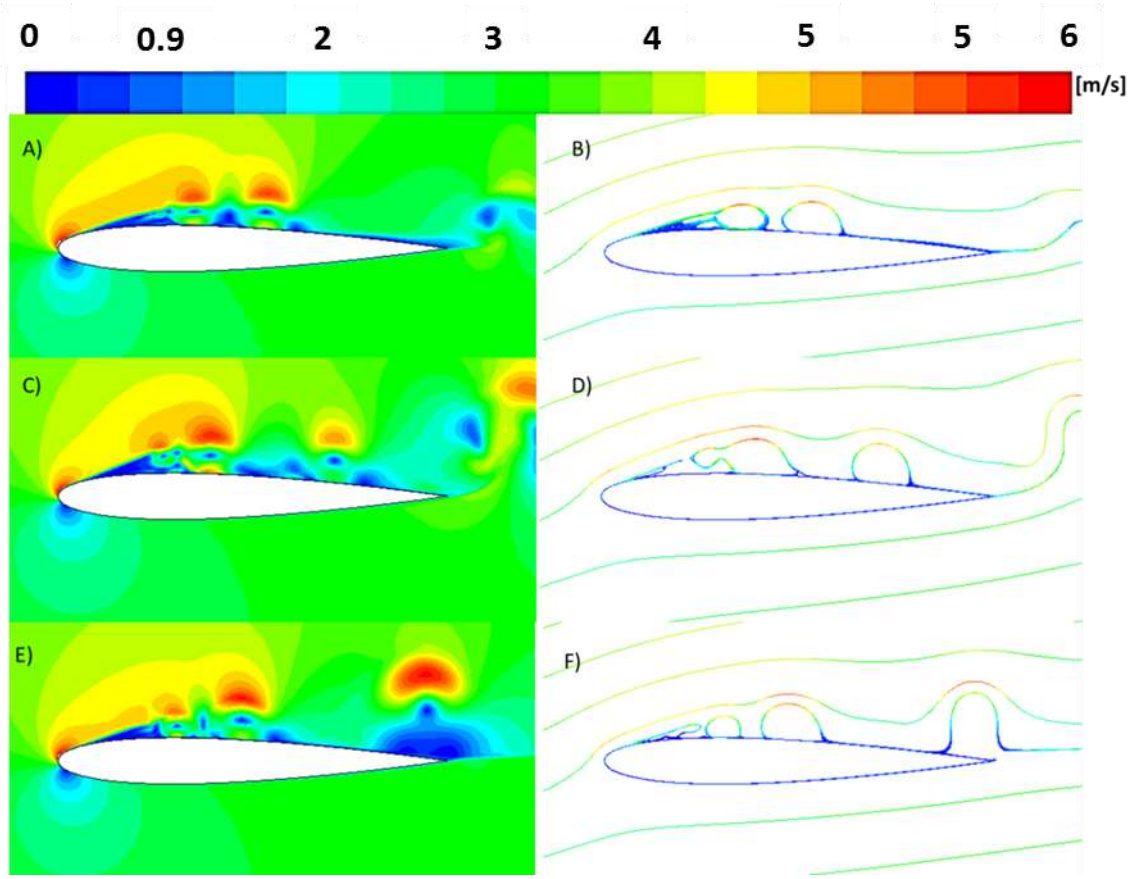

Figure 5.25 Contours of velocity magnitude A) $\boldsymbol{t_{sin}}$= 4 sec, C) $\boldsymbol{t_{sin}}$= 6 sec, E) $\boldsymbol{t_{sin}}$= 8 sec, and Path line coloured by velocity magnitude B) $\boldsymbol{t_{sin}}$= 4 sec, D) $\boldsymbol{t_{sin}}$= 6 sec, F) $\boldsymbol{t_{sin}}$= 8 sec

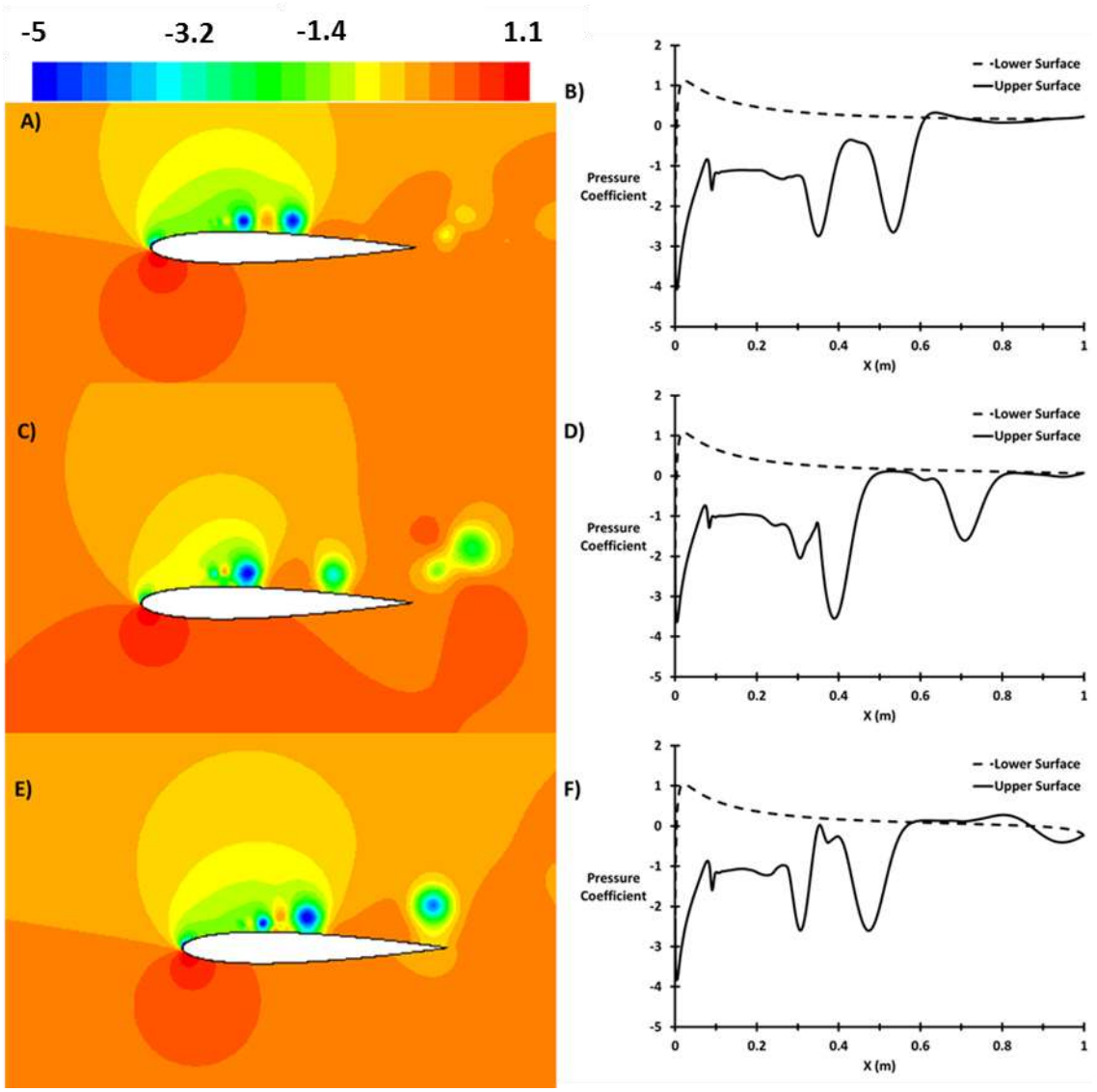

Figure 5.26 Contours of pressure coefficient A) t_{sin}= 4 sec, C) t_{sin}= 6 sec, E) t_{sin}= 8 sec, and Pressure coefficient distribution on the upper and lower surface of the aerofoil B) t_{sin}= 4 sec, D) t_{sin}= 6 sec, F) t_{sin}= 8 sec

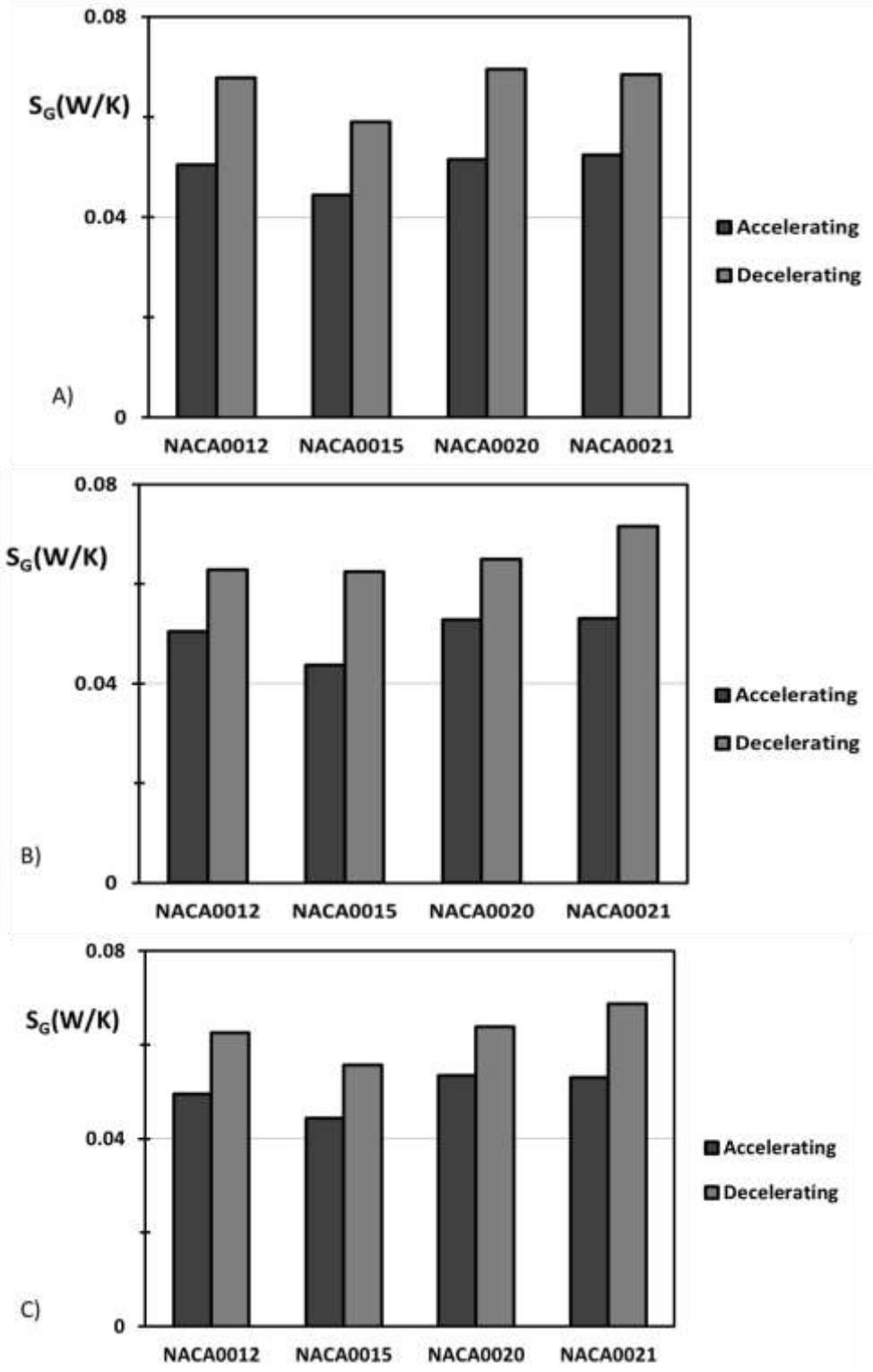

Figure 5.27 Comparisons between S_G during the accelerating and decelerating flow for the four different aerofoils, A) t_{sin}= 4 sec, B) t_{sin}= 6 sec and C) t_{sin}= 8 sec

Table 5.3 A summary of the torque coefficient values at different time periods for the four aerofoils

Aerofoil section	Accelerating flow			Decelerating flow			Average		
	4 sec	6 sec	8 sec	4 sec	6 sec	8 sec	4 sec	6 sec	8 sec
NACA0012	0.096	0.078	0.073	0.118	0.089	0.083	0.107	0.0834	0.078
NACA0015	0.094	0.08	0.069	0.136	0.08	0.077	0.115	0.080	0.073
NACA0020	0.077	0.068	0.062	0.164	0.099	0.070	0.120	0.083	0.066
NACA0021	0.07	0.068	0.061	0.163	0.090	0.073	0.118	0.079	0.067

Table 5.4 The percentage S_G difference between decelerating and accelerating flow

Aerofoil section	S_G at decelerating flow is higher than that in accelerating flow by		
	For t_{sin} equal to 4 sec	For t_{sin} equal to 6 sec	For t_{sin} equal to 8 sec
NACA0012	34%	25%	26%
NACA0015	33%	43%	26%
NACA0020	35%	23%	19%
NACA0021	31%	35%	30%
Average value	33.3%	31.5%	25.3%

The contours of global entropy generation rate around the NACA0021 at the instantaneous velocity (2.08 m/s) for the accelerating and decelerating flow were represented in Figure 5.28. It can be seen that the global entropy generation rate around the aerofoil section in the decelerating flow is higher than that in the accelerating flow at the three different time periods (as noted above in Figure 5.27). From Figures 5.18 and 5.28 it can be noted that the increase in velocity contours around the aerofoil lead to increase also in the entropy generation. Where, the entropy value depends on the velocity gradient see equation (3.42).

The average value of the global entropy generation rate for each aerofoil during the sinusoidal cycle with three different time periods was shown in Figure 5.29. It can be concluded that the NACA0015 has the lowest value of the global entropy generation rate at the three different time periods (4 sec, 6 sec and 8 sec), when it was compared with other aerofoils (NACA0012, NACA0020 and NACA0021). See Table 5.5 for more details.

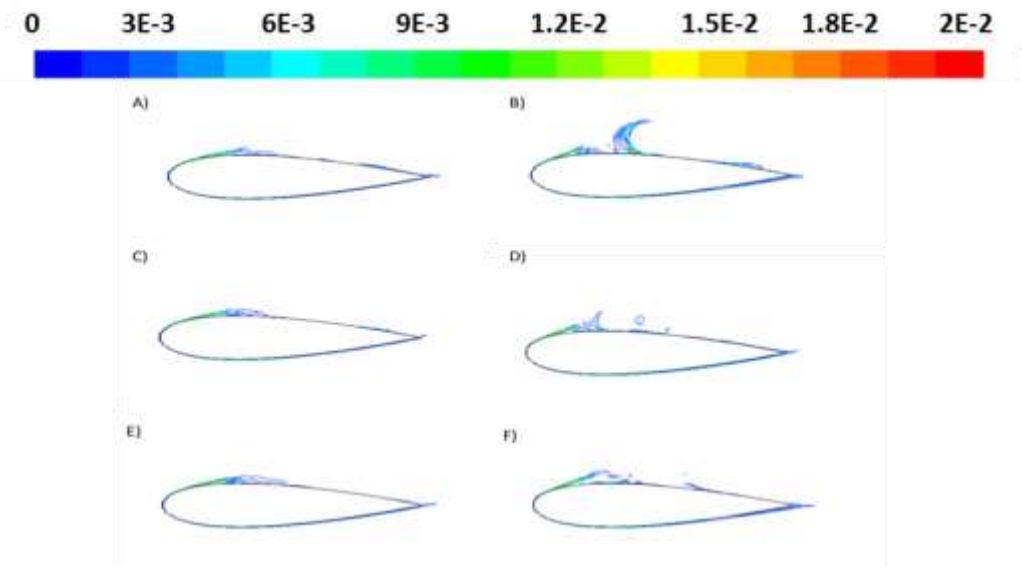

Figure 5.28 Contour of S_G for sinusoidal input flow, Accelerating flow A) t_{sin} = 4 sec, C) t_{sin}= 6 sec, E) t_{sin}= 8 sec and Decelerating flow B) t_{sin} = 4 sec, D) t_{sin}= 6 sec, F) t_{sin}= 8 sec

Figure 5.30 shows the contour of the global entropy generation rate at a maximum velocity (2.92 m/s) around NACA0015 aerofoil with three different time periods. It can be seen that NACA0015 at sinusoidal wave with t_{sin} equal to 8 sec has a lower global entropy generation rate than other time periods for the same aerofoil (NACA0015) and same velocity (2.92 m/s). Hence, Figure 5.31 compares between the values of S_G (Figure 5.31 A) and η_S (Figure 5.31 B) for NACA0015 at three different time periods. It can be concluded that the NACA0015 (with t_{sin} equal to 8 sec) has a lower S_G than NACA0015 (with t_{sin} equal to 6 sec) by 6% and NACA0015 (with t_{sin} equal to 4 sec) by 3%. In addition, the η_S of NACA0015 (with t_{sin} equal to 8 sec) is higher than NACA0015 (with t_{sin} equal to 6 sec) by 1% and NACA0015 (with t_{sin} equal to 4 sec) by 2%. Table

5.6 summarizes the global entropy generation rate values at different time periods (t_{sin} equal to 4 sec, 6 sec and 8 sec) for the four aerofoils (NACA0012, NACA0015, NACA0020 and NACA0021).

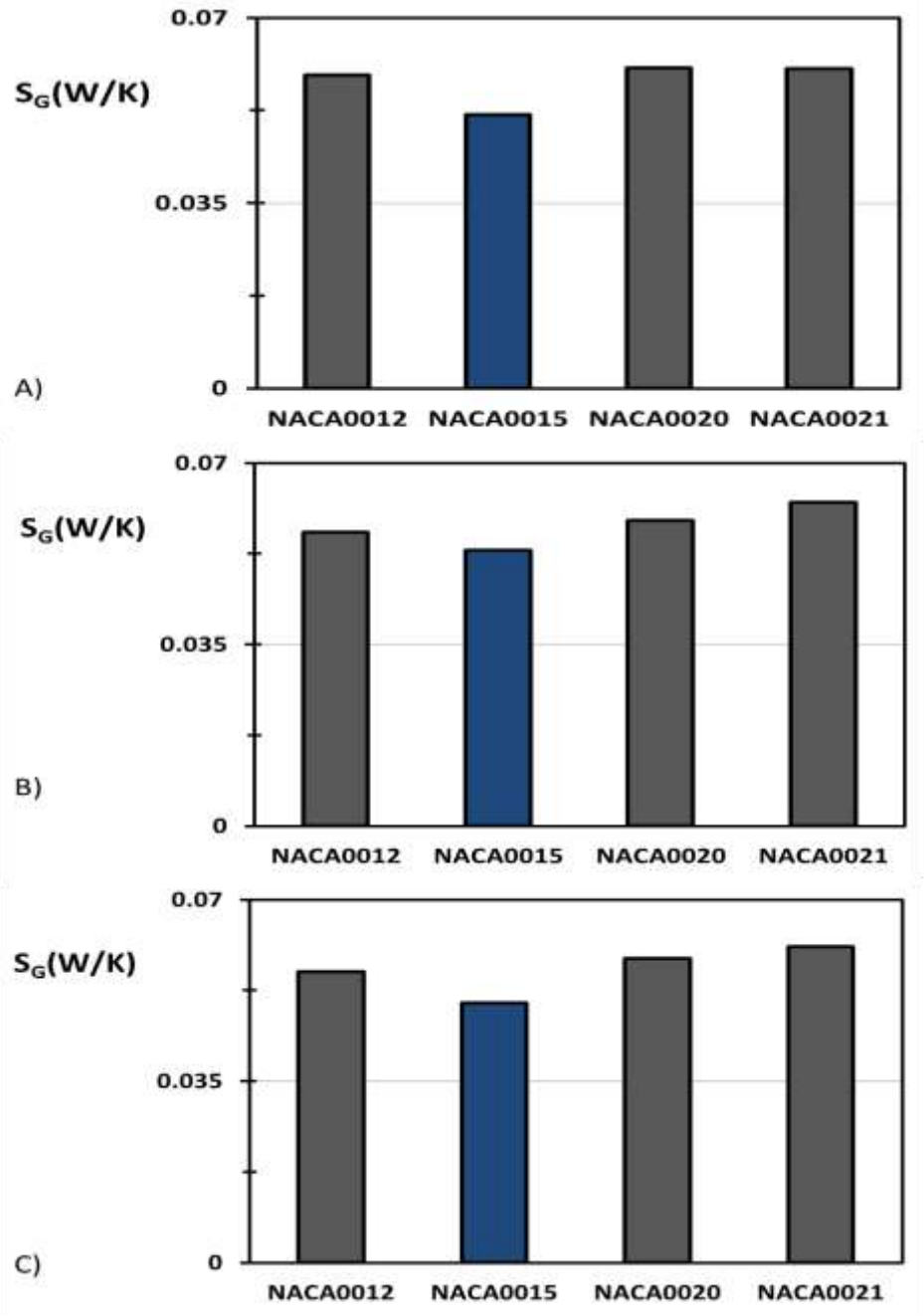

Figure 5.29 Total average values for $\boldsymbol{S_G}$during the velocity cycle for four different aerofoils, A) $\boldsymbol{t_{sin}}$= 4 sec, B) $\boldsymbol{t_{sin}}$= 6 sec and D) $\boldsymbol{t_{sin}}$= 8 sec

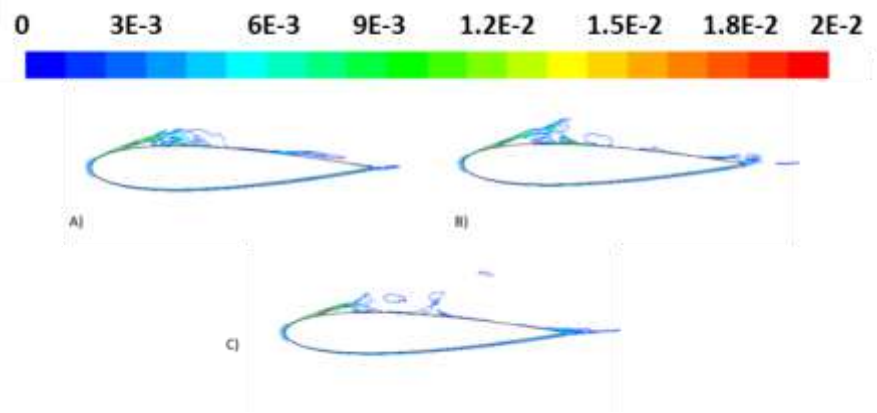

Figure 5.30 Contour of S_G around the NACA0015 aerofoil for sinusoidal input flow, A) t_{sin}= 4 sec, Bt_{sin}= 6 sec and D) t_{sin}= 8 sec

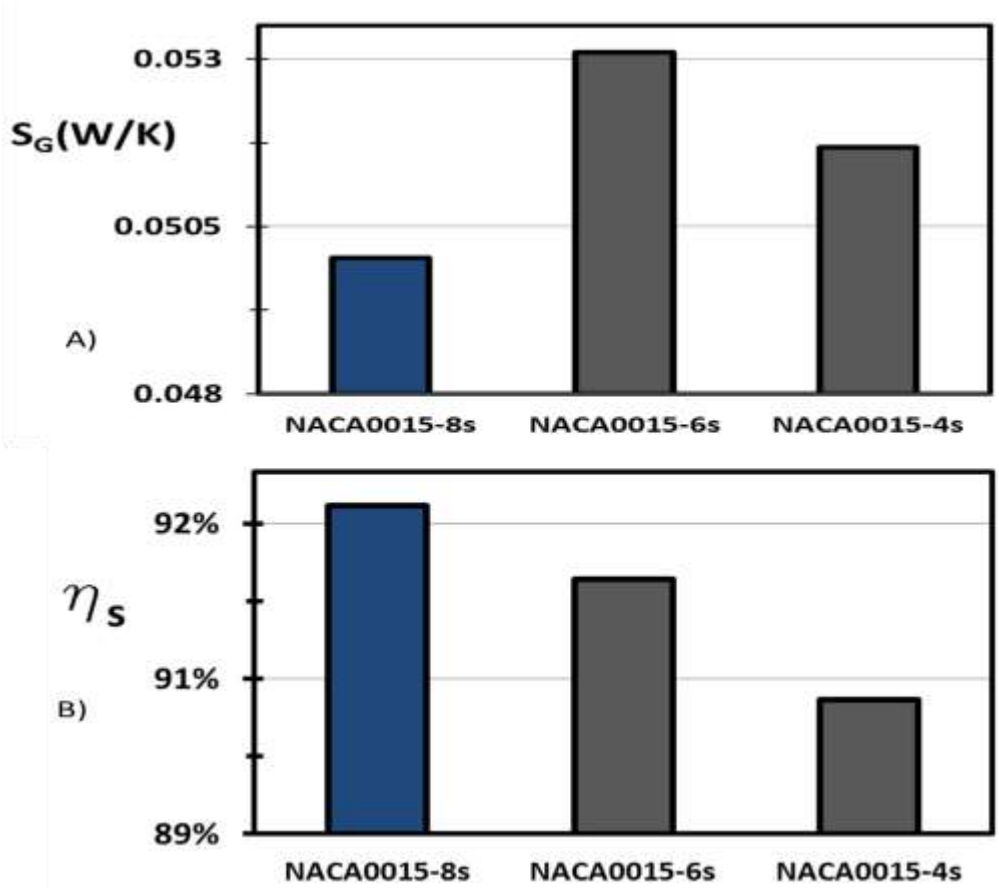

Figure 5.31 The comparison between the NACA0015 at three different time periods (8 sec, 6 sec and 4 sec), A) S_G and B) the second law efficiency

Table 5.5 Comparison between S_G for the NACA0015 and other aerofoils

Aerofoil section	NACA0015 less than		
	NACA0012	NACA0020	NACA0021
t_{sin} equal to 4 sec	-13%	-15%	-14%
t_{sin} equal to 6 sec	-6%	-10%	-15%
t_{sin} equal to 8 sec	-11%	-15%	-18%

Table 5.6 A summary of S_G values at different time periods for the four aerofoils

Aerofoil section	S_G (W/K) t_{sin} = 4 sec			S_G (W/K) t_{sin} = 6 sec			S_G (W/K) t_{sin} = 8 sec		
	Accelerate	Decelerate	Average	Accelerate	Decelerate	Average	Accelerate	Decelerate	Average
NACA0012	0.0505	0.0679	0.0592	0.05	0.063	0.057	0.05	0.063	0.056
NACA0015	0.0444	0.059	0.052	0.044	0.0625	0.053	0.044	0.056	0.050
NACA0020	0.0515	0.0696	0.061	0.053	0.065	0.059	0.054	0.064	0.059
NACA0021	0.0524	0.0684	0.06	0.053	0.072	0.062	0.053	0.069	0.061

5.5 Summary

The performance of Wells turbine was investigated by the aerodynamic force (i.e. first law of thermodynamics analysis) efficiency as well as the entropy (i.e. second law of thermodynamics analysis) efficiency under oscillating flow conditions. The work is performed by using time-dependent CFD models of different NACA aerofoils under sinusoidal flow boundary conditions. The geometry and the operating conditions have radical effects on the global entropy generation rate in the flow around turbine aerofoil. The next chapter will use passive flow control to improve the Wells turbine performance depending on the entropy minimization method that was used in this chapter.

The output publications from this chapter are: 1) “Entropy Generation due to Viscous Dissipation around a Wells Turbine Blade: A Preliminary Numerical Study” Energy Procedia, 50 (2014) 808-816, 2) “Performance analysis of Wells turbine blades using the entropy generation minimization method” Renewable Energy 86 (2016) 1123-1133, and 3) “Comparative analysis of different wave turbine designs based on conditions relevant to northern coast of Egypt” (Energy (2016)- In Press).

Chapter 6 Improvement of Wells Turbine Performance during Stall Using Passive Flow Control

6.1 Introduction

In this chapter, a passive flow control method is applied to improve the performance of Wells turbine in the stall regime. The present study utilized an entropy generation minimization method to examine the impact of the flow control method on the entropy generation characteristics around the turbine blade.

Techniques developed to manipulate the boundary layer, either to increase the lift or to decrease the drag, are classified under the general heading of boundary layer control or flow control. Methods of flow control to achieve separation postponement, lift enhancement and drag reduction have been considered. Such studies have demonstrated that suction slot can modify the pressure distribution over an aerofoil surface and have a substantial effect on lift and drag coefficients (Yousefi et al., 2014, Chapin and Benard, 2015, Schatz et al., 2007, Chawla et al., 2014, Fernandez et al., 2013, Volino et al., 2011). The CFD method has been increasingly used to investigate boundary layer control. Many flow control studies by CFD approaches (Kim and Kim, 2009, Genc et al., 2011, Rumsey and Nishino, 2011, B. Yagiz et al., 2012) have been conducted to investigate the effects of blowing and suction jets on the aerodynamic performance of aerofoils.

This section is performed using a time-dependent CFD model of NACA aerofoil (NACA0015) under sinusoidal flow boundary conditions with Reynolds number equal to 2×10^5, which emulates the actual operating conditions. As the stall behaviour investigating is the aim of this Chapter 6, the LES model is used during all the simulation in Chapter 6. Where, the V_o and V_{am} are equal to 0.04 and 2.88 m/s

respectively, in addition the time period equal to 6 seconds (f equal to 0.167 Hz) is set as one period in this simulation. According to the literature, this will be the first study to use the suction or blowing slot in Oscillating Water System and Wells turbine design.

6.2 Optimum location and diameter for single slot

A slot with certain diameter at various locations from the leading edge was created, with a shape of NACA0015 from reference (Torresi et al., 2009, Torresi et al., 2007b, Torresi et al., 2007a), see Figure 6.1 A. The diameter and location for the slot were changed in order to obtain an optimum value. During the compression cycle, this slot suctions the flow from lower surface (high pressure) and blows it to the upper surface (low pressure). On the other hand, during the suction cycle, the slot suctions the flow from the upper surface (high pressure) and blows it to the lower surface (low pressure), see Figure 6.1 B, C and D. The slot will be defined as a suction slot in the analysis and results which were presented henceforth. The test cases investigated are under 1) unsteady flow with non-oscillating velocity and 2) sinusoidal wave condition.

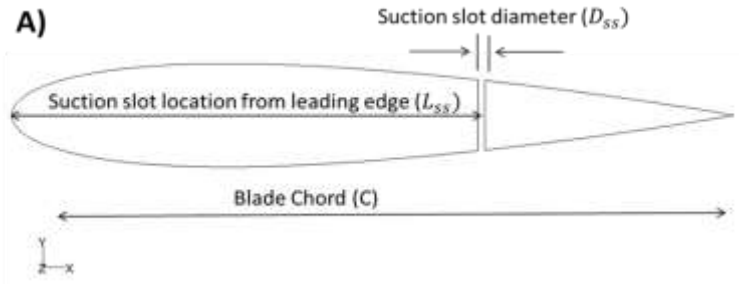
A)
Suction slot diameter (D_{ss})
Suction slot location from leading edge (L_{ss})
Blade Chord (C)

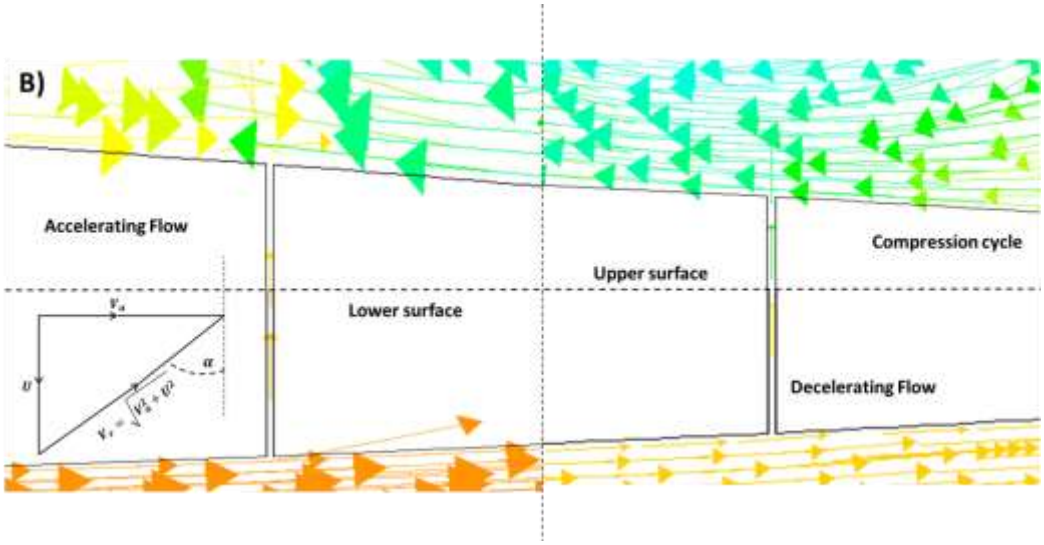
B)
Accelerating Flow
Compression cycle
Upper surface
Lower surface
Decelerating Flow

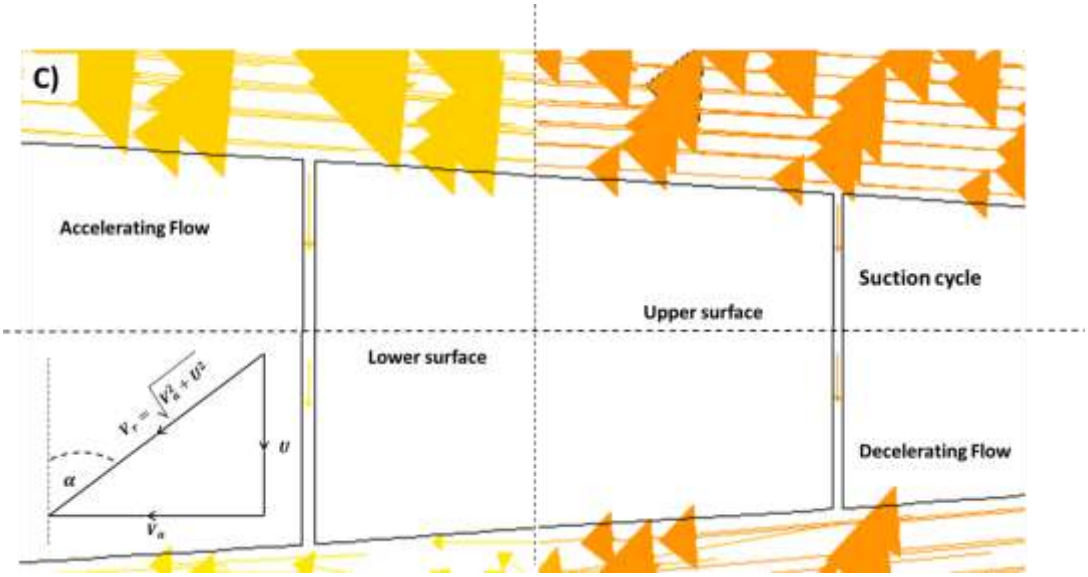
C)
Accelerating Flow
Suction cycle
Upper surface
Lower surface
Decelerating Flow

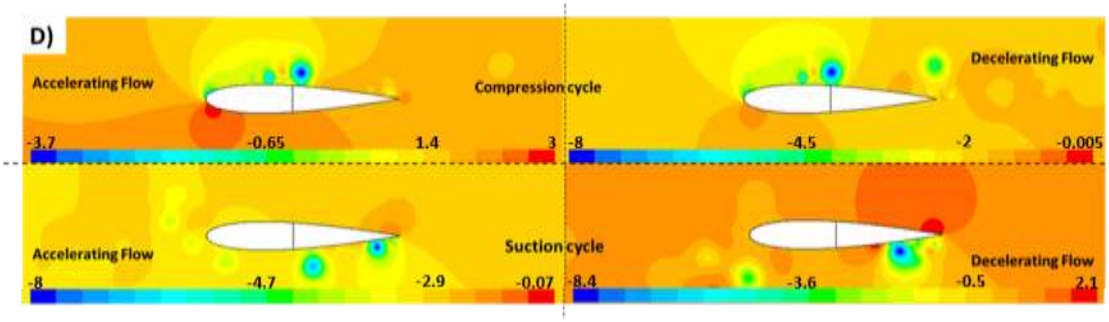

Figure 6.1 Aerofoil with slot A) 2D aerofoil diagram with a slot B) Velocity vector direction during the compression cycle C) Velocity vector direction during the suction cycle D) Pressure distribution during the sinusoidal cycle

6.2.1 Unsteady flow with non-oscillating velocity

The effect of suction slot in the aerofoils behaviour will be shown in the following three sections.

6.2.1.1 Torque coefficient and Stall angle

Figure 6.2 shows the effect of varying D_{ss} on the torque coefficient at the stall angle (13.6 Degree) with Reynolds number equal to 2×10^5 from reference (Torresi et al., 2009, Torresi et al., 2007b, Torresi et al., 2007a). All suction slots have L_{ss} equal to 65%. It can be noted that the suction slot with D_{ss} of 0.001 gives a higher torque coefficient than others. The torque coefficient increases about 26% than the aerofoil without suction slot.

The effect of different L_{ss} on the torque coefficient at the stall angle (13.6 Degree) with D_{ss} equal to 0.001 was presented in Figure 6.3. It can be noted that, the L_{ss} equal to 45%, gives a higher torque coefficient than other L_{ss}, where the torque coefficient increases about 42% higher than the aerofoil without a suction slot. Figure 6.4 demonstrates the effect of a suction slot with optimum L_{ss} and optimum D_{ss} on the torque coefficient at different angles. It is clearly noted that the improvement in the torque coefficient before the stall was ranged (from 7% to 19%) and also at stall regime was ranged (from 44% to 45%), which is caused by the delay in stall angle compare with the experimental data (Torresi et al., 2009, Torresi et al., 2007a) and the simulation for

the aerofoil without slot. For more details about the value of improvement in torque coefficient, see Table 6.1.

6.2.1.2 Flow field around the aerofoil

Figure 6.5 shows the effect of suction slot on the boundary layer and flow field around the aerofoil at maximum value of velocity. Also, the amount of the difference between the effects of suction slot before and after the stall condition. This difference was clearly indicated between Figures a, b for 12.3 degrees and Figures c, d for 13.6 degrees. The effect of suction slot on the separation layer at the end of blade in Figures a, b was small because the stall conditions were not yet present in these two degrees. On the other hand, the effect of suction slot on separation layer in Figures c, d was significant. Because Figure c represents the data in the stall condition however, Figure d has not yet. For the Figures e and f, the two aerofoils were in stall regime. Figures 6.6 and 6.7 show the pressure distribution around the upper and lower surface of aerofoil at maximum velocity (2.92 m/s) with different angles of attack. It can be shown that the low pressure area at the trailing edge increases with the increase in angle of attack for the aerofoil without slots. From Figure 6.7 A), C) and E) it can be noted that the low pressure zones and disturbances at the trailing edge for the upper surface creates the layer separation at the trailing edge and it also increased by the increase in angle of attack. The effect of suction slot was very clear at the pressure distribution around the aerofoil, where, it was more significant after the stall angles (13.6 and 14.4 degrees) than that before the stall (12.3 degrees). The difference between the pressure value for the upper and lower surface at the trailing edge was decreased by adding suction slot to the aerofoil especially at the stall angles.

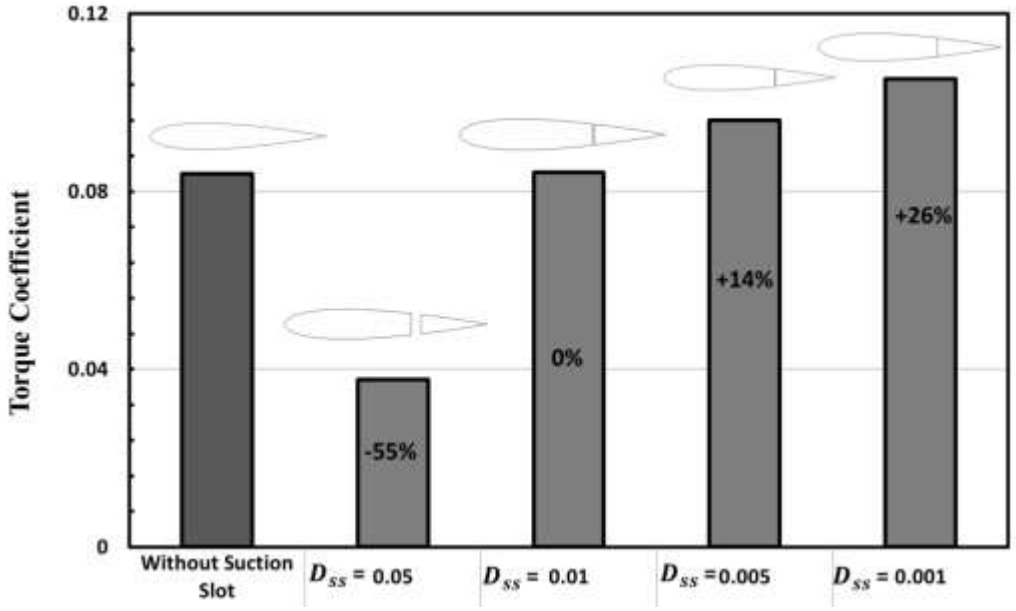

Figure 6.2 Torque coefficient for different D_{ss} at stall angle13.6 degree

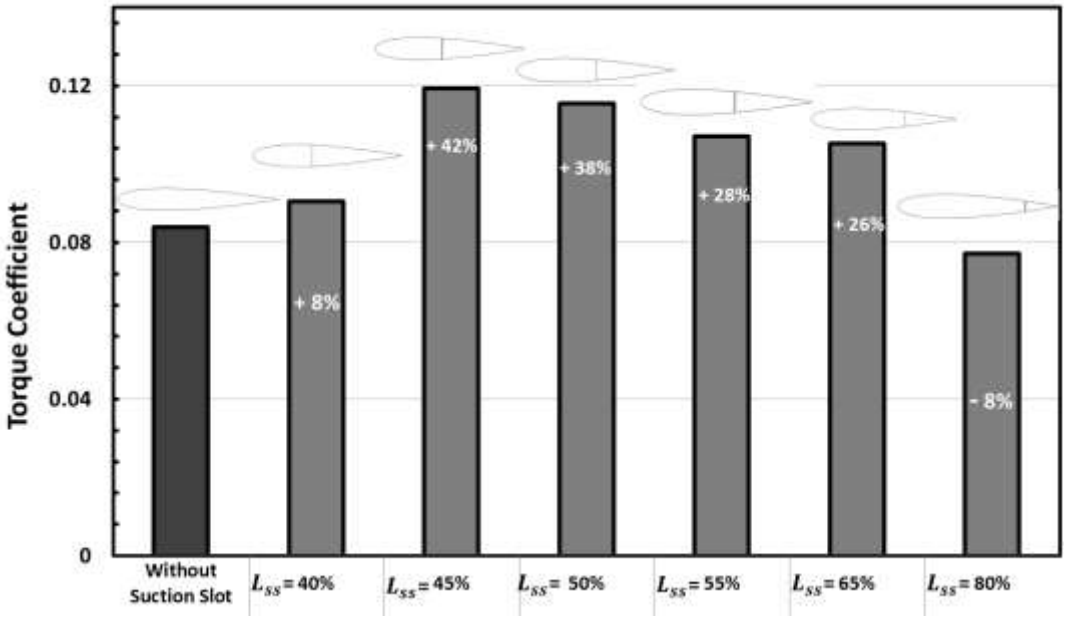

Figure 6.3 Torque coefficient for suction slots at different L_{ss} at stall angle 13.6 degree

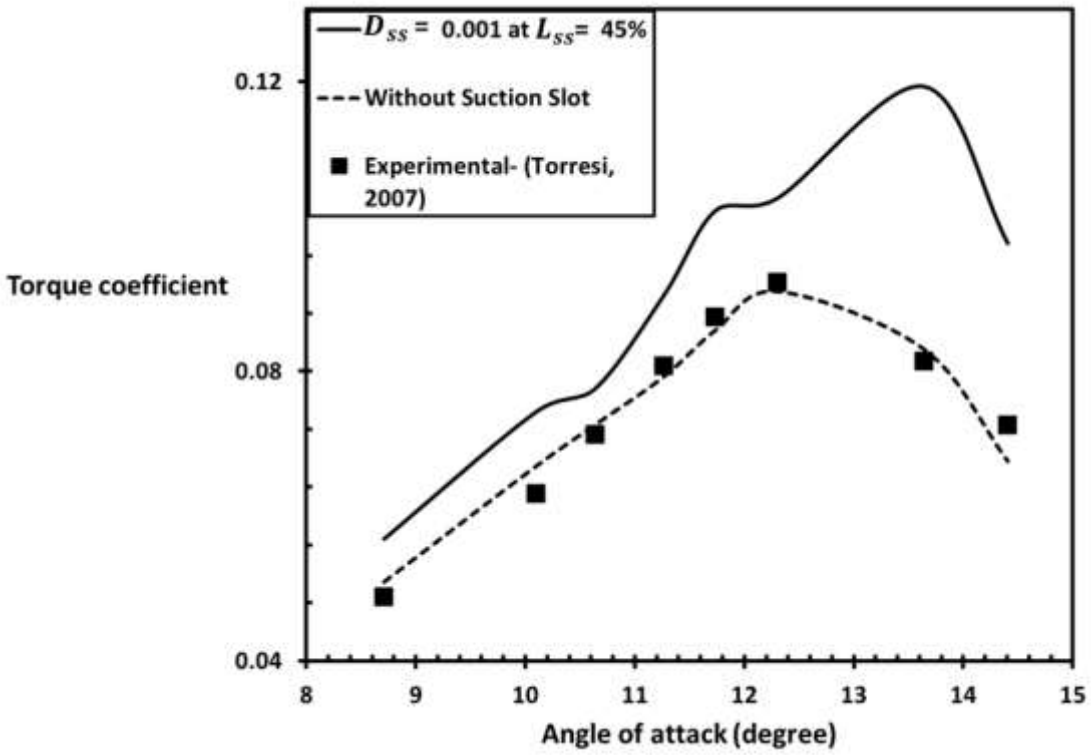

Figure 6.4 Suction slot with optimum L_{ss} (45%) and optimum D_{ss} (0.001) at different angles of attack

Table 6.1 The improvement percentage between NACA0015 without slot and with suction slot at optimum L_{ss} and D_{ss} under unsteady flow with non-oscillating velocity

Torque Coefficient	**Angle of attack (Degree)**							
	8.7	10.1	10.6	11.3	11.7	12.3	13.6	14.4
Without Suction Slot	0.051	0.067	0.073	0.079	0.086	0.091	0.083	0.068
$D_{ss} = 0.001$ **at** $L_{ss} = 45\%$	0.057	0.074	0.078	0.091	0.102	0.104	0.119	0.098
Improvement %	12	11	7	14	19	14	44	45

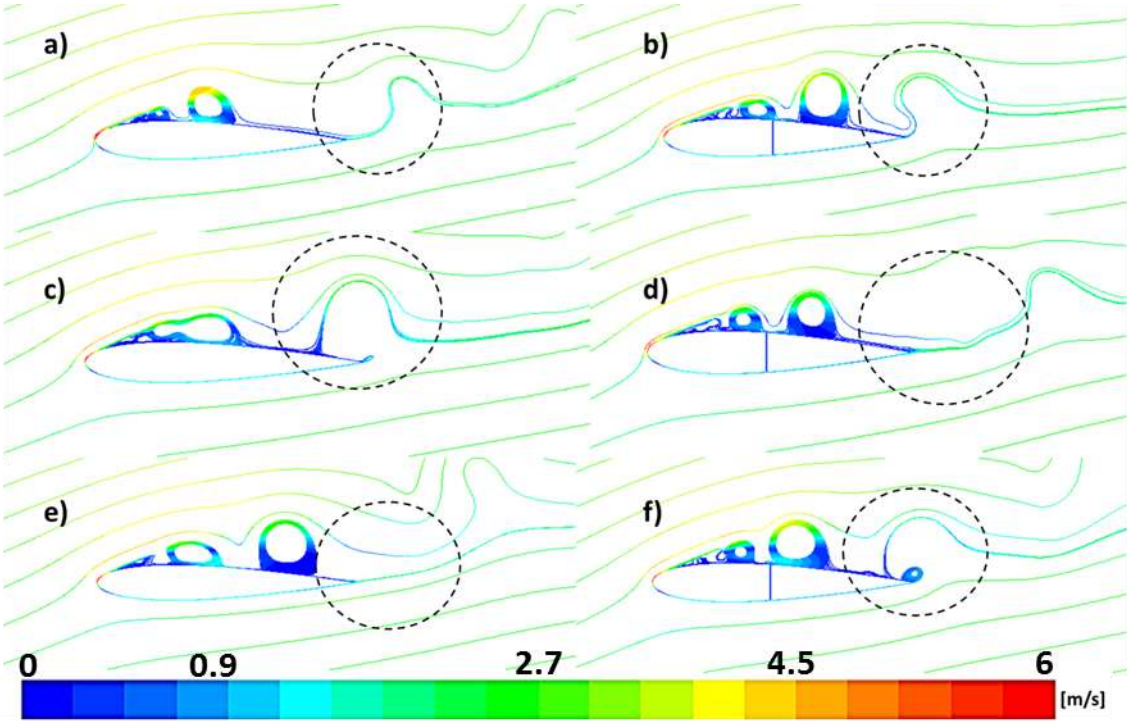

Figure 6.5 Path-line coloured by mean velocity magnitude at velocity equal to 2.92m/s unsteady input flow with non-oscillating velocity, a) and b) 12.3 degree, c) and d) 13.6 degree, e) and f) 14.4 degree

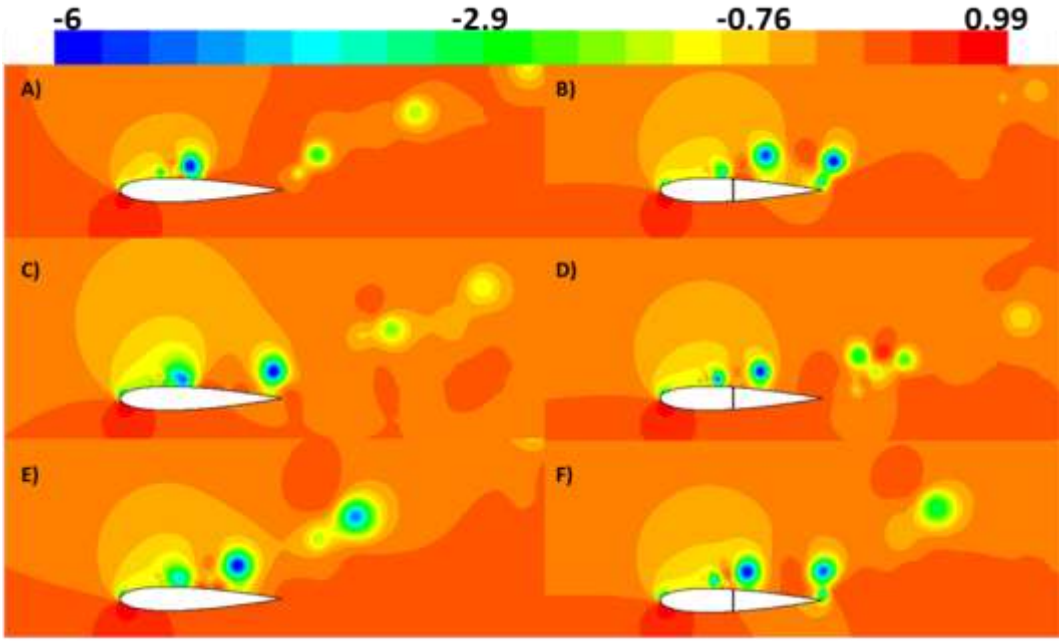

Figure 6.6 Contours of pressure coefficient around the aerofoil, unsteady input flow with non-oscillating velocity, A) and B) 12.3 degree, C) and D) 13.6 degree, E) and F) 14.4 degree

6.2.1.3 Second law analysis

Figure 6.8 shows that the suction slot has a negative effect on the second law efficiency, where the global entropy generation rate increases at all angles from (14% to 41%). The 10.6 degrees angle of attack (before the stall) has the greatest difference in global entropy generation rate by 41% due to suction slot. On the other hand, 8.7 (before the stall) and 13.6 (after the stall) degrees angle of attack have the lowest different in global entropy generation rate by 14 % due to suction slot. However, the 10.1, 11.3, 11.7 and 12.3 (before the stall) degrees have the same difference in global entropy generation rate by 21.5% due to suction slot. Also, the 14.4 (after the stall) degrees has difference in global entropy generation rate by 30%. This phenomenon suggests that the change in velocity gradient due to the suction slot has a direct impact on the entropy generation.

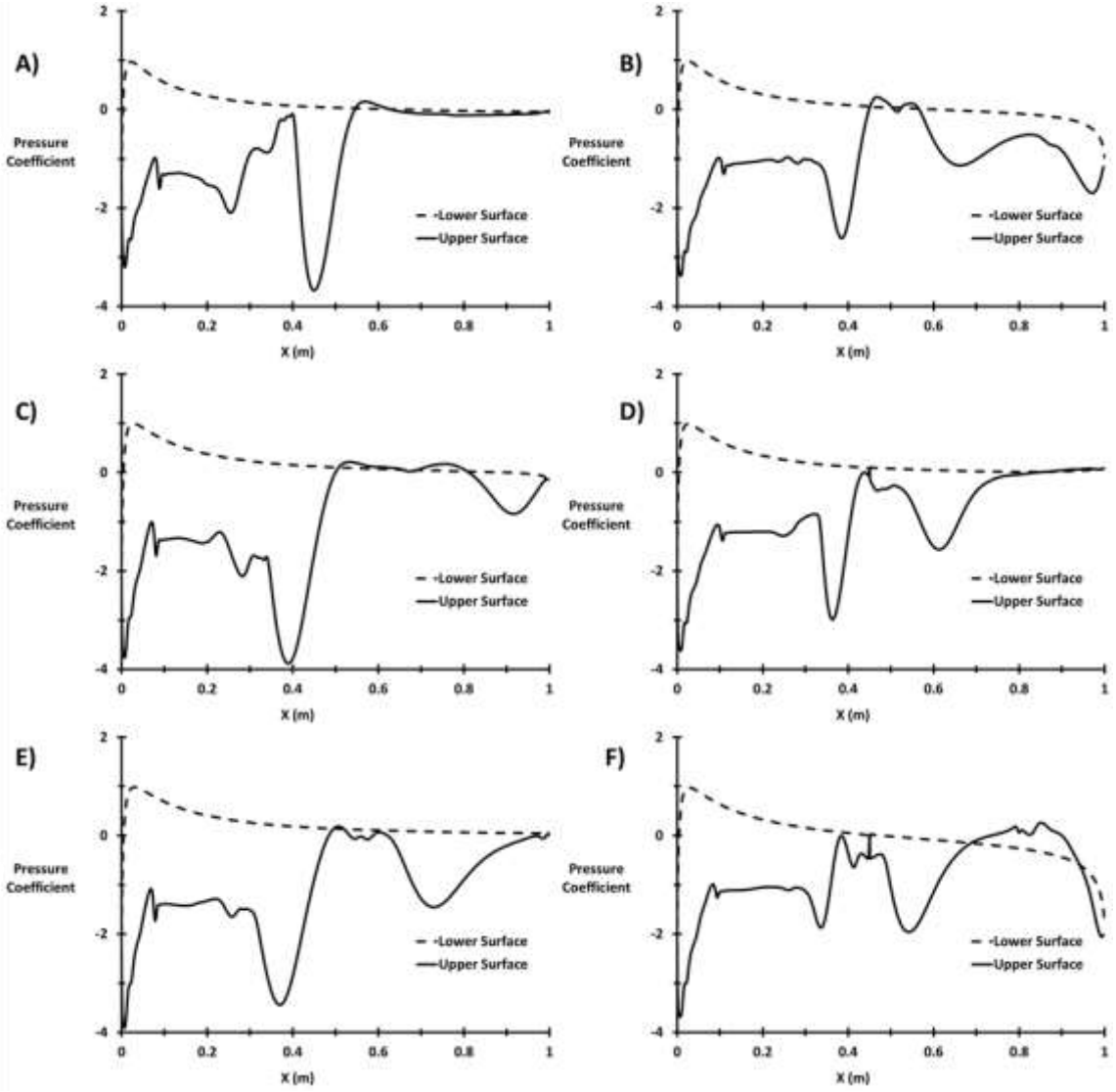

Figure 6.7 Pressure coefficient distribution on the upper and lower surface of the aerofoil, A) and B) 12.3 degree, C) and D) 13.6 degree, E) and F) 14.4 degree

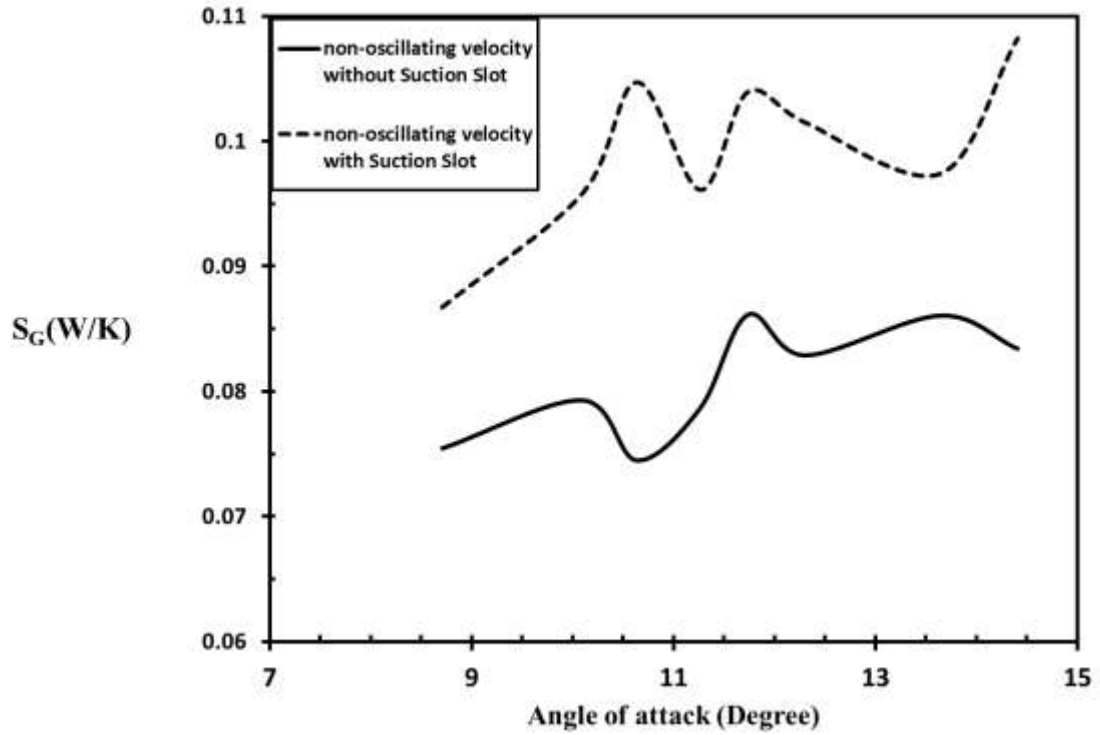

Figure 6.8 The effect of suction slot on S_G with different angle of attack

6.2.2 Sinusoidal wave

The axial flow of Wells turbine was modelled as a sinusoidal wave in the simulations of this section, see Figure 6.9. Therefore, inlet boundary conditions were set to change as time. Where, the V_o were equal to 0.04 and V_{am} were equal to 2.88 m/s, in addition the time period equal to 6 seconds (f equal to 0.167 Hz) was set as one period in this simulation considering to the literature survey (Setoguchi et al., 2003a, Kinoue et al., 2003a, Kinoue et al., 2004, Mamun et al., 2004). Time step was set as 0.0089 second in order to satisfy CFL condition equal to 1. The sinusoidal wave condition creates various Reynolds number up to 2×10^5 according to the reference (Torresi et al., 2009). This sinusoidal wave specification was used in all upcoming simulation that has sinusoidal flow inlet condition in Chapter 6.

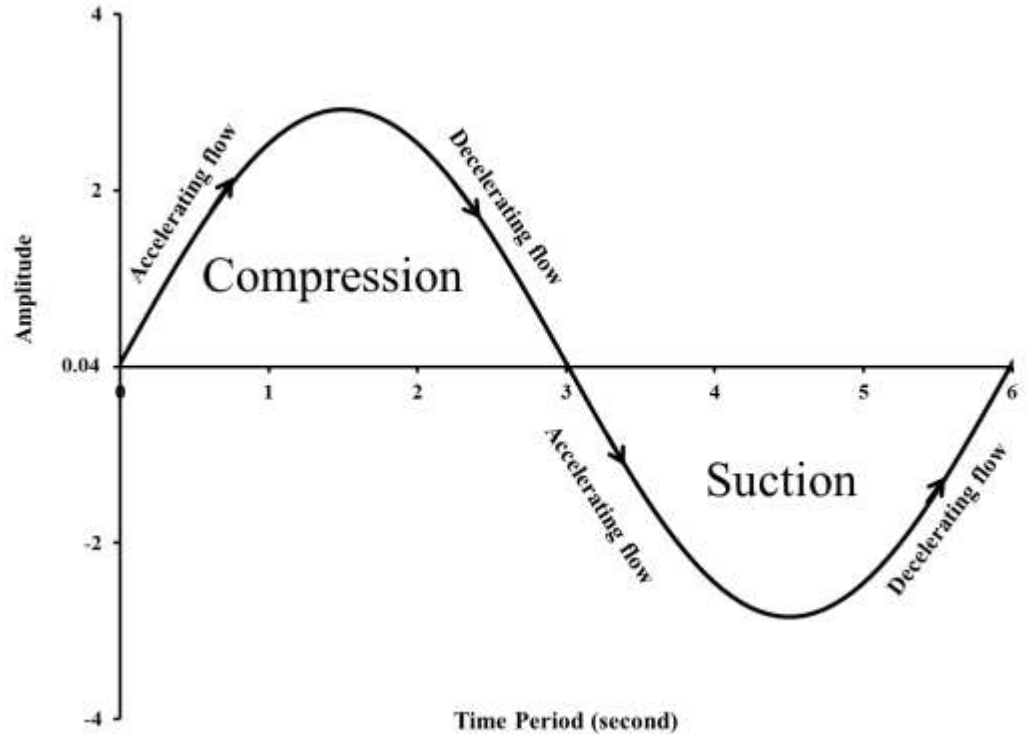

Figure 6.9 The sinusoidal wave boundary condition, which represents a regular oscillating water column

6.2.2.1 Torque coefficient and Stall angle

Figure 6.10 a) shows the instantaneous torque coefficient at compression cycle for different L_{ss}, while Figure 6.10 b) shows the average value of torque coefficient. These values were at citrine angle of attack of 13.6 (Degree) and citrine D_{ss} equal to 0.001. The L_{ss} equal to 45%, gives a higher torque coefficient value than other L_{ss} (such as the previous section). Figure 6.11 shows the effect of L_{ss} with 45% and D_{ss} equal to 0.001, on torque coefficient at different angles. It is clearly noted that the improvement of torque coefficient before the stall regime (from 11% to 26%) and at stall regime (from 32% to 53%) compare with the experimental data (Torresi et al., 2009, Torresi et al., 2007a) and the simulation for the aerofoil without slot. Table 6.2 shows more details about the value of improvement in torque coefficient.

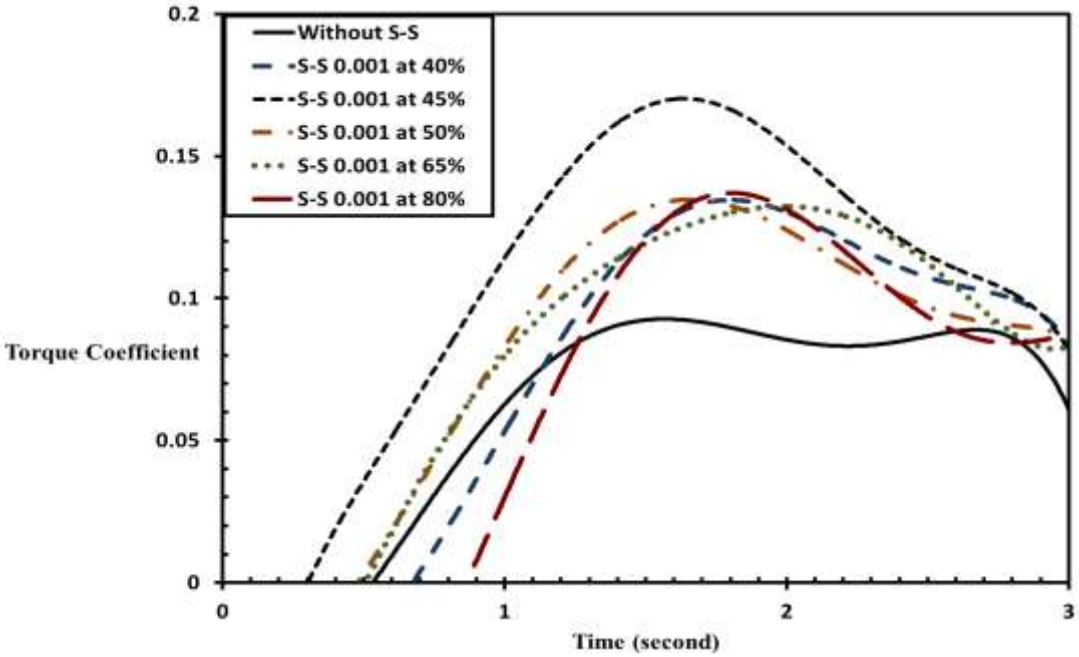

a) Instantaneous torque coefficient

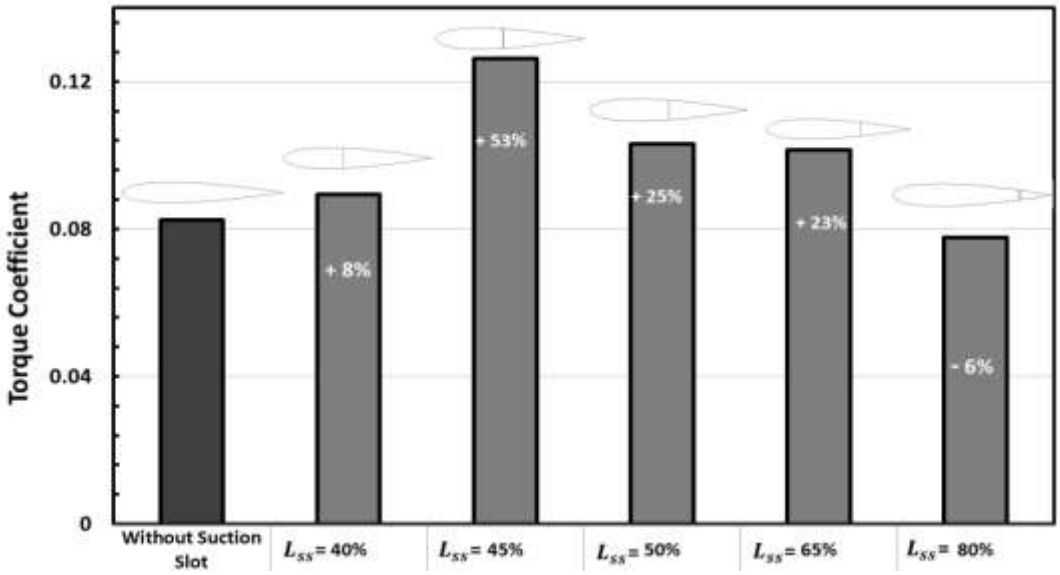

b) Average torque coefficient

Figure 6.10 Suction slot with D_{ss} equal to 0.001 at different L_{ss} at 13.6 degree under sinusoidal inlet velocity a) Instantaneous torque coefficient b) Average torque coefficient

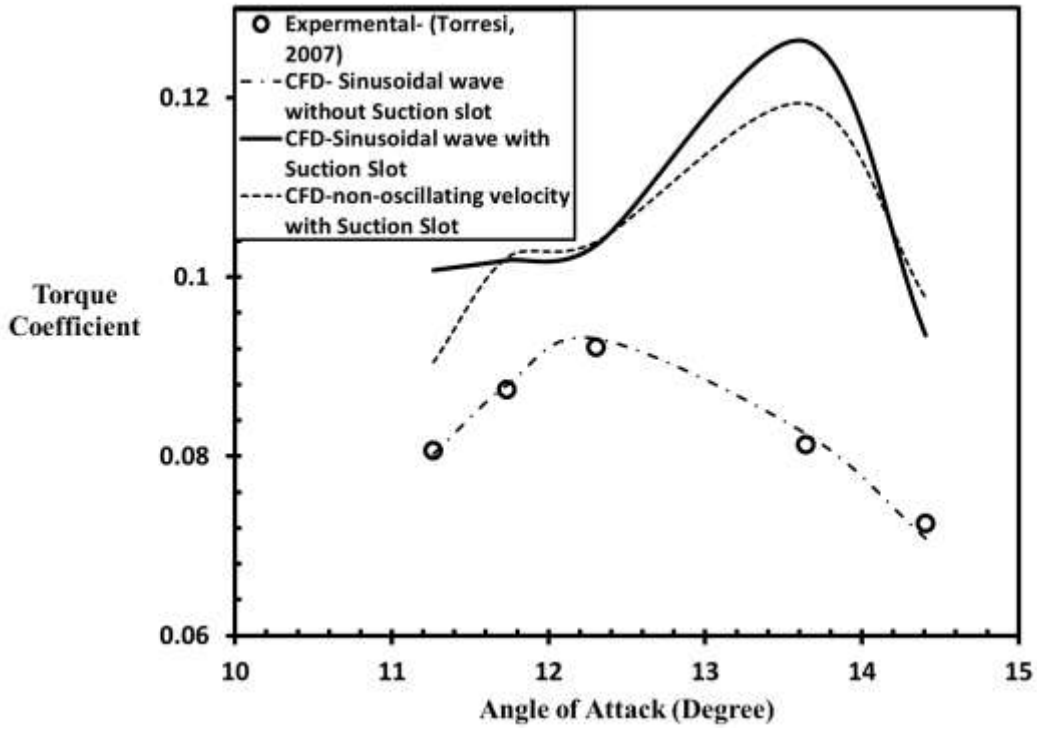

Figure 6.11 Suction slot with optimum $\boldsymbol{L_{ss}}$ (45%) and optimum $\boldsymbol{D_{ss}}$ (0.001) at different angles of attack under sinusoidal inlet velocity

Table 6.2 The improvement percentage between NACA0015 without suction slot and with suction slot at optimum $\boldsymbol{L_{ss}}$ and $\boldsymbol{D_{ss}}$ under with sinusoidal inlet velocity

Torque Coefficient	**Angle of attack (Degree)**				
	11.3	11.7	12.3	13.6	14.4
Without Suction Slot	0.080	0.088	0.093	0.083	0.071
$\boldsymbol{D_{ss} = 0.001}$ **at** $\boldsymbol{L_{ss} = 45\%}$	0.101	0.102	0.104	0.126	0.094
Improvement %	26	16	11	53	32

Figure 6.12 shows the hysteretic behaviour due to the reciprocating flow, the performance of the Wells turbine has a hysteretic loop in which the values of torque coefficient in the accelerating flow was smaller than in the decelerating flow. The hysteretic behaviour was studied experimentally and numerically in the references of (Mamun, 2006, Kim et al., 2002b, Kinoue et al., 2003a, Setoguchi et al., 2003a, Kinoue et al., 2004, Mamun et al., 2004, Setoguchi et al., 2003c, Kinoue et al., 2003b, Setoguchi

T, 1998, Thakker and Abdulhadi, 2008, Thakker and Abdulhadi, 2007). It can be observed that the only study which simulated the hysteretic behaviour after the stall is (Setoguchi et al., 2003c), by a numerical simulation using a quasi-steady analysis. Also, Figure 6.12 highlights the hysteretic behaviour after adding a suction slot to the aerofoil which has the same behaviour but, it was delays the stall regime and improves the torque coefficient. The torque coefficients at compression cycle for different angles of attack were shown in Figure 6.13. It can be observed that for all angles, the suction slot increases the torque coefficient. Figures d) and e) have the highest increase value than other Figures, where the torque coefficient increased by (approximately) 26% in Figure 6.13 a), 16% in Figure 6.13 b) and 11% in Figure 6.13 c). The stall regime was delayed in Figure 6.13 d); in addition, the torque coefficient increased by (approximately) 53% and by (approximately) 32% in Figure 6.13 e). Furthermore, the behaviour of torque coefficient with suction slot curve was more stable than that without suction slot, which increases from the amount of highest value, as seen in Figure d) and e).

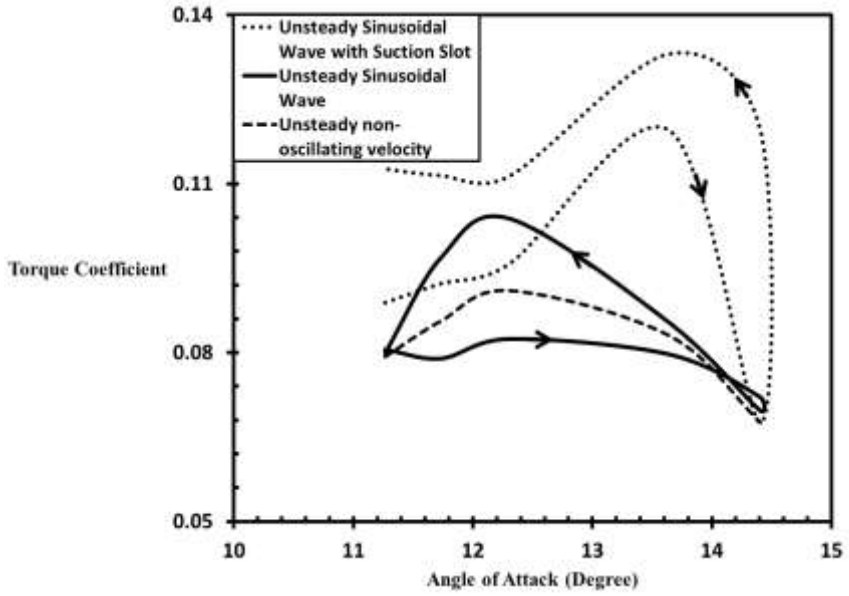

Figure 6.12 The hysteretic behaviour due to the sinusoidal inlet velocity at different angles of attack with optimum $\boldsymbol{L_{ss}}$ (45%) and optimum $\boldsymbol{D_{ss}}$ (0.001)

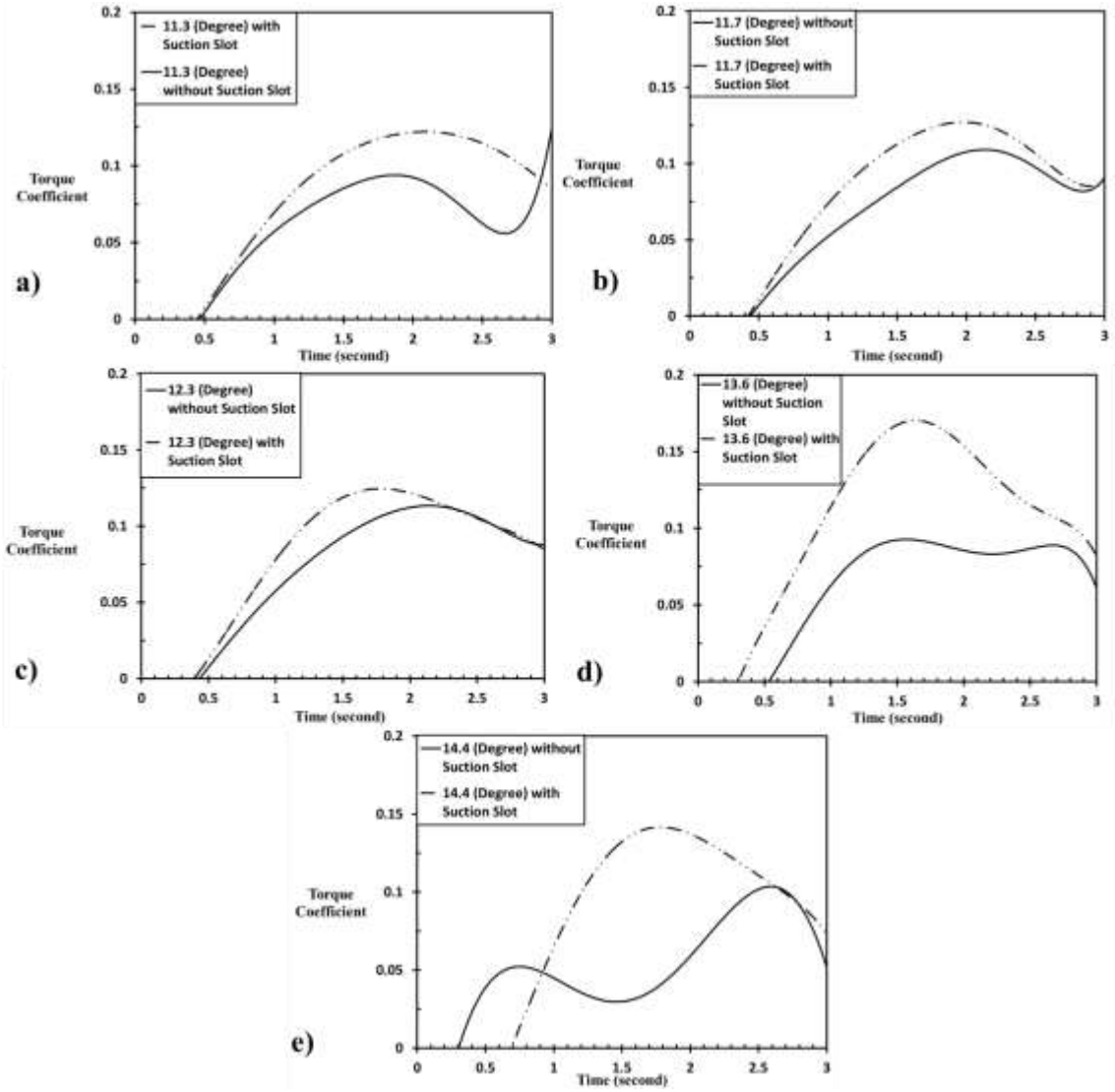

Figure 6.13 Torque coefficients under sinusoidal inlet velocity with optimum L_{ss} (45%) and optimum D_{ss} (0.001), a) 11.3 degree, b) 11.7 degree, c) 12.3 degree, d) 13.6 degree, e) 14.4 degree

6.2.2.2 Flow field around the aerofoil

The flow structures over the NACA0015 aerofoil in oscillating flow was shown in Figure 6.14 and Figure 6.15. Figure 6.14 shows the contour of velocity magnitude at maximum velocity and angle of attack equal to 12.3 degree (before the stall). The improvement effect of suction slot on flow structures was clear when compared between Figures a) and b), especially in the separated layer regime at the end of aerofoil. The same behaviour occurs in Figures 6.15 a) and b) for the contour of velocity magnitude,

also in Figures c) and d) for mean velocity magnitude from unsteady statistics. Figure 6.15 shows the improvement effect of suction slot on flow structures at maximum velocity and angle of attack equal to 13.6 degree (after the stall). The suction slot has a direct effect on the flow structures at the end of blade, which leads to an improvement in the separation regime.

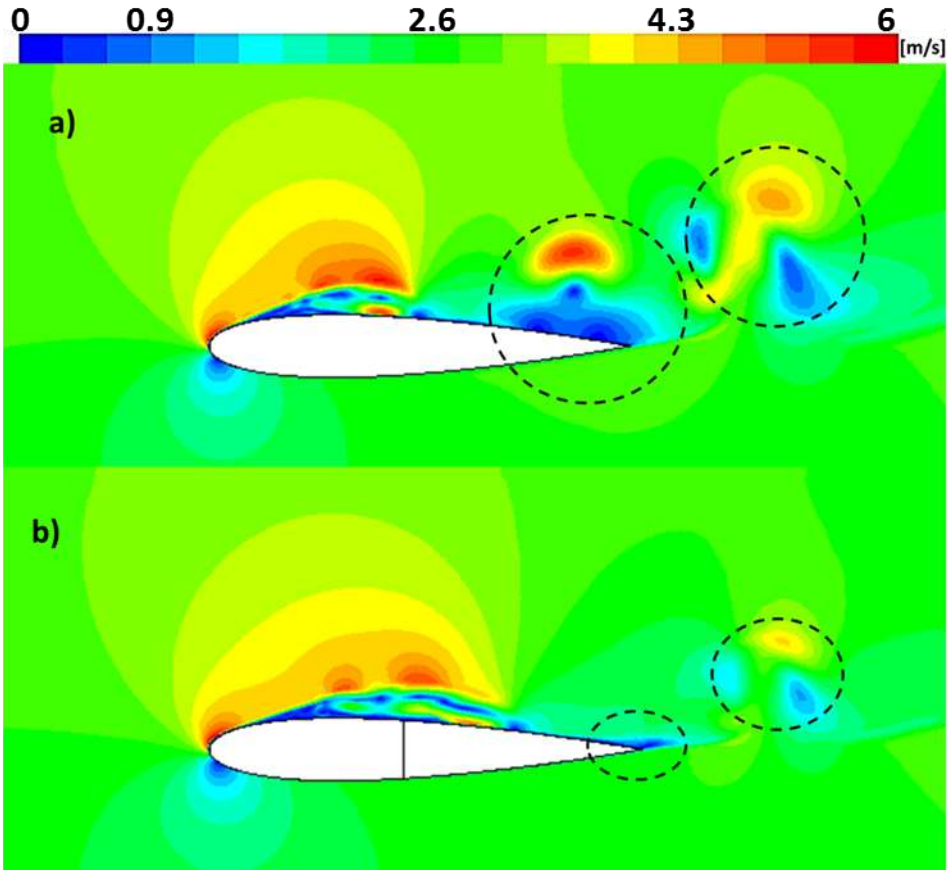

Figure 6.14 Contour of velocity magnitude at maximum velocity equal to 2.92 (m/s) for sinusoidal input flow, at 12.3 (Degree), Before the Stall

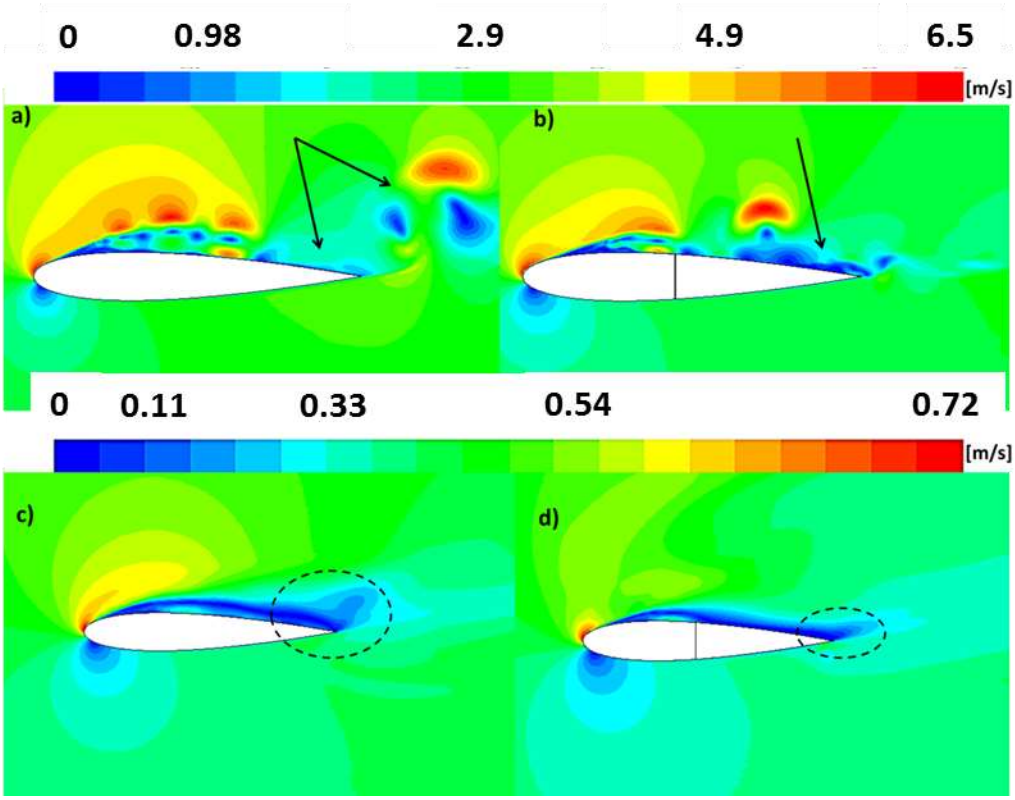

Figure 6.15 a) and b) Contour of velocity magnitude, c) and d) Mean Velocity Magnitude, at maximum velocity equal to 2.92 (m/s) for sinusoidal input flow, at13.6 degrees, After the Stall

The path-lien coloured by mean velocity magnitude highlights the improvement effect of suction slot on separation layers in Figures 6.16 and 6.17. It can be noted that by adding a suction slot in the aerofoil, this suction slot decreased from the separation layer at the end of aerofoil. When comparing between Figure 6.16 (before the stall) and Figure 6.17 (after the stall), it can be also noted that the improvement effect of suction slot on separation layers increased in stall regime. The pressure distribution around the upper and lower surface at 12.3 degrees before the stall (Figure 6.18) and 13.6 degrees after the stall (Figure 6.19) were presented. The effect of suction slot on the trailing edge area was appearing through the decrease from the low pressure area that cause disturbances in the path line at the trailing edge area and it extend to the area beyond the trailing edge (Figures 6.17 and 6.17). The pressure distribution after suction slot location (L_{SS} = 45%) at the upper surface is having direct effect in his value before and after the stall. The different in pressure value between the upper and lower surface after the slot

location (Figure 6.19) was decreased due to the slot effect. This decrease was make the pressure distribution behaviour similar to the pressure distribution for the upper surface of the aerofoil before the stall (Figure 6.18) which it lead to delay on the stall condition.

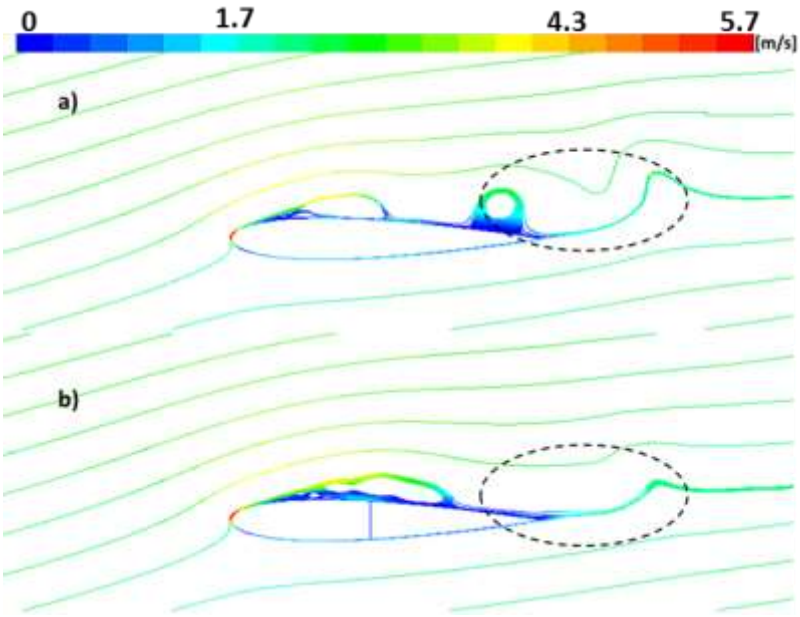

Figure 6.16 Path-line coloured by mean velocity magnitude at maximum velocity equal to 2.92 (m/s) for sinusoidal input flow, at 12.3 (Degree), Before the Stall

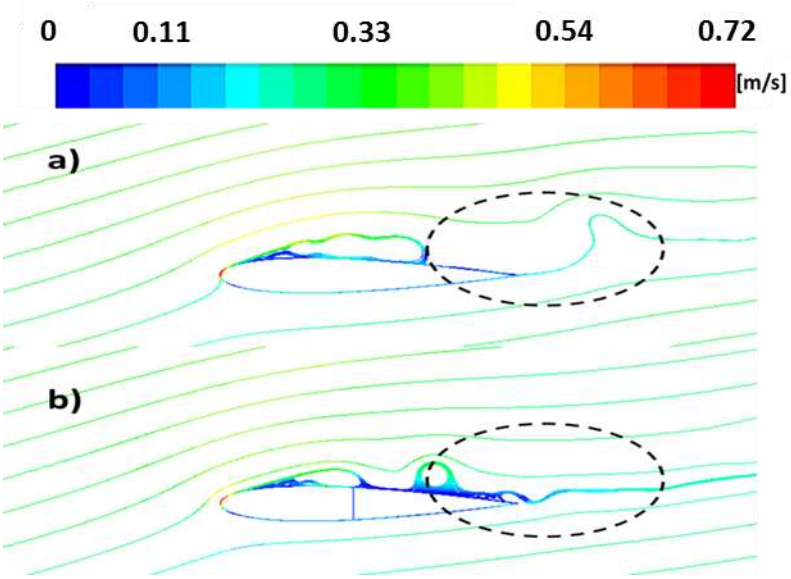

Figure 6.17 Path-line coloured by mean velocity magnitude at maximum velocity equal to 2.92 (m/s) for sinusoidal input flow, at 13.6 (Degree), After the Stall

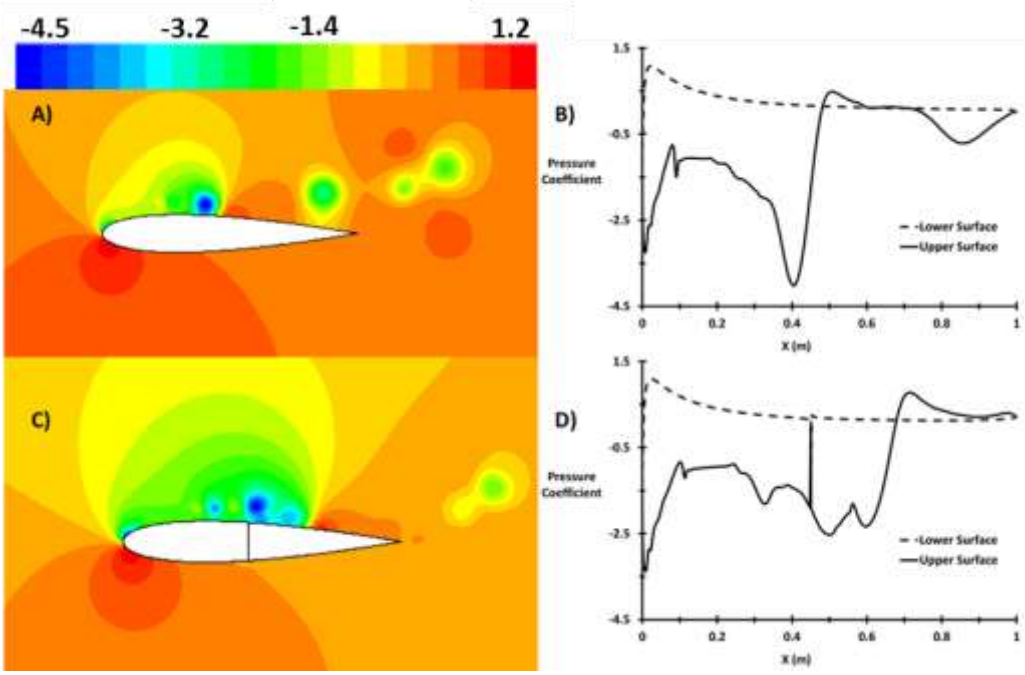

Figure 6.18 The pressure distribution at maximum velocity equal to 2.92 (m/s) for sinusoidal input flow, at 12.3 (Degree), Before the Stall

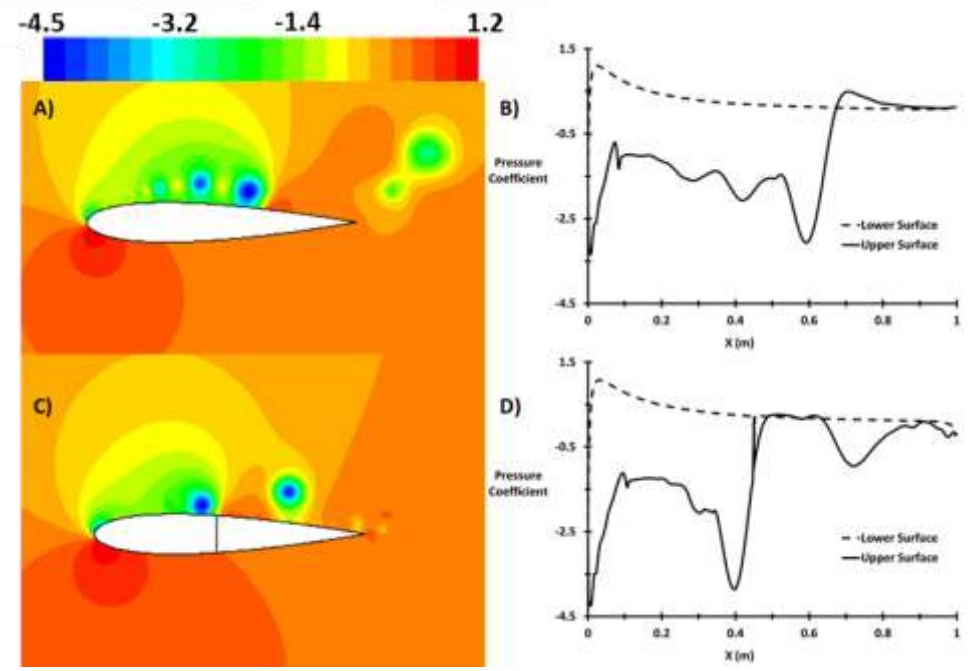

Figure 6.19 The pressure distribution at maximum velocity equal to 2.92 (m/s) for sinusoidal input flow, at 13.6 (Degree), After the Stall

6.2.2.3 Second law analysis

The numerical simulations were used to obtain local entropy viscosity predictions of the different angles of attack. Figures 6.20 and 6.21 highlight the suction slot effect in the entropy behaviour when a flow is accelerating and decelerating in compression cycle. Consequently, the entropy generations rate varies with the Reynolds number. The change of Reynolds number values is due to using sinusoidal wave boundary conditions. Suction slots have negative effect on the entropy behaviour in both accelerating and decelerating flow. However, at some Reynolds number the suction slot decreased from the entropy generation, such as Figure 6.20 e) at Reynolds number less than 1×10^5 in accelerating flow and also Figure 6.21 a) at Reynolds number equal to 1.6×10^5 in decelerating flow. The aerofoil with suction slot at 11.3 degrees has an average increase in the entropy generation rate by 22% higher than that without suction slot for the accelerating flow, where the maximum difference in the entropy generation rate was found at Reynolds number equal to 1.93×10^5 and 2×10^5 by 36% higher than that without suction slot. On the other hand, the minimum difference in the entropy generation rate was found at Reynolds number from 5×10^4 to 1×10^5 by 11% higher than that without a suction slot; see Figure 6.21 a). For decelerating flow at 11.3 degrees, it can be noted that the maximum increase in the entropy generation rate due to suction slot was 35% at Reynolds number equal to 5.5×10^4. On the other side, the entropy generation rate decreased than that without suction slot by 23% at 1.6×10^5 Reynolds number. This increase and decrease in the entropy generation rate for the aerofoil with suction slot gives an average value equal to 0% at decelerating flow, see Figure 6.21 a). From Figure 6.20 b), it can be noted that the maximum increase in the entropy generation rate was 39% due to suction slot for accelerating flow at 1.98×10^5 Reynolds number. On the other hand, the minimum increase in the entropy generation rate was 11% at Reynolds number from 7.8×10^4 to 1×10^5, with an average percentage 22% for the 11.7 degree. For decelerating flow at 11.7 degree, the maximum increase in the entropy generation rate was 31% at 3×10^4 Reynolds number and the minimum value was 14% at 1.75×10^5 Reynolds number. This fluctuating in the entropy generation rate

value for the NACA0015 with suction slot gives an average value equal to 14% at decelerating flow, see Figure 6.21 b). The 12.3 degree at accelerating flow gives maximum increase by 35% at 2×10^5 Reynolds number and minimum increase by 6% Reynolds number from 7.8×10^4 to 1×10^5 with an average percentage 21%, see Figure 6.20 c). However, Figure 6.21 c) shows the maximum increase by 34% at 8×10^4 Reynolds number and minimum increase by 3% 1.6×10^5 Reynolds number with an average percentage 18%.

The aerofoil with suction slot at 13.6 degree has an average increase in the entropy generation rate by 51% than that without suction slot for the accelerating flow, where the maximum difference in the entropy generation rate was found at Reynolds number equal to 2.84×10^4 by 152% than that without suction slot. Also, the minimum difference in the entropy generation rate was found at 1.6×10^5 Reynolds number by 17% than that without suction slot, see Figure 6.20 d). For decelerating flow at 13.6 degree, the maximum increase in the entropy generation rate was 36% at 1.6×10^5 Reynolds number and the minimum value was 5% at 8×10^4 Reynolds number (19% as average value), see Figure 6.21 d). The 14.4 degree at accelerating flow gives maximum increase by 26% at 1.85×10^5 and 1.98×10^5 Reynolds number, and minimum increase by 30% Reynolds number from 5.4×10^4 to 8×10^4 with average value equal to 3%, see Figure 6.21 e). However, Figure 6.21 e) shows the maximum increase by 46% at 8×10^4 and 1.43×10^5 Reynolds number, and minimum increase by 0% 1×10^5 Reynolds number with an average percentage 21%.

Furthermore, as an average value for the compression cycle, the suction slot was increased from the global entropy generation rate, see Figure 6.22, which led to a decrease in second law efficiency, see Figure 6.23. From Figures 6.22 and 6.23, it can be noted that the minimum value for the global entropy generation rate and maximum second law efficiency occurs at 11.7 degree for aerofoil without suction slot. On the other hand, the minimum value for the global entropy generation rate and maximum second law efficiency occurs at 11.3 degree for NACA0015 with suction slot.

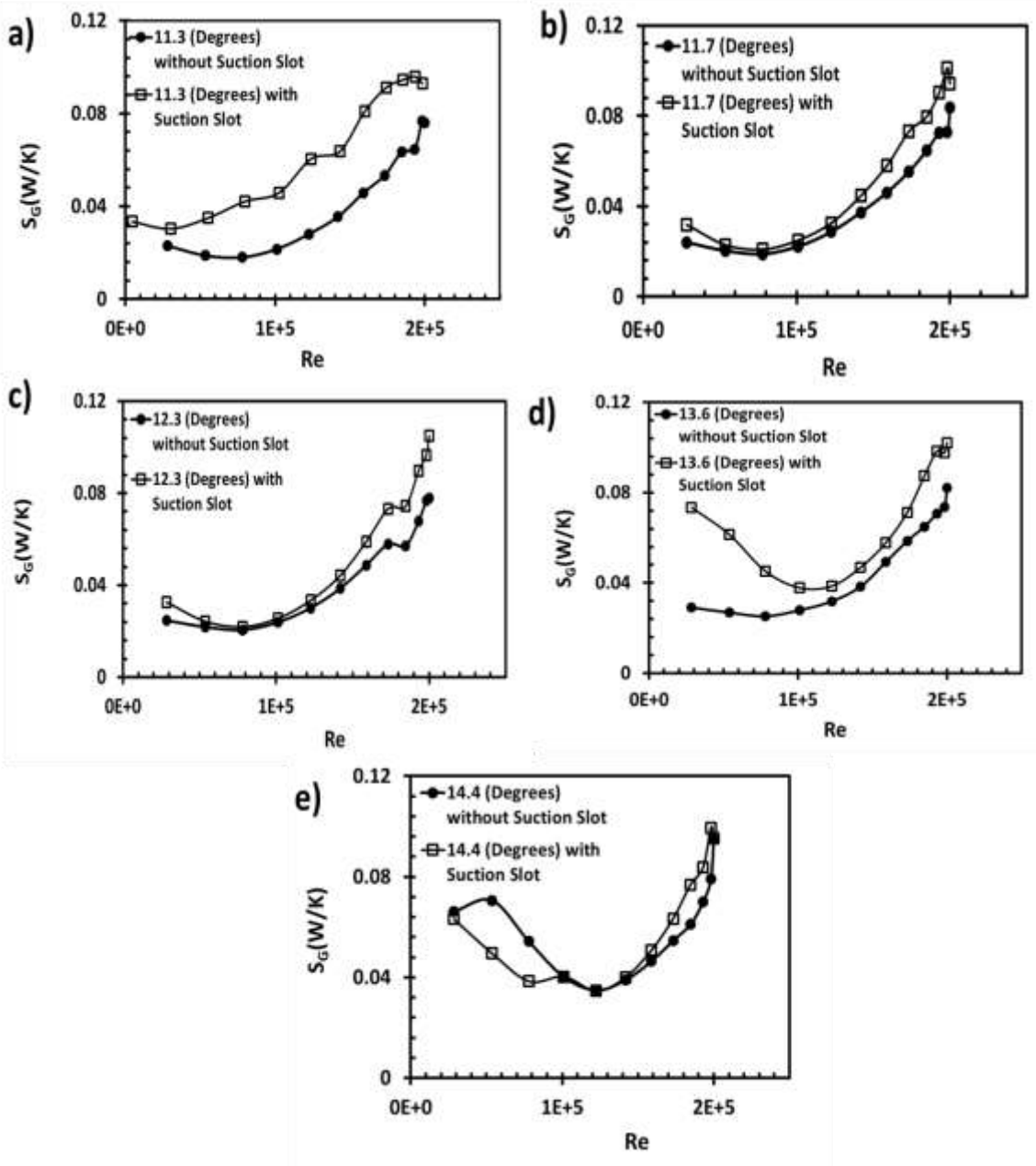

Figure 6.20 S_G variation with different Reynolds number at accelerating flow in compression cycle with optimum L_{ss} (45%) and optimum D_{ss} (0.001)

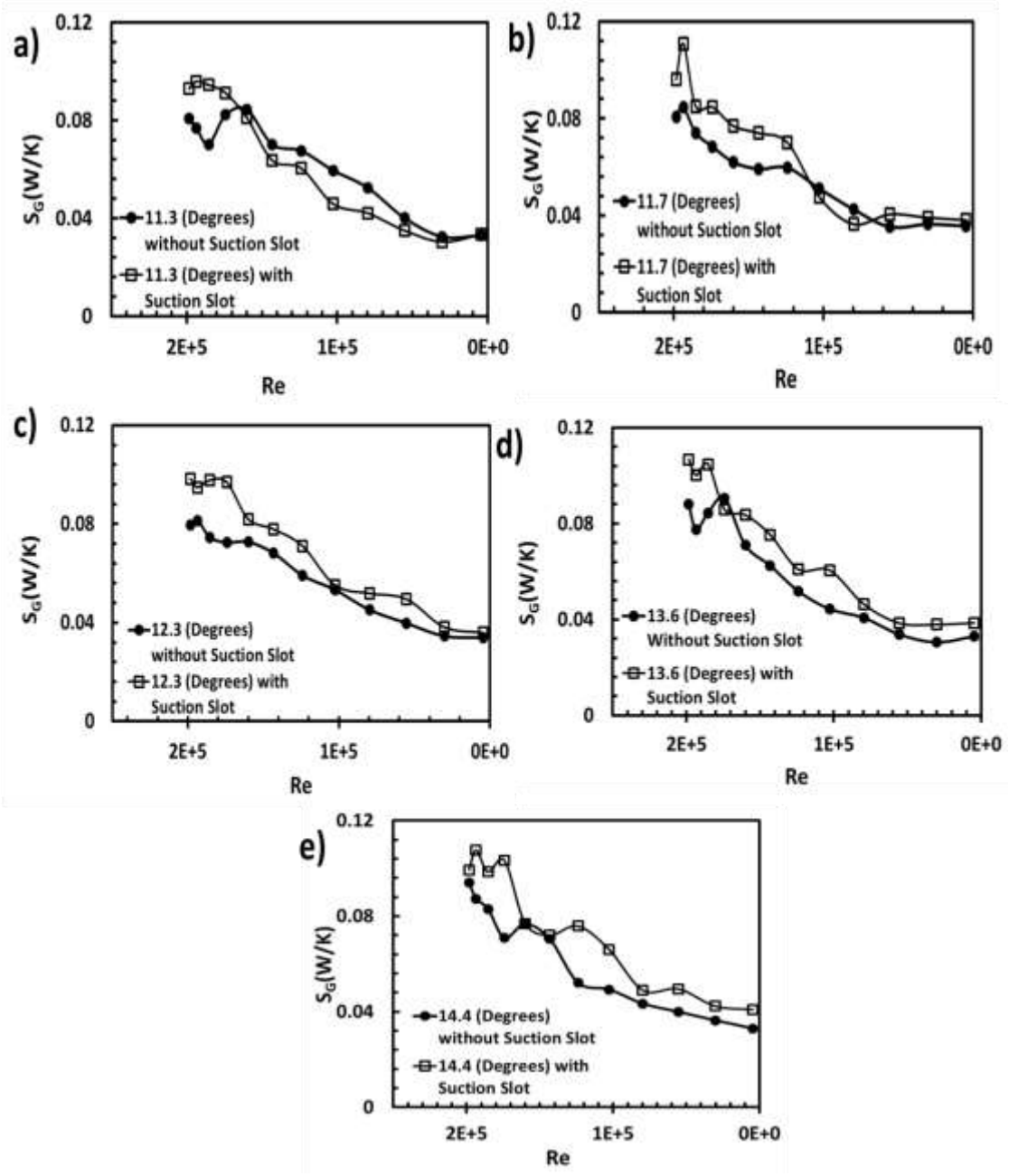

Figure 6.21 S_G variation with different Reynolds number at decelerating flow in compression cycle with optimum L_{ss} (45%) and optimum D_{ss} (0.001)

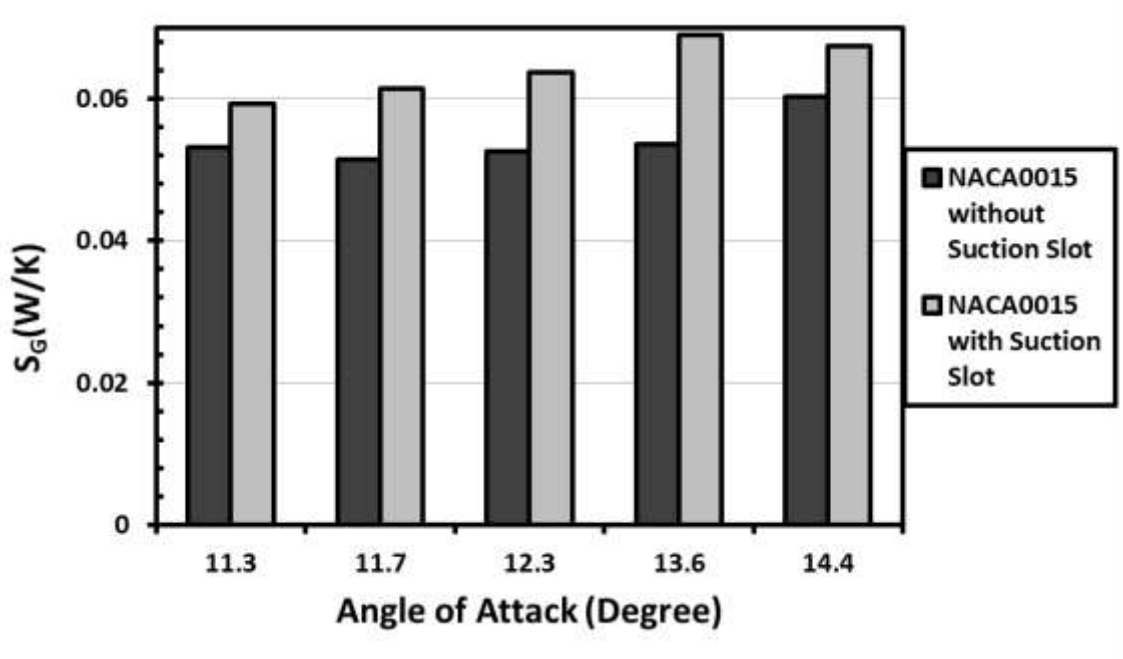

Figure 6.22 S_G in compression cycle for different angles of attack with optimum L_{ss} (45%) and optimum D_{ss} (0.001)

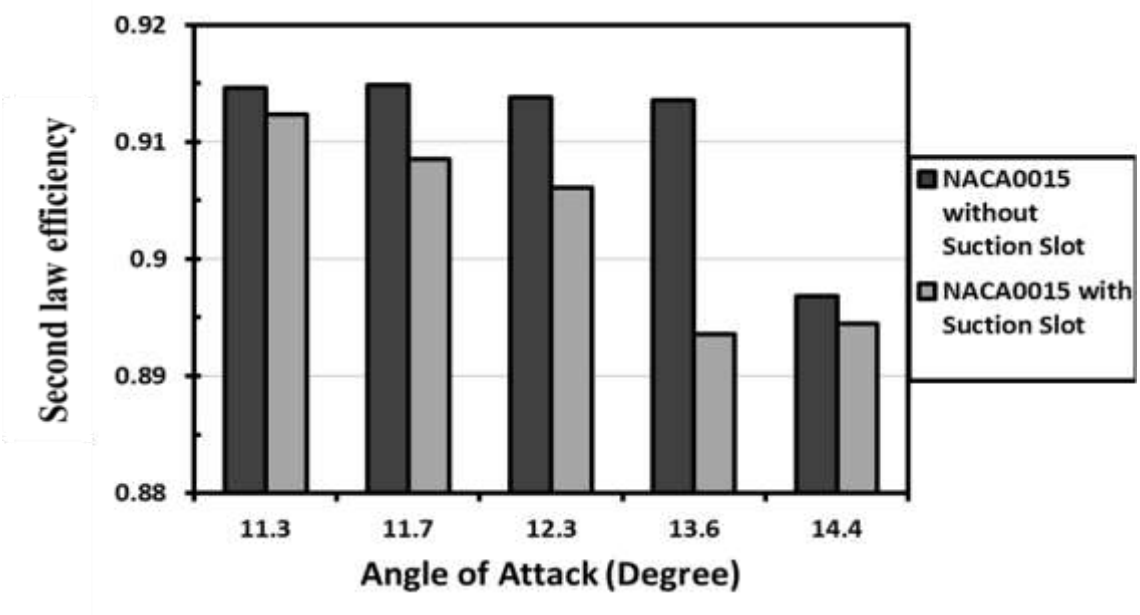

Figure 6.23 The second law efficiency in compression cycle for different angles of attack with optimum L_{ss} (45%) and optimum D_{ss} (0.001)

6.3 Optimum location for multi suction slots

A multi-suction slot with a certain diameter (D_{ss}) equal to 0.1% from the blade chord at various locations from the leading edge was created, with a shape of NACA0015 with stall angle equal to13.6 degrees and Reynolds number equal to 2×10^5 from reference (Torresi et al., 2009, Torresi et al., 2007b, Torresi et al., 2007a), see Figure 6.24. The locations for the suction slots were changed in order to obtain an optimum value of C_T. The test cases investigated were under unsteady flow with non-oscillating velocity at the first to indicate to the best locations and then take the best cases to investigate under sinusoidal wave condition to decide which one has the highest C_T and which one has the lowest S_G. The sinusoidal wave inlet flow boundary condition is having the same specifications as that in the section 6.2.2 and equation (4.1). Finally, a comparative analysis was made based on conditions relevant to northern coast of Egypt with different sinusoidal wave frequencies (f equal to 0.25, 0.167 and 1.25 Hz) see Figure 5.16.

6.3.1 Multi suction slots (Two, Three and Four)

The two suction slots were investigated by making the first suction slots as a reference (L_{Rss}) and changing the location (x axis direction) of the second suction slots (L_{ss}) by pitch distance (P_{ss}) equal to 0.05 at each trial. Considering that, the minimum distance between the two suction slots (ΔP_{ss}) was equal to 0.05.

Table 6.3 provides the details about all two suction slots trial with $P_{ss}$and ΔP_{ss} equals to 0.05 to improve the torque coefficient at the stall angle 13.6 degrees (Figure 4.8). It can be noted that the L_{Rss} equal to 40% and L_{ss} equal to 45% gives a higher torque coefficient than others, where the torque coefficient increases about 82% higher than the aerofoil without suction slot at the stall angle. Therefore, to get more improvement in the torque coefficient, the value of P_{ss} and ΔP_{ss} was changes to 0.01 around the L_{ss} 40% and L_{ss} 45%. It can be concluded that two suction slots at L_{Rss} 40% and L_{ss} 44% with P_{ss} equal to 0.01 give a higher torque coefficient than others by 84% at the stall angle in

Figure 6.25 A). On the other hand, two suction slots at L_{Rss} 45% and L_{ss} 49% give also a higher torque coefficient than others by 84% at the stall angle from Figure 6.25 B).

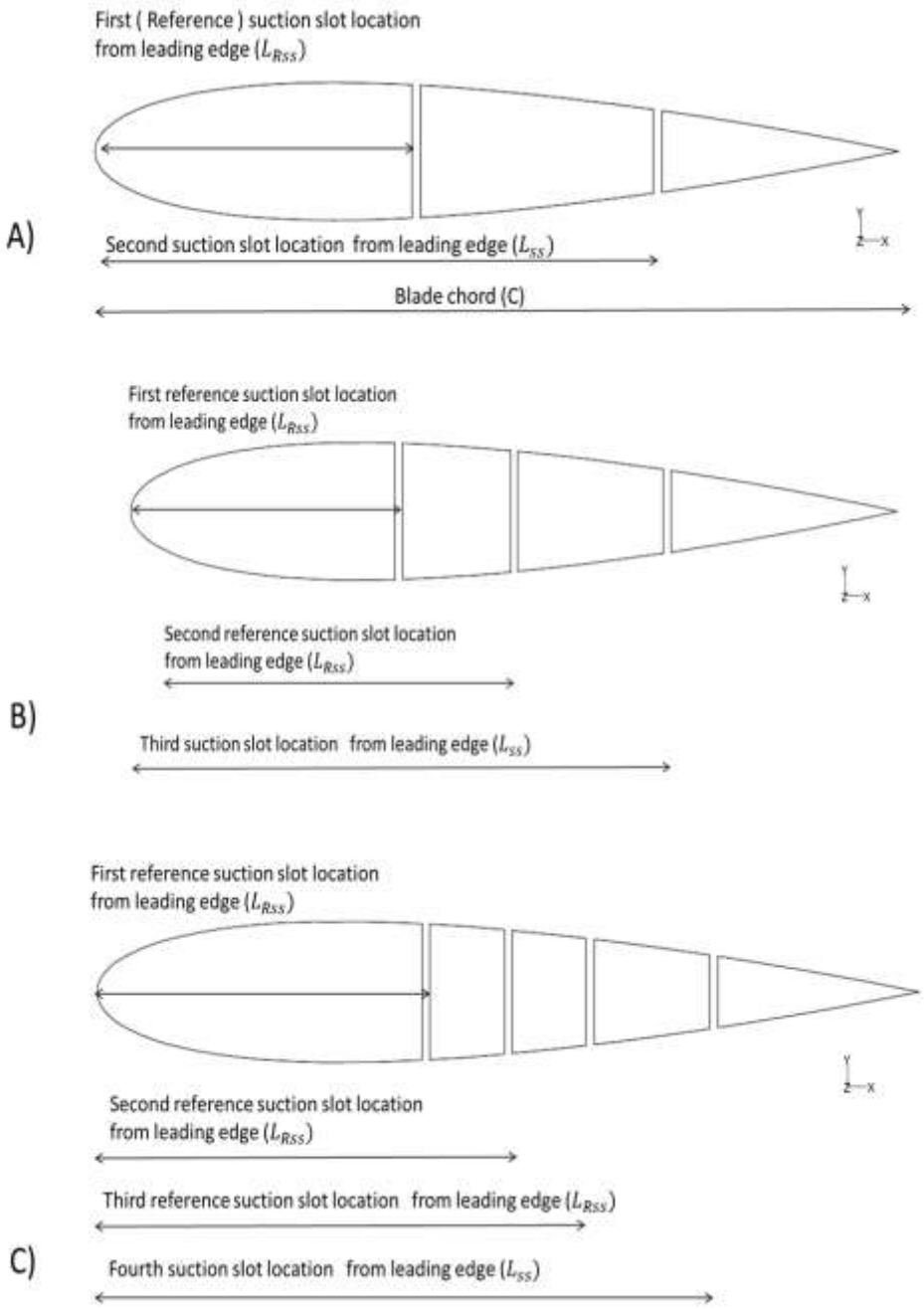

Figure 6.24 Aerofoil diagram with two, three and four suction slots A) Two suction slots B) Three suction slots C) four suction slots

From Table 6.3 and Figure 6.25, it can be noted that the three optimum locations for two suction slots were L_{ss}40% and 45% with P_{ss} equal to 0.05, in addition to L_{ss} 40% and 44% and L_{ss} 45% and 49% with P_{ss} equal to 0.01. Table 6.4 demonstrates the effect of the three optimum locations for two suction slots on the torque coefficient at different angles. It can be noted that the two suction slots at L_{ss} 40% and 45% improve the torque coefficient before the stall by 37.2% and after the stall by 95.5%. Also, the two suction slots at L_{ss} 40% and 44% improve the torque coefficient before the stall by 33.5% and after the stall by 97.5%. Finally, the two suction slots at L_{ss} 45% and 49% improve the torque coefficient before the stall by 36.7% and after the stall by 99%.

The suction slots have a negative effect on the entropy generation, where the global entropy generation rate increases at all angles by 24% before the stall and 23% after the stall due to suction slots at (L_{ss}40% and 45%). Where, the 11.3 degrees angle of attack (before the stall) has the highest difference in global entropy generation rate by 38%. On the other hand, 11.7 degrees angle of attack (before the stall) has the lowest difference in global entropy generation rate by 13 % due to suction slots at Figure 6.26 A). Furthermore, the suction slots at (L_{ss}40% and 44%) cause increase in the global entropy generation rate value as average for all angles by 21% before the stall and 26% after the stall at Figure 6.26 B). The 10.1 degree angle of attack (before the stall) has the lowest difference in global entropy generation rate by 14% due to suction slots and, the 14.4 degrees angle of attack (after the stall) has the highest difference by 29 %. Finally, for suction slots at (L_{ss}45% and 49%) at Figure 6.26 C), the global entropy generation rate increases as average in all angles by 21% before the stall and 22% after the stall. Where, the 10.6 degrees (before the stall) has the highest difference in global entropy generation rate by 44% and, the 12.3 degrees (before the stall) has the lowest by 11 % due to suction slots. This phenomenon suggests that the change in velocity gradient due to the suction slot has a direct impact on the entropy generation.

Table 6.3 Two suction slots with P_{ss} and ΔP_{ss} equal to 0.05

Reference suction slot	Location of second suction slot															Max. value %
	20%	25%	30%	35%	40%	45%	50%	55%	60%	65%	70%	75%	80%	85%	90%	
R 20%	-	0.121	0.083	0.12	0.102	0.13	0.126	0.123	0.117	0.11	0.101	0.102	0.094	0.1	0.087	56
R 25%	0.121	-	0.126	0.124	0.121	0.12	0.123	0.146	0.122	0.114	0.117	0.125	0.108	0.11	0.115	76
R 30%	0.083	0.126	-	0.125	0.123	0.14	0.118	0.119	0.127	0.118	0.113	0.121	0.117	0.11	0.1	65
R 35%	0.12	0.124	0.125	-	0.133	0.15	0.125	0.122	0.134	0.125	0.138	0.119	0.116	0.12	0.107	74
R 40%	0.102	0.121	0.123	0.133	-	0.15	0.144	0.148	0.136	0.133	0.127	0.137	0.134	0.14	0.142	81
R 45%	0.129	0.123	0.137	0.145	0.151	-	0.131	0.131	0.132	0.137	0.123	0.137	0.128	0.12	0.106	81
R 50%	0.126	0.123	0.118	0.126	0.144	0.13	-	0.125	0.138	0.142	0.137	0.127	0.138	0.13	0.134	74
R 55%	0.123	0.146	0.119	0.122	0.148	0.13	0.125	-	0.114	0.122	0.104	0.121	0.131	0.13	0.126	78
R 60%	0.117	0.122	0.127	0.134	0.136	0.13	0.138	0.114	-	0.108	0.13	0.136	0.128	0.11	0.115	66
R 65%	0.11	0.114	0.118	0.125	0.133	0.14	0.142	0.122	0.108	-	0.131	0.111	0.131	0.12	0.123	71
R 70%	0.101	0.117	0.113	0.138	0.127	0.12	0.137	0.104	0.13	0.131	-	0.116	0.117	0.11	0.113	66
R 75%	0.102	0.125	0.121	0.119	0.137	0.14	0.127	0.121	0.136	0.111	0.116	-	0.118	0.12	0.086	65
R 80%	0.094	0.108	0.117	0.116	0.134	0.13	0.138	0.131	0.128	0.131	0.117	0.118	-	0.12	0.1	66
R 85%	0.099	0.111	0.113	0.117	0.135	0.12	0.13	0.129	0.11	0.117	0.113	0.117	0.115	-	0.102	62
R 90%	0.087	0.115	0.1	0.107	0.142	0.11	0.134	0.126	0.115	0.123	0.113	0.086	0.1	0.10	-	71

Maximum value

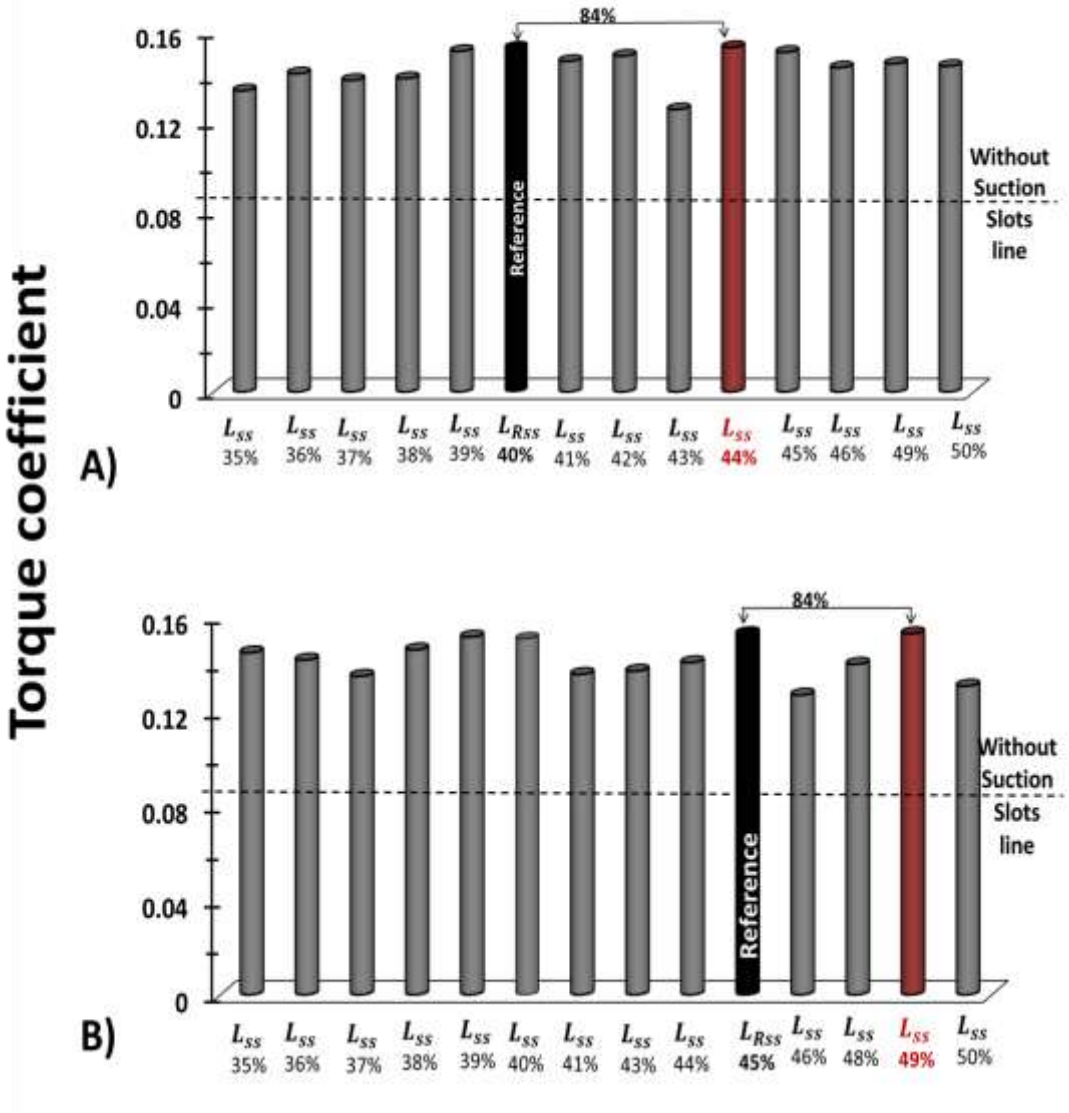

Figure 6.25 The effect of tow suction slots on the torque coefficient at the stall angle (13.6 degrees) with $\boldsymbol{P_{ss}}$and $\Delta\boldsymbol{P_{ss}}$ equal to 0.01 A) $\boldsymbol{L_{Rss}}$= 40% and 44%. B) $\boldsymbol{L_{Rss}}$= 45% and 49%

Table 6.4 The value of improvement in torque coefficient for the optimum locations for two suction slots at different angles with non-oscillating velocity

Torque Coefficient	**Angle of attack (Degree)**							
	8.7	10.1	10.6	11.3	11.7	12.3	13.6	14.4
Without Suction Slot	0.0509	0.0669	0.0726	0.0793	0.0856	0.0910	0.0830	0.0676
Two Suction Slots at $L_{ss} = 40\%$ and $L_{ss} = 45\%$	0.0654	0.0904	0.0973	0.1122	0.1210	0.1300	0.1505	0.1420
Improvement %	28	35	34	42	41	43	81	110
Two Suction Slots at $L_{ss} = 40\%$ and $L_{ss} = 44\%$	0.0659	0.0848	0.0980	0.1087	0.1175	0.1238	0.1526	0.1428
Improvement %	29	27	35	37	37	36	84	111
Two Suction Slots at $L_{ss} = 45\%$ and $L_{ss} = 49\%$	0.0627	0.0923	0.1011	0.1095	0.1194	0.1297	0.1526	0.1444
Improvement %	23	38	39	38	39	43	84	114

A third suction slot by P_{ss} equal to 0.05 was added to all aerofoils with two suction slots that have higher than 70% improvement in the torque coefficient at the stall angle 13.6 degrees. Table 6.5 provides all three suction slots trial with $P_{ss}$and ΔP_{ss} equal to 0.05 to improvement the torque coefficient at the stall angle (13.6 degrees). It can be noted that the L_{Rss} equal to 40% - 55% and L_{ss} equal to 90% gives a higher torque coefficient than others, where the torque coefficient increases about 94% higher than the aerofoil without suction slot. Therefore, to get more improvement in the torque coefficient, the value of $P_{ss}$and ΔP_{ss} was changes to 0.01 around the L_{ss}40%, 55% and 90%. From Table 6.6, it can be noted that no improvement on the torque coefficient by change P_{ss} from 0.05 to 0.01 around the L_{ss}40%, 55% and 90%.

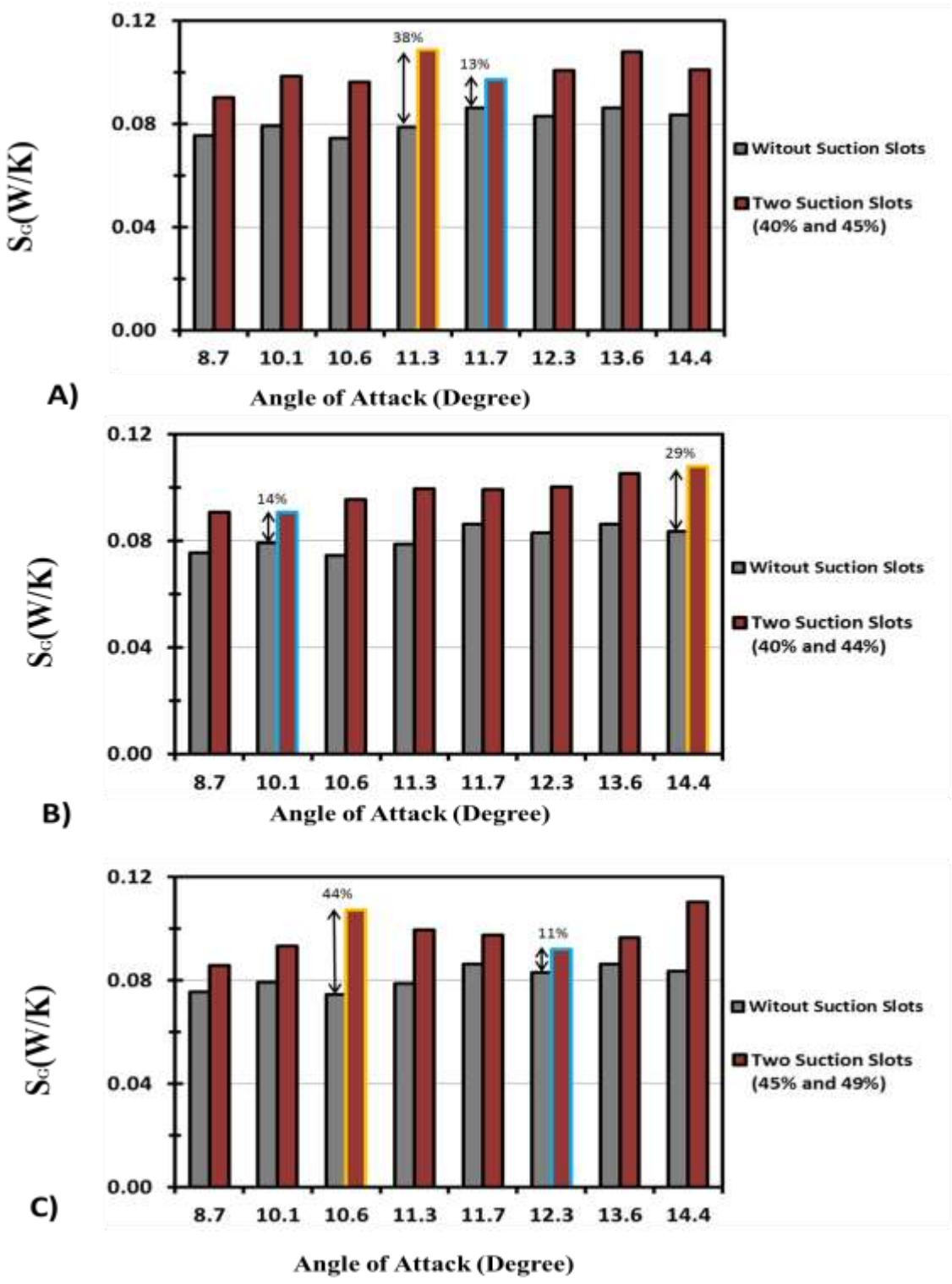

Figure 6.26 S_G for the optimum locations for two suction slots with non-oscillating velocity A) (L_{ss}40% and 45%) B) (L_{ss}40% and 44%). C) (L_{ss}45% and 49%)

Table 6.5 Three suction slots with P_{ss} and ΔP_{ss} equal to 0.05

Reference suction slot	Location of third suction slot												Max. value
	20%	25%	30%	35%	40%	45%	50%	55%	60%	65%	70%	75%	80%	85%	90%	
R 25% and R 55%	0.084	—	0.155	0.149	0.132	0.149	0.100	—	0.136	0.130	0.145	0.130	0.113	0.147	0.144	86%
R 35% and R 45%	0.130	0.131	0.104	—	0.143	—	0.137	0.142	0.140	0.133	0.127	0.142	0.130	0.136	0.138	72%
R 40% and R 45%	0.109	0.144	0.133	0.143	—	—	0.151	0.152	0.155	0.141	0.147	0.151	0.137	0.152	0.126	86%
R 40% and R 50%	0.121	0.104	0.139	0.129	—	0.151	—	0.137	0.146	0.151	0.146	0.142	0.140	0.137	0.144	82%
R 40% and R 55%	0.119	0.132	0.129	0.137	—	0.152	0.137	—	0.147	0.130	0.147	0.159	0.157	0.130	0.161	94%
R 40% and R 90%	0.083	0.135	0.135	0.142	—	0.126	0.144	0.161	0.140	0.137	0.138	0.129	0.140	0.129	—	94%
R 50% and R 65%	0.130	0.146	0.130	0.126	0.151	0.139	—	0.129	0.133	—	0.127	0.133	0.119	0.123	0.130	82%

Maximum value

Table 6.6 Three suction slots with $P_{ss}$and ΔP_{ss} equal to 0.01

Reference suction slot	Location of third suction slot											Max. value
	95%	94%	93%	92%	91%	90%	89%	88%	87%	86%	85%	
R 40% and R 55%	0.1577	0.1387	0.1369	0.1510	0.1536	0.1610	0.1543	0.1556	0.1542	0.138	0.130	94%
Reference suction slot	60%	59%	58%	57%	56%	55%	54%	53%	52%	51%	50%	Max. value
R 40% and R 90%	0.1397	0.1492	0.1437	0.1421	0.1414	0.1610	0.1425	0.1476	0.1423	0.124	0.144	94%
Reference suction slot	45%	44%	43%	42%	41%	40%	39%	38%	37%	36%	35%	Max. value
R 55% and R 90%	0.1318	0.1401	0.1433	0.1246	0.1386	0.1610	0.1553	0.1256	0.1306	0.125	0.125	94%

Maximum value

It is clearly noted that the three suction slots at (L_{ss}40%, 55% and 90%) improve the torque coefficient before the stall by 35.2% and after the stall by 97%, see Figure 6.27 A). On the other hand, the global entropy generation rate increases for all angles by 29% before the stall and 25% after the stall as average value at Figure 6.27 B). Where, the 10.1 degrees angle of attack (before the stall) has the highest difference in global entropy generation rate by 36% due to suction slots at (L_{ss}40%, 55% and 90%), and the 11.7 (before the stall) and 13.6 (after the stall) degrees have the lowest difference by 23 %.

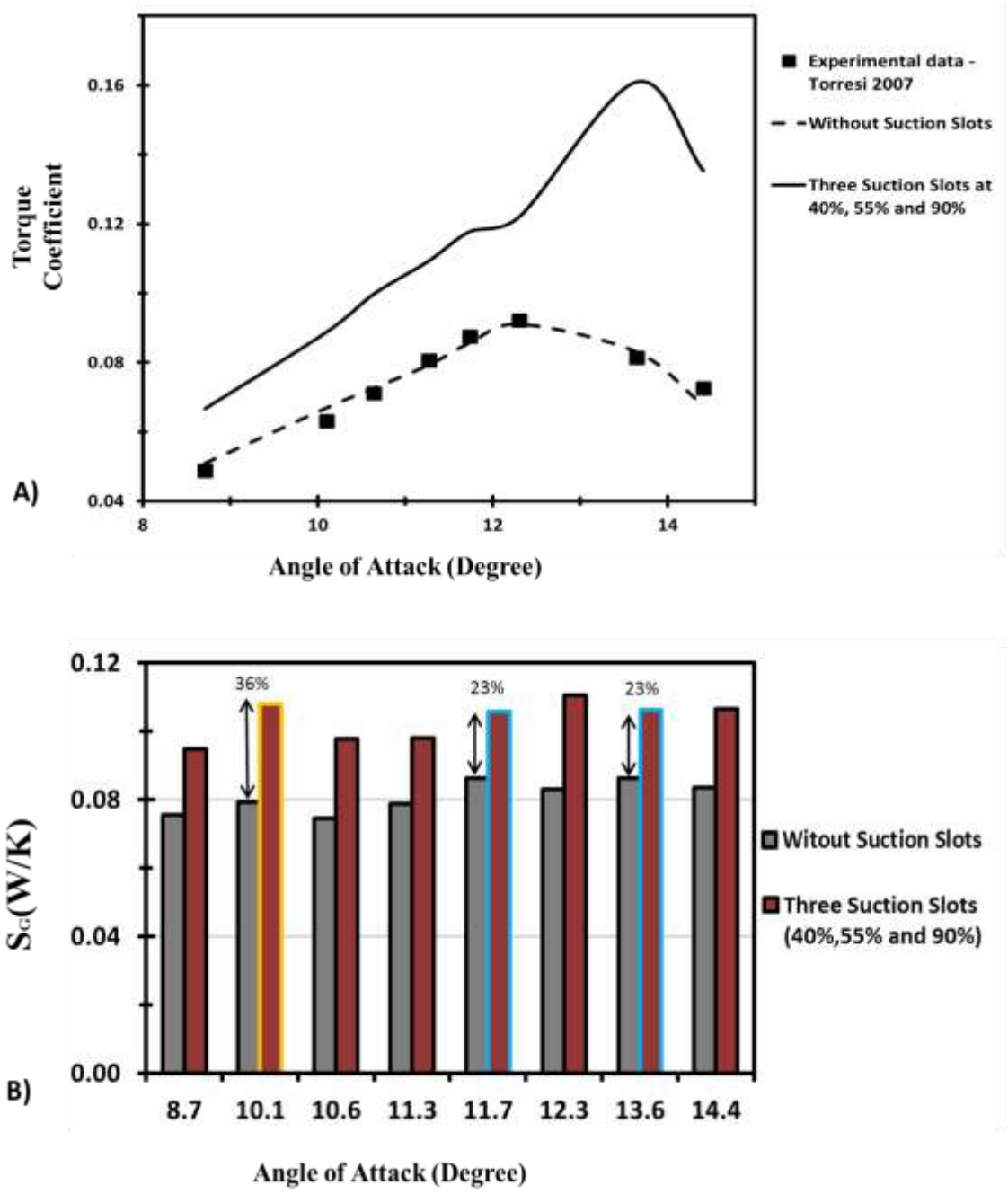

Figure 6.27 The optimum location for three suction slots at different angles with non-oscillating velocity. A) Torque coefficient. B) $\boldsymbol{S_G}$

A fourth suction slot with P_{ss} equal to 0.05 was added to all aerofoils with three suction slots that have higher than 80% improvement in the torque coefficient at the stall angle (13.6) degrees. Table 6.7 shows the effect of four suction slots on the torque coefficient

at the stall angle (13.6 Degree) with $P_{ss}$and ΔP_{ss} equal to 0.05 to improvement the torque coefficient. The L_{Rss} equal to 40% - 45% - 55% and L_{ss} equal to 60% gives a higher improvement in the torque coefficient by 92%. As in two and three suction slots, the value of $P_{ss}$and ΔP_{ss} changes to 0.01 around the L_{ss}40%, 45%, 55% and 60% to get more improvement in the torque coefficient. From Table 6.8, it can be noted that the L_{ss}40%, 45%, 55% and 60% give highest improvement on the torque coefficient with P_{ss} equal to 0.01.

The four suction slots (L_{ss}40%, 45%, 55% and 60%) improve the torque coefficient before the stall by 35.8% and after the stall by 99%, see Figure 6.28 A). Otherwise, the global entropy generation rate increases by 29% before the stall and 26% after the stall at Figure 6.28 B).Where, the 10.1 degrees has the lowest difference in global entropy generation rate by 16% and, the 10.6 degrees has the highest difference by 52 %.

The path line coloured by the mean velocity magnitude around the NACA0015 without and with slots at the stall angle 13.6 degrees was presented at Figure 6.29. The slots effect was very cleared on the separation layers at the trailing edge area and it extends to the area beyond the trailing edge which, leads to delay the stall. Therefore, the NACA0015 with suction slots and Reynolds number equal to 2×10^5 not have the stall condition at 13.6 degrees. This improvement can be achieved by two, three or four slots at different location. Where, each case of them has different behaviour.

Table 6.7 Four suction slots with P_{ss} and ΔP_{ss} equal to 0.05

Reference suction slot	Location of fourth suction slot												Max. value
	20%	25%	30%	35%	40%	45%	50%	55%	60%	65%	70%	75%	80%	85%	90%	
R 25%, 30% and R 55%	0.143	—	—	0.151	0.13	0.142	0.124	—	0.155	0.122	0.144	0.155	0.123	0.148	0.156	88%
R 40%, 45% and R 50%	0.131	0.122	0.144	0.149	—	—	—	0.13	0.144	0.158	0.153	0.150	0.146	0.156	0.154	90%
R 40%, 45% and R 55%	0.141	0.137	0.132	0.137	—	—	0.143	—	0.160	0.135	0.157	0.151	0.156	0.155	0.125	92%
R 40%, 45% and R 60%	0.132	0.131	0.136	0.142	—	—	0.144	0.10	—	0.148	0.148	0.145	0.150	0.151	0.137	92%
R 40%, 45% and R 75%	0.121	0.148	0.133	0.144	—	—	0.150	0.11	0.145	0.147	0.135	—	0.149	0.145	0.147	82%
R 40%, 45% and R 85%	0.128	0.143	0.136	0.136	—	—	0.156	0.65	0.151	0.142	0.138	0.745	0.136	—	0.139	88%
R 40%, 50% and R 65%	0.147	0.134	0.125	0.140	—	0.158	—	0.13	0.140	—	0.101	0.148	0.142	0.128	0.147	90%
R 40%, 55% and R 75%	0.143	0.099	0.136	0.141	—	0.151	0.157	—	0.150	0.150	0.148	—	0.147	0.139	0.156	89%
R 40%, 55% and R 80%	0.137	0.134	0.131	0.133	—	0.125	0.122	—	0.139	0.151	0.138	0.147	—	0.141	0.136	82%
R 40%, 55% and R 90%	0.141	0.134	0.135	0.149	—	0.134	0.148	—	0.143	0.137	0.155	0.156	0.136	0.157	—	89%

Maximum value

Table 6.8 Four suction slots with $P_{ss}$and ΔP_{ss} equal to 0.01

Reference suction slot	Location of fourth suction slot										Max. value
	65%	**64%**	**63%**	**62%**	**61%**	**60%**	**59%**	**58%**	**57%**	**56%**	
R 40%, 45% and R 55%	0.1348	0.1396	0.1507	0.1477	0.1400	0.1596	0.1501	0.1316	0.1359	0.1229	92%
Reference suction slot	**59%**	**58%**	**57%**	**56%**	**55%**	**54%**	**53%**	**52%**	**51%**	**50%**	**Max. value**
R 40%, 45% and R 60%	0.1409	0.1368	0.1306	0.1376	0.1596	0.1410	0.1344	0.1411	0.1427	0.1441	92%
Reference suction slot	**50%**	**49%**	**48%**	**47%**	**46%**	**45%**	**44%**	**43%**	**42%**	**41%**	**Max. value**
R 40%, 55% and R 60%	0.1239	0.1326	0.1338	0.1366	0.1291	0.1596	0.1364	0.1253	0.1126	0.1349	92%
Reference suction slot	**44%**	**43%**	**42%**	**41%**	**40%**	**39%**	**38%**	**37%**	**36%**	**35%**	**Max. value**
R 45%, 55% and R 60%	0.1302	0.1073	0.1397	0.1421	0.1596	0.1438	0.1318	0.1387	0.1307	0.1369	92%

Maximum value

The low pressure areas, at the trailing edge of the NACA0015 without slots, were caused the separation layer. On the other hand, the suction slots affect directly on these areas and decrease from its value and this leads to decrease the separation layers (Figure 6.30). The difference between the upper and lower surface was decreased by the suction slots and this leads to decrease from the disturbance and the separation layers (Figure 31). The pressure distribution at the upper and lower surface was depending on the number and location of the slots. Therefore, the two, three and four slots were investigated under sinusoidal wave condition in next section.

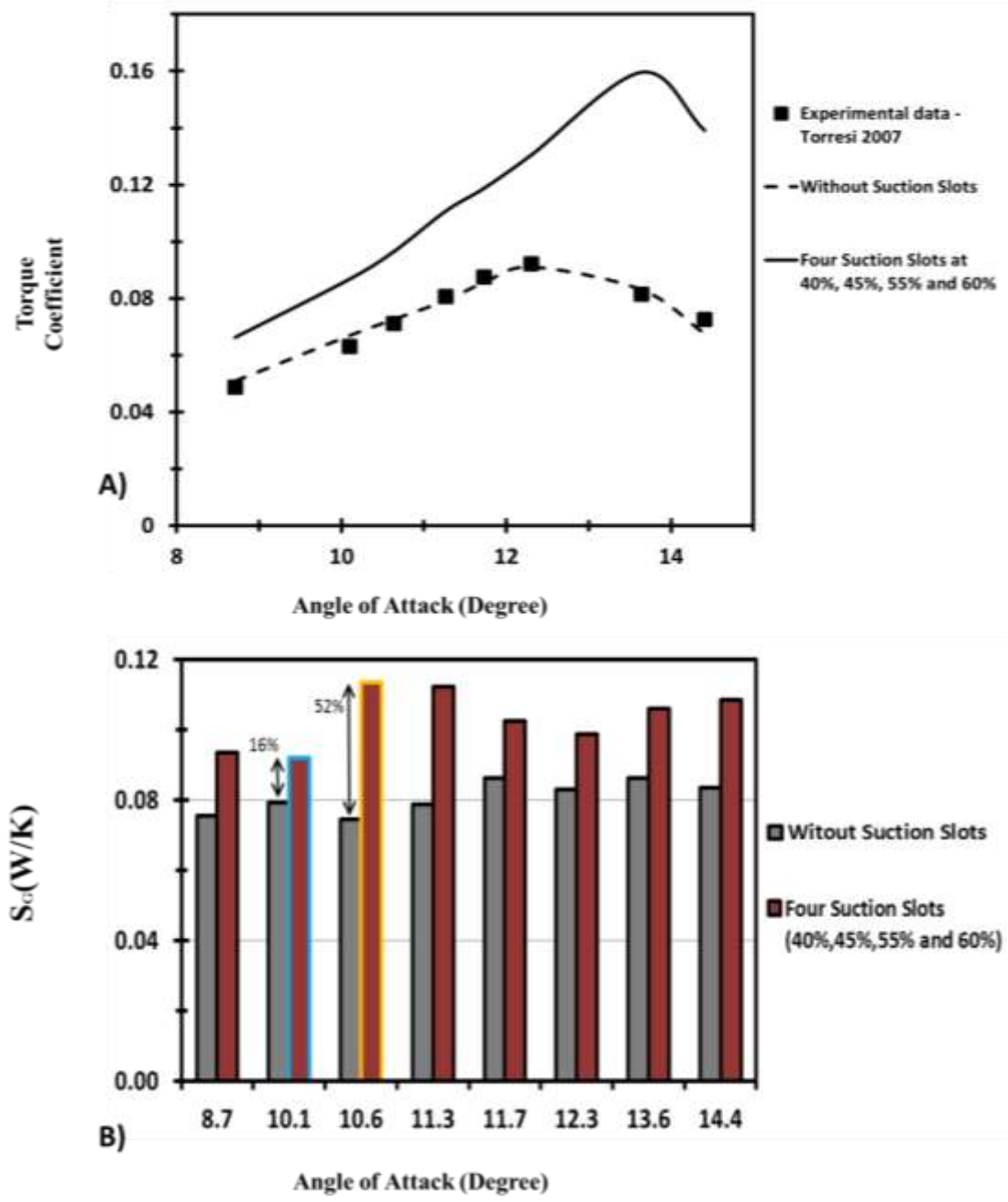

Figure 6.28 The optimum location for four suction slots at different angles with non-oscillating velocity A) Torque coefficient B) $\boldsymbol{S_G}$

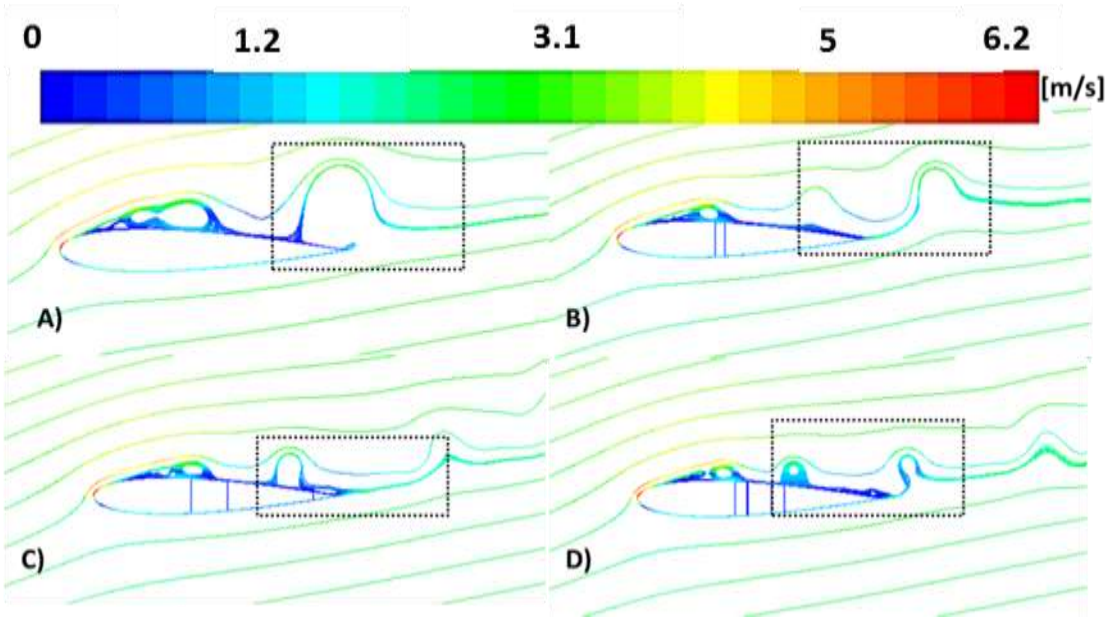

Figure 6.29 Path-line coloured by mean velocity magnitude at 13.6 degrees, A) NACA0015 without slots B) L_{ss}40% and 44% C) L_{ss}40%, 55% and 90% D) L_{ss}40%,45%, 55%, and 60%

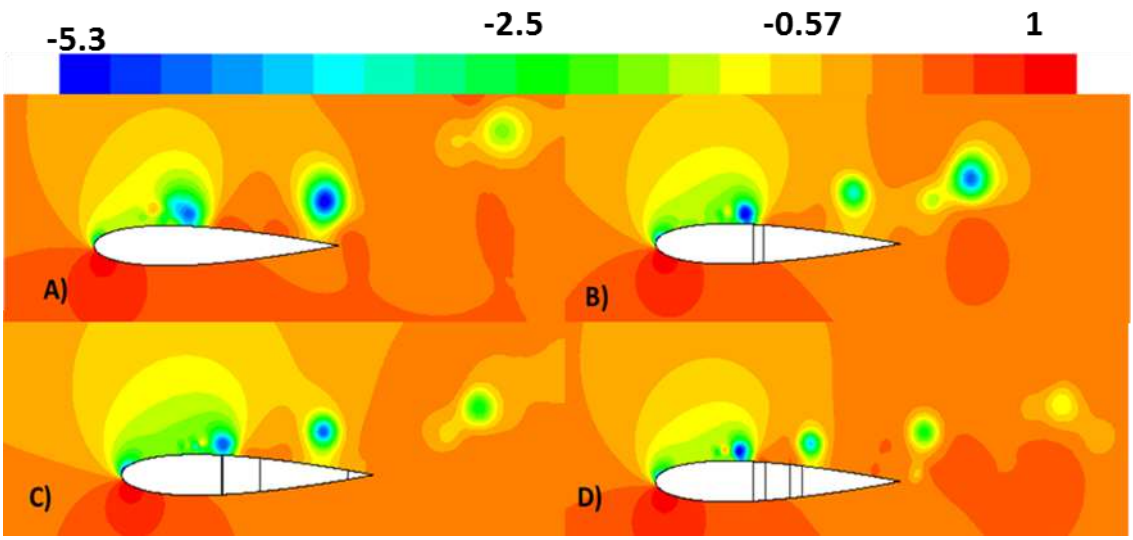

Figure 6.30 Contours of pressure coefficient around the aerofoil at 13.6 degrees, A) NACA0015 without slots B) L_{ss}40% and 44% C) L_{ss}40%, 55% and 90% D) L_{ss}40%,45%, 55%, and 60%

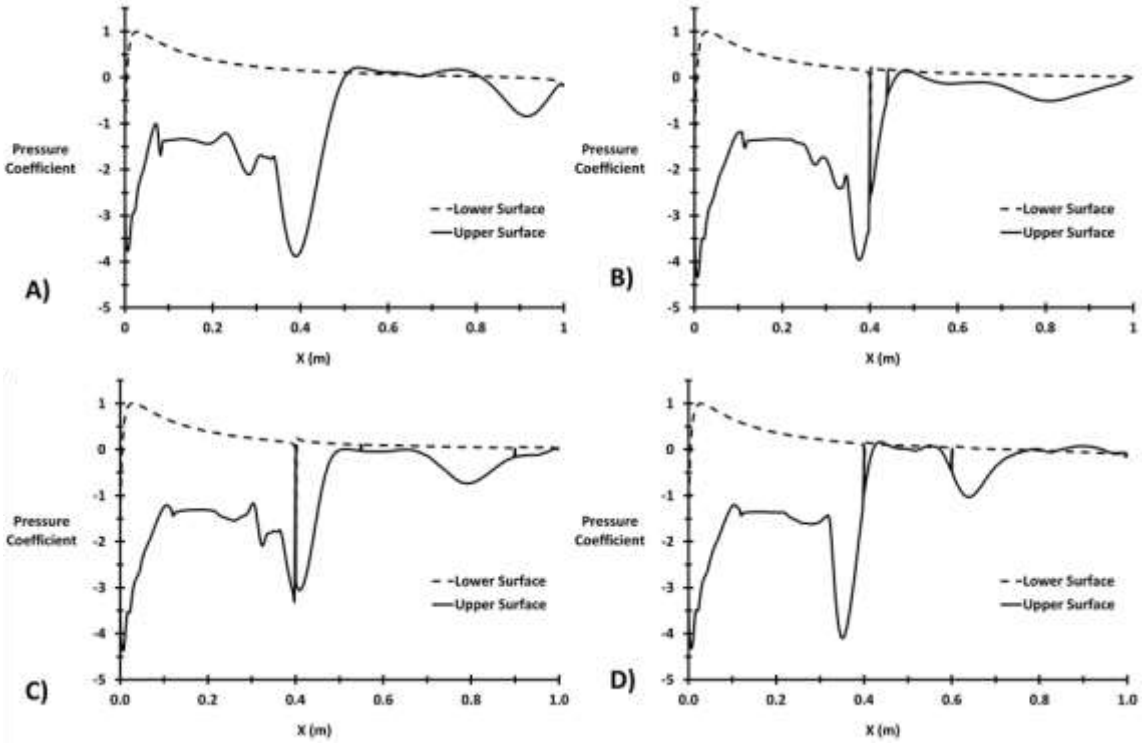

Figure 6.31 Pressure distribution on the upper and lower surface at 13.6 degrees, A) NACA0015 without slots B) L_{ss}40% and 44% C) L_{ss}40%, 55% and 90% D) L_{ss}40%,45%, 55%, and 60%

6.3.2 Optimum location for multi-suction slots based on first law analysis

From the previous section, it was noted that there are five scenarios for the suction slots location, which gives higher torque coefficient at the stall regime:

1- Two Suction Slots (L_{ss}40% and 45%) with P_{ss} = 0.05
2- Two Suction Slots (L_{ss}40% and 44%) with P_{ss} = 0.01
3- Two Suction Slots (L_{ss}45% and 49%) with P_{ss} = 0.01
4- Three Suction Slots (L_{ss}40%, 55% and 90%) with P_{ss} = 0.05
5- Four Suction Slots (L_{ss}40%,45%, 55%, and 60%) with P_{ss} = 0.05

In this section, the optimum locations for multi-suction slots based on the torque coefficient were determined under sinusoidal wave condition. Figure 6.32 compares the torque coefficients for the two suction slots aerofoil at different locations (L_{ss}40% and

45%), (L_{ss}40% and 44%) and (L_{ss}45% and 49%). Figure 6.32 A) illustrates the hysteretic behaviour due to the reciprocating flow which shows a delay in the stall regime and an improvement in the torque coefficient. The two suction slots aerofoil with L_{ss} of 40% and 44% has a higher improvement of torque coefficient than that with L_{ss} of 40% and 45% by 6.3% before the stall and 1.5 % after the stall. Moreover, the former aerofoil also has a higher torque coefficient than that with L_{ss} of 45% and 49% by 1% before the stall and 2.5 % after the stall (Figure 6.32 B).

Figure 6.33 shows the effect of adding three suction slots at (L_{ss}40%, 55% and 90%) and four suction slots at (L_{ss}40%, 45%, 55%, and 60%) under sinusoidal flow condition on the hysteretic behaviour. From this Figure, it can be noted that in both cases a delay in the stall regime occurred. In addition, the torque coefficient was improved by 26.7% before the stall and 51 % after the stall due to the addition of three suction slots (Figure 6.33 A). However, the addition of four suction slots resulted in torque coefficient improvement by 25.7% before the stall and 40.5% after the stall (Figure 6.33 B).

From Figure 6.34, it is clearly noted that adding three suction slots at (L_{ss}40%, 55% and 90%) provided the highest improvement of torque coefficient, from both the instantaneous and average value, compared to all the scenarios that were mentioned in this section. By comparing this aerofoil against the two suction slots aerofoil with optimum locations (L_{ss}40% and 44%), an improvement of torque coefficient of 2.7% before the stall and 22.5% after the stall was observed. Moreover, by comparing the same aerofoil against the four suction slots aerofoil (L_{ss}40%, 45%, 55%, and 60%), an improvement of torque coefficient of 1% before the stall and 10.5% after the stall was observed.

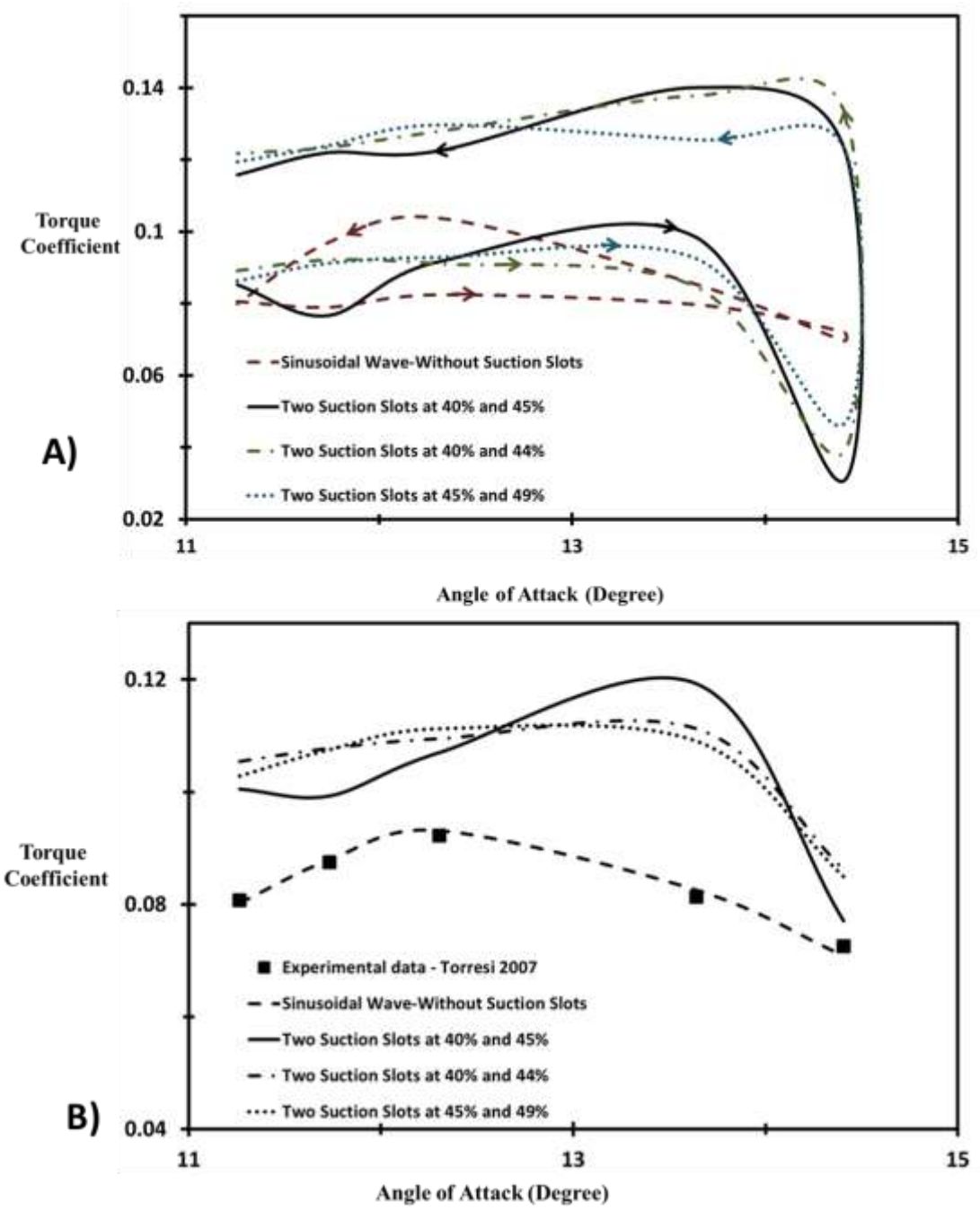

Figure 6.32 Comparison between the optimum locations for two suction slots at different angles with sinusoidal inlet velocity A) The hysteretic behaviour B) The average torque coefficient

The path-line coloured by mean velocity magnitude highlights the improvement effect of adding a suction slot on the separation layers in Figures 6.35, 6.36 and 6.37. The effect of adding a suction slot on the separation layers at the trailing edge region in Figure 6.35

(acceleration flow) was small compared with Figures 6.36 and 6.37. Where, the separation layers at the area around the trailing edge increased especially at the deceleration flow in the second half of the compression cycle (Figure 6.37). Furthermore, it can be noted that the low pressure areas around the trailing edge decrease due to the slots addition from Figures 6.38 and 6.39. The pressure difference between the lower and upper surfaces was decreased as a result of adding the slots. Therefore, the disturbances in the path line at the trailing edge area and the area extended beyond it was decreased. This leads to delay the stall and improve the torque coefficient.

Figure 6.40 shows the effect of adding three suction slots on the boundary layer separation before and after the stall condition via the mean velocity magnitude path-lines. It can be noted that the improvement effect of adding suction slot on separation layers increased in stall regime for both 13.6 and 14.4 degrees. The pressure distributions around the aerofoil and at the upper and lower surfaces for different angles of attack were shown in Figures 6.41 and 6.42. Where, the lift column is for the NACA0015 without slots and the right column is for the NACA0015 with three slots at L_{ss}40%, 55% and 90% with maximum velocity equal to 2.92 m/s. The addition of three slots affects directly the low pressure zones that appear around the trailing edge area and the upper surface of the aerofoil. Where, this low pressure zones were the main reason for the separation layers to be formed. For all angles, the aerofoil with three slots showed an improvement in the pressure distribution and decreased the separation layers especially for the stall angle of 14.4 degrees in Figure 6.40 I) and J).

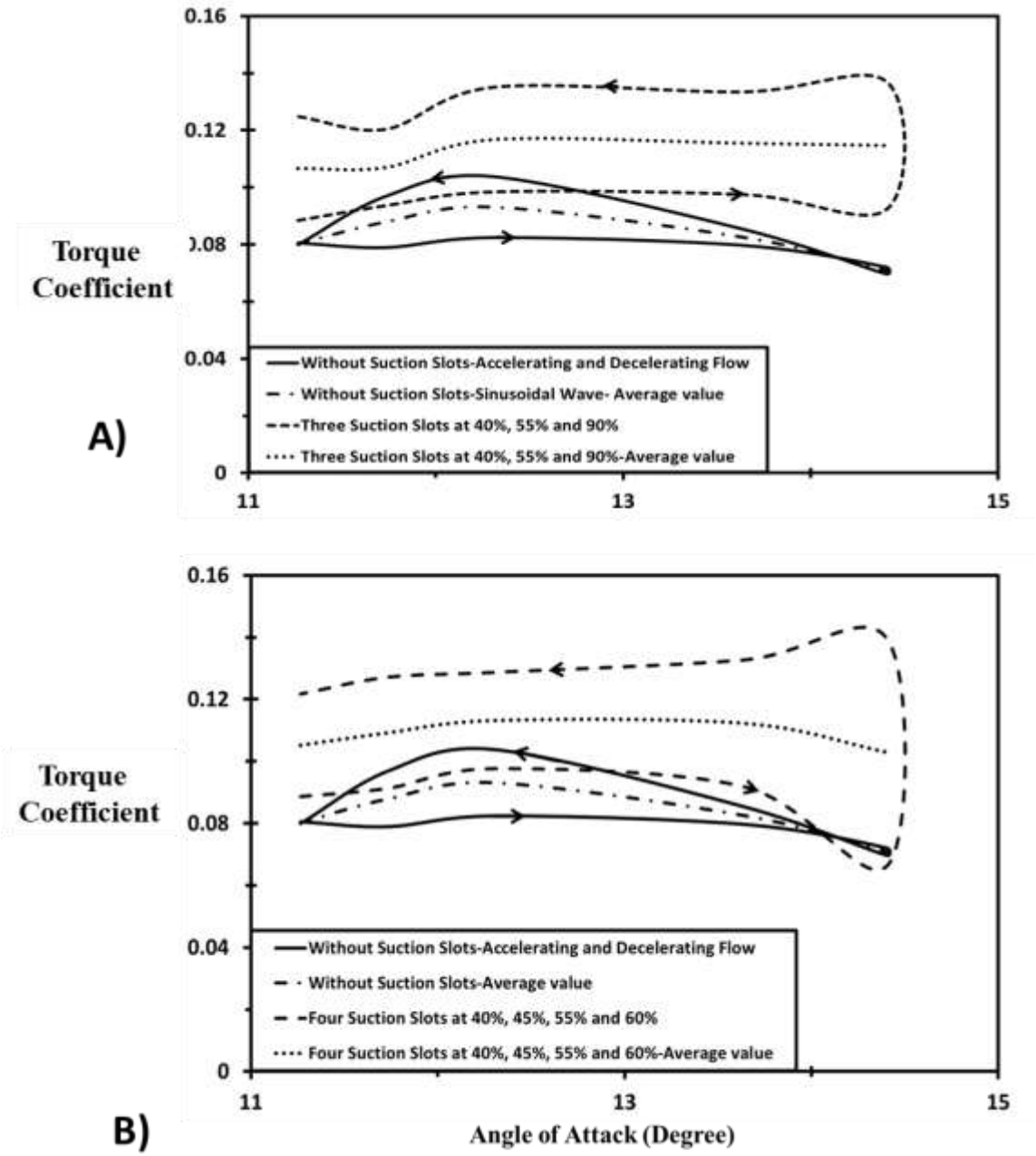

Figure 6.33 The hysteretic behaviour and the average torque coefficient for the optimum locations of the suction slots with sinusoidal velocity, A) Three suction slots B) Four suction slots

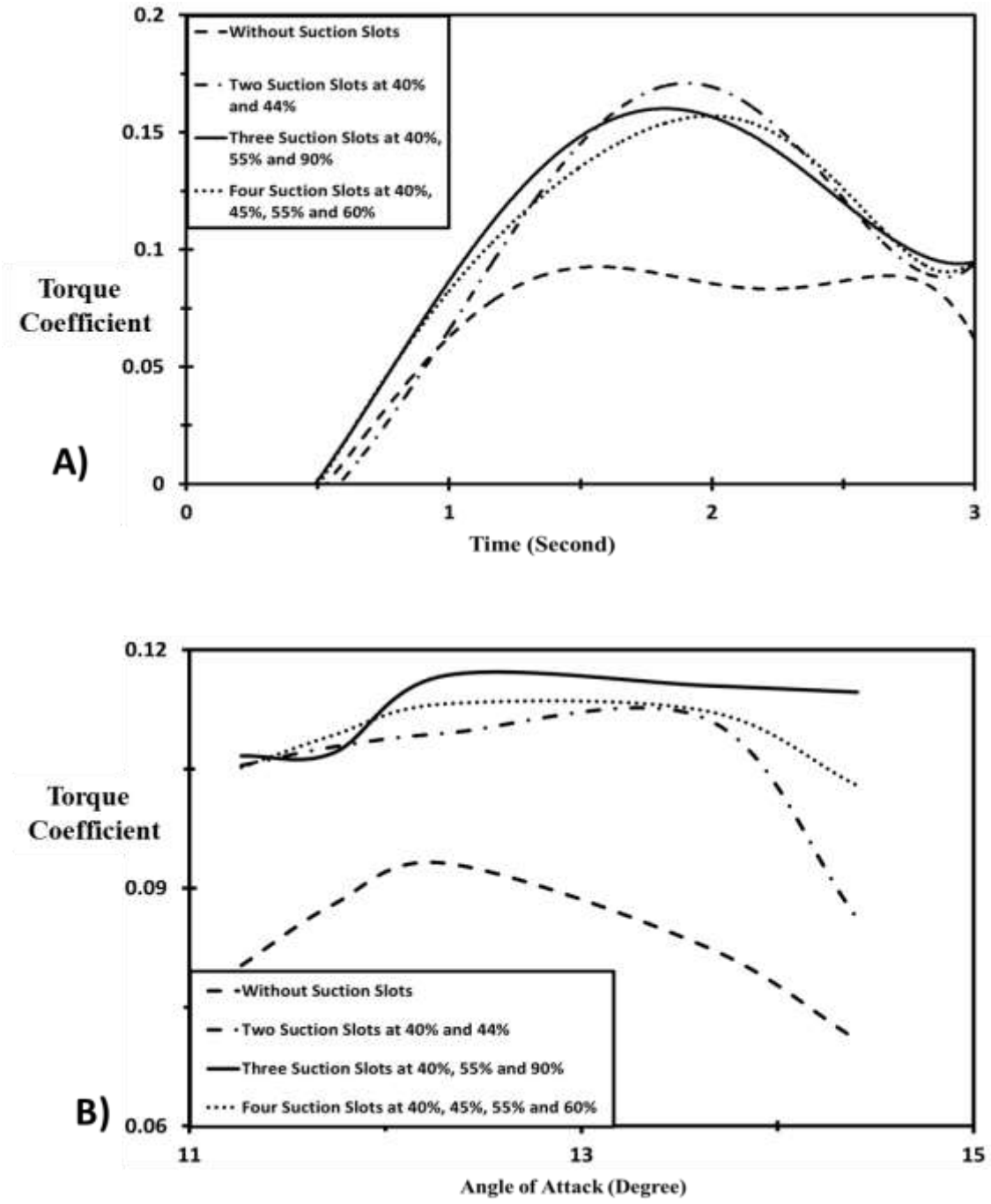

Figure 6.34 The comparison between the two suction slots, three suction slots and four suction slots A) The instantaneous torque coefficient B) Average value of torque coefficient

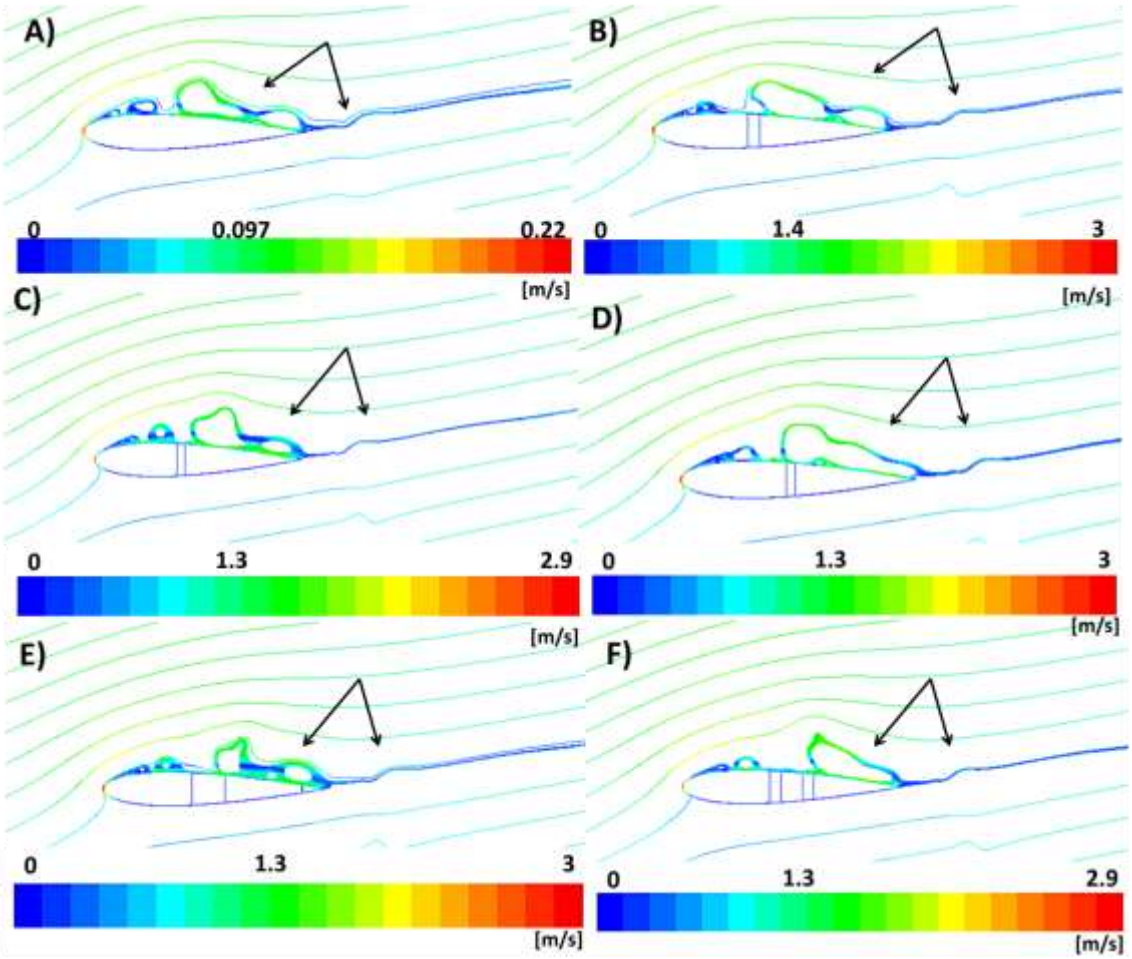

Figure 6.35 Path-line coloured by mean velocity magnitude at velocity equal to 1.8 m/s (acceleration flow) A) NACA0015 without slots B) L_{ss}40% and 45% C) L_{ss}40% and 44% D) L_{ss}45% and 49% E) L_{ss}40%, 55% and 90% F) L_{ss}40%,45%, 55%, and 60%

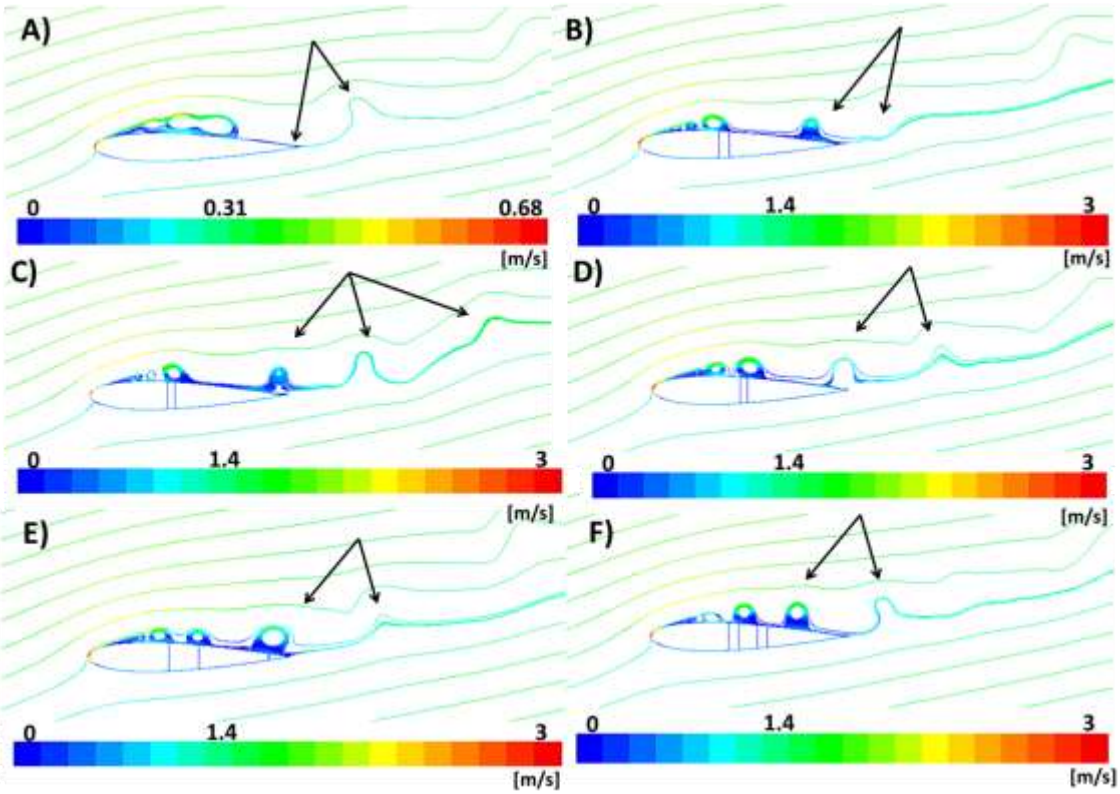

Figure 6.36 Path-line coloured by mean velocity magnitude at maximum velocity equal to 2.92 m/s A) NACA0015 without slots B) L_{ss}40% and 45% C) L_{ss}40% and 44% D) L_{ss}45% and 49% E) L_{ss}40%, 55% and 90% F) L_{ss}40%,45%, 55%, and 60%

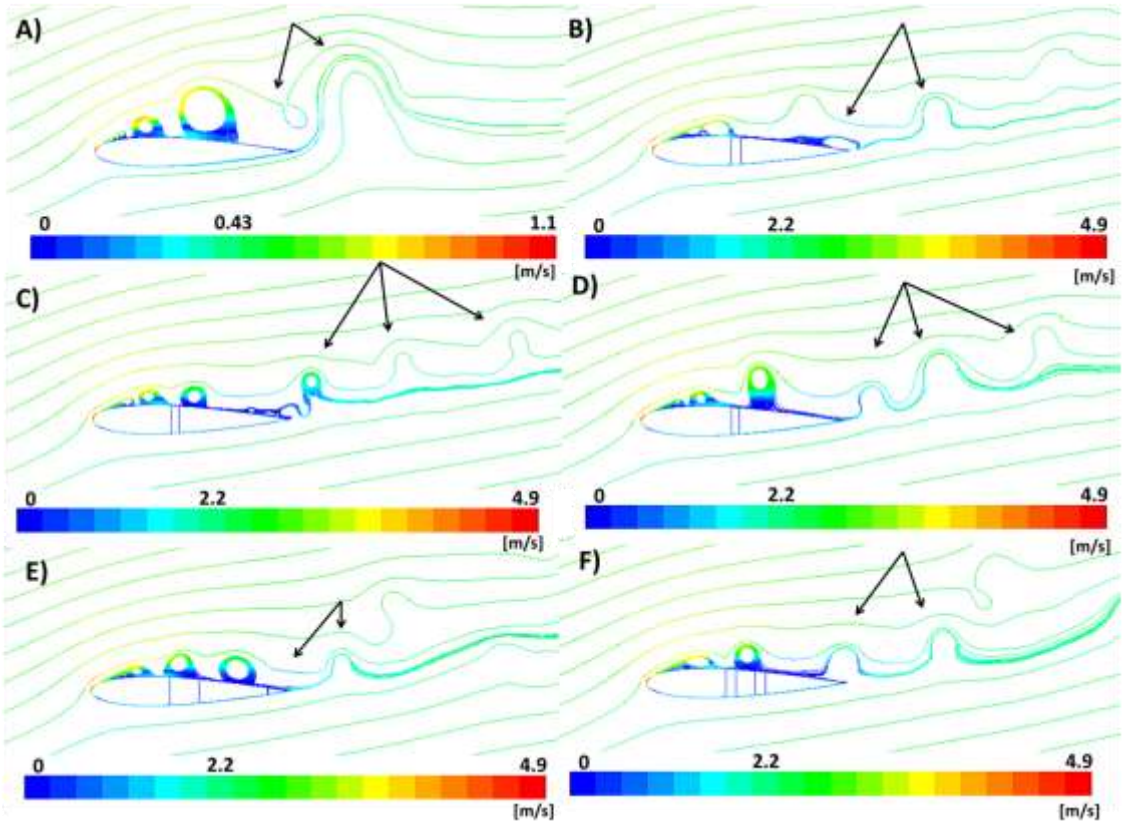

Figure 6.37 Path-line coloured by mean velocity magnitude at velocity equal to 1.8 m/s (deceleration flow), A) NACA0015 without slots B) L_{ss}40% and 45% C) L_{ss}40% and 44% D) L_{ss}45% and 49% E) L_{ss}40%, 55% and 90% F) L_{ss}40%,45%, 55%, and 60%

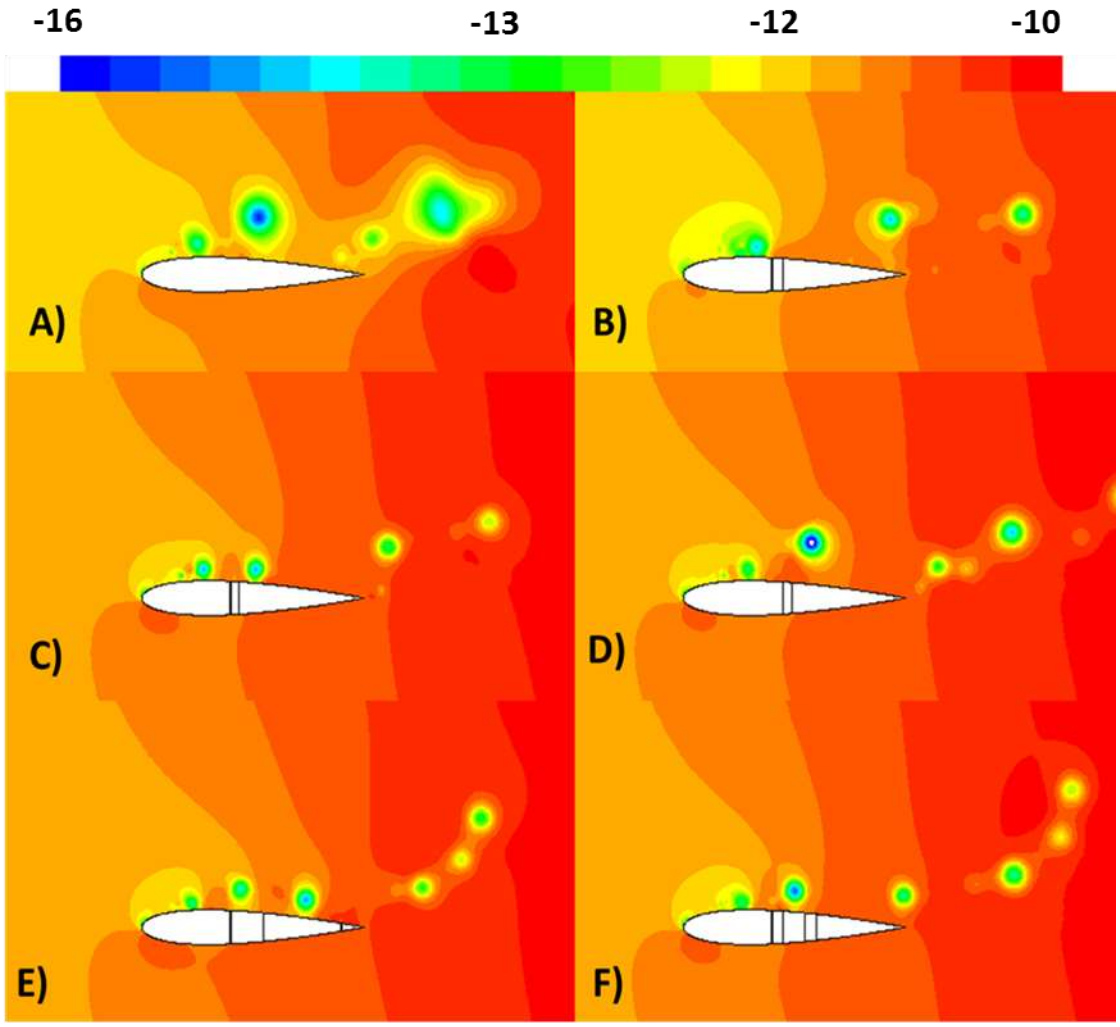

Figure 6.38 Contours coloured by pressure coefficient at velocity equal to 1.8 m/s (deceleration flow), A) NACA0015 without slots B) L_{ss}40% and 45% C) L_{ss}40% and 44% D) L_{ss}45% and 49% E) L_{ss}40%, 55% and 90% F) L_{ss}40%,45%, 55%, and 60%

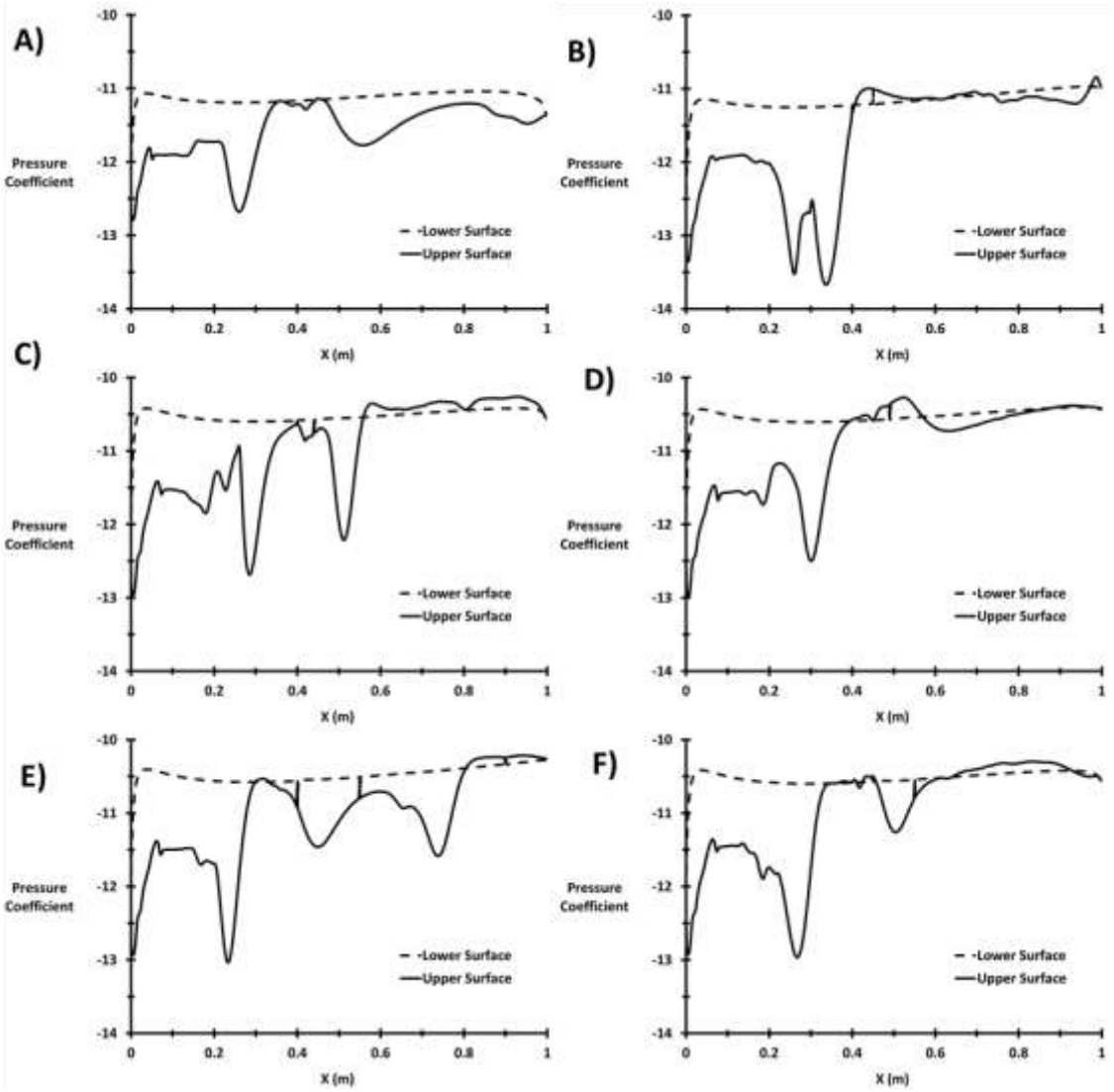

Figure 6.39 Pressure coefficient at upper and lower surface with velocity equal to 1.8 m/s (deceleration flow), A) NACA0015 without slots B) L_{ss}40% and 45% C) L_{ss}40% and 44% D) L_{ss}45% and 49% E) L_{ss}40%, 55% and 90% F) L_{ss}40%,45%, 55%, and 60%

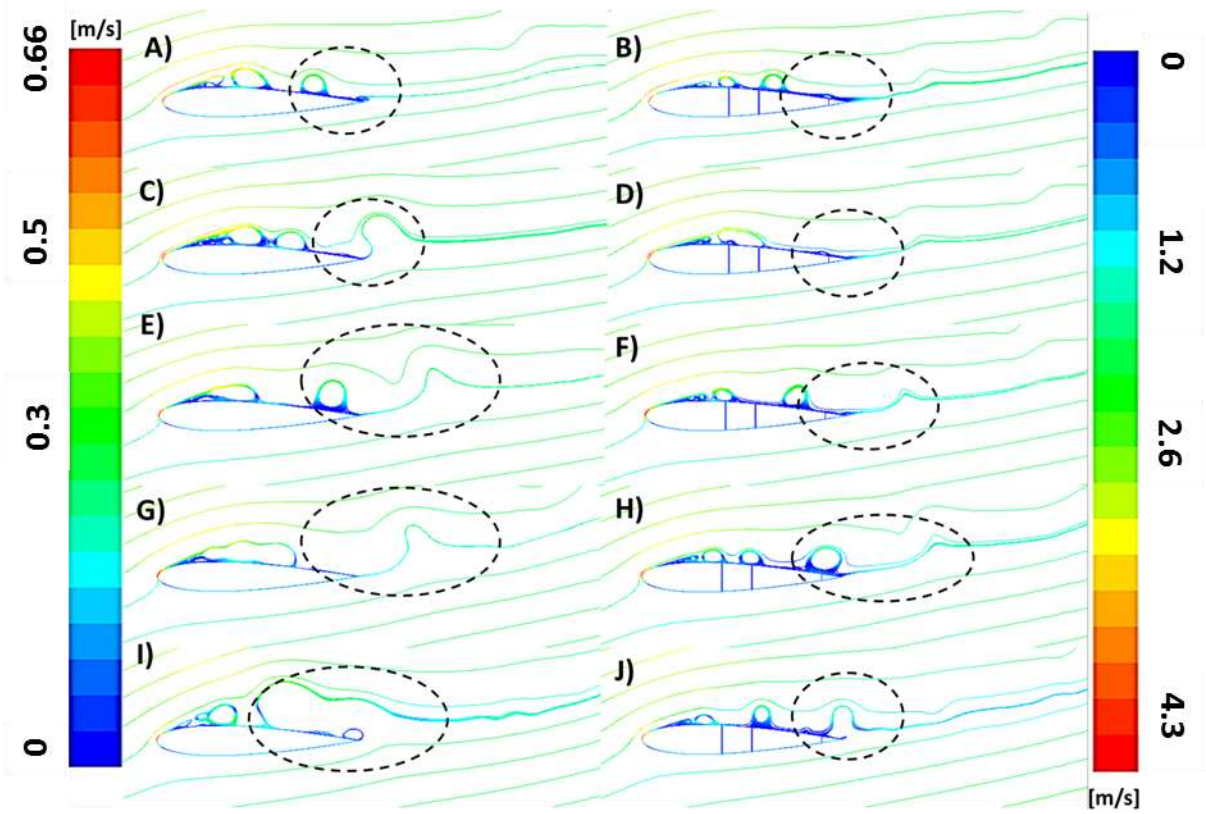

Figure 6.40 Path-line coloured by mean velocity magnitude around NACA0015 without and with slots at L_{ss}40%, 55% and 90% at maximum velocity equal to 2.92 (m/s) A) and B) 11.3, C) and D) 11.7, E) and F) 12.3, G) and H) 13.6, I) and J) 14.4

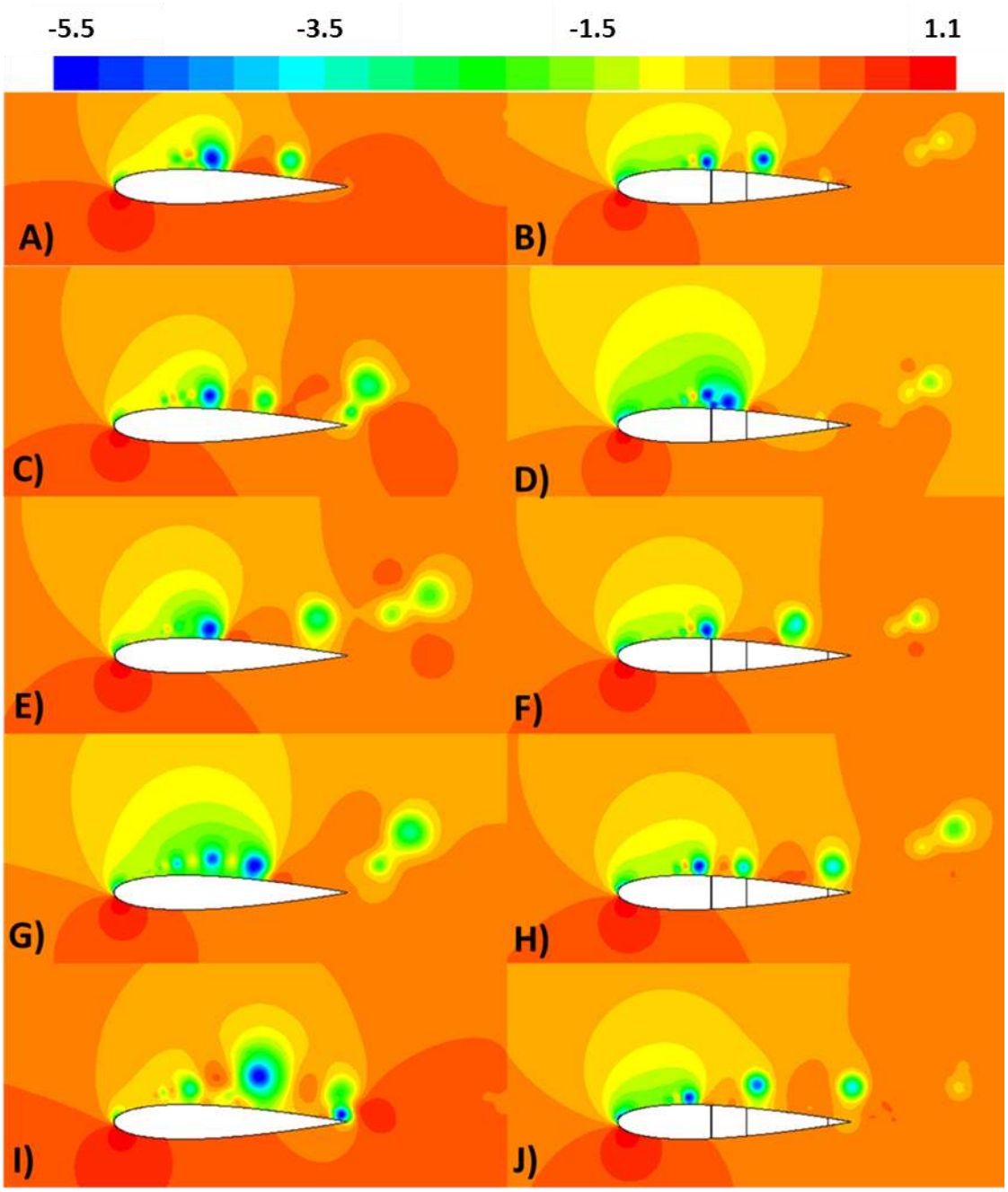

Figure 6.41 Contours of the pressure coefficient around NACA0015 A) and B) 11.3, C) and D) 11.7, E) and F) 12.3, G) and H) 13.6, I) and J) 14.4

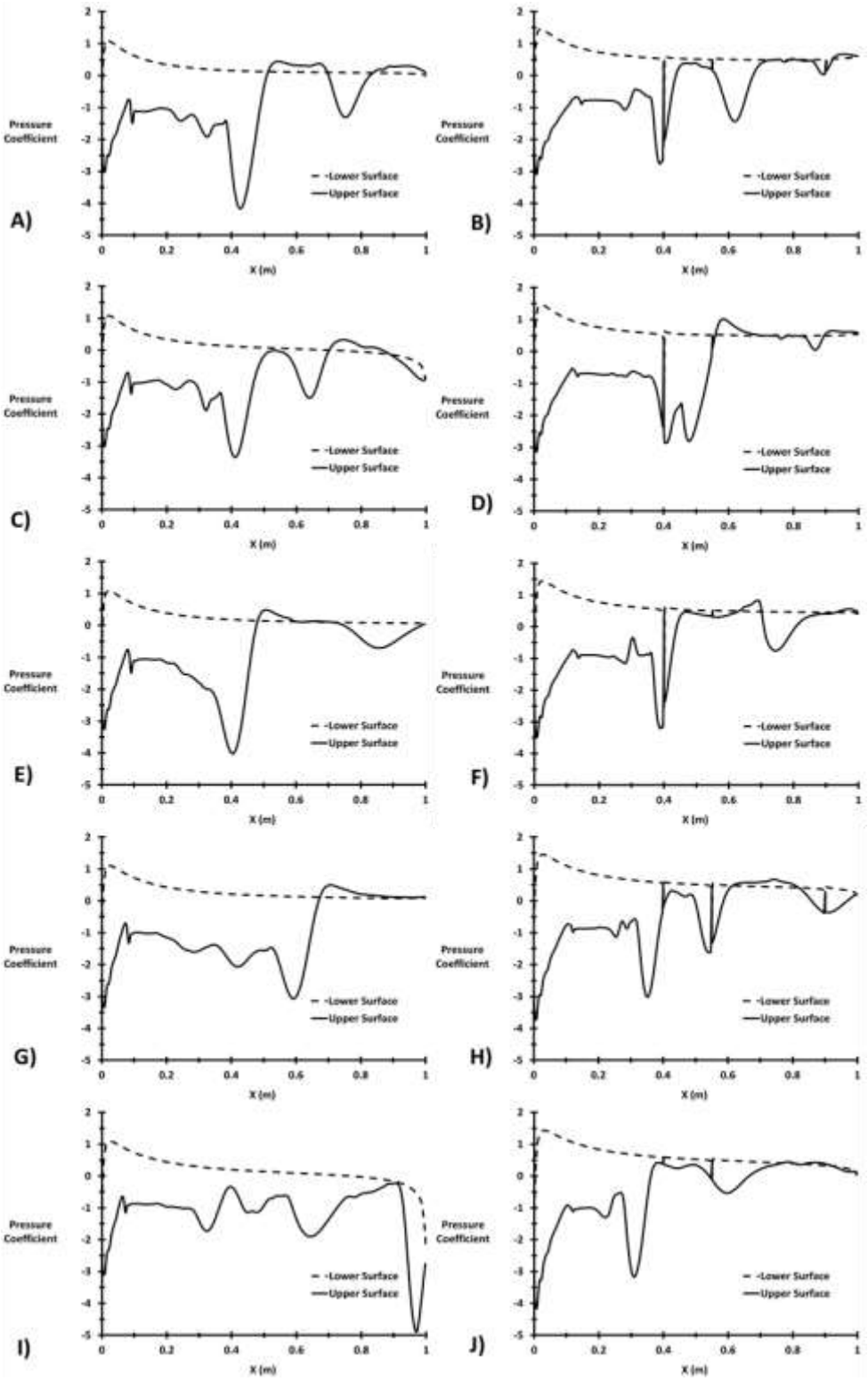

Figure 6.42 Pressure coefficient at upper and lower surface of NACA0015 A) and B) 11.3, C) and D) 11.7, E) and F) 12.3, G) and H) 13.6, I) and J) 14.4

6.3.3 EGM method

The numerical simulations were used to obtain local entropy viscosity predictions from the different five scenarios for the locations of suction slots. Figures 6.43 and 6.44 highlight the comparison between the (L_{ss}40% and 45%), (L_{ss}40% and 44%), (L_{ss}45% and 49%), (L_{ss}40%, 55% and 90%) and (L_{ss}40%, 45%, 55%, and 60%). The comparison was provided as an average value for the compression cycle with different angles of attack. From Figure 6.43 A) it can be noted that the minimum value for the global entropy generation rate occurs with (L_{ss}45% and 49%) by 20.24% increase in S_G before the stall. On the other hand, the minimum value for the global entropy generation rate occurs with (L_{ss}40% and 45%) by 14.54% increase in S_G after the stall; see Figure 6.43 B). Furthermore, the two suction slots (L_{ss}40% and 45%) give minimum S_G as an average value for the compression cycle before and after the stall by 20.5% increase in S_G value.

From Figure 6.44 it can be concluded that the (L_{ss}45% and 49%) gives the maximum value of second law efficiency by 0.38% before the stall, and, the (L_{ss}40% and 45%) gives the maximum value after the stall by 1.19%. Furthermore, the two suction slots (L_{ss}40% and 45%) give maximum value for the second law efficiency as an average value for the compression cycle before and after the stall by 0.72%. The increases in S_G (Figure 6.43) leads to decrease in second law efficiency in some cases than that without suction slots, such as the two suction slots at $L_{ss} = 40\%$ and $L_{ss} = 44\%$ before the stall which the second law efficiency decreased by (0.01%), and three suction slots at $L_{ss} = 40\%$, $L_{ss} = 55\%$ and $L_{ss} = 90\%$ after the stall which the second law efficiency decreased by (0.61%). There were no significant changes in both the global entropy generation rate values and the second law efficiency due to the different slots number and location.

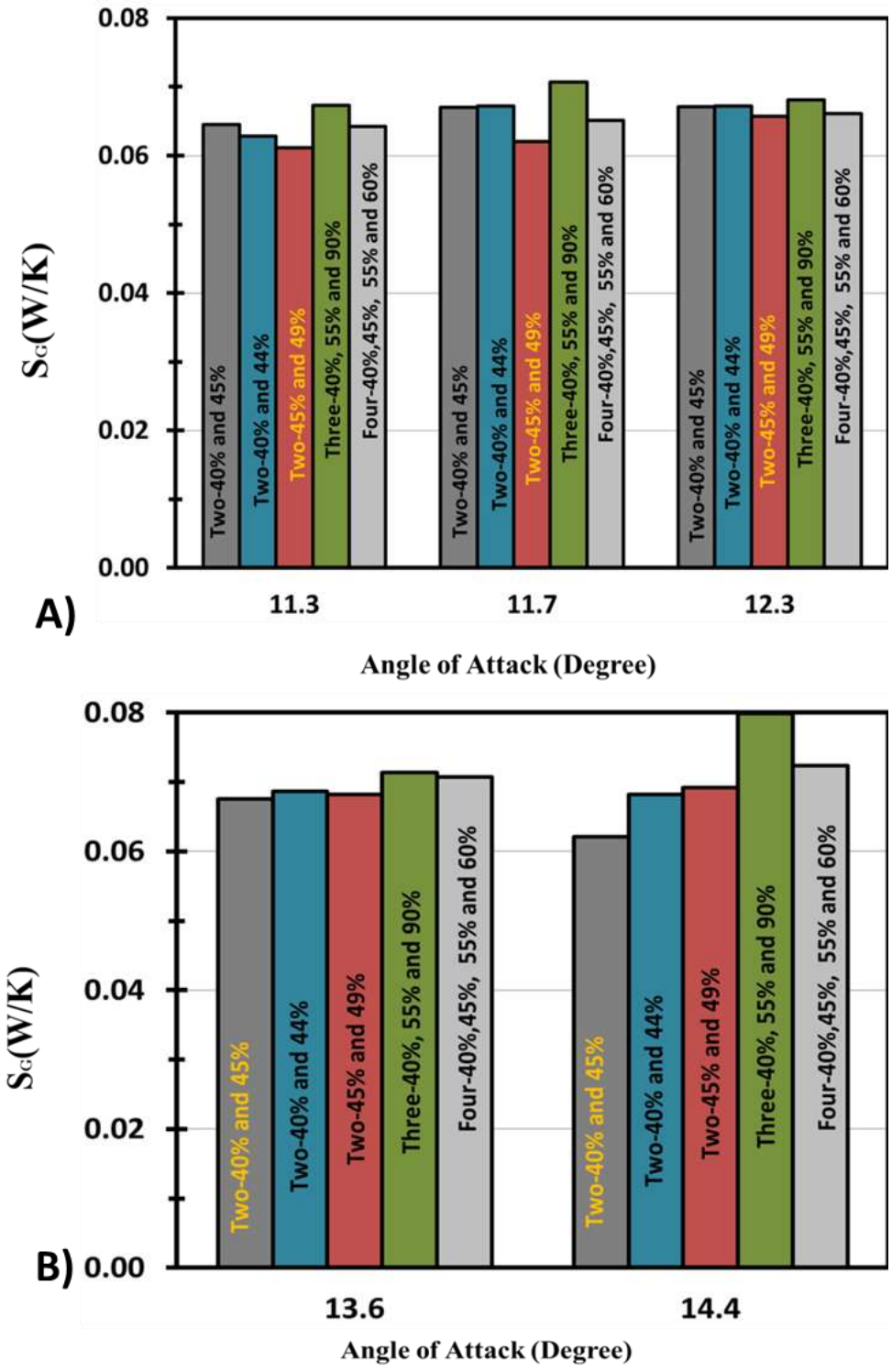

Figure 6.43 Comparison between the average value of the S_G for the compression cycle for NACA0015 with two, three and four suction slots, A) Before the stall B) After the stall

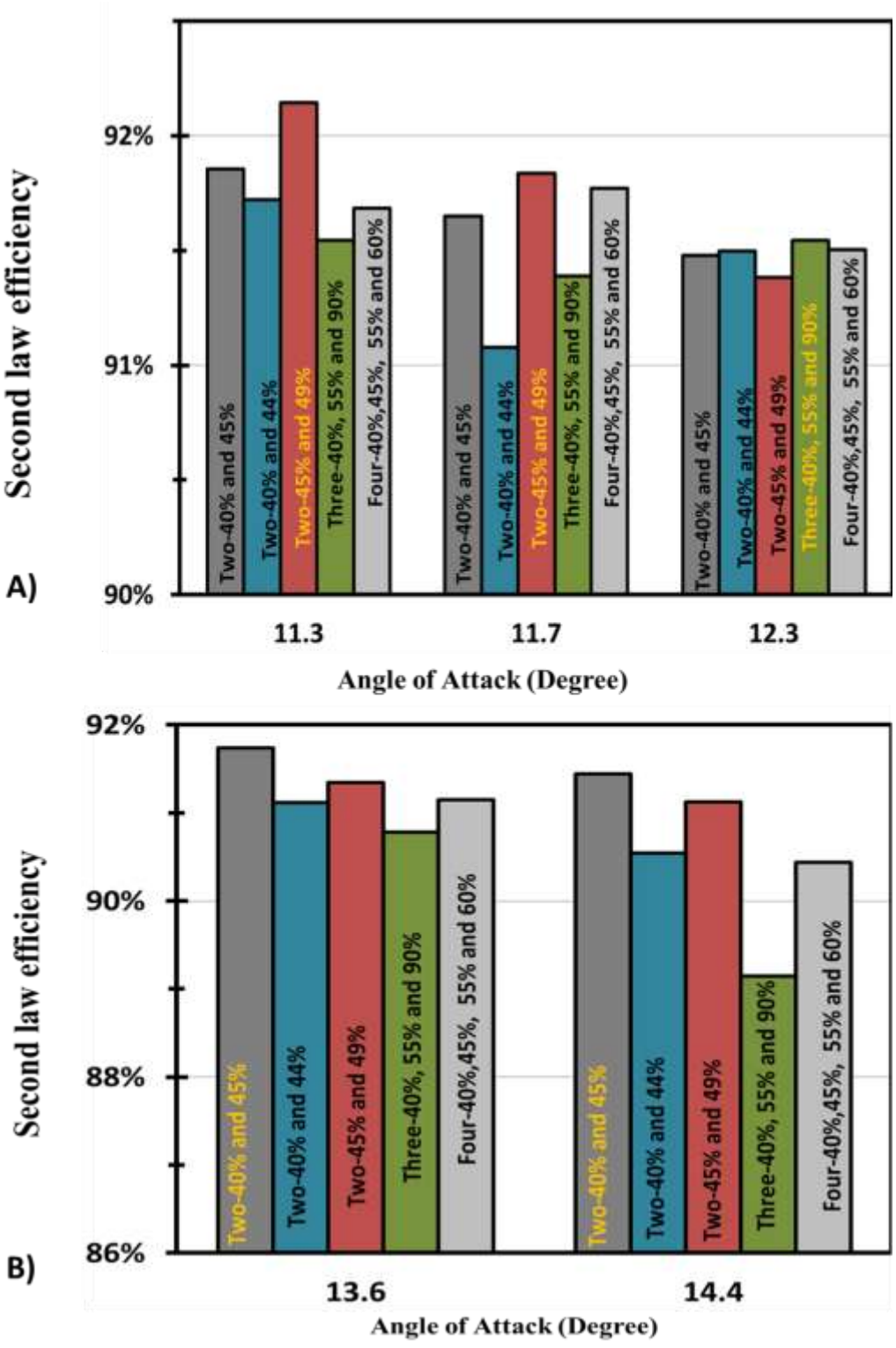

Figure 6.44 Comparison between the second law efficiency for the compression cycle for NACA0015 with two, three and four suction slots A) Before the stall B) After the stall

The contours of global entropy generation rate around the NACA0015 at the instantaneous velocity 1.8 m/s for the accelerating (Figures 6.45) and decelerating flow (Figures 6.47) in addition 2.92 m/s (Figures 6.46) were represented. Where, the 2.92 m/s was the maximum velocity which create the peak Reynolds number (2×10^5), from Figure 6.9, and 1.8 m/s is approximately at the middle to compare between the accelerating and decelerating flow. It can be shown that the suction slots have a negative effect on the entropy generation, where the global entropy generation rate increases at the three stages, accelerating flow, maximum velocity and decelerating flow at 13.6 degrees. The two-suction slots at (L_{ss}40% and 45%) and (L_{ss}45% and 49%) have the lowest difference in global entropy generation rate by 32% at the accelerating flow in Figure 6.45. Otherwise, the three-suction slots at (L_{ss}40%, 55% and 90%) have the highest difference in global entropy generation rate by 44 % at the same Figure. However, the global entropy generation rate has lowest difference due to suction slots at the maximum velocity by 28% with the two-suction slots at (L_{ss}40% and 45%). Also, the highest value occurs due to the two suction slots at (L_{ss}40% and 44%) by 35% in Figure 6.46.

From Figure 6.47 it can be noted that the two suction slots at (L_{ss}40% and 45%) has the lowest difference in global entropy generation rate by 37% and the highest value occurs due to the three suction slots at (L_{ss}40%, 55% and 90%) by 53% at the decelerating flow. Finally, the global entropy generation rate around the NACA0015 without and with suction slots have the highest value at the maximum velocity and the lowest value at the accelerating flow as a general. From Figures 6.35, 6.36, 6.37, and 6.40 it can be noted that the attached multi-slots to the aerofoil lead to increase in velocity magnitude around the aerofoil, furthermore, it lead also to increase in the entropy generation in Figures 6.45, 6.46, and 6.47. Where, the entropy value depends on the velocity gradient see equation (3.42).

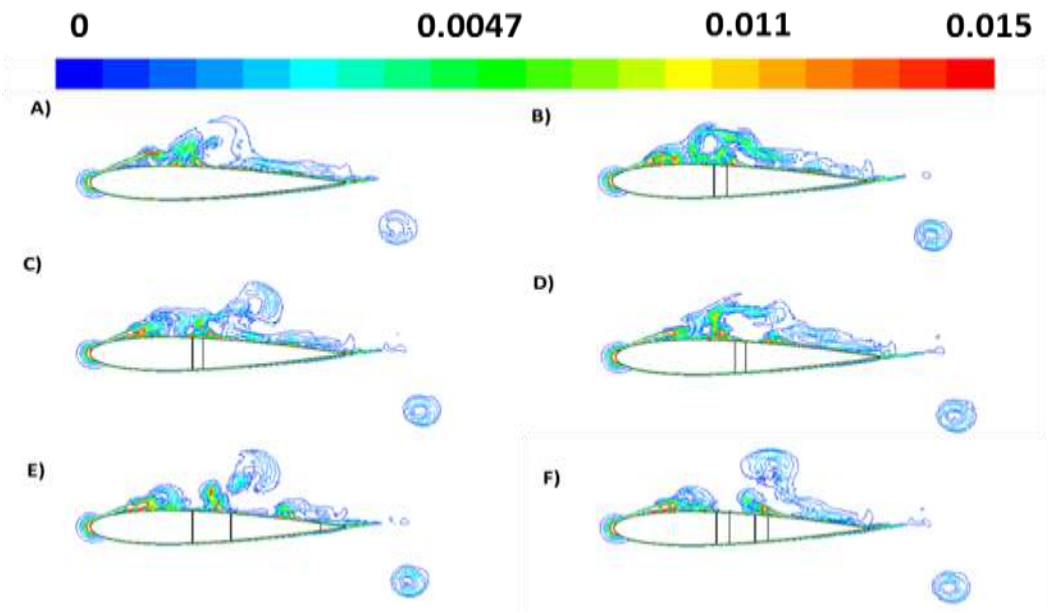

Figure 6.45 Contour of S_G at 1.8 m/s (accelerating) A) NACA0015 without slots B) L_{ss}40% and 45% C) L_{ss}40% and44% D) L_{ss}45% and 49% E) L_{ss}40%, 55% and 90% F) L_{ss}40%,45%, 55%, and 60%

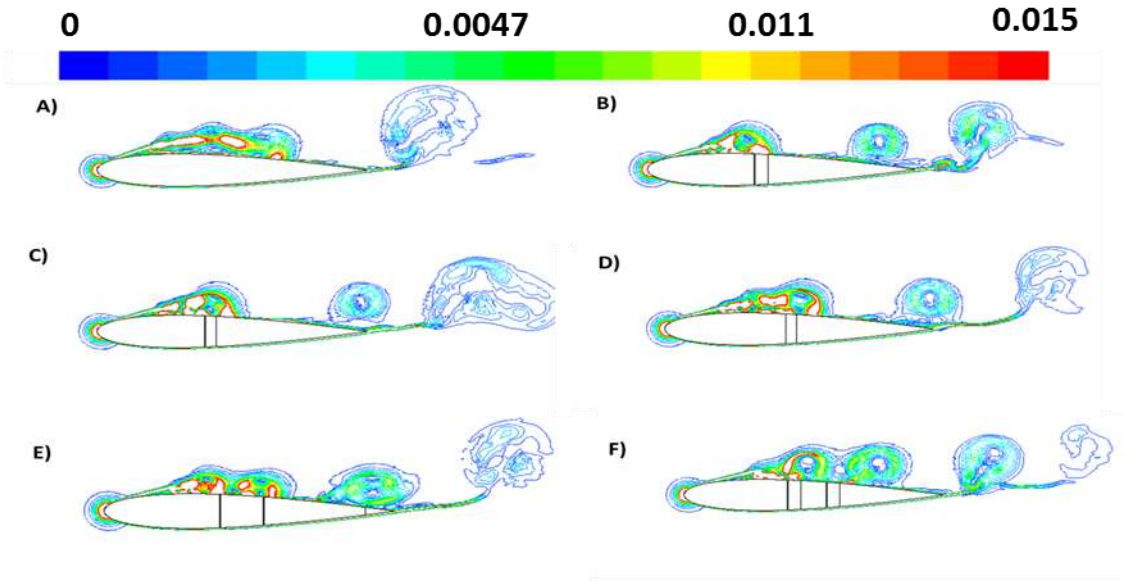

Figure 6.46 Contour of S_G at 2.92 m/s (maximum velocity) A) NACA0015 without suction slots B) L_{ss}40% and 45% C) L_{ss}40% and 44% D) L_{ss}45% and 49% E) L_{ss}40%, 55% and 90% F) L_{ss}40%,45%, 55%, and 60%

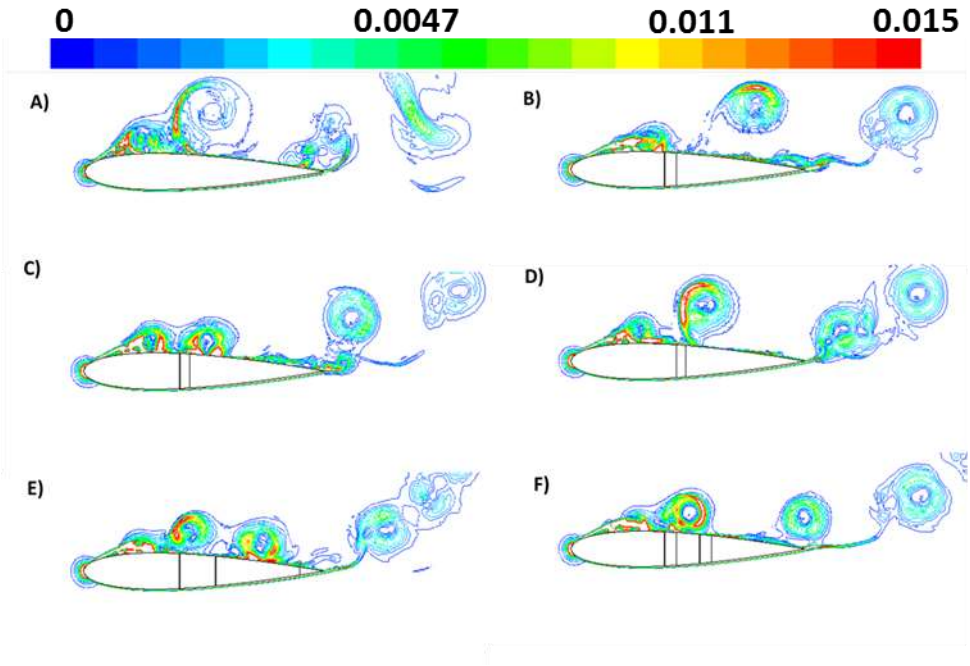

Figure 6.47 Contour of S_G at 1.8 m/s (decelerating) A) NACA0015 without slots B) L_{ss}40% and 45% C) L_{ss}40% and 44% D) L_{ss}45% and 49% E) L_{ss}40%, 55% and 90% F) L_{ss}40%, 45%, 55%, and 60%

6.3.4 Comparative analysis based on conditions relevant to northern coast of Egypt

From the previous section, it can be concluded that the three-suction slots (L_{ss}40%, 55% and 90%) give maximum C_T and the two-suction slots (L_{ss}40% and 45%) have the lowest S_G from the five scenarios, which give higher torque coefficient. Therefore, these two scenarios were investigated using the oscillating water system based on the real data from the site with different time periods and frequencies (f equal to 0.25, 0.167 and 1.25 Hz) see section 5.4 and Figure 5.16. The hysteretic behaviour due to the reciprocating flow and the total average torque coefficient during the cycle for aerofoil with suction slots at different time periods were shown in Figure 6.48. It can be concluded that the aerofoil with three-suction slots (L_{ss}40%, 55% and 90%) give higher C_T than that with two-suction slots (L_{ss}40% and 45%) at 4, 6 and 8 second time period. Also, the increase in time period led to a decrease in the total average torque coefficient in general. At the

time period equal to 4 second, the aerofoil with two-suction slots (L_{ss}40% and 45%) has an average torque coefficient after the stall less than the aerofoil without suction slots by 8.5%. Furthermore, the aerofoil with two suction slots (L_{ss}40% and 45%) with 8 second time period has improvement in the total average torque coefficient before the stall by 17% and after the stall by 8%.

Figures 6.49 and 6.50 show the instantaneous torque coefficient in addition to average torque coefficient at the accelerating and decelerating cycle for aerofoil with two-suction slots and with three-suction slots. These values were at angle of attack of 13.6 degrees at different time periods (4 sec, 6 sec and 8 sec). It can be seen that the improvement in the torque coefficient has the lowest value at the cycle with time period equal to 4 second. Furthermore, the torque coefficient value and improvement in the torque coefficient at decelerating flow are always higher than that at accelerating flow (see section 5.4.1).

The total average torque coefficients during the compression cycle for different angles of attack were shown in Figure 6.51. It can be observed that for all angles, the suction slot increases the torque coefficient except at the 14.4 degree Figure 6.51 E), where the torque coefficient for the aerofoil with two-suction slots (L_{ss}40% and 45%) was lower than that without suction slots by 24% at time period 4 second. Also, the torque coefficient at time period 8 second for the aerofoil with two-suction slots (L_{ss}40% and 45%) was same for that without suction slots. The aerofoil with three-suction slots (L_{ss}40%, 55% and 90%) mostly has a higher torque coefficient than that of the two-suction slots (L_{ss}40% and 45%) at different time period.

Tables 6.9, 6.10 and 6.11 show the comparison between the global entropy generation rate before and after the stall for the aerofoil with two-suction slots (L_{ss}40% and 45%) and with three-suction slots (L_{ss}40%, 55% and 90%) at different time periods (4 sec, 6 sec and 8 sec). There were no significant changes in the global entropy generation rate values due to the different time periods. As an average for all time period, the aerofoil with two-suction slots (L_{ss}40% and 45%) has a lower difference in S_G before and after the stall than the aerofoil with three- suction slots (L_{ss}40%, 55% and 90%).

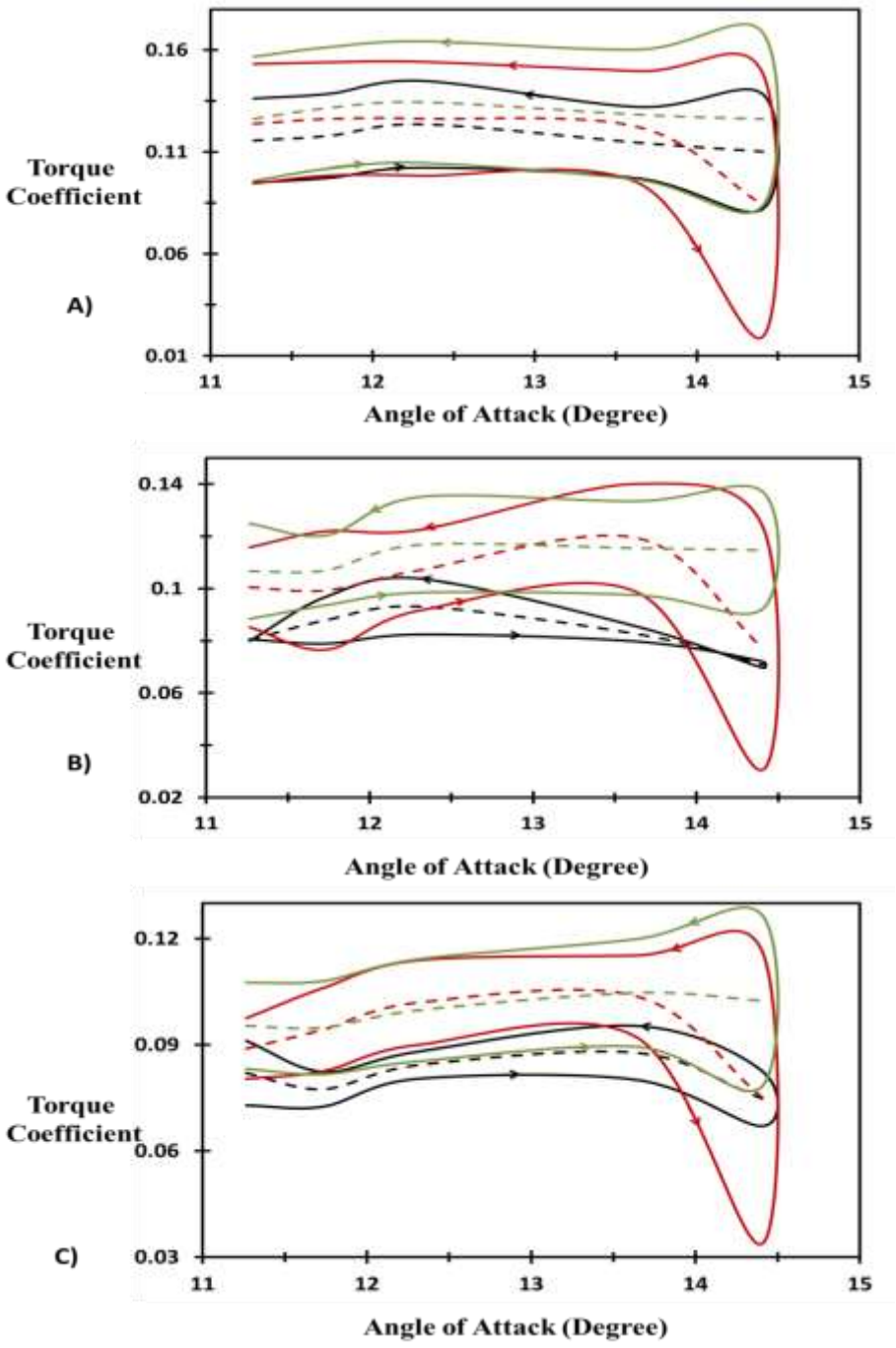

Figure 6.48 The hysteretic behaviour and the average torque coefficient " —— without slots ---average value", " —— (L_{ss}40% and 45%) ---average value", " —— (L_{ss}40%, 55% and 90%) ---average value", A) t_{sin} = 4 sec B) t_{sin} = 6 sec C) t_{sin} = 8 sec

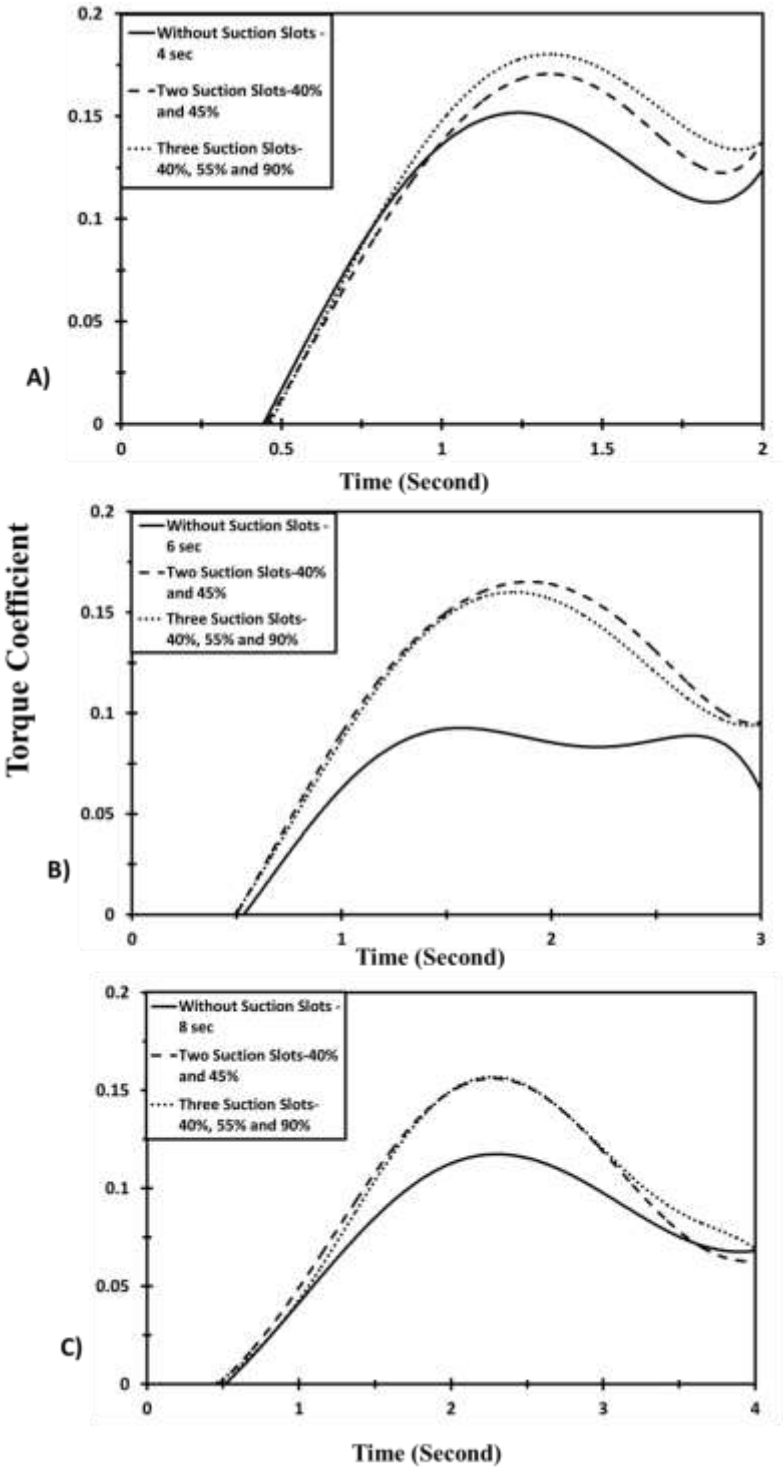

Figure 6.49 The instantaneous torque coefficient for the NACA0015 without and with suction slots at optimum locations in 13.6 degrees A) t_{sin} = 4 sec B) t_{sin} = 6 sec C) t_{sin} = 8 sec

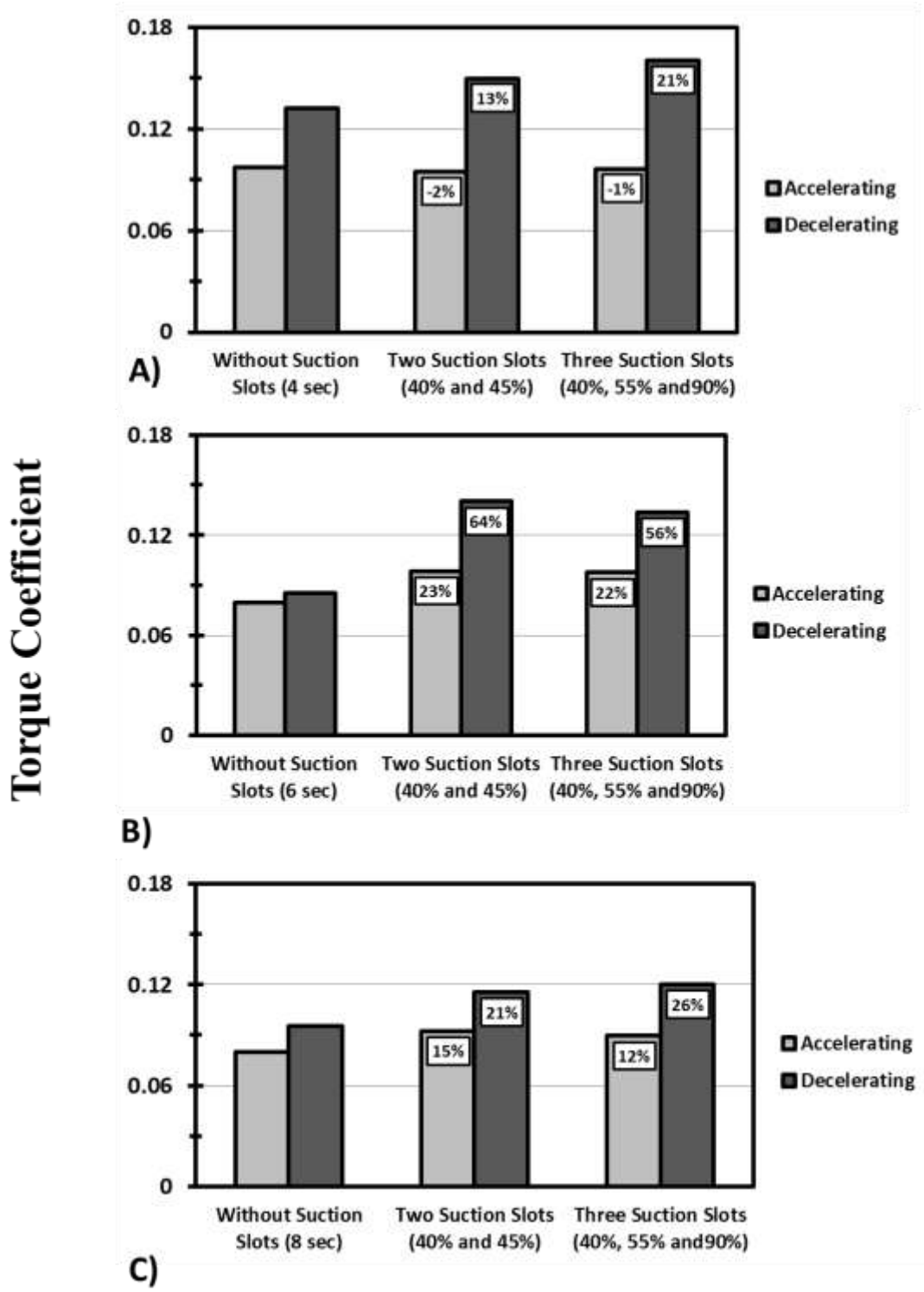

Figure 6.50 The average torque coefficient at the accelerating and decelerating flow for the NACA0015 without and with suction slots at optimum locations A) t_{sin} = 4 sec B) t_{sin} = 6 sec C) t_{sin} = 8 sec

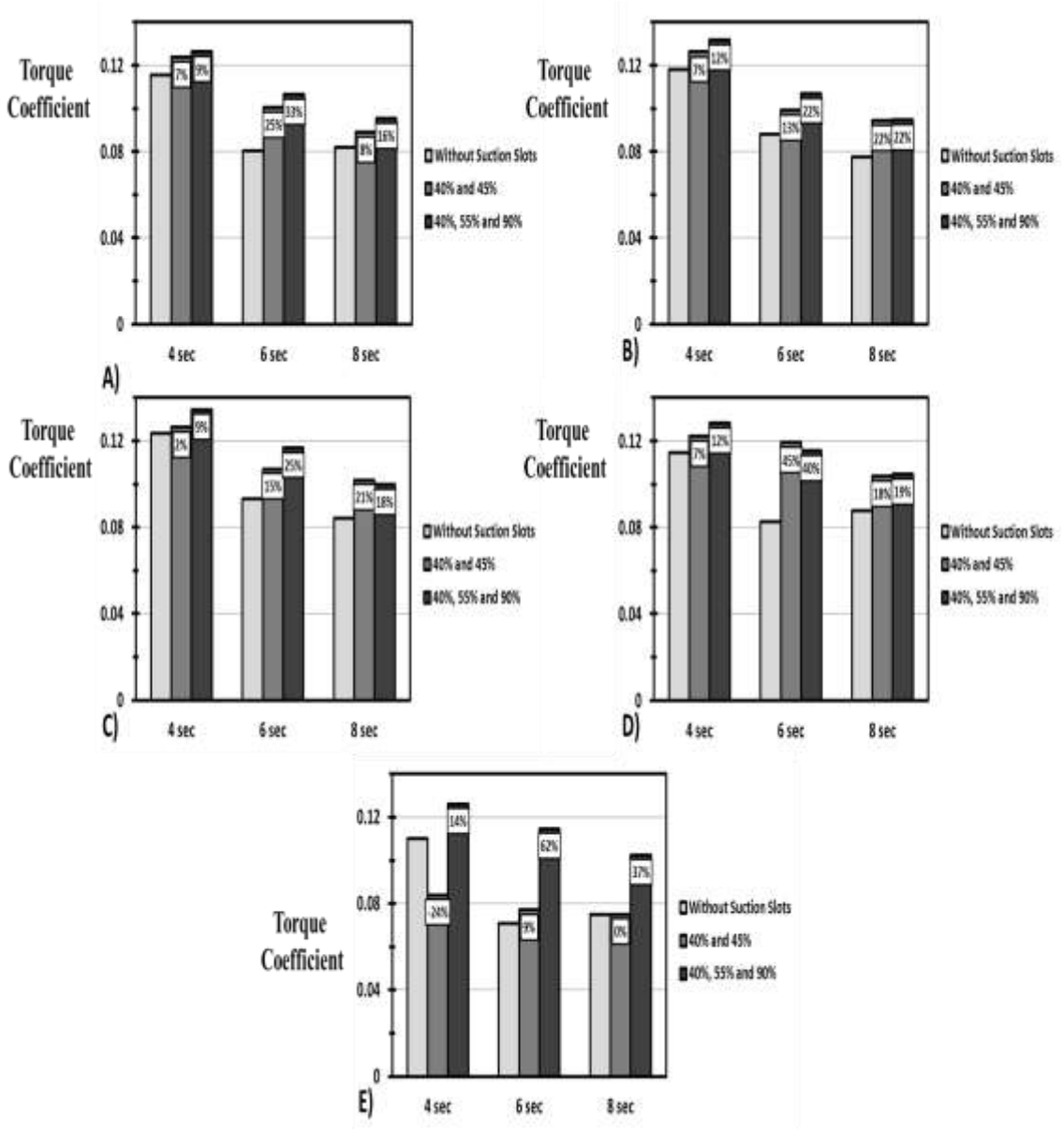

Figure 6.51 The average torque coefficient at the compression cycle for the NACA0015 without and with suction slots at optimum locations with sinusoidal velocity A) 11.3 B) 11.7 C) 12.3 D) 13.6 E) 14.4

Table 6.9 The global entropy generation rate at different angles of attack with wave time period equal to 4 sec

S_G (W/K)	Angle of attack (Degree)				
	11.3	11.7	12.3	13.6	14.4
$L_{ss} = 40\%$ and $L_{ss} = 45\%$	0.066	0.066	0.067	0.074	0.063
Average value	Before the stall (6.6%)			After the stall (6.8%)	
$L_{ss} = 40\%$, $L_{ss} = 55\%$ and $L_{ss} = 90\%$	0.066	0.067	0.071	0.073	0.079
Average value	Before the stall (6.8%)			After the stall (7.6%)	

Table 6.10 The global entropy generation rate at different angles of attack with wave time period equal to 6 sec

S_G (W/K)	Angle of attack (Degree)				
	11.3	11.7	12.3	13.6	14.4
$L_{ss} = 40\%$ and $L_{ss} = 45\%$	0.065	0.067	0.067	0.068	0.062
Average value	Before the stall (6.6%)			After the stall (6.5%)	
$L_{ss} = 40\%$, $L_{ss} = 55\%$ and $L_{ss} = 90\%$	0.067	0.071	0.068	0.071	0.080
Average value	Before the stall (6.9%)			After the stall (7.6%)	

Table 6.11 The global entropy generation rate at different angles of attack with wave time period equal to 8 sec

S_G (W/K)	Angle of attack (Degree)				
	11.3	11.7	12.3	13.6	14.4
$L_{ss} = 40\%$ and $L_{ss} = 45\%$	0.064	0.063	0.064	0.070	0.064
Average value	Before the stall (6.4%)			After the stall (6.7%)	
$L_{ss} = 40\%$, $L_{ss} = 55\%$ and $L_{ss} = 90\%$	0.066	0.065	0.065	0.073	0.075
Average value	Before the stall (6.5%)			After the stall (7.4%)	

Suction slots have a negative effect on both the entropy behaviour and the second law efficiency. Therefore, most of cases at Figure 6.52 have lower second law efficiency for aerofoils with slots than the aerofoils without slots. As it noted in the entropy behaviour, there were also no significant changes in the second law efficiency value due to the different slots number and location. However, the second low efficiency at 14.4 degree for the aerofoil with two suction slots (L_{ss}40% and 45%) was the highest value at 4, 6 and 8 second by 1%, 2% and 3% respectively, Figure 6.52 E). The wave cycle with 8 second has the highest value of the second law efficiency as a general. On the other hand, the wave cycle with 6 second has the lowest value. The aerofoil with two-suction slots (L_{ss}40% and 45%) always has higher second law efficiency than that with three-suction slots (L_{ss}40%, 55% and 90%) at the different time periods.

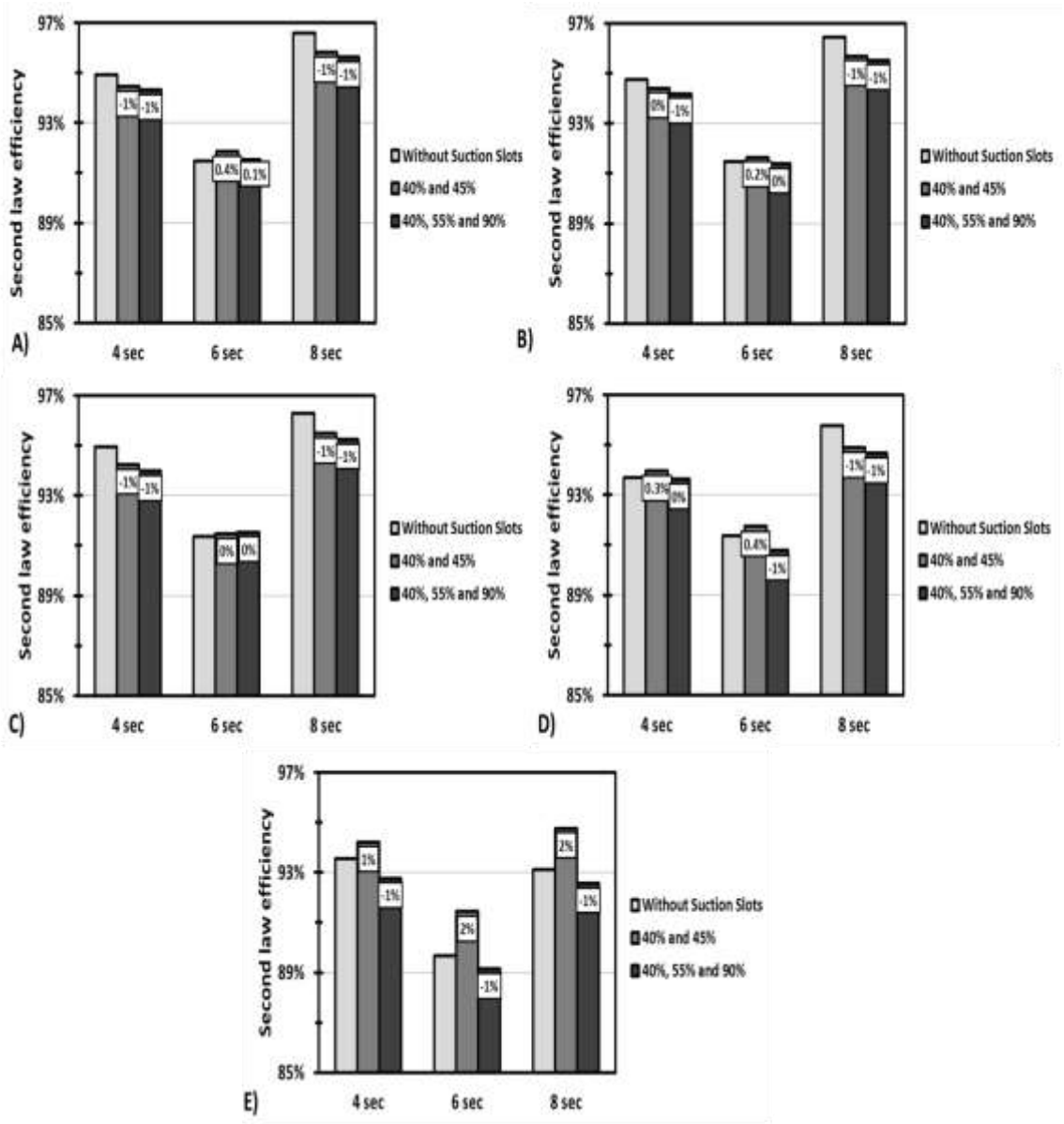

Figure 6.52 The second law efficiency at the compression cycle for the NACA0015 without and with suction slots at optimum locations with sinusoidal velocity A) 11.3 B) 11.7 C) 12.3 D) 13.6 E) 14.4

The flow structures over the NACA0015 aerofoil in oscillating flow was shown in Figure 6.53 at angle of attack equal to 12.3 degrees (before the stall) and 14.4 degrees (after the stall) in Figure 6.54. The improvement effect of suction slot on flow structures was clear when comparing the NACA0015 without and with suction slots, especially in

the separated layer regime at the end of aerofoil, which leads to an improvement in the separation regime.

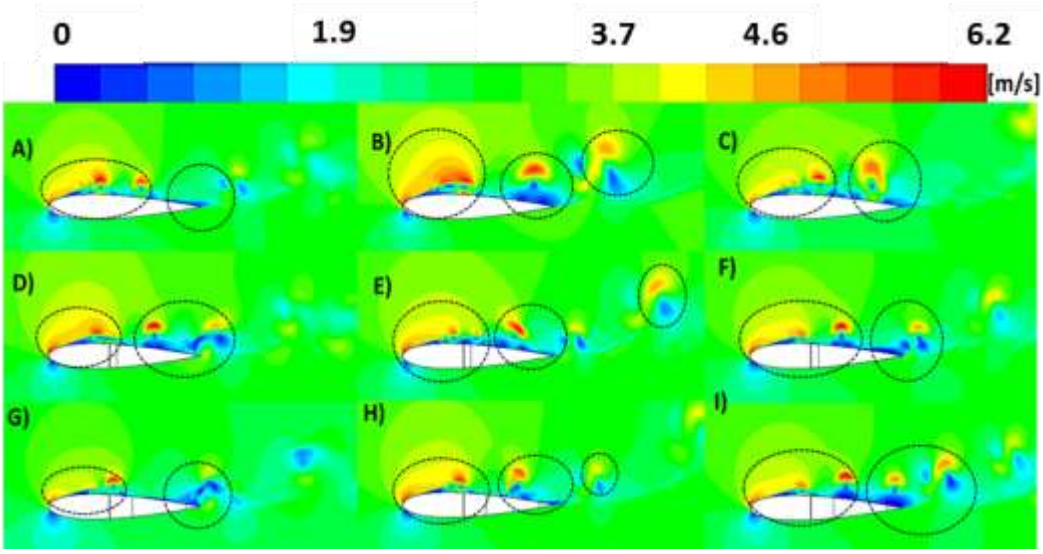

Figure 6.53 Contour of velocity magnitude at 12.3 degree A), B) and C) NACA0015 without slots with t_{sin} = 4, 6 and 8 sec respectively D), E) and F) two slots with t_{sin} = 4, 6 and 8 sec respectively G), H) and I) three slots with t_{sin} = 4, 6 and 8 sec respectively

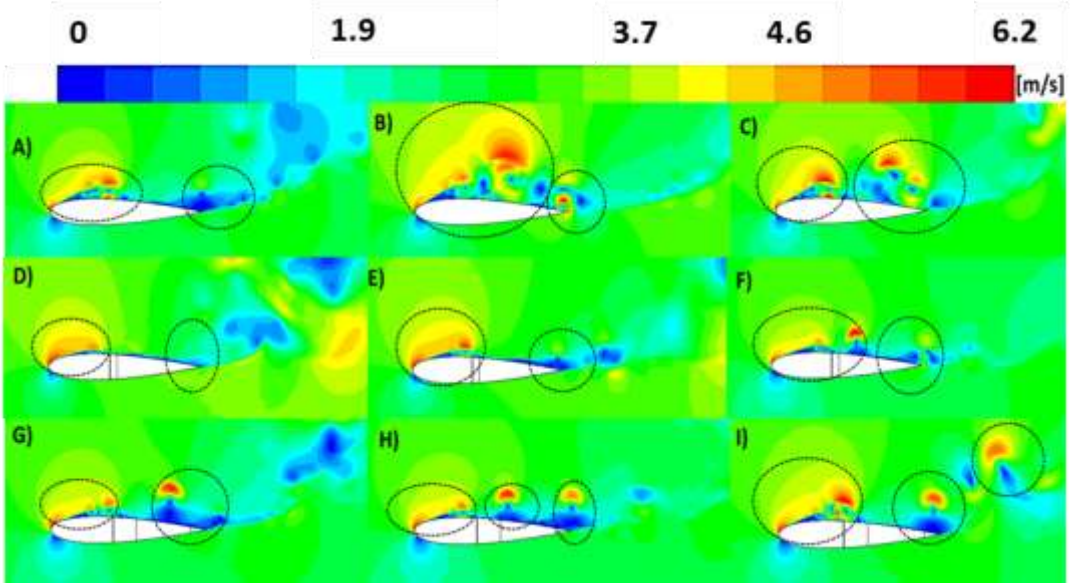

Figure 6.54 Contour of velocity magnitude at 14.4 degree A), B) and C) for NACA0015 without slots with t_{sin} = 4, 6 and 8 sec respectively D), E) and F) two slots with t_{sin} = 4, 6 and 8 sec respectively G), H) and I) three slots with t_{sin} = 4, 6 and 8 sec respectively

6.4 Optimum angle for suction slot

A single suction slot with diameter (D_{ss}) equal to 0.1% of the blade chord and located at distance (L_{ss}) equal to 50% of the blade chord with different angles for the suction slot positions (α_{ss}) (anticlockwise and clockwise) was created, with a shape of NACA0015 from reference (Torresi et al., 2009, Torresi et al., 2007b, Torresi et al., 2007a), see Figure 6.55. The angles for the suction slot were changed in order to obtain an optimum value of C_T and S_G. Table 6.12 highlights the different test cases that were investigated in this work. The angle of suction slots at upper and lower surface was defined with (α_{ss}) of upper surface only in the analysis and results, which were presented hereafter. First, test cases under unsteady flow with non-oscillating velocity were investigated in order to obtain an indication about the well-performing suction slot angles. Second, these well-performing angles were investigated under sinusoidal wave condition (Figure 6.7) to decide which angle provides an optimum value of C_T and S_G. Finally, a comparative analysis with different sinusoidal wave frequencies (Figure 5.16) based on conditions relevant to northern coast of Egypt was investigated as well.

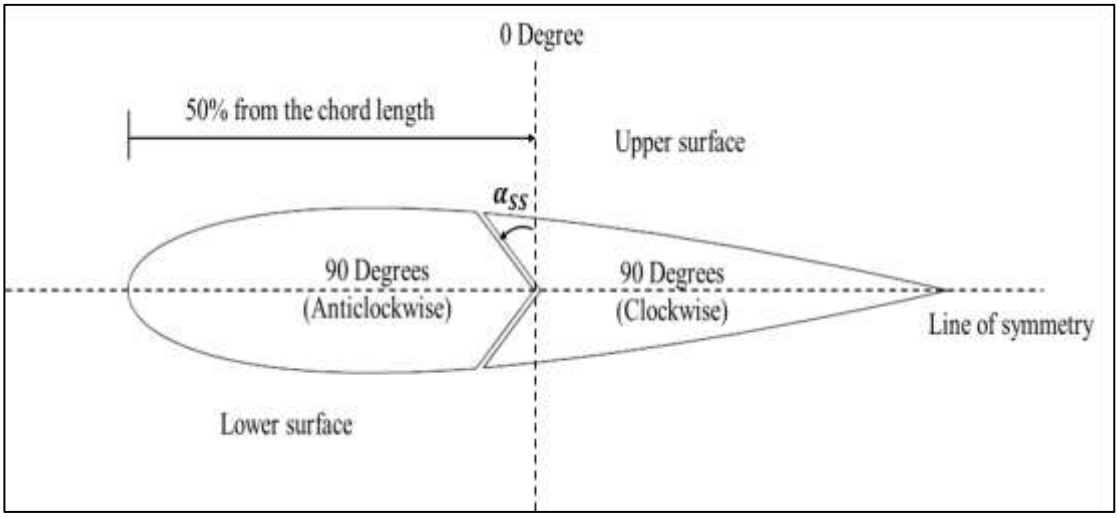

Figure 6.55 Aerofoil diagram with suction slot has angle

6.4.1 Different suction slot angles under non-oscillating inlet velocity

Figure 6.56 A) shows the C_T values of suction slot with different angles. It can be noted that the suction slot with a non-zero angle gives a higher C_T than that with 0 degree. For instance, the suction slots with α_{ss} equal to 35 degrees clockwise, 65 degrees anticlockwise and 55 degrees anticlockwise give C_T higher than that with 0 degree by 22%, 20% and 19%, respectively. Table 6.13 lists C_T values for the investigated α_{ss} angles. The S_G values of suction slot with different angles are shown in Figure 6.56 B). It can be concluded that the suction slot with α_{ss} equal to 15 degrees anticlockwise, 10 degrees clockwise and 10 degrees anticlockwise gives S_G lower than that with 0 degree by 13%, 13% and 3%, respectively, see Table 6.14 for more details.

Table 6.12 The suction slot with different position angles at NACA0015

α_{SS} at upper surface	α_{SS} at lower surface	Figure	α_{SS} at upper surface	α_{SS} at upper surface	Figure
85 Degrees anticlockwise	**85 Degrees** clockwise		**0 Degree** (+Y axis)	**0 Degree** (-Y axis)	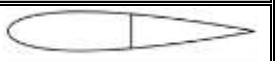
80	**80**		**5 Degrees** clockwise	**5 Degrees** anticlockwise	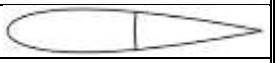
75	**75**		**10**	**10**	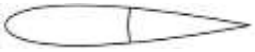
70	**70**	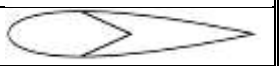	**15**	**15**	
65	**65**		**20**	**20**	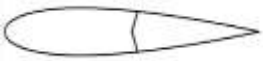
60	**60**		**25**	**25**	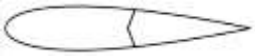
55	**55**		**30**	**30**	
50	**50**		**35**	**35**	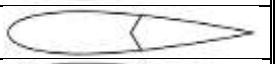
45	**45**	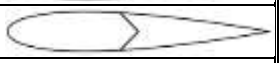	**40**	**40**	
40	**40**		**45**	**45**	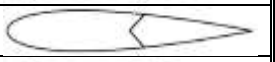
35	**35**		**50**	**50**	
30	**30**		**55**	**55**	
25	**25**		**60**	**60**	
20	**20**	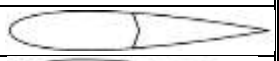	**65**	**65**	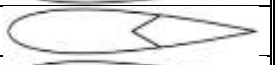
15	**15**	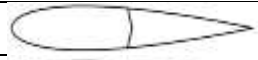	**70**	**70**	
10	**10**	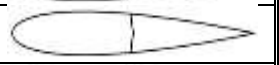	**75**	**75**	
5	**5**	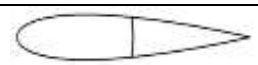	**80**	**80**	
0 Degree (+Y axis)	**0 Degree** (-Y axis)	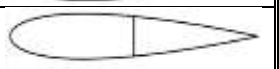	**85**	**85**	

Table 6.13 The value of improvement in torque coefficient for suction slot with different position angles under non-oscillating velocity

α_{SS} (anticlockwise)	C_T	improvement	α_{SS} (clockwise)	C_T	improvement
85 Degrees	0.098	17%	**0 Degree**	0.115	38%
80	0.111	32%	**5**	0.106	26%
75	0.097	16%	**10**	0.130	55%
70	0.097	16%	**15**	0.095	13%
65	0.133	58%	**20**	0.125	49%
60	0.129	53%	**25**	0.113	35%
55	0.132	57%	**30**	0.101	20%
50	0.121	44%	**35**	0.134	60%
45	0.100	19%	**40**	0.107	27%
40	0.094	11%	**45**	0.114	35%
35	0.106	26%	**50**	0.116	38%
30	0.104	24%	**55**	0.118	40%
25	0.128	52%	**60**	0.112	33%
20	0.102	21%	**65**	0.112	33%
15	0.125	49%	**70**	0.096	15%
10	0.120	42%	**75**	0.107	28%
5	0.118	41%	**80**	0.112	33%
0	0.115	38%	**85**	0.099	18%

Improvement in C_T value higher than that for slot with 0 Degree

Table 6.14 The value of S_G for suction slot with different position angles under non-oscillating velocity

α_{SS} (anticlockwise)	S_G	increased by	α_{SS} (clockwise)	S_G	increased by
85 Degrees	0.147	71%	**0 Degree**	0.104	21%
80	0.138	60%	**5**	0.105	22%
75	0.144	68%	**10**	0.093	8%
70	0.138	60%	**15**	0.104	21%
65	0.121	40%	**20**	0.113	31%
60	0.143	66%	**25**	0.120	39%
55	0.112	30%	**30**	0.117	36%
50	0.118	37%	**35**	0.106	23%
45	0.158	84%	**40**	0.148	72%
40	0.166	93%	**45**	0.117	36%
35	0.108	25%	**50**	0.139	62%
30	0.131	52%	**55**	0.118	37%
25	0.119	38%	**60**	0.143	66%
20	0.104	21%	**65**	0.111	29%
15	0.093	8%	**70**	0.119	39%
10	0.101	18%	**75**	0.129	50%
5	0.110	28%	**80**	0.124	44%
0	0.104	21%	**85**	0.137	59%

1 2

Increased in S_G value lower than that for slot with 0 Degree

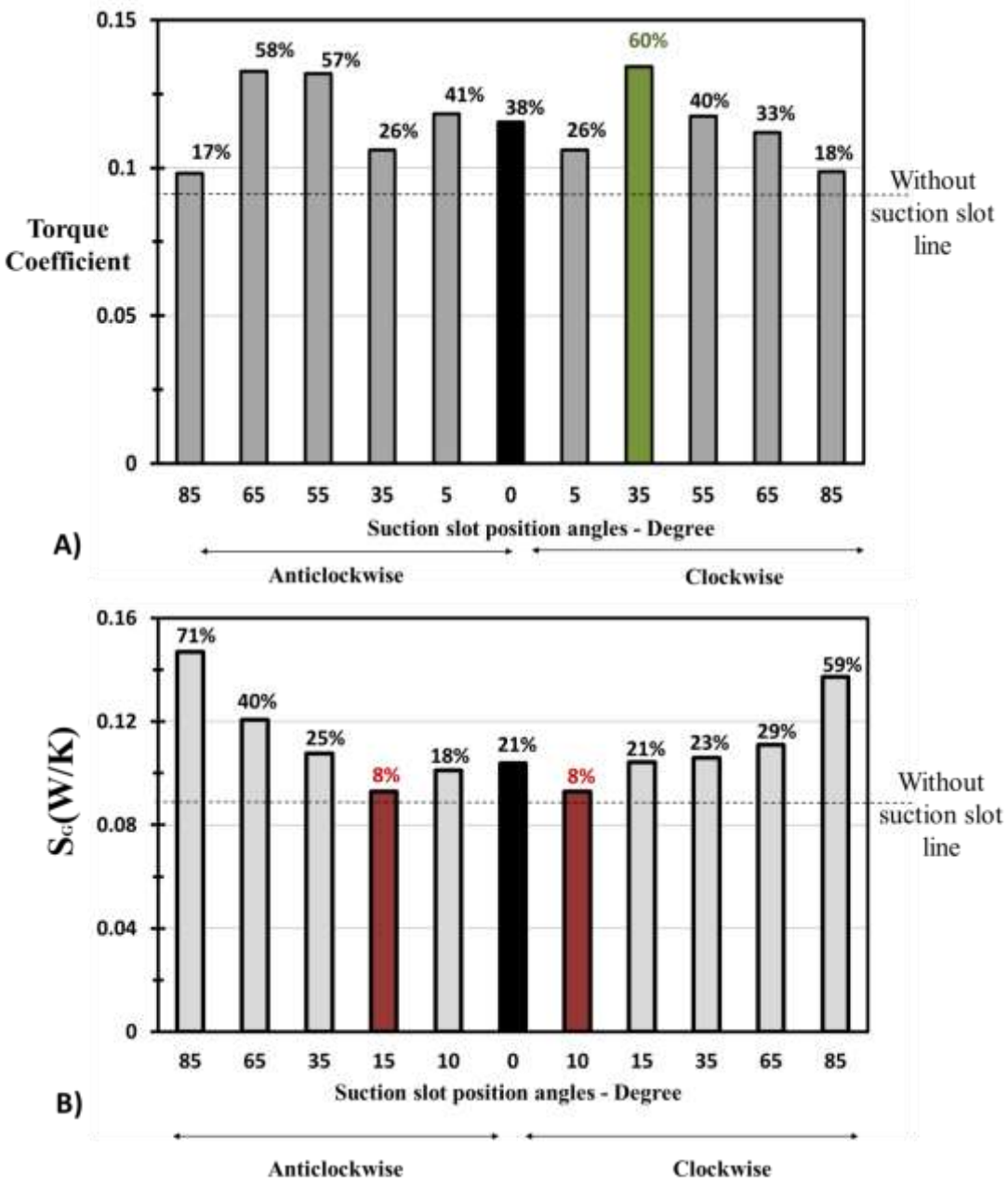

Figure 6.56 The effect of suction slot with different α_{SS} at the stall angle (13.6 degrees) A) Torque coefficient B) S_G

6.4.2 Optimum suction slot angles based on First and second law analysis under sinusoidal inlet velocity

From the previous section, it was noted that three values of α_{ss} (35 degrees clockwise and 65, 55 degrees anticlockwise) provide the highest values of C_T (60%, 58%, and 57%) at the stall regime. In addition, two values of α_{ss} (15 degrees anticlockwise and 10 degrees clockwise) have shown to provide the lowest S_G value (8%) at the stall regime. In this section, the optimum α_{ss} for single suction slot at the middle of the aerofoil was investigated based on both C_T and S_G values under sinusoidal wave condition.

Figure 6.57 and 6.58 illustrate the hysteretic behaviour due to the reciprocating flow. Figure 6.57 A) shows the comparison between the suction slot with 0 degree and that with 55 degrees anticlockwise. It can be noted that both the accelerating flow and decelerating flow of suction slot with α_{ss} equal to 55 degrees anticlockwise have a higher C_T than that with suction slot angel α_{ss} equal to 0 degree by 6% (accelerating) and 5% (decelerating). Furthermore, the accelerating flow for α_{ss} equal to 65 degrees anticlockwise has a lower C_T than that for α_{ss} equal to 0 degree by 7%, see Figure 6.57 B), while for the decelerating flow it provides a 3% higher C_T than that for α_{ss} equal to 0 degree. From the comparison in Figure 6.57 C) between the suction slot with 0 degree and that with 35 degrees clockwise, it can be noted that the C_T was the same as an average value in accelerating flow but for the decelerating flow the 35 degrees clockwise has higher C_T than the 0 degree by 7%. Figure 6.58 A) shows that the accelerating flow for suction slot with α_{ss} equal to 15 degrees anticlockwise has a lower C_T than that of the suction slot with α_{ss} equal to 0 degree by 2%, while the decelerating flow has a higher C_T than the suction slot with α_{ss} equal to 0 degree by 4%. Finally, Figure 6.58 B) shows that both the accelerating flow and decelerating flow of suction slot with α_{ss} equal to 10 degrees clockwise have a higher C_T than that of the suction slot with α_{ss} equal to 0 degree by 4% (accelerating) and 9% (decelerating).

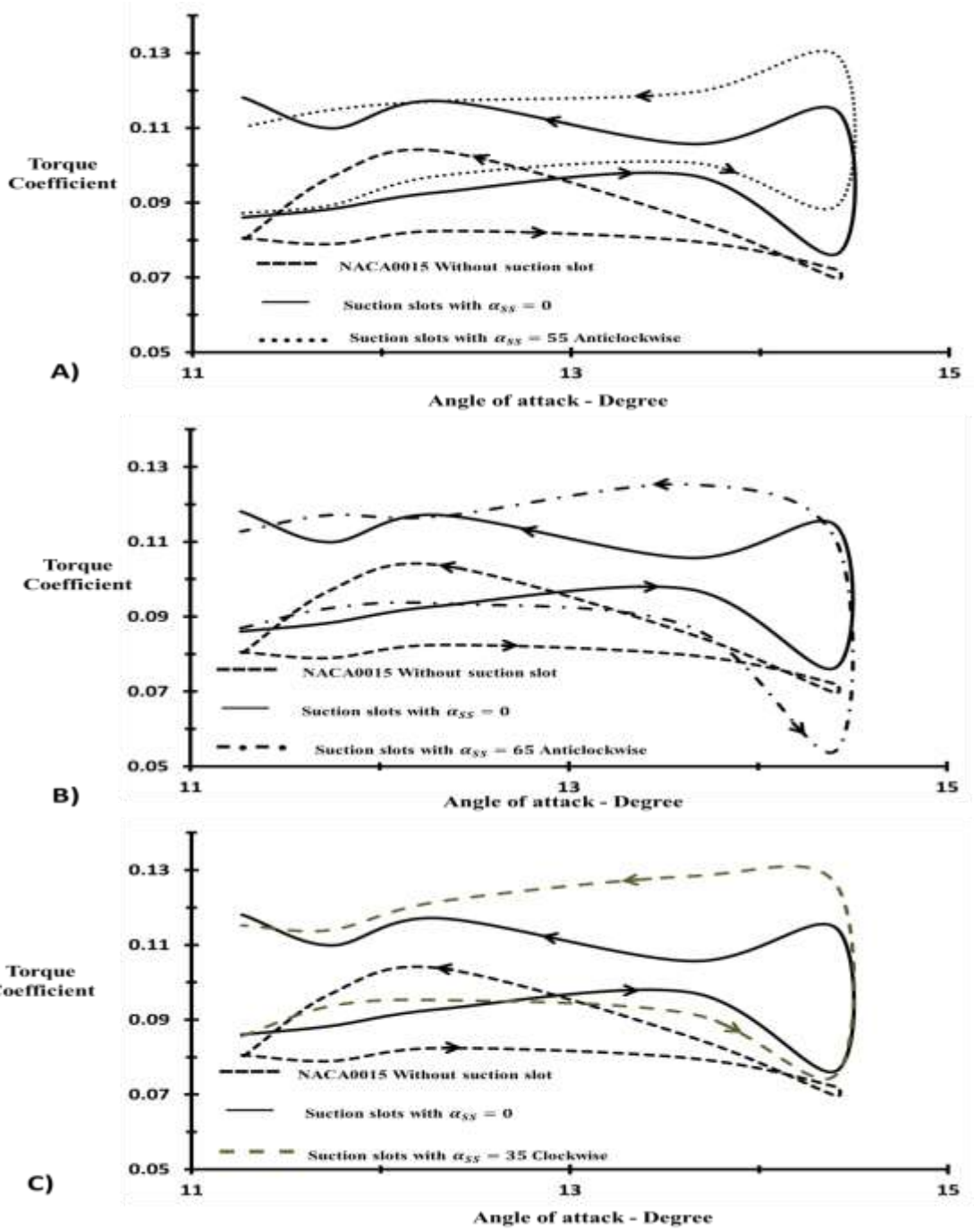

Figure 6.57 Hysteretic behaviour for the optimum angles of suction slot A) 55 degrees anticlockwise B) 65 degrees anticlockwise C) 35 degrees clockwise

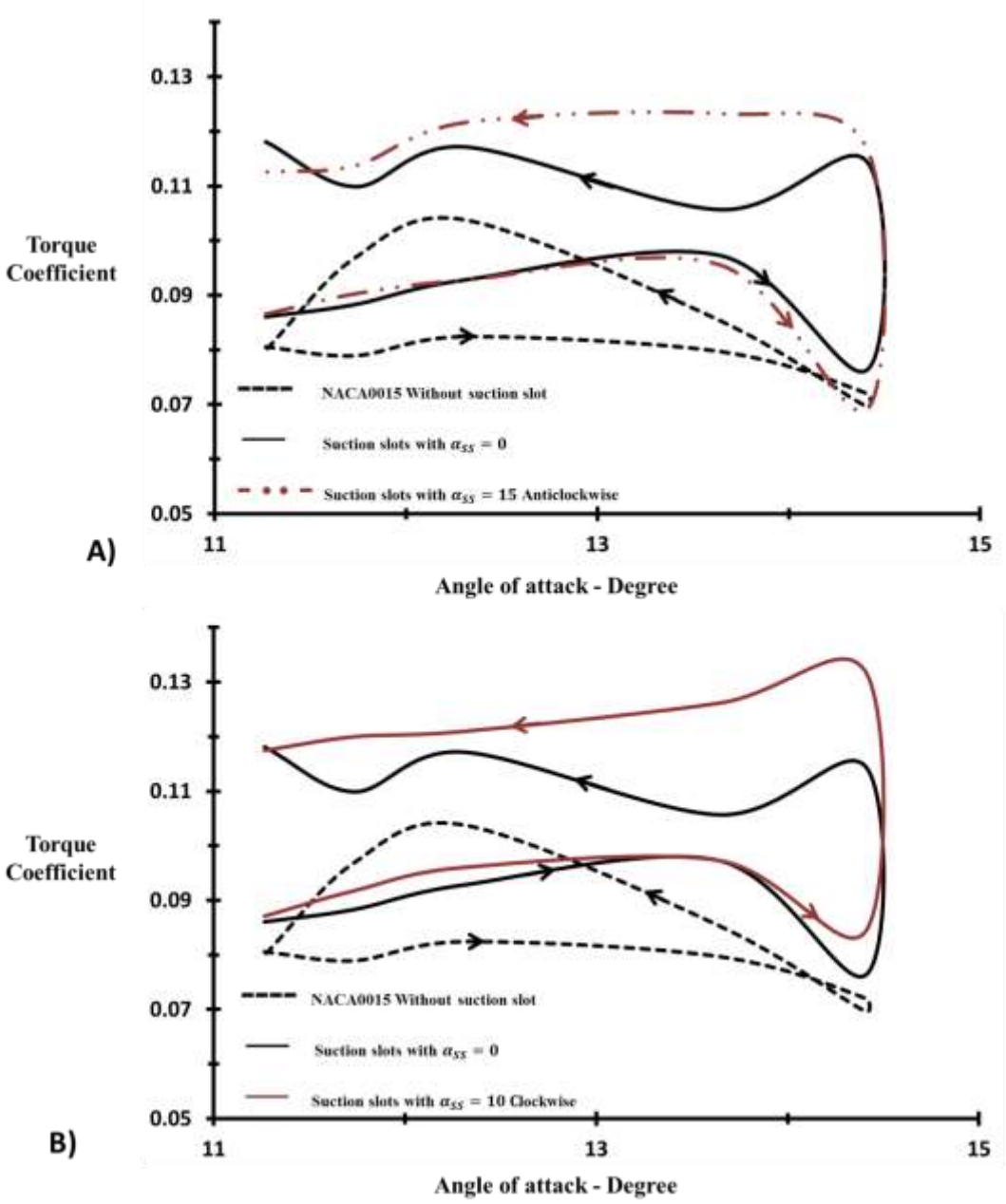

Figure 6.58 Hysteretic behaviour for the optimum angles of suction slot A) 15 degrees anticlockwise B) 10 degrees clockwise

Figure 6.59 shows the instantaneous torque coefficient at compression cycle for different suction slot angles; these values are at angle of attack of 13.6 degrees. It can be concluded that all five angles in Figure 6.59 A) and B) have higher peak value of C_T than the suction slot with α_{SS} equal to 0 degree and also as average value for the

compression cycle. For more details about other angles of attack, see Table 6.15. Furthermore, the average value of torque coefficient during the compression cycle was presented in Figure 6.60. The suction slot with α_{ss} equal to 10 degrees clockwise has the highest improvement in C_T value before the stall by 21%. Furthermore, both the suction slot with α_{ss} equal to 55 degrees anticlockwise and the suction slot with 10 degrees clockwise have the highest improvement in C_T value after the stall by 44%, see Table 6.15.

Table 6.15 The value of improvement in torque coefficient for NACA0015 with suction slot at different position angles under sinusoidal inlet velocity

Torque Coefficient	**Angle of attack (Degree)**				
	11.3	11.7	12.3	13.6	14.4
NACA0015 Without suction slot	0.080	0.088	0.093	0.083	0.071
Suction slots with $\alpha_{ss} = 0$ (degree)	0.102	0.099	0.105	0.102	0.095
Improvement by	27%	13%	13%	23%	35%
Average value	Before the stall (18%)			After the stall (29%)	
Suction slots with $\alpha_{ss} = 55$ Anticlockwise	0.099	0.102	0.107	0.110	0.109
Improvement by	23%	16%	15%	33%	54%
Average value	Before the stall (18%)			After the stall (44%)	
Suction slots with $\alpha_{ss} =$ 65 Anticlockwise	0.1	0.105	0.105	0.106	0.083
Improvement by	24%	19%	13%	29%	16%
Average value	Before the stall (19%)			After the stall (23%)	
Suction slots with $\alpha_{ss} = 35$ *C*lockwise	0.100	0.104	0.108	0.110	0.101
Improvement by	25%	18%	16%	33%	42%
Average value	Before the stall (20%)			After the stall (38%)	
Suction slots with $\alpha_{ss} =$ 15 Anticlockwise	0.1	0.102	0.107	0.109	0.093
Improvement by	24%	16%	15%	33%	31%
Average value	Before the stall (18%)			After the stall (32%)	
Suction slots with $\alpha_{ss} = 10$ *C*lockwise	0.102	0.106	0.109	0.112	0.108
Improvement by	27%	20%	16%	35%	53%
Average value	**Before the stall (21%)**			After the stall (44%)	

Maximum value

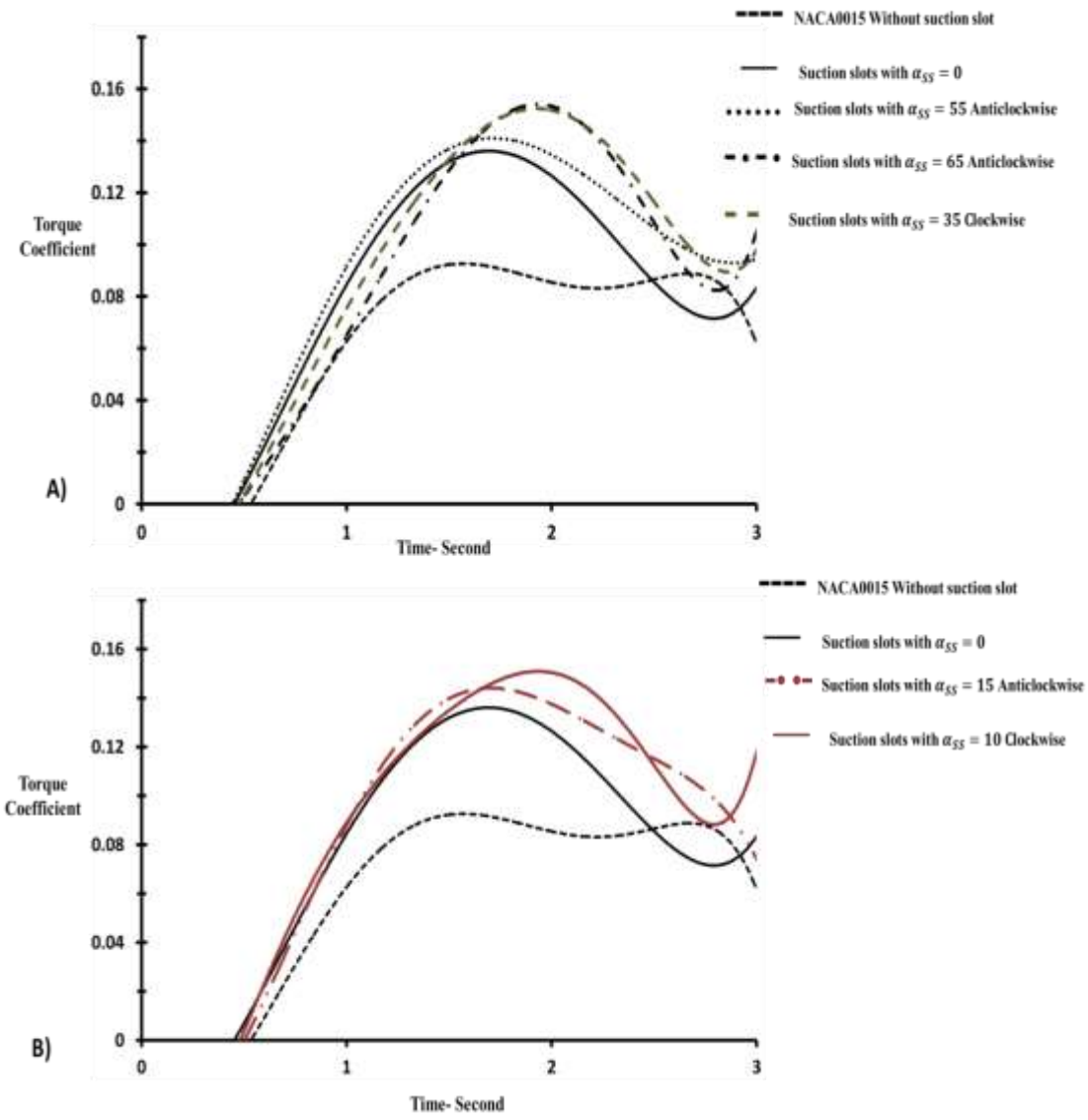

Figure 6.59 Comparison between the instantaneous torque coefficients for the optimum angles of suction slot A) based on first law analysis B) based on second law analysis

Table 6.16 highlights the comparison between the values of S_G for NACA0015 with suction slot at different position angles under sinusoidal inlet velocity. It can be concluded that the suction slot with α_{ss} equal to 10 degrees clockwise has the lowest increase in S_G value before the stall by 20%. Furthermore, the suction slot with α_{ss}

equal to 15 degrees anticlockwise has the lowest increase in S_G value after the stall by 18% than the NACA0015 without slot.

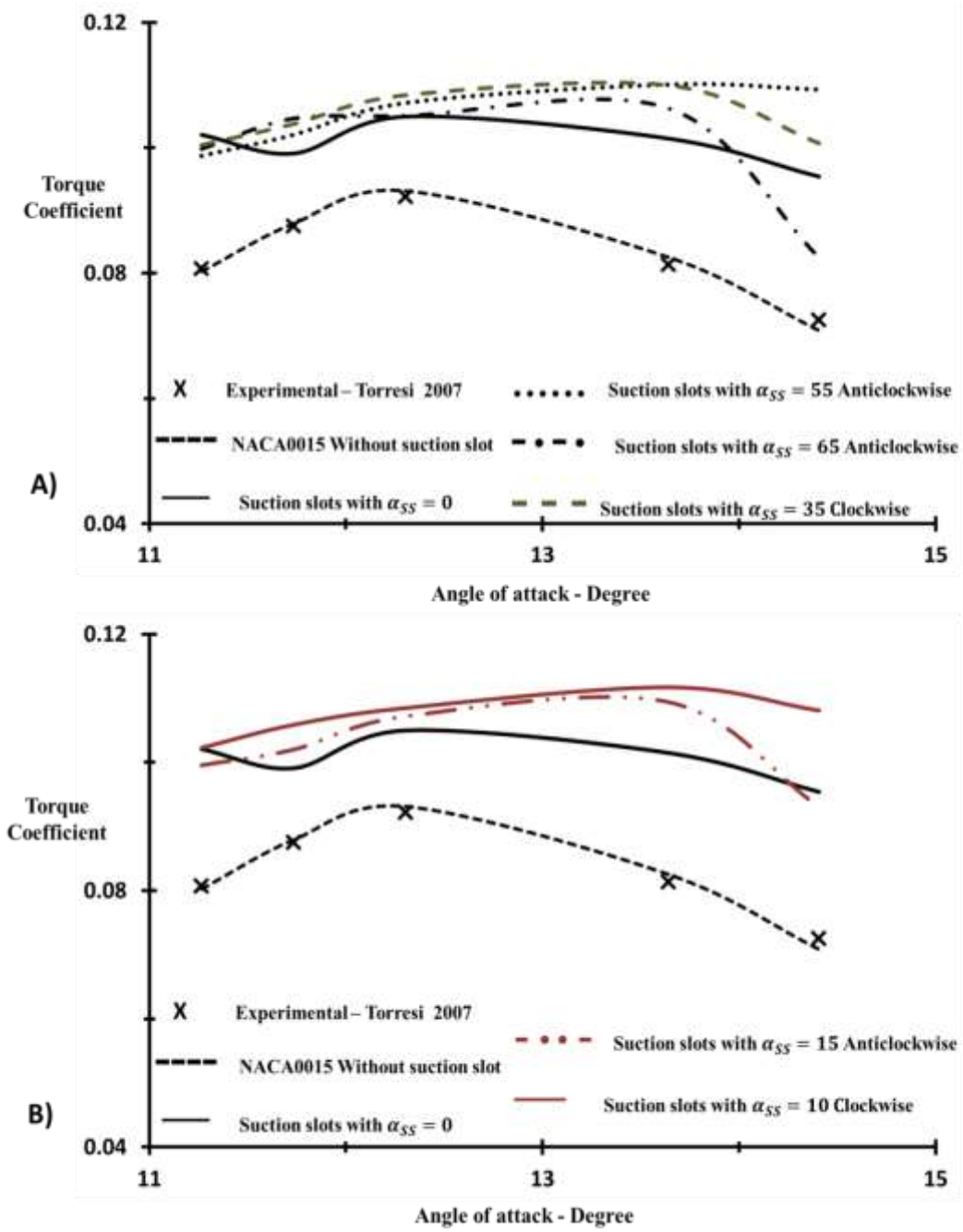

Figure 6.60 Comparison between the average torque coefficients for the optimum angles of suction slot A) based on first law analysis B) based on second law analysis

Table 6.16 The value of global entropy generation rate for NACA0015 with suction slot at different position angles under sinusoidal inlet velocity

The global entropy generation rate (W/K)	**Angle of attack (Degree)**				
	11.3	11.7	12.3	13.6	14.4
NACA0015 Without suction slot	0.053	0.052	0.053	0.054	0.060
Suction slots with α_{SS} = 0 (degree)	0.064	0.065	0.066	0.071	0.072
S_G increased by	20%	27%	26%	33%	19%
Average value	Before the stall (24%)			After the stall (26%)	
Suction slots with α_{SS} = 55 Anticlockwise	0.077	0.082	0.081	0.087	0.087
S_G increased by	45%	59%	55%	63%	43%
Average value	Before the stall (53%)			After the stall (52%)	
Suction slots with α_{SS} = 65 Anticlockwise	0.078	0.081	0.081	0.083	0.081
S_G increased by	47%	57%	54%	55%	35%
Average value	Before the stall (53%)			After the stall (45%)	
Suction slots with α_{SS} = 35 *C*lockwise	0.072	0.074	0.075	0.077	0.085
S_G increased by	35%	43%	42%	44%	41%
Average value	Before the stall (40%)			After the stall (42%)	
Suction slots with α_{SS} = 15 Anticlockwise	0.062	0.065	0.064	0.068	0.067
S_G increased by	16%	27%	21%	26%	10%
Average value	Before the stall (21%)			**After the stall (18%)**	
Suction slots with α_{SS} = 10 *C*lockwise	0.063	0.062	0.063	0.068	0.073
S_G increased by	18%	20%	21%	27%	20%
Average value	**Before the stall (20%)**			After the stall (23%)	

Minimum value

Figure 6.61 shows the comparison between the second law efficiency of NACA0015 without and with suction slot, which have different angles. The comparison was provided as an average value for the compression cycle with different angles of attack. The increase in S_G (Table 6.16) leads to a decrease in second law efficiency in most cases than that without suction slots. However, the suction slot with α_{ss} equal to 15 degrees anticlockwise provides a higher second law efficiency than the NACA0015 without suction slot by 0.4% before the stall (Figures 6.61 A, B and C) and 0.7% after the stall (Figures 6.61 D and E) as an average value. Also, it provides a higher second law efficiency than suction slot with α_{ss} equal to 0 degree by 0.5% after the stall (Figures 6.61 D and E) but the same value as average before the stall (Figures 6.61 A, B and C). On the other hand, the suction slot with α_{ss} equal to 10 degrees clockwise has higher second law efficiency than the NACA0015 without suction slot by 0.5% before the stall (Figures 6.61 A, B and C) and 0.2% after the stall (Figures 6.61 D and E) as an average value. Furthermore, it has the same improvement in second law efficiency from suction slot with α_{ss} equal to 0 degree as an average value before the stall (Figures 6.61 A, B and C) and after the stall (Figures 6.61 D and E).

The effect of suction slot on the separation layers around the trailing edge area can be noted at Figure 6.62. Where, the mean velocity magnitude path lines around the NACA0015 without and with suction slot for different α_{ss} were presented. These values were at the instantaneous velocities of 2.92 m/s (Figure 6.62 A) and 1.8 m/s (Figure 6.62 B) for the decelerating flow and at angle of attack of 13.6 degrees (stall angle). Also, the improvement effect of suction slot on separation layer increased in the second half of the cycle (deceleration flow) because the separation region around the end of the blade increased, especially at the decelerating flow at Figure 6.62 B).

From Figure 6.63, it can be noted that the low pressure zones around the aerofoil, especially at the trailing edge area, were reduced by adding the suction slot. The slot with angle not equal to zero gives better result from that with zero degree, for example, 35 (clockwise) degrees or 10 (clockwise) degrees. The slot with 35 or 10 degrees were reduced the low pressure area around the aerofoil and also the difference between the

pressure at the upper and lower surface higher than the slot with zero degree. Therefore, the slot with 35 or 10 degrees have more improvement in the separation layer and the torque coefficient than the slot with zero degree.

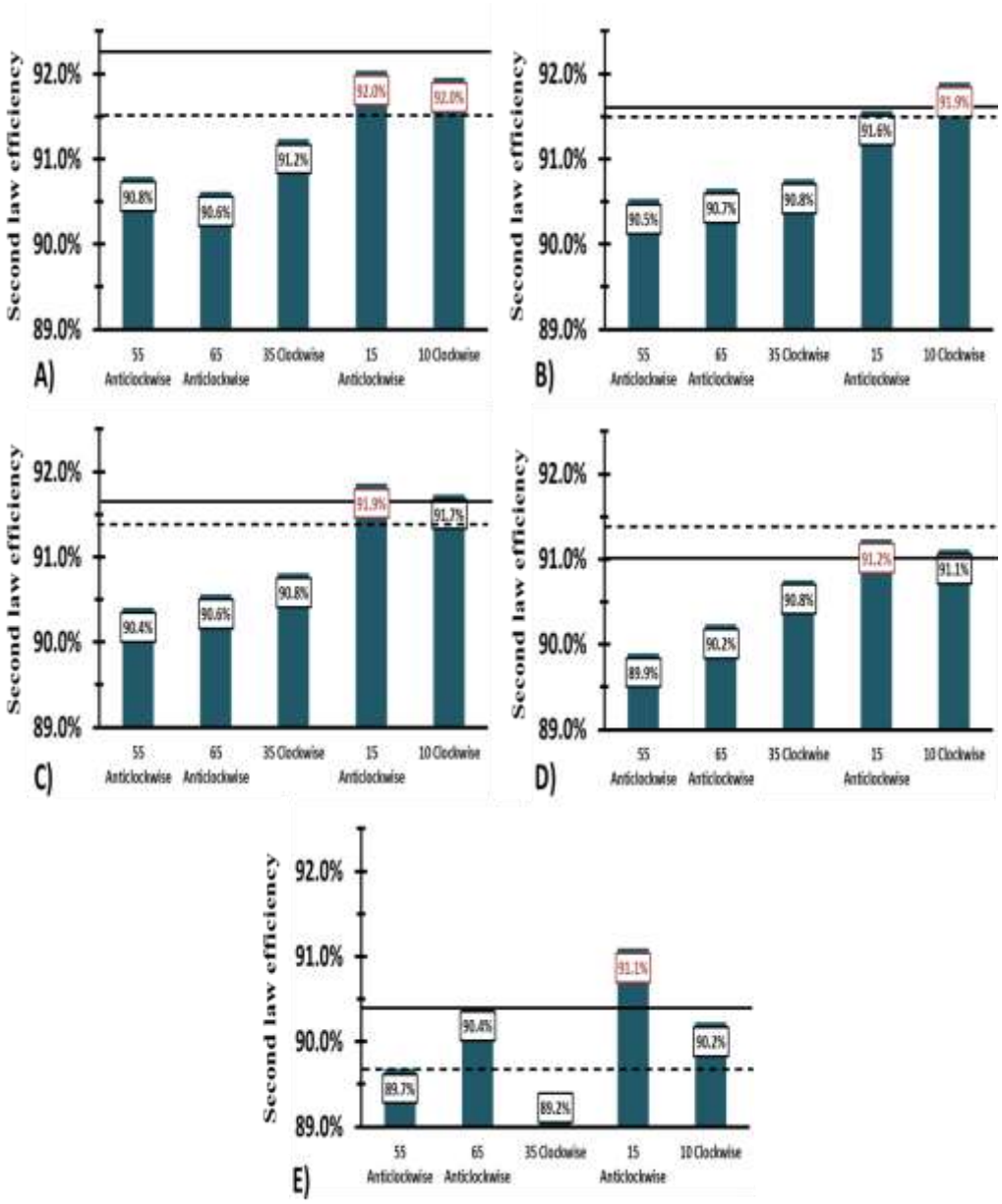

Figure 6.61 Comparison between the second law efficiency for the compression cycle for NACA0015 with slot at different α_{ss} "---without slot" " —— α_{ss} =0 degree" A) 11.3 B) 11.7 C) 12.3 D) 13.6 E) 14.4

The flow structures over the NACA0015 aerofoil without and with suction slot has different slot angles in oscillating flow are shown in Figure 6.64. Figure 6.64 shows the contours of velocity magnitude (Figure 6.64A) and entropy (Figure 6.64B) at maximum velocity 2.92 m/s and angle of attack equal to 13.6 degrees (stall angle). The improvement effect of suction slot on flow structures was clear when comparing the NACA0015 without and with slot, especially in the separated layer regime at the end of aerofoil. The suction slot has a direct effect on the flow structures at the end of blade, which leads to an improvement in the separation regime. However, adding a suction slot shows a negative effect on the entropy generation, where higher entropy generation values were obtained for all suction slots cases. The suction slot with α_{ss} equal to 55 degrees anticlockwise generates the highest value of entropy with an increase of 63% than the NACA0015 without suction slot case. In addition the lowest value for aerofoil with suction slot was obtained with α_{ss} equal to 15 degrees anticlockwise, with an increase of 18% only than the NACA0015 without suction slot case. From Figure 6.62 A and B it can be noted that the attached slot with angle not equal to zero to the aerofoil lead to increase in velocity magnitude around the aerofoil, furthermore, it also lead to increase in the entropy generation in Figure 6.64 B where the entropy value depends on the velocity gradient, see equation (3.42).

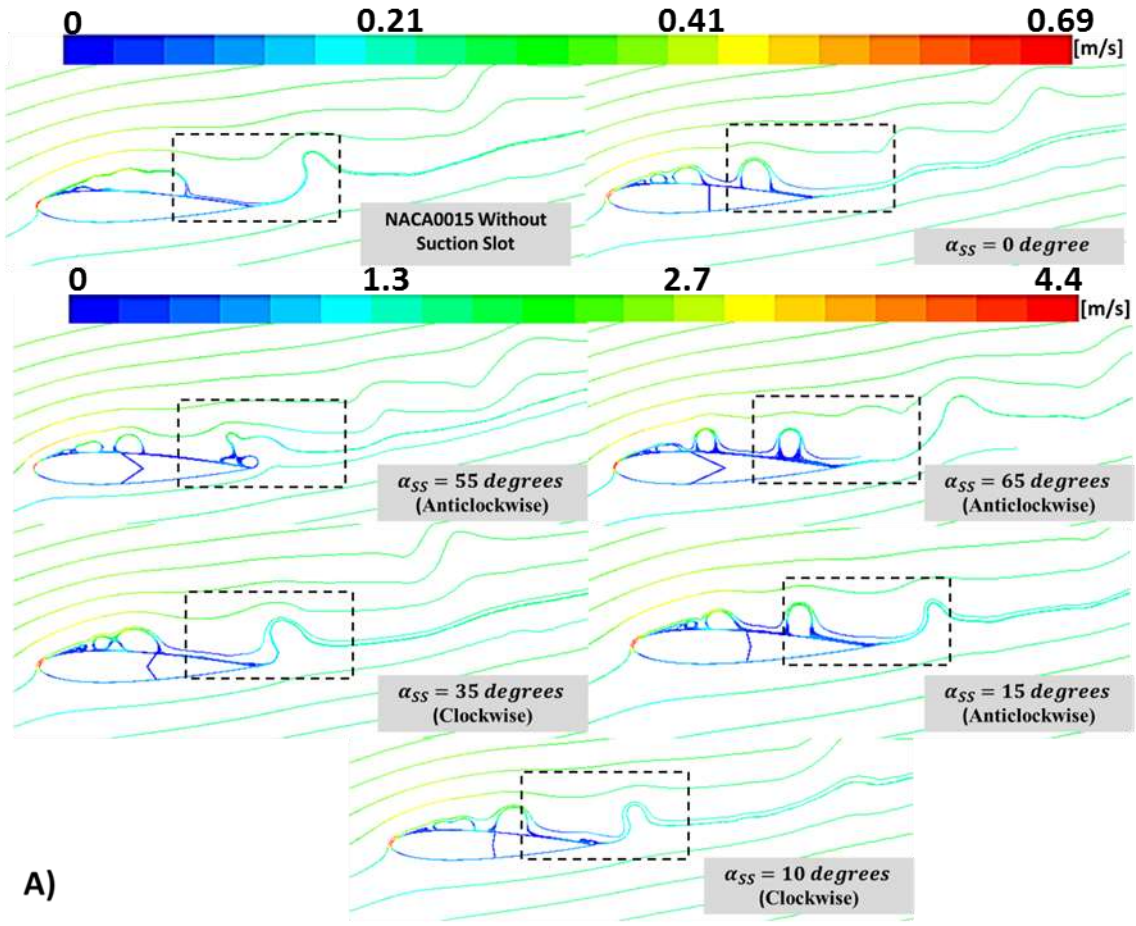
0
0.21
0.41
0.69
[m/s]
NACA0015 Without Suction Slot
$\alpha_{SS} = 0\ degree$
0
1.3
2.7
4.4
[m/s]
$\alpha_{SS} = 55\ degrees$ (Anticlockwise)
$\alpha_{SS} = 65\ degrees$ (Anticlockwise)
$\alpha_{SS} = 35\ degrees$ (Clockwise)
$\alpha_{SS} = 15\ degrees$ (Anticlockwise)
$\alpha_{SS} = 10\ degrees$ (Clockwise)
A)

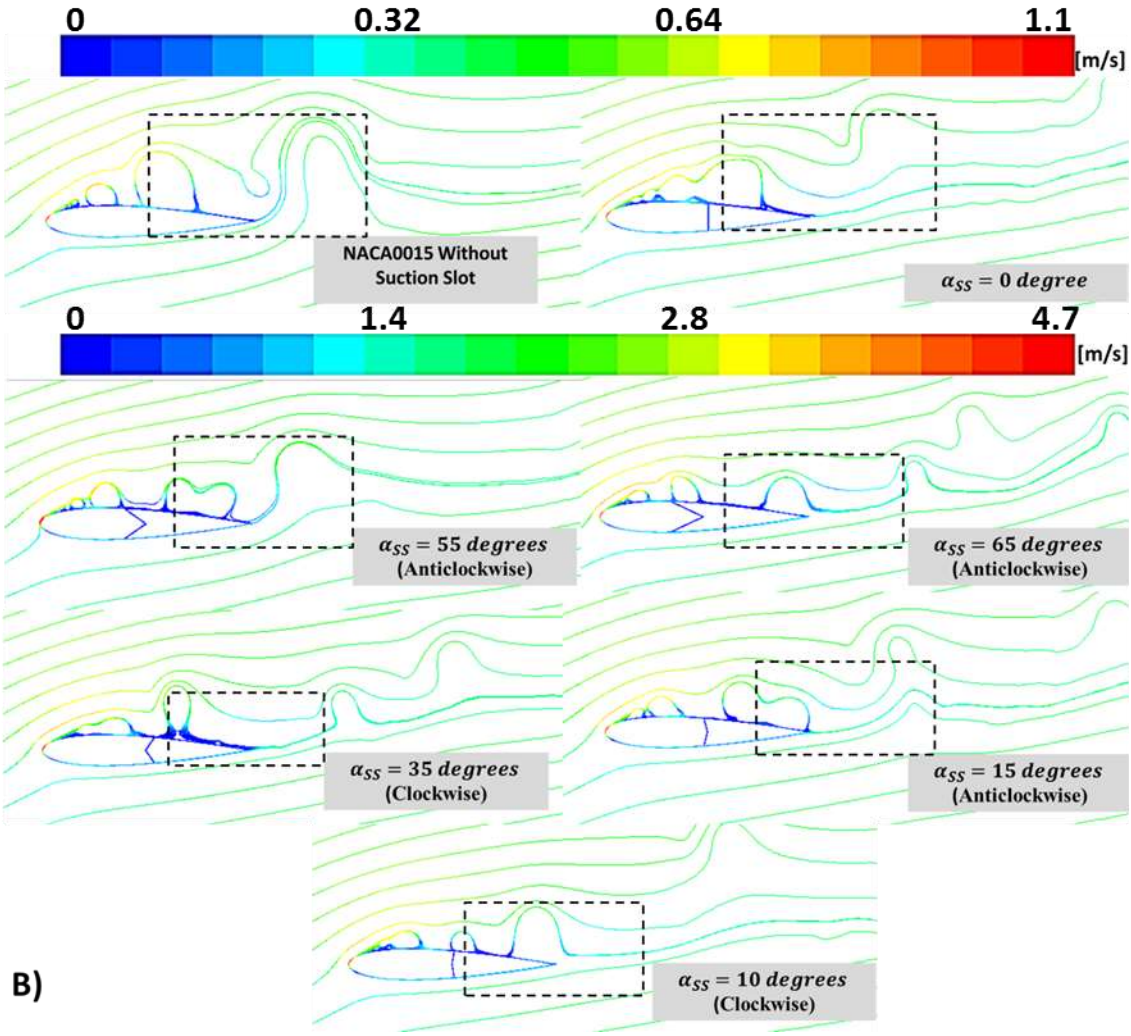

Figure 6.62 Path-line coloured by mean velocity magnitude around NACA0015 without slot and with the optimum angles of suction slot under sinusoidal inlet velocity A) 2.92 m/s -maximum velocity B) 1.8 m/s -decelerating flow

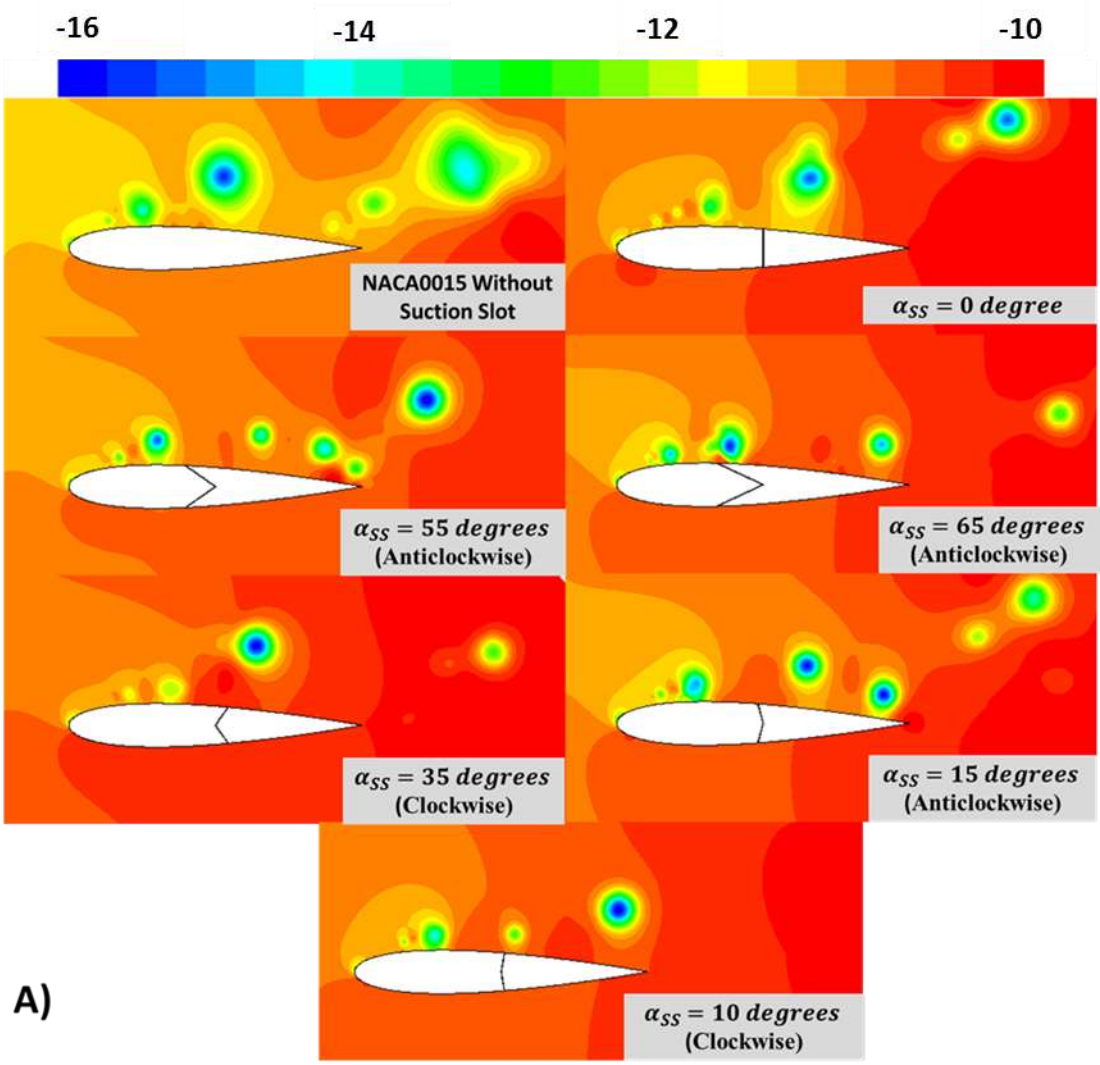
-16
-14
-12
-10
NACA0015 Without Suction Slot
$\alpha_{SS} = 0\ degree$
$\alpha_{SS} = 55\ degrees$ (Anticlockwise)
$\alpha_{SS} = 65\ degrees$ (Anticlockwise)
$\alpha_{SS} = 35\ degrees$ (Clockwise)
$\alpha_{SS} = 15\ degrees$ (Anticlockwise)
$\alpha_{SS} = 10\ degrees$ (Clockwise)

A)

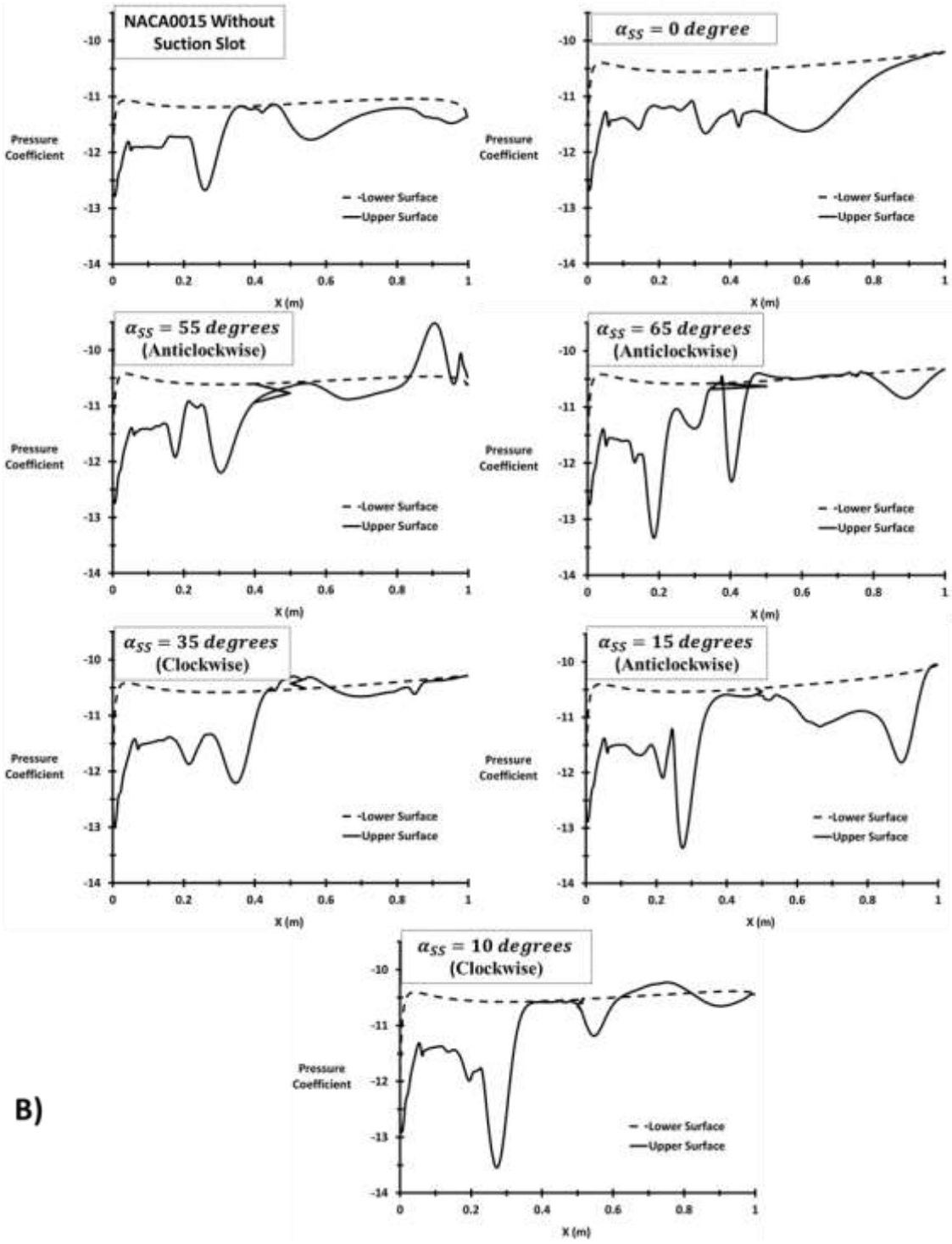

Figure 6.63 The pressure distribution around NACA0015 without slot and with the optimum angles of suction slot under sinusoidal velocity A) Contours of pressure coefficient B) pressure coefficient at the upper and lower surface

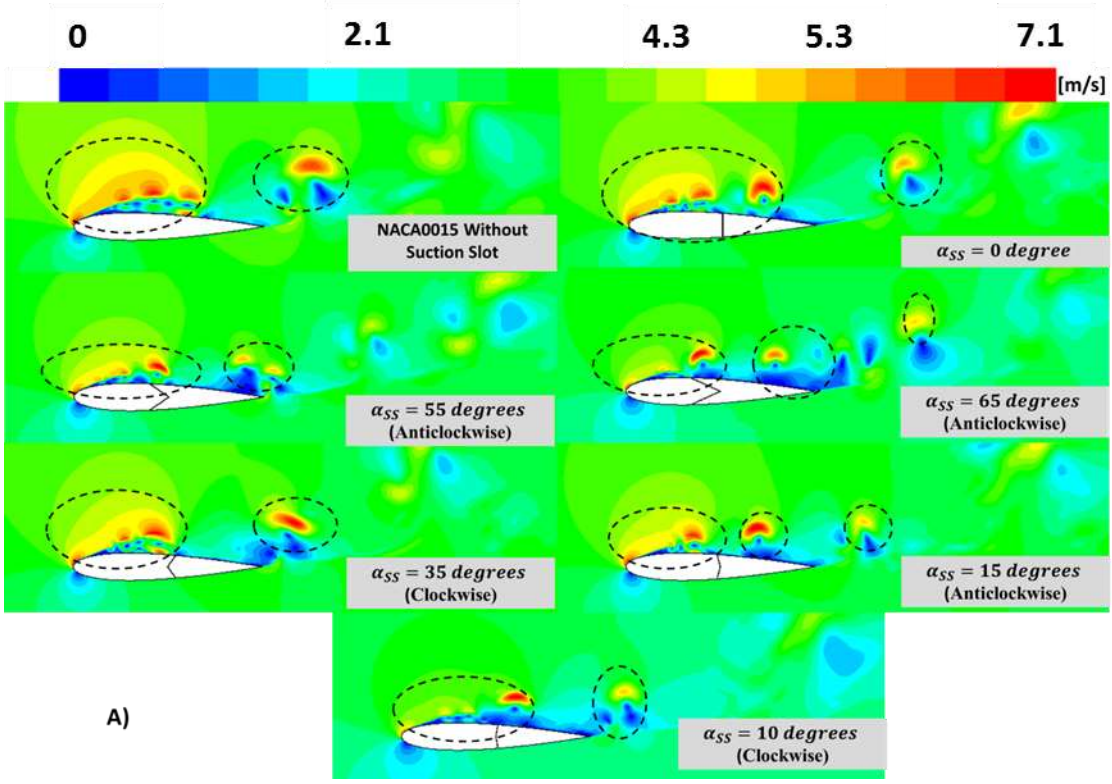
0
2.1
4.3
5.3
7.1
[m/s]
NACA0015 Without Suction Slot
$\alpha_{SS} = 0\ degree$
$\alpha_{SS} = 55\ degrees$ (Anticlockwise)
$\alpha_{SS} = 65\ degrees$ (Anticlockwise)
$\alpha_{SS} = 35\ degrees$ (Clockwise)
$\alpha_{SS} = 15\ degrees$ (Anticlockwise)
$\alpha_{SS} = 10\ degrees$ (Clockwise)

A)

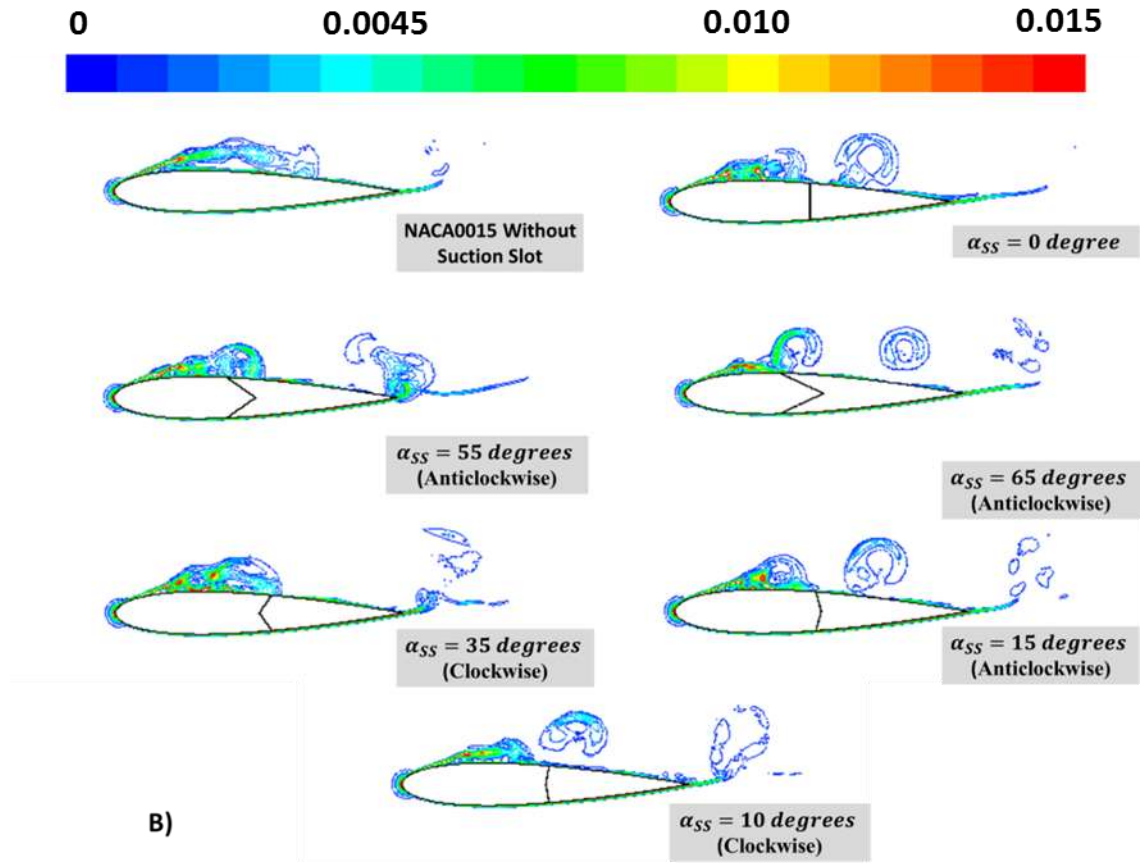

Figure 6.64 The Contour around NACA0015 without slot and with the optimum angles of suction slot under sinusoidal velocity A) Velocity magnitude B) Global entropy generation rate

6.4.3 Different frequencies effects

From the previous section, it was concluded that the optimum α_{SS} was 10 degrees clockwise since this suction slot angle gives the highest C_T before and after the stall (Table 6.15). On the other hand, it gives a lower S_G than other angles before the stall and also it gives lower S_G than 0 degree angle after the stall (Table 6.16). Therefore, this optimum α_{SS} was investigated using the oscillating water system based on the real data from the site under different frequencies (f equal to 0.25, 0.167 and 1.25 Hz) and time periods (4, 6 and 8 seconds) see section 5.4 and Figure 5.16.

The C_T for both α_{SS} equal to 0 degree and 10 degrees clockwise have the same value (as an average) at the accelerating flow but for decelerating flow the 10 degrees clockwise has higher C_T than the 0 degree by 1% (Figure 6.65 A). The suction slot with α_{SS} equal to 10 degrees clockwise has a higher peak value of C_T than the suction slot with α_{SS} equal to 0 degree at angle of attack of 13.6 degrees. On the other hand, as an average value for the compression cycle, the α_{SS} equal to 10 degrees clockwise has a lower value of C_T than the α_{SS} equal to 0 degree by 3% (Figure 6.65 B). For more details about other angles of attack for sinusoidal wave with time period equal to 4 second, see Table 6.17. It can be noted that from Figure 6.65 C), the suction slot with α_{ss} equal to 10 degrees clockwise has higher improvement in C_T value before the stall than the aerofoil without slot by 7%. However, the suction slot with α_{ss} equal to 0 degree gives higher improvement in C_T value after the stall by degrees 10% than the aerofoil without slot. See Table 6.17 for more details about sinusoidal wave with time period equal to 4 seconds.

It can be noted that from Figure 6.66 A), the suction slot with α_{ss} equal to 10 degrees clockwise at both accelerating and decelerating flows has a higher C_T than the 0 degree by 6% (accelerating) and 4% (decelerating). For the average value for the compression cycle, the suction slot with α_{SS} equal to 10 degrees clockwise provides a higher value of C_T than the α_{SS} equal to 0 degree by 2% at angle of attack of 13.6 degrees. Also, the α_{SS} equal to 10 degrees clockwise provides a higher peak value of C_T than α_{SS} equal to 0 degree, Figure 6.66 B). For more details about other angles of attack for sinusoidal wave with time period equal to 8 seconds see Table 6.17. It can be noted that from Figure 6.66 C) and Table 6.17, the suction slot with α_{ss} equal to 10 degrees clockwise provides the highest improvement in C_T value before the stall by 13% and after the stall by 20%.

It can be concluded that from Table 6.18, the suction slot with α_{ss} equal to 10 degree clockwise gives S_G value lower than the suction slot with α_{ss} equal to 0 degree at different time period before and after the stall, except at the time period equal to 4

seconds, where the suction slot with α_{ss} equal to 0 degree has the lowest increase in S_G value after the stall by 12%.

The increase in S_G (Table 6.18) leads to the decrease in second law efficiency in most cases than that without suction slots, see Figure 6.67.Where, the suction slot with α_{ss} equal to 10 degrees clockwise under sinusoidal wave with time period equal to 4 seconds has lower second law efficiency than the NACA0015 without suction slot by 0.3% before the stall (Figures 6.67 A, B and C) and after the stall (Figures 6.56 D and E) as an average value. Furthermore, it also has the highest second law efficiency than suction slot with α_{ss} equal to 0 degree as an average value before the stall (Figures 6.67 A, B and C) by 0.1% and lower than it after the stall (Figures 6.67 D and E) by 0.2%. On the other hand, the suction slot with α_{ss} equal to 10 degrees clockwise under sinusoidal wave with time period equal to 6 seconds has a higher second law efficiency than the NACA0015 without suction slot by 0.5% before the stall (Figures 6.67 A, B and C) and 0.2% after the stall (Figures 6.67 D and E) as an average value. Also, the 10 degrees clockwise has the same improvement in second law efficiency compare with the 0 degree as an average value before the stall (Figures 6.67 A, B and C) and after the stall (Figures 6.67 D and E).

Finally, the suction slot with α_{ss} equal to 10 degrees clockwise under sinusoidal wave with time period equal to 8 seconds gives a lower second law efficiency than the NACA0015 without suction slot by 0.6% before the stall (Figures 6.67 A, B and C) and after the stall (Figures 6.67 D and E) as an average value. Furthermore, it has the highest second law efficiency when compared to suction slot with α_{ss} equal to 0 degree as an average value before the stall (Figures 6.67 A, B and C) by 0.1% and lower than it after the stall (Figures 6.67 D and E) by 0.6%.

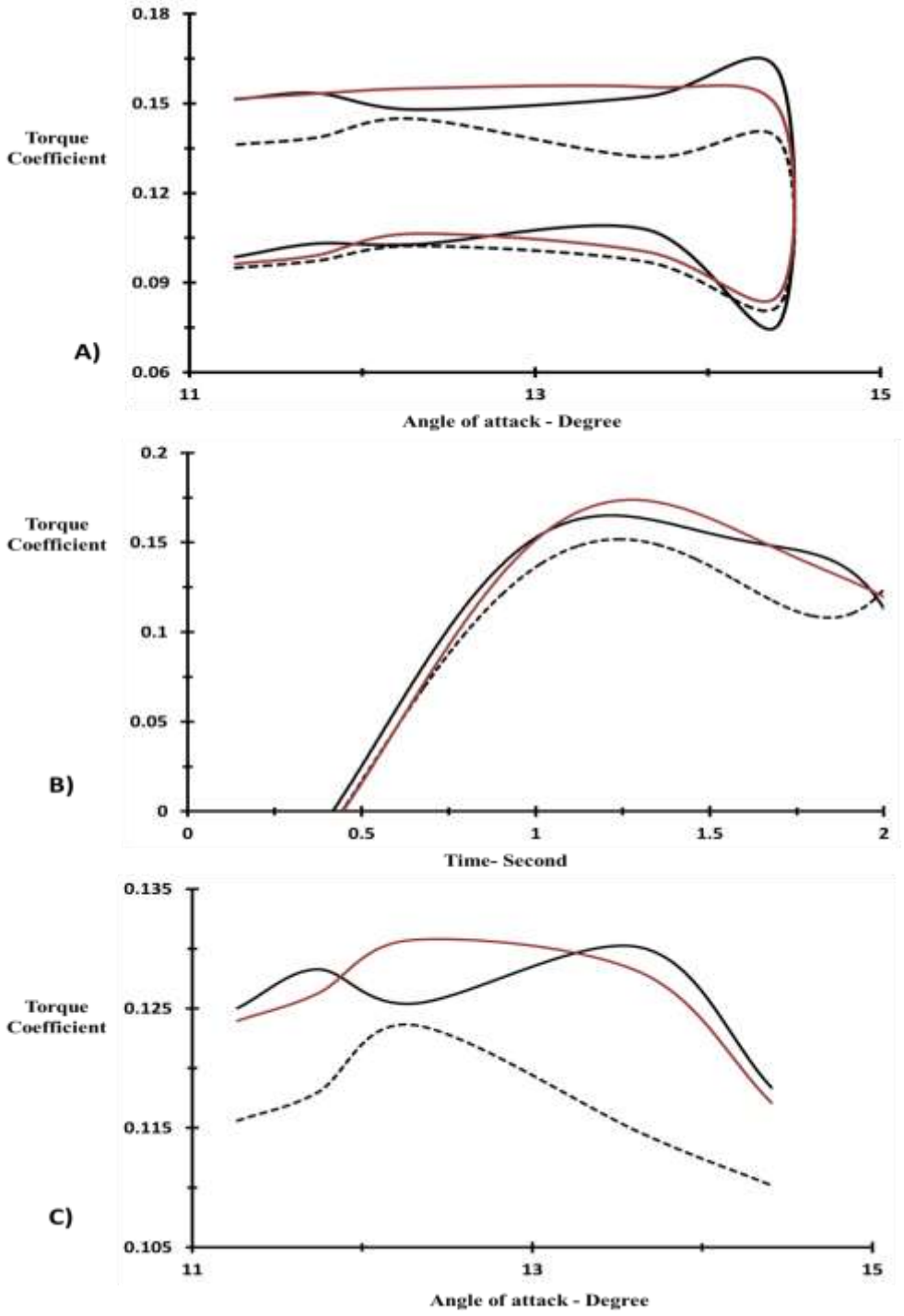

Figure 6.65 The NACA0015 without and with suction slot at optimum angle with time period 4 second "- - without slot —— α_{SS} =0 degree","—— α_{SS} =10 degrees clockwise A) The hysteretic behaviour B) The instantaneous torque coefficient C) The average torque

Table 6.17 Comparison between the torque coefficients values at different time periods under sinusoidal inlet velocity

Torque Coefficient (4 Second)	**Angle of attack (Degree)**				
	11.3	11.7	12.3	13.6	14.4
NACA0015 Without suction slot	0.116	0.118	0.124	0.115	0.110
Suction slots with $\alpha_{SS} = 0$ (degree)	0.125	0.128	0.125	0.130	0.118
Improvement by	Before the stall (6%)			**After the stall (10%)**	
Suction slots with $\alpha_{SS} =$ 10 *C*lockwise	0.124	0.126	0.131	0.128	0.117
Improvement by	**Before the stall (7%)**			After the stall (9%)	
Torque Coefficient (6 Second)					
NACA0015 Without suction slot	0.080	0.088	0.093	0.083	0.071
Suction slots with $\alpha_{SS} = 0$ (degree)	0.102	0.099	0.105	0.102	0.095
Improvement by	Before the stall (18%)			After the stall (29%)	
Suction slots with $\alpha_{SS} =$ 10 *C*lockwise	0.102	0.106	0.109	0.112	0.108
Improvement by	**Before the stall (21%)**			**After the stall (44%)**	
Torque Coefficient (8 Second)					
NACA0015 Without suction slot	0.082	0.078	0.084	0.088	0.075
Suction slots with $\alpha_{SS} = 0$ (degree)	0.086	0.092	0.093	0.099	0.081
Improvement by	Before the stall (11%)			After the stall (11%)	
Suction slots with $\alpha_{SS} =$ 10 *C*lockwise	0.088	0.092	0.097	0.101	0.093
Improvement by	**Before the stall (13%)**			**After the stall (20%)**	

Maximum value

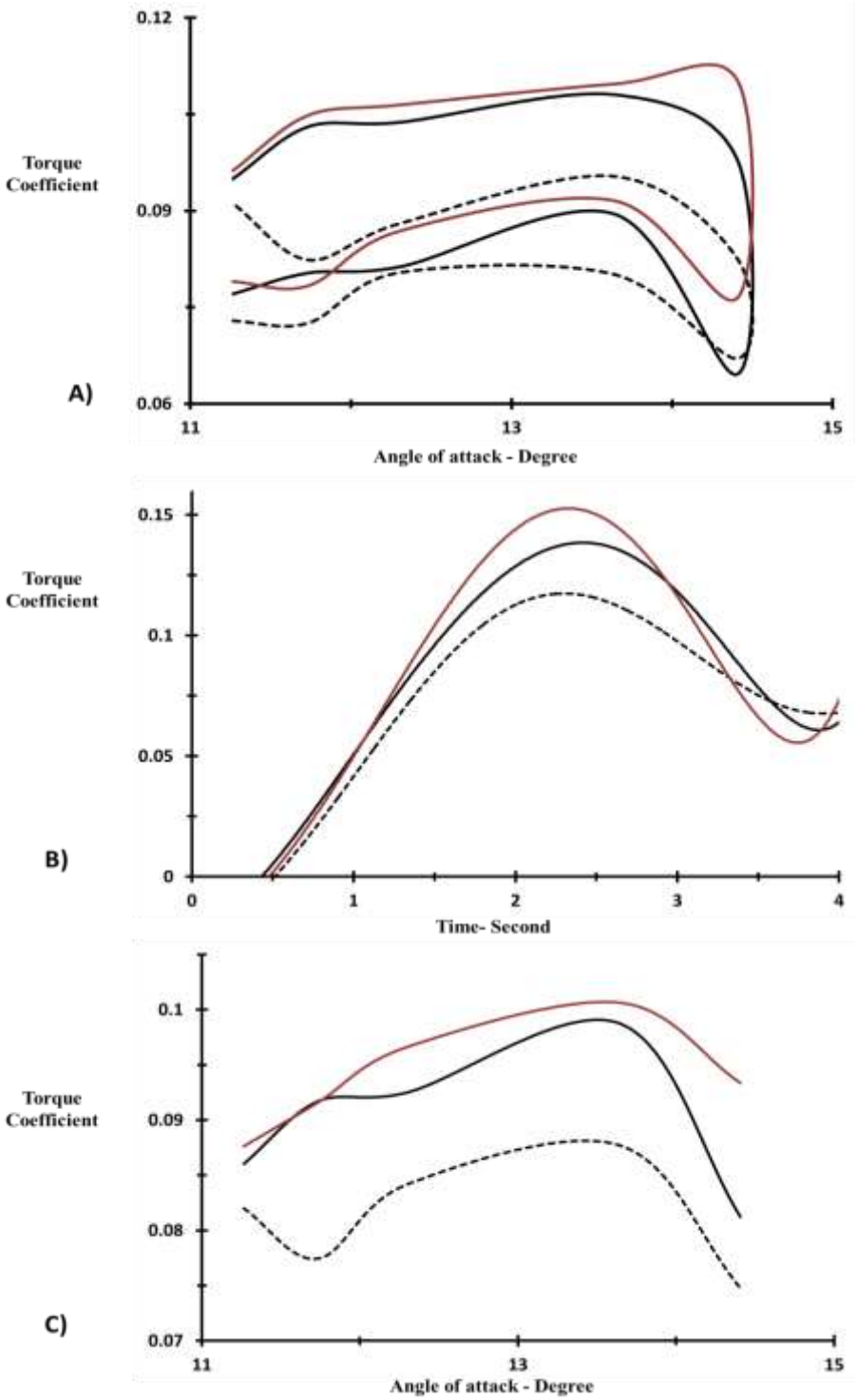

Figure 6.66 The NACA0015 without and with suction slot at optimum angle with time period 8 second "- - -without slot —— α_{ss} =0 degree","—— α_{ss} =10 degrees clockwise A) The hysteretic behaviour B) The instantaneous torque coefficient C) The average torque coefficient

Table 6.18 Comparison between the global entropy generation rate values at different time periods under sinusoidal inlet velocity

Global entropy generation rate (4 Second)	**Angle of attack (Degree)**				
	11.3	11.7	12.3	13.6	14.4
NACA0015 Without suction slot	0.057	0.059	0.057	0.065	0.066
Suction slots with $\alpha_{SS} = 0$ (degree)	0.066	0.066	0.069	0.073	0.074
S_G increased by	Before the stall (16%)			**After the stall (12%)**	
Suction slots with $\alpha_{SS} =$ 10 *C*lockwise	0.063	0.063	0.065	0.071	0.079
S_G increased by	**Before the stall (10%)**			After the stall (14%)	
Global entropy generation rate (6 Second)					
NACA0015 Without suction slot	0.053	0.052	0.053	0.054	0.060
Suction slots with $\alpha_{SS} = 0$ (degree)	0.064	0.065	0.066	0.071	0.072
S_G increased by	Before the stall (24%)			After the stall (26%)	
Suction slots with $\alpha_{SS} =$ 10 *C*lockwise	0.063	0.062	0.063	0.068	0.073
S_G increased by	**Before the stall (20%)**			**After the stall (23%)**	
Global entropy generation rate (8 Second)					
NACA0015 Without suction slot	0.053	0.053	0.054	0.056	0.060
Suction slots with $\alpha_{SS} = 0$ (degree)	0.063	0.062	0.064	0.065	0.073
S_G increased by	Before the stall (18%)			After the stall (19%)	
Suction slots with $\alpha_{SS} =$ 10 *C*lockwise	0.061	0.061	0.064	0.066	0.072
S_G increased by	**Before the stall (16%)**			**After the stall (18%)**	

Minimum value

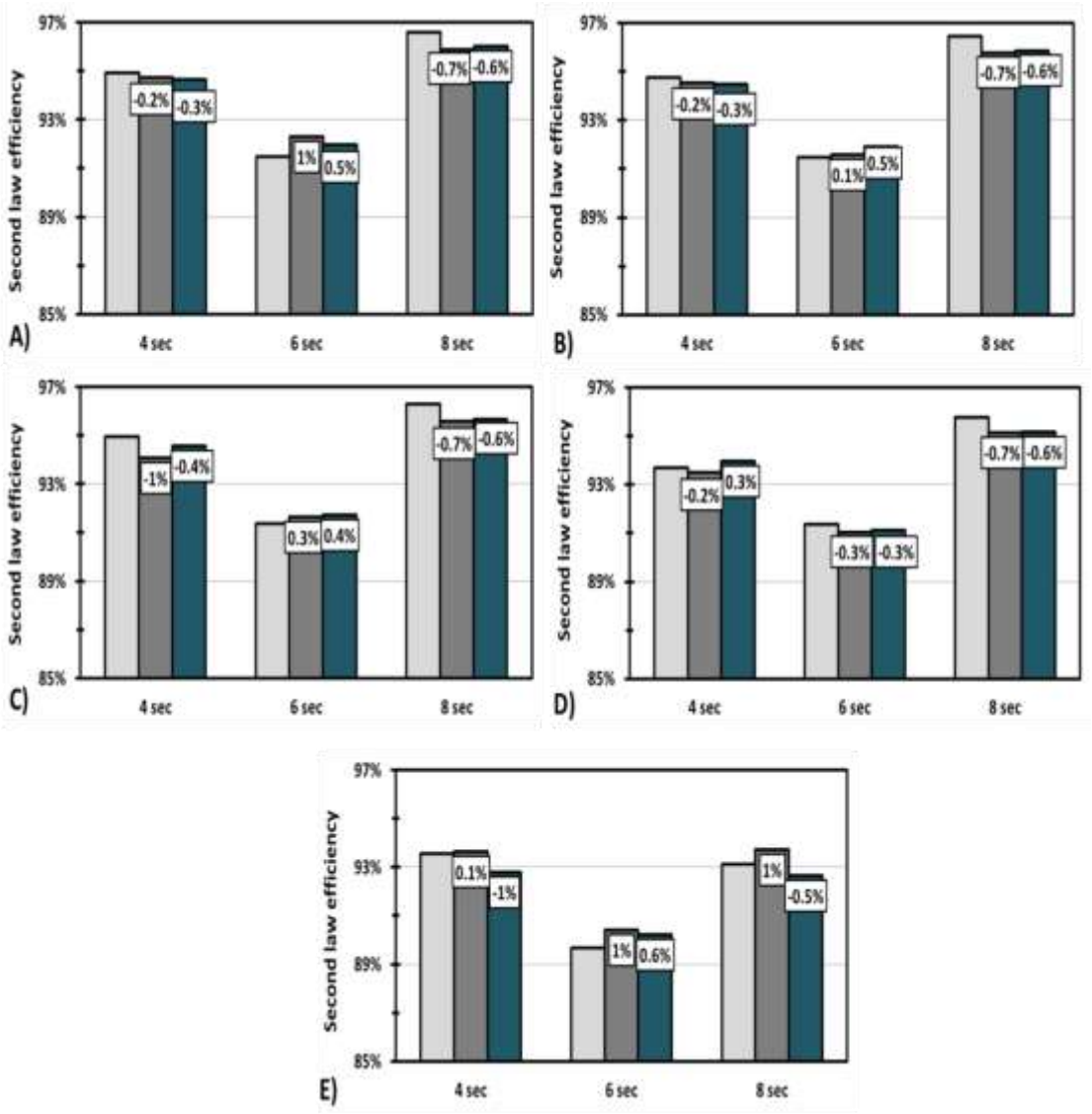

Figure 6.67 The second law efficiency at the compression cycle for the NACA0015 without and with suction slot " without suction slot α_{ss} =0 degree"," α_{ss} =10 degrees clockwise A) 11.3 B) 11.7 C) 12.3 D) 13.6 E) 14.4

The effect of suction slot on the separation layer at the end of blade (Figure 6.68 A) can be noted at the different time periods from the path lines coloured by mean velocity magnitude around the NACA0015 at 1.8 m/s velocity for the decelerating flow and at angle of attack of 13.6 degrees (stall angle). More than that, both the low pressure zones and the difference between the upper and lower surface were decreased especially for the slot with α_{ss} equal to 10 degrees clockwise at different time periods, see Figures 6.68 B and C. It can be noted that from Figure 6.69 the suction slots have a negative effect on the entropy generation at the different time periods. However, the suction slot with α_{ss} equal to 10 degrees clockwise has the lower S_G value with an increase of only 10% before the stall and 14% after the stall than the NACA0015 without suction slot by under sinusoidal wave with time period equal to 4 seconds. In addition, it has the lowest value under sinusoidal wave with time period equal to 8 seconds with an increase than the NACA0015 without suction slot by 16% before the stall and 18% after the stall.

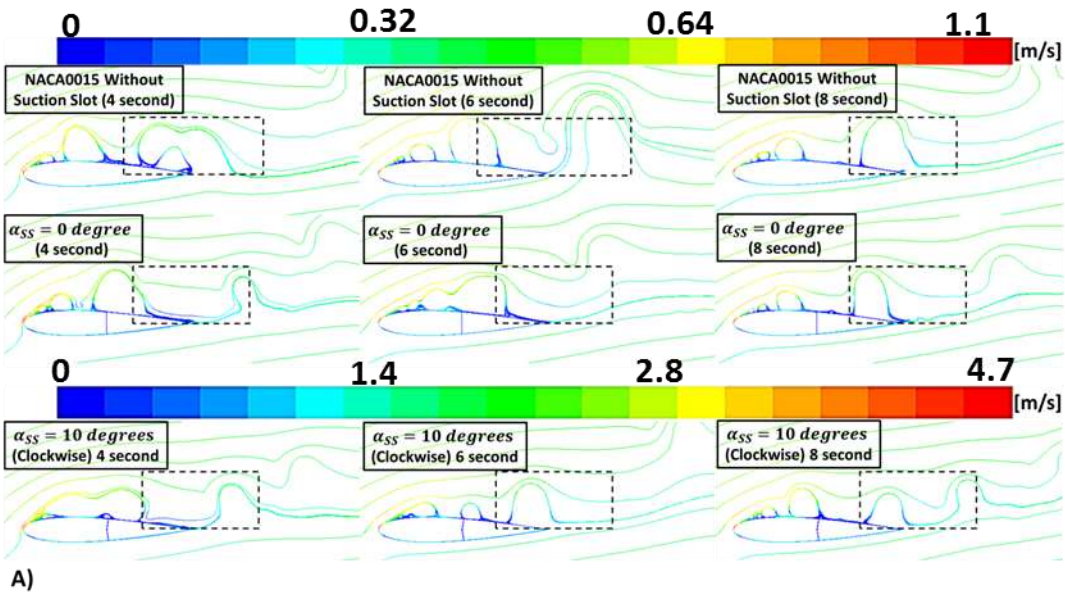

A)

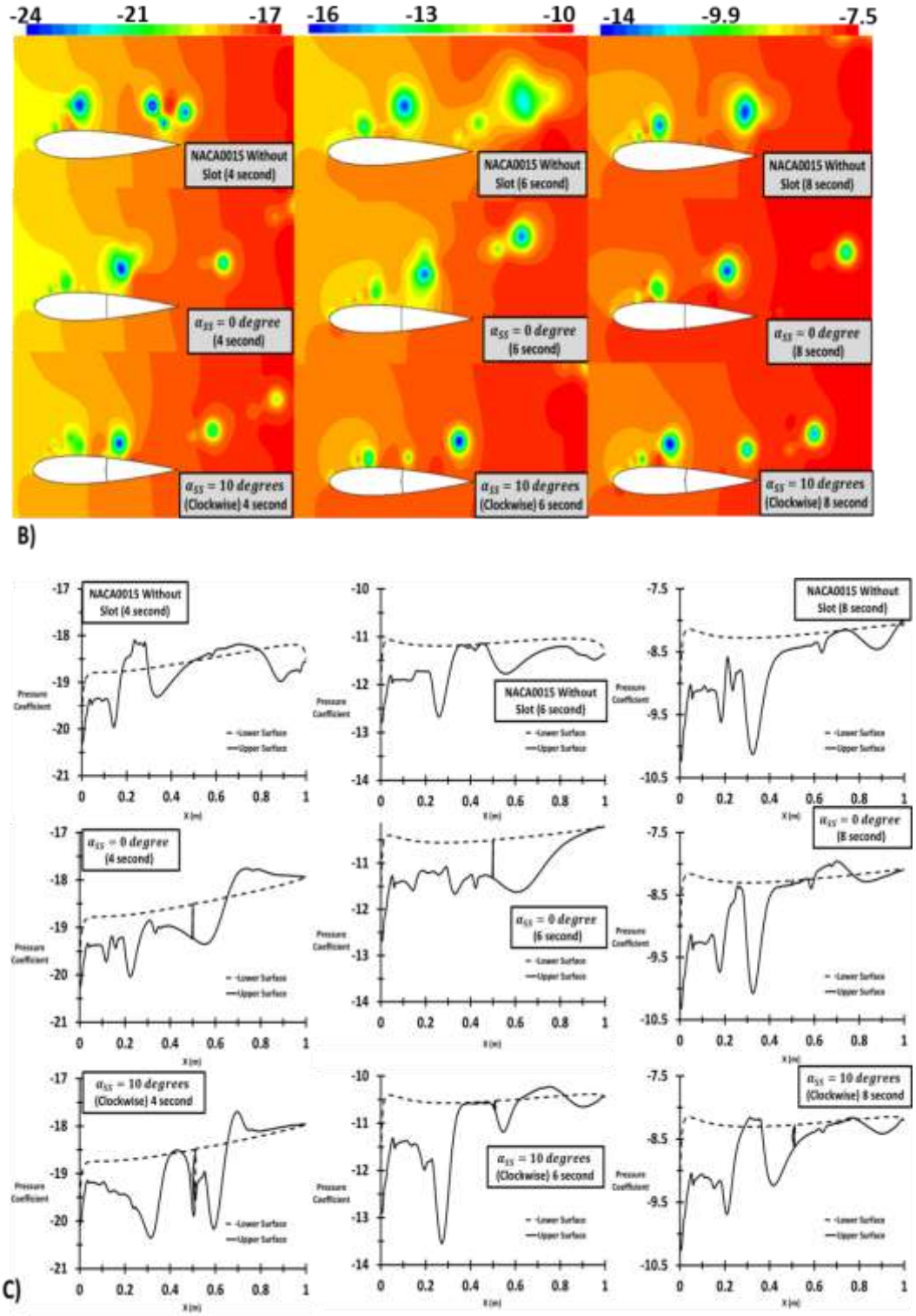

Figure 6.68 Flow structure around the NACA0015 A) Path-line coloured by mean velocity magnitude B) Contour of pressure coefficient C) pressure distribution at upper and lower surface

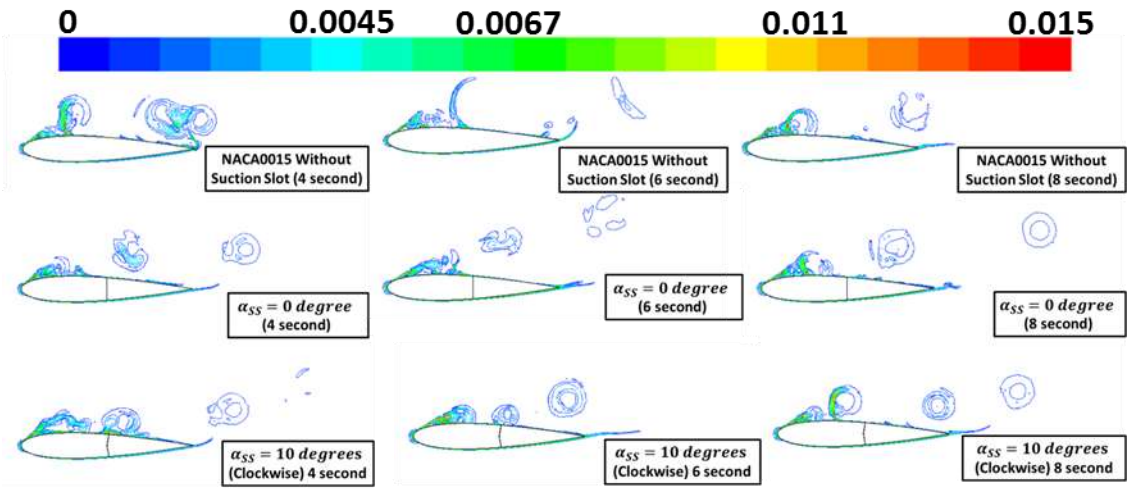

Figure 6.69 The sinusoidal flow around NACA0015 without slot and with the optimum angle of suction slot at decelerating flow A) Path-line coloured by mean velocity magnitude B) Contour of global entropy generation rate

6.5 Summary

In this chapter, the performance of Wells turbine at stall and near-stall conditions can be radically improved by using passive flow control methods, such as single and multi-suction slots in addition to the suction slot with different angles. This was achieved by conducting CFD based first and second law analysis for the Wells turbine aerofoil, without and with suction slot, under oscillating and non-oscillating flow conditions. Furthermore, the turbine blade with optimum suction slot number, location and angle was investigated using the oscillating water system based on the real data from the northern coast of Egypt.

Based on the result from this chapter it can noted that the best design for the aerofoil (NACA0015) based on the torque coefficient value is that one with three slots at L_{ss} 40%, 55% and 90% by 38.9% improvement in C_T. Furthermore, the best design based on the global entropy generation rate value is that one with two slots at L_{ss} 40% and 45% by 20.5% increase in S_G. Finally, the best design for the aerofoil (NACA0015) based on both the torque coefficient and the global entropy generation rate value is that

one with single slot with α_{ss} equal to 10 degrees clockwise by 32.5% improvement in C_T and by 21.5% increase in S_G.

The output publications from this chapter are: 1) "Improvement of the performance of air turbine for wave energy conversion using first and second law analysis" under review in Ocean Engineering, 2) "Enhancement of performance of wave turbine during stall using passive flow control: first and second law analysis" under review in Renewable Energy, and 3) "Improvement of aerodynamic performance of axial turbines for wave energy extractor" under review in Applied Ocean Research.

PART IV Conclusions and Future Work

Chapter 7 Conclusions and Future Work

7.1 Conclusions remarks

The majority of the studies in the literature, that focus on the performance of different Wells turbine designs and different operational conditions, were analysing the problem based only on the parameters of the first law of thermodynamic. This fundamental method is essential from a conservation of energy point of view; however it may be inconclusive on a vital question from a natural systems point of view: "How might the second low analysis and the entropy generation be related to the Wells turbine performance improvement under sinusoidal inlet velocity condition?" The answers to this question were sought in this research, and novel contributions were made to the state-of-the-art knowledge.

Second law analysis of Wells turbine required an accurate estimation of flow irreversibilities around the turbine blades. This can be effectively done via accurate CFD models. Two-dimensional incompressible unsteady flow simulations of different aerofoils demonstrated that the geometry, as well as the operating conditions, has radical effects on the total entropy generation in the flow around turbine aerofoil. The results have evidently shown that the entropy generation minimization is an important measure for improving the aerodynamics, hence overall performance, of Wells turbine.

It was evidently seen in Chapter 5 that the relationship between Reynolds number and the global entropy generation rate (S_G) does not have a direct correlation. However, by comparing between NACA0012, NACA0015, NACA0020, and NACA0021, it was found that increasing Reynolds number from 1.2×10^5 to at 1.7×10^5 (2×10^5 for NACA0012 in compression cycle) results in a drop in the maximum global entropy generation rate up to 50%. It was found that NACA0015 gives a lower global entropy generation rate and a higher efficiency compared to other aerofoils. For the four different aerofoils, the second law efficiency in compression cycle is higher than that in

suction cycle at 2 degree angle of attack. On the other hand, when the angle of attack increases, the efficiency for the suction cycle increases and exceeds that of the compression cycle. For angles of attack lower than 2 degrees, a higher global entropy generation rate was predicted compared to higher angles of attack. From the study of the flow behaviour around the four different aerofoils, NACA0015 was found to provide a better entropy generation rates for most of the tested operating conditions, however not in all conditions. For example, at maximum Reynolds number, NACA0012 gives a lower global entropy generation rate than NACA0015 and NACA0020 gives the minimum value among the four aerofoils. Therefore, it is recommended to create an optimum design aerofoil that gives better results at all operating conditions. In general, the global entropy generation rate due to viscous dissipation is a very sensitive indicator of aerofoil behaviour for any change in design parameters, operating conditions, and flow direction.

Furthermore, Chapter 5 was also investigating the Wells turbine under operating condition based on the real data relevant to northern coast of Egypt, via a study on the first law analysis (torque coefficient) and second law analysis (global entropy generation rate - S_G) for different turbine aerofoils. It can be noted that NACA0015 has the lowest value of S_G at the three different t_{sin} (4 sec, 6 sec and 8 sec) by 14%, 10.3% and 14.7%, respectively as an average value. On the other hand, for NACA0015, the lowest S_G was generated when t_{sin} was equal to 8 sec with an average of 4.5% less $S_G$than that of t_{sin} equal to 4 and 6 sec.

In Chapter 6, several cases were solved to determine 1) optimum suction slot location and diameter, 2) optimum location and number for multi-suction slots, and 3) optimum angle for single-suction slot based on the first and second law of thermodynamics. They aimed to investigate the effect of aerofoil with those optimum parameters on the entropy generation due to viscous dissipation as well as the torque coefficient and stall condition. After that, the comparative analysis based on real data relevant to northern coast of Egypt was applied using the aerofoil with optimum suction slot parameters.

The modelling results show that D_{ss} and L_{ss} have different effects on the torque coefficient and stall condition. Therefore, not all parameters tested in the present study achieve positive effect in terms of improved blade torque. In general, it can be concluded that the decrease in D_{ss} comes with an increase in torque coefficient. The smallest tested D_{ss} is 0.1% of the chord length, since any smaller value would not be practical in real industries. Also, the best L_{ss} is located at 45 % from the leading edge for stall angle of 13.6 degrees. By applying these conditions, we can achieve a 53% increase in the torque coefficient at the same stall angle. The increase in torque coefficient, due to adding a single suction slot, ranges from 11% to 26% before the stall regime and from 32% to 53% after the stall regime.

Another outcome of this chapter was determining the optimum locations for two-suction slots aerofoil (L_{ss} of 40% and 44%), for three-suction slots aerofoil (L_{ss} of 40%, 55% and 90%), and for four-suction slots aerofoil (L_{ss} of 40%, 45%, 55%, and 60%). The three-suction slots aerofoil with L_{ss} of 40%, 55% and 90% gives the highest torque coefficient with 26.7% before the stall and 51% after the stall when compared to the aerofoil without suction slots. On the other hand, the two-suction slots aerofoil with L_{ss} of 40% and 45% gives the highest second law efficiency by 0.72% compared to the aerofoil without suction slots. The aerofoils with optimum locations for multi-suction slots under conditions relevant to northern coast of Egypt with different wave frequencies were investigated. For NACA0015, adding three-suction slots at optimum locations (L_{ss} of 40%, 55% and 90%) mostly gives a torque coefficient higher than that of adding two suction slots at optimum locations (L_{ss} of 40% and 45%) for different t_{sin} (4, 6 and 8 second). However, adding two-suction slots at optimum locations (L_{ss} of 40% and 45%) always gives a second law efficiency higher than that of adding three-suction slots at optimum locations (L_{ss} of 40%, 55% and 90%) for different t_{sin} (4, 6 and 8 second).

In addition, the optimum angle for single suction slot aerofoil, added at the middle of the chord, is 10 degrees clockwise, where it gives the highest improvement in the torque

coefficient by 21% before the stall and 44% after the stall when compared to the aerofoil without suction slots. Also, this optimum angle gives a higher torque coefficient by 3% before the stall and 15% after the stall when compared to the 0 degree clockwise single suction slot aerofoil. On the other hand, it gives a lower global entropy generation rate than the suction slot with 0 degree by 4% before the stall and 3% after the stall. The aerofoils with optimum suction slot angle under conditions relevant to northern coast of Egypt with different wave frequencies were investigated. It was found that the suction slot with angle equal to 10 degrees clockwise gives a higher torque coefficient and a lower global entropy generation rate than the suction slot with angle equal to 0 degree at different t_{sin} (4, 6 and 8 second) before and after the stall.

The main reason behind the improvement in the torque coefficient after the stall is due to the delay of stall condition. The suction slot increases the torque coefficient and delays the stall angle which further leads to an increase of first law efficiency. On the other hand, it increases the entropy generation rate which leads to decreasing the second law efficiency. The main reason also behind this increase in the entropy generation rate is due to the increases in velocity magnitude around the aerofoil lead to increase also in the entropy generation. Where, the entropy value depends on the velocity gradient. Thus, if the turbine operates under high flow coefficient (high angle of attack), it is strongly recommended to add suction slots to improve the performance at the stall condition. Otherwise, if the turbine is not operating under high flow coefficient, it may not be effective to add suction slots. In addition, if the turbine is under the passive flow control by using the suction slot, it is strongly recommended to use the suction slot with the optimum parameters achieved in this study to improve the performance at the stall condition while minimizing the increase in entropy generation.

7.2 Suggestions for further research

Due to the limited research period and limited calculation resources, the present study cannot cover every relevant topic. Based on the results of the present study, the following items have been pointed out as recommendations for future research.

1- At the present study, the optimization parameters have been varied within a certain range with a fixed increment and all parameter values have been analysed. An alternative approach that could save time and effort would be to use an automated optimization technique, such as greedy algorithm, which picks a certain population of samples and predicts what scenarios to run.

2- The slot with angle not equal to zero gives very promising results than that with zero angle, where, the torque coefficient at the stall condition is increase and also minimizes the entropy generation. Therefore, the multi slots with angle not equal to zero could also be carried out in the next step.

3- Future work could investigate the characteristics of entropy generation around different blade designs under unsteady three-dimensional flows with a special emphasis on the viscous dissipation term and its production limits.

4- Multi-suction slots and their angles in the third direction (Z axis) are necessary to be calculated in future work via three-dimensional simulation.

5- Wells turbine impeller using the suction slot with optimum parameters needs to be investigated experimentally in the future.

References

A. STODOLA 1910. Steam and Gas Turbines (McGraw-Hill, New York).

ACıKKALP, E., ARAS, H. & HEPBASLI, A. 2014a. Advanced exergoenvironmental assessment of a natural gas-fired electricity generating facility. Energy Conversion and Management, 81, 112-119.

ACıKKALP, E., ARAS, H. & HEPBASLI, A. 2014b. Advanced exergy analysis of a trigeneration system with a diesel–gas engine operating in a refrigerator plant building. Energy and Buildings, 80, 268-275.

ADEYINKA O., N. G. 2005. Entropy-based metric for component-level energy management: application to diffuser performance. International Journal of Energy Research 29, 1007-1024.

AHMADI, A. & EHYAEI, M. 2009. Exergy analysis of a wind turbine. International Journal of Exergy, 6, 457-476.

AHMED, N. & MUELLER, M. 2013. Impact of varying clearances for the Wells turbine on heat transfer from electrical generators in oscillating water columns. Eighth International Conference and Exhibition on Ecological Vehicles and Renewable Energies (EVER). Monte Carlo, Monaco.

AL-AJMI, R. M., SYRED, N., BOWEN, P., KHALATOV, A. & AL-SHAGHDARI, M. A. 1998. A comparison of CFD and LDA studies of internal vortex cooling systems for turbine blades. Journal of Flow Visualization and Image Processing, 5, 197-210.

ALAIN CLE´MENT , P. M., ANTO´NIO FALCA˜O,, ANTONIO FIORENTINO , F. G., KARIN HAMMARLUND,, GEORGE LEMONIS, T. L., KIM NIELSEN,, SIMONA PETRONCINI, M.-T. P., PHILLIPPE SCHILD,, BENGT-OLOV SJO¨STRO¨M, H. C. S. & THORPE, T. 2002. Wave energy in Europe: current status and perspectives. Renewable and Sustainable Energy Reviews, 6, 405–431.

ALFEREZ, N., MARY, I. & LAMBALLAIS, E. 2013. Study of Stall Development Around an Airfoil by Means of High Fidelity Large Eddy Simulation. Flow, Turbulence and Combustion, 91, 623-641.

ALLEN, J. N. & GERALD, E. 1947. The effect of compressibility on the growth of the laminar boundary layer on low-drag wings and bodies. NACA TN-1255.

ALMUTAIRI, J., ALQADI, I. & ELJACK, E. 2015. Large Eddy Simulation of a NACA-0012 Airfoil Near Stall. 20, 389-395.

AMITAY, M., HONOHAN, A., TRAUTMAN, M. & GLEZER, A. 1997. Modification of the Aerodynamic Characteristics of Bluff Bodies Using Fluidic Actuators.

AIAA-97-2004, 28th AIAA Fluid Dynamics Conference, June 29 – Jul. 2, Snowmass Village, CO.

AMUNDARAIN, M., ALBERDI, M., GARRIDO, A. J., GARRIDO, I. & MASEDA, J. 2010. Wave energy plants: Control strategies for avoiding the stalling behaviour in the Wells turbine. Renewable Energy, 35, 2639-2648.

ANDREJ HORVATA, I. K., JURE MARNB 2001. Two dimensional large eddy simulation of turbulent natural convection due to internal heat generation. international journal of heat and mass transfer, 44, 3985–3995.

ARMENIO, V., GEURTS, B. & FRöHLICH, J. 2010. Large Eddy Simulation of Flow Around an Airfoil Near Stall. 13, 541-545.

ASHVINKUMAR CHAUDHARI, ANTTI HELLSTEN, OXANA AGAFONOVA & HäMäLäINEN, J. 2012. Large Eddy Simulation of Boundary-Layer Flows over Two-Dimensional Hills. Industrial Mathematics at ECMI 2012. Springer International Publishing Switzerland 2014.

AVDIS, A., LARDEAU, S. & LESCHZINER, M. 2009. Large Eddy Simulation of Separated Flow over a Two-dimensional Hump with and without Control by Means of a Synthetic Slot-jet. Flow, Turbulence and Combustion, 83, 343-370.

AYAT, B. 2013. Wave power atlas of Eastern Mediterranean and Aegean Seas. Energy, 54, 251-262.

B. YAGIZ, KANDIL, O. & PEHLIVANOGLU, Y. V. 2012. Drag minimization using active and passive flow control techniques. Aerospace Science and Technology, 17, 21-31.

BARSTOW, S., MøRK, G., LøNSETH, L. & MATHISEN, J. P. 2009. WorldWaves wave energy resource assessments from the deep ocean to the coast. The 8th European Wave and Tidal Energy Conference. Uppsala, Sweden: Proceedings of the 8th European Wave and Tidal Energy Conference.

BASKUT, O., OZGENER, O. & OZGENER, L. 2011. Second Law Analysis of Wind Turbine Power Plants: Cesme, Izmir Example. Energy, 36, 2535-2542.

BEJAN, A. 1988. Advanced Engineering Thermodynamics (Wiley, New York).

BEJAN, A. 1996. Entropy Generation Minimization- The New Thermodynamics of Finite-Size Devices and Finite-Time Processes. Applied Physics Reviews, 79, 1191-1218.

BELFAST, T. Q. S. U. O. 2002. Islay LIMPET Wave Power Plant, Non-nuclear Energy Programme Joule III, CORDIS, JOR3-CT98-0312.

BERTON, E., FAVIER, D., MARESCA, C. & BENYAHIA, A. 2002. Flow field visualizations around oscillating airfoils. Report UMSR, 2164.

BIRNIR, B. 2013. The Kolmogorov-Obukhov Theory of Turbulence: A Mathematical Theory of Turbulence, Springer New York.

BOAKE, C. B., WHITTAKER, T. J. T., FOLLEY, M. & ELLEN, H. 2002. Overview and Initial Operational Experience of the LIMPET Wave Energy Plant. The Twelfth International Offshore and Polar Engineering Conference. Kitakyushu, Japan: The International Society of Offshore and Polar Engineers.

BOGART, W. T., MORRISS, A. P., MEINERS, R. E. & DORCHAK, A. 2011. The Challenge of Green Energy. The False Promise of Green Energy. U.S.A.: Cato Institute.

BOSE, B. K. 2002. Modern Power Electronics and AC Drives, United States of America, Prentice-Hall, Inc.

BOUSSINESQ, J. 1877. Théorie de l'Écoulement Tourbillant. Mem. Présentés par Divers Savants Acad. Sci. Inst. Fr., 23, 46-50.

BRAGG, M. B. & GREGOREK, G. M. 1987. Experimental Study of Airfoil Performance with Vortex Generators. Journal of Aircraft, 24, 305-309.

BRITO-MELO, A., GATO, L. M. C. & SARMENTO, A. J. N. A. 2002. Analysis of Wells turbine design parameters by numerical simulation of the OWC performance. Ocean Engineering, 29, 1463–1477.

BROMBY, D. Y. A. W. 2012. Large-Eddy Simulation of Unsteady Separation Over a Pitching Airfoil at High Reynolds Number. Seventh International Conference on Computational Fluid Dynamics (ICCFD7). Big Island, Hawaii.

BUSHNELL, D. M. & MCGINLEY, C. B. 1989. Turbulence Control in Wall Flows. Annual Review of Fluid Mechanics, 21, 1-20.

C.E.TINDALL & XU, M. 1996. Optimising a Wells-turbine-type wave energy system. IEEE Transactions on Energy Conversion, 11, 631 - 635.

CAMPOREALE, S. M. & FILIANOTI, P. 2009. Behaviour of a small Wells turbine under randomly varying oscillating flow. the 8th European Wave and Tidal Energy Conference EWTEC. Uppsala, Sweden.

CAMPOREALE, S. M., FILIANOTI, P. & TORRESI, M. 2011. Performance of a Wells turbine in a OWC device in comparison to laboratory tests. the Ninth European Wave and Tidal Energy Conference (EWTEC). Southampton, UK.

CARIJA, Z., KRANJCEVIC, L., V.BANIC & M.CAVRAK 2012. NUMERICAL ANALYSIS OF WELLS TURBINE FOR WAVE POWER CONVERSION. Engineering Review, 32, 141-146.

CARR, L. W. 1988. Progress in Analysis and Prediction of Dynamic Stall. J. Aircraft, 25, 6-17.

CELIK, I., CEHRELI, Z. & YAVUZ, I. 2005. Index of resolution quality for large eddy simulations. Journal of fluids engineering, 127, 949-958.

CHANDRASEKHARA, M. & AHMAD, S. 1991. Laser velocimetry measurements of oscillating airfoil dynamic stall flow field. AIAA 22nd Fluid Dynamics, Plasma Dynamics & Lasers Conference. DTIC Document.

CHAPIN, V. G. & BENARD, E. 2015. Active Control of a Stalled Airfoil Through Steady or Unsteady Actuation Jets. Journal of Fluids Engineering, 137, 091103.

CHAWLA, J. S., SURYANARAYANAN, S., PURANIK, B., SHERIDAN, J. & FALZON, B. G. 2014. Efficiency improvement study for small wind turbines through flow control. Sustainable Energy Technologies and Assessments, 7, 195-208.

CHEN, Q. & GLATZMAIER, G. A. 2005. Large eddy simulations of two-dimensional turbulent convection in a density-stratified fluid. Geophysical & Astrophysical Fluid Dynamics, 99, 355-375.

CHENG, W.-C. & PORTE-AGEL, F. 2013. Evaluation of subgrid-scale models in large-eddy simulation of flow past a two-dimensional block. International Journal of Heat and Fluid Flow, 44, 301-311.

CHRISTIAN TENAUD & PHUOC, L. T. 1997. Large eddy simulation of unsteady, compressible, separated flow around NACA 0012 airfoil. Fifteenth International Conference on Numerical Methods in Fluid Dynamics.

CHRISTOPHER KORONEOS, THOMAS SPACHOS & MOUSSIOPOULOS, N. 2003. Exergy analysis of renewable energy sources. Renewable Energy, 28, 295–310.

CHUNG, T. N. H. & LIU, C.-H. 2013. On the Mechanism of Air Pollutant Removal in Two-Dimensional Idealized Street Canyons: A Large-Eddy Simulation Approach. Boundary-Layer Meteorology, 148, 241-253.

COE, D. L., ALLEN, M. G., SMITH, B. L. & GLEZER, A. 1995. Addressable Micro-machined Jet Arrays. Transducers ’95, Stockholm, Sweden, June 25-29.

COLLIS, S., JOSLIN, R. D., SEIFERT, A. & THEOFILIS, V. 2004. Issues in active flow control: theory, control, simulation and experiment. Progress in Aerospace Sciences, 40, 237-289.

CRABTREE, L. 1958. Prediction of Transition in the Boundary Layer of An Aerofoil. Journal of Royal Aeronautical Society, 62, 525-537.

CRIMI, P., YAGGY, P. F. 1972. Dynamic stall. In: AGARD-AG-172 (ed.). Paris, France.: Advisory Group for Aerospace Research and Development (North Atlantic Treaty Organisation).

CRUZ, J. 2008. OceanWave Energy, Verlag Berlin,Heidelberg, springer.

CSANADY, G. T. 1964. Theory of turbomachines, London., McGraw-Hill.

CURLE, N. & S., S. 1957. Approximate Methods for Predicting Properties of Laminar Boundary Layers. Aeronautical Quarterly, 8, 257-268.

CURRAN, R. 2008. Ocean Wave Energy Systems Design: Conceptual Design Methodology for the Operational Matching of the Wells Air Turbine. the 15th ISPE International Conference on Concurrent Engineering Belfast, Northern Ireland: Springer London.

CURRAN, R. & M. FOLLEY 2008. Air turbine design for OWCs. In: CRUZ, I. J. (ed.) Ocean Wave Energy. Springer, Berlin. .

CURRAN, R., WHITTAKER, T. J. T., RAGHUNATHAN, S. & BEATTIE, W. C. 1998. Performance Prediction of Contrarotating Wells Turbines for Wave Energy Converter Design. Journal of Energy Engineering, 124, 35-53.

DAHLSTROM, S. 2003. LARGE EDDY SIMULATION OF THE FLOW AROUND A HIGH-LIFT AIRFOIL. DOCTOR OF PHILOSOPHY, CHALMERS UNIVERSITY OF TECHNOLOGY.

DAVIDSON, P. A. 2004. Turbulence: an introduction for scientists and engineers, New York, United States of America, Oxford University Press.

DBEDT 2002. Feasibility of Developing Wave Power as Renewable Energy Resource for Hawaii. Honolulu - State of Hawaii: Department of Business, Economic Development and Tourism (DBEDT)

DE MOURA, C. A. K., CARLOS S. 2013. The Courant–Friedrichs–Lewy (CFL) Condition: 80 Years After Its Discovery, Boston, Birkhäuser Basel.

DHANASEKARAN, T. S. & GOVARDHAN, M. 2005. Computational Analysis of Performance and Flow Investigation on Wells Turbine for Wave Energy Conversion. Renewable Energy, 30, 2129-2147.

DINCER, I. & ROSEN, M. 2005. Thermodynamic aspects of renewable and sustainable development. enewable and Sustainable Energy Reviews 2005, 169-189.

DIXON, S. L. 1998. Fluid Mechanics, Thermodynamics of Turbomachinery, Pergamon Press Ltd.

DK., L. 1992. A proposed modification of the Germano subgrid-scale closure method. Physics Fluids A, 4, 633–5.

EIAMSA-ARD, S. & PROMVONGE, P. 2007. Numerical investigation of the thermal separation in a Ranque-Hilsch vortex tube. International Journal of Heat and Mass Transfer, 50, 821-832.

EKATERINARIS, J. A. & MENTER, F. R. 1994. Computation of oscillating airfoil flows with one- and two-equation turbulence models. AIAA Journal, 32, 2359-2365.

ERBAY, Z. & HEPBASLI, A. 2014. Advanced exergoeconomic evaluation of a heat pump food dryer. Biosystems Engineering, 124, 29-39.

ERICSSON, L. E. A. R., J.P. 1987. Fluid Dynamics of Unsteady Separated Flow, Part II. Lifting Surface. Prog. Aerospace Sci., 24, 249-356.

FALCAO, A. F. D. 2000. The shoreline OWC wave power plant at the Azores. Proceedings of 4th European Wave Energy Conference. Denmark.

FALCAO, A. F. D. 2002. Control of an oscillating-water-column wave power plant for maximum energy production. Applied Ocean Research 24.

FALCAO, A. F. D. 2003. Control of an oscillating-water-column wave power plant for maximum energy production. Applied Ocean Research, 24, 73-82.

FALCAO, A. F. D. 2004. Stochastic Modelling in wave power-equipment optimisation: maximum energy production versus maximum profit. Ocean Engineering, 31, 1407-1421.

FALCãO, A. F. D. O. 2010. Wave energy utilization: A review of the technologies. Renewable and Sustainable Energy Reviews, 14, 899-918.

FALCAO, A. F. D. O. J., P.A.P. 1999. OWC wave energy devices with air flow control. Ocean Engineering, 26, 1275-1295.

FALCAO, A. F. D. S., M.; WHITTAKER, T.J.T. & LEWIS, A.W. 1995. Design of a shoreline wave power plant for the island of Pico, Azores. Proceedings of the 2nd European Wave Power Conference.

FALCãO, A. F. O. & GATO, L. M. C. 2012. Air Turbines. In: SAYIGH, A. A. (ed.) Comprehensive Renewable Energy Ocean Energy, Elsevier,Oxford .

FERNANDEZ, E., KUMAR, R. & ALVI, F. 2013. Separation Control on a Low-Pressure Turbine Blade using Microjets. Journal of Propulsion and Power, 29, 867-881.

FIEDLER, H. E. & FERNHOLZ, H.-H. 1990. On Management and Control of Turbulent Shear Flows. Progress in Aerospace Sciences, 27, 305-387.

FOLLEY, M., CURRAN, R. & WHITTAKER, T. 2006. Comparison of LIMPET Contra-rotating Wells Turbine with Theoretical and Model Test Predictions. Ocean Engineering, 33, 1056-1069.

FRISCH, U. & KOLMOGOROV, A. N. 1995. Turbulence: The Legacy of A. N. Kolmogorov, Cambridge University Press.

FUREBY, C. 2017. Challenges for Large Eddy Simulation of Engineering Flows. Whither Turbulence and Big Data in the 21st Century? : Springer.

GAD-EL-HAK, POLLARD & BONNET 1998. Flow Control: Fundamentals and Practices, Springer-Verlag Berlin Heidelberg.

GAD-EL-HAK, M. 1994. Interactive Control of Turbulent Boundary Layers: A Futuristic Overview. AIAA Journal, 32, 1753-1765.

GAD-EL-HAK, M. 2000. Flow Control: Passive, Active and Reactive Flow Management Cambridge University Press.

GAD-EL-HAK, M. 2001. Flow Control: The Future. Journal of Aircrafts, 38.

GAD-EL-HAK, M. & BUSHNELL, D. M. 1991. Separation Control: Review. Journal of Fluids Engineering, 113, 5-30.

GAREEV, A., KOSASIH, B. & COOPER, P. 2013. Analysis of interference factors of air turbine cascades. Engineering Applications of Computational Fluid Mechanics, 7, 496-506.

GATO, L. M. C. & CURRAN, R. 1996. Performance of the Contrarotating Wells Turbine. International Journal of Offshore and Polar Engineering, 6, 68-75.

GATO, L. M. C. & CURRAN, R. 1997. The Energy Conversion Performance of Several Types of Wells Turbine Designs. Proceedings of the Institution of Mechanical Engineers, Part A: Journal of Power and Energy, 211, 133-145.

GATO, L. M. C. & FALCAO, A. F. O. 1988. Aerodynamics of the Wells Turbine. International Journal of Mechanical Sciences, 30, 383-395.

GATO, L. M. C., HENRIQUES, J.C.C. 1996. Optimization of symmetrical profiles for Wells turbine rotor blades. Proceedings of the ASME Fluids Engineering Division Summer Meeting, , FED-238, 623–630.

GATO, L. M. C. & WEBSTER, M. 2001. An experimental investigation into the effect of rotor blade sweep on the performance of the variable-pitch Wells turbine. Journal of Power and Energy, 215 Part A, 611-622.

GENC, M. S., KEYNAK, U. & YAPICI, H. 2011. Performance of transition model for predicting low re aerofoil flows without/with single and simultaneous blowing and suction. European Journal of Mechanics B/Fluids, 30, 218-235.

GEORGIADIS, N. J., RIZZETTA, D. P. & FUREBY, C. 2010. Large-eddy simulation: current capabilities, recommended practices, and future research. AIAA journal, 48, 1772-1784.

GHISU, T., PUDDU, P. & CAMBULI, F. 2015. Numerical analysis of a wells turbine at different non-dimensional piston frequencies. Journal of Thermal Science, 24, 535-543.

GILARRANZ, J. L. & REDINIOTIS, O. K. 2001. Compact, High-Power Synthetic Jet Actuators for Flow Separation Control. 39th AIAA Aerospace Sciences Meeting and Exhibit, 2001-0737.

GILARRANZ, J. L., YUE, X. & REDINIOTIS, O. K. 1998. PIV Measurements and Modeling of Synthetic Jet Actuators for Flow Control. Proceedings of FEDSM'98, ASME Fluids Engineering Meeting.

GLEIZE, V., SZYDLOWSKI, J. & COSTES, M. 2004. Numerical and physical analysis of turbulent viscous flow around a NACA 0015 profile at stall. ONERA, 92, 1-20.

GLEZER, A. 1999. Shear Flow Control Using Fluidic Actuator Technology. Proceedings of the 1st Symposium on Smart Control of Turbulence, Tokyo, Japan.

GLEZER, A., ALLEN, M. G., COE, D. J., BARTON, S. L., TRAUTMAN, M. A. & WILTSE, J. W. 1998. Synthetic Jet Actuator and Applications Thereof.

GONG, S. & GONI BOULAMA, K. 2014. Parametric study of an absorption refrigeration machine using advanced exergy analysis. Energy, 76, 453-467.

GREENBLATT, D. & WYGNANSKI, I. J. 2000. Control of flow separation by periodic excitation. Progress in Aerospace Sciences, 36, 487-545.

GREGORY, N. & O'REILLY, C. 1970. Low-speed aerodynamic characteristics of NACA 0012 aerofoil section, including the effects of upper-surface roughness simulating hoar frost, National Physical Laboratory Teddington, England.

GU, W., ROBINSON, O. & ROCKWELL, D. 1993. Control of vortices on a delta wing by leadingedge injection. AIAA Journal, 31, 1177-1186.

HALDER, P. & SAMAD, A. 2015a. Casing Treatment of a Wave Energy Extracting Turbine. Aquatic Procedia, 4, 516-521.

HALDER, P. & SAMAD, A. 2015b. Wave Energy Harvesting Turbine: Performance Enhancement. Procedia Engineering, 116, 97-102.

HALDER, P., SAMAD, A., KIM, J.-H. & CHOI, Y.-S. 2015. High performance ocean energy harvesting turbine design–A new casing treatment scheme. Energy, 86, 219-231.

HEATH, T. 2002. Islay LIMPET project monitoring, ETSU V/06/00180/00/Rep, Dti Pup URN No 02/1435.

HEATH, T., WHITTAKER, T.J.T & BOAKE, C.B. 2000. The design, construction and operation of the LIMPET wave energy converter. In: S, O. I. A. I. (ed.) the 4th European Wave Energy Conference, Danish Technological Institute, Denmark. Aalborg, Denmark.

HINZE, J. O. 1975. Turbulence, New York, McGraw-Hill Publishing Co.

HIRSCH, C. 2007. Numerical Computation of Internal and External Flows: The Fundamentals of Computational Fluid Dynamics, Elsevier Science.

HITIWADI, M., DULINI, V., MUDUNKOTUWA, Y. & CHISACHI, K. 2013. Large Eddy Simulations of 2D and Open-tip Airfoils Using Voxel Meshes. Procedia Engineering, 61, 32-39.

HOFFMANN, K. A. & CHIANG, S. T. 2000a. Computational Fluid Dynamics Volume 1, USA, A Publication of Engineering Eeducation System.

HOFFMANN, K. A. & CHIANG, S. T. 2000b. Computational Fluid Dynamics Volume 2, USA, A Publication of Engineering Eeducation System.

HORLOCK, J. H. 1958. Axial Flow Compressors, Oxford, Butterworths scientific publications.

HORLOCK, J. H. 1978. Actuator disk theory, London, McGraw-Hill International Book Co.

HRIBERNIK, A., FIKE, M., BOMBEK, G. & HRIBERSEK, M. 2012. Experimental investigation of an unsteady flow field around an airfoil. XX IMEKO World Congress, Metrology for Green Growth Busan, Republic of Korea

IA, B. 1975. Apparatus for Converting Sea Wave Energy into Electrical Energy. US Patent 3,922,739 2 December 1975.

IANDOLI, C. L. 2005. 3-D Numerical Calculation of the Local Entropy Generation Rates in a Radial Compressor Stage. International journal of thermodynamics, 8, 83-94.

IEA 2014. Medium-Term Renewable Energy Market Report 2014 : Market Analysis and Forecasts to 2020. International Energy Agency.

INOUE, M., KANEKO, K, SETOGUCHI T, AND HAMAKAWA, H 1989. Air turbine with self-pitch-controlled blades for wave power generator (Estimation of performances by model testing). JSME International Journal, Ser II, 32, 19-24.

INOUE, M., KANEKO, K., SETOGUCHI, T. AND RAGHUNATHAN, S. 1987. The fundamental characteristics and future of Wells turbine for wave power generator. Science of Machines, 39, 275-280.

JASSIM, R. 2004. Exergy analysis of carryover leakage irreversibilities of a power plant regenerative air heater. Proceedings of the Institution of Mechanical Engineers, Part A: Journal of Power and Energy, 218, 23-32.

JAYAKUMAR, NEELAMANI, S. & AND RAJU, V. S. 1993. An experimental investigation of wave forces on an oscillating water column type wave energy caisson. European Wave Energy Symposium. Edinburgh, UK.

JAYASHANKAR, V., UDAYAKUMAR, K., B.KARTHIKEYAN, MANIVANNAN, K., VENKATRAMAN, N. & RANGAPRASAD, S. 2000. Maximizing Power Output from A Wave Energy Plant. Power Engineering Society Winter Meeting, 2000. IEEE. IEEE.

JOCHMANN, P., SINIGERSKY, A., HEHLE, M., SCH¦¤FER, O., KOCH, R. & BAUER, H. J. 2006. Numerical simulation of a precessing vortex breakdown. International Journal of Heat and Fluid Flow, 27, 192-203.

JOHNSON, G. L. 2006. Wind Turbine Power. Wind Energy Systems. Second Edition ed.

KATAM, V. 2005. Simulation of low-Re flow over a modified NACA 4415 airfoil with oscillating camber. University of Kentucky.

KAWAI, S. & ASADA, K. 2013. Wall-modeled large-eddy simulation of high Reynolds number flow around an airfoil near stall condition. Computers & Fluids, 85, 105-113.

KECEBAŞ, A. & HEPBASLI, A. 2014. Conventional and advanced exergoeconomic analyses of geothermal district heating systems. Energy and Buildings, 69, 434-441.

KELLY, S., TSATSARONIS, G. & MOROSUK, T. 2009. Advanced exergetic analysis: Approaches for splitting the exergy destruction into endogenous and exogenous parts. Energy, 34, 384-391.

KIDDY, J., CHEN, P., NIEMCZUK, J., DEVOE, D. & KIGER, K. 2000. Active Flow Control using Micro-electromechanical Systems. Systems Planning and Analysis Inc., AIAA SDM Conference.

KIM, S. H. & KIM, C. 2009. Separation control on NACA23012 using synthetic jet. Aerospace Science and Technology, 13, 172-182.

KIM, T. H., SETOGUCHI, T., KANEKO, K. & RAGHUNATHAN, S. 2002a. Numerical investigation on the effect of blade sweep on the performance of Wells turbine. Renewable Energy, 25, 235-248.

KIM, T. H., SETOGUCHI, T., KINOUE, Y., KANEKO, K. & INOUE, M. 2002b. Hysteretic Characteristics of Wells Turbine for Wave Power Conversion. The Twelfth International Offshore and Polar Engineering Conference. Kitakyushu, Japan: The International Society of Offshore and Polar Engineers.

KIM, Y., CASTRO, I. P. & XIE, Z. T. 2015. Large-Eddy Simulations for Wind Turbine Blade: Dynamic Stall and Rotational Augmentation. 20, 369-375.

KINOUE, Y., KIM, T. H., SETOGUCHI, T., MOHAMMAD, M., KANEKO, K. & INOUE, M. 2004. Hysteretic Characteristics of Monoplane and Biplane Wells Turbine for Wave Power Conversion. Energy Conversion and Management, 45, 1617-1629.

KINOUE, Y., SETOGUCHI, T., KIM, T. H., KANEKO, K. & INOUE, M. 2003a. Mechanism of Hysteretic Characteristics of Wells Turbine for Wave Power Conversion. Journal of Fluids Engineering, 125, 302.

KINOUE, Y., SETOGUCHI, T., KURODA, T., KANEKO, K., TAKAO, M. & THAKKER, A. 2003b. Comparison of Performances of Turbines for Wave Energy Conversion. Journal of Thermal Science, 12, 323-328.

KOOCHESFAHANI, M. M. 1989. Vortical patterns in the wake of an oscillating airfoil. AIAA journal, 27, 1200-1205.

KOTA, S., HETRICK, J., OSBORN, R., PAUL, D., PENDLETON, E., FLICK, P. & TILMANN, C. 2003. Design and application of compliant mechanisms for morphing aircraft structures. Proceedings of SPIE - The International Society for Optical Engineering, 5054, 24-33.

L. BAHI, J. M. R. & NAGAMATSU, H. T. 1983. Passive Shock Wave/Boundary Layer Control for Transonic Airfoil Drag Reduction. AIAA Journal, 1983-0137.

L. M. C. GATO, A. A. F. D. O. F. 1984. On the Theory of the Wells Turbine Trans. ASME: J. Eng. Gas Turbines Power. Trans.

LAUNDER, B., REECE, G. J. & RODI, W. 1975. Progress in the development of a Reynolds-stress turbulence closure. Journal of fluid mechanics, 68, 537-566.

LAUNDER, B. & SHARMA, B. 1974. Application of the energy-dissipation model of turbulence to the calculation of flow near a spinning disc. Letters in heat and mass transfer, 1, 131-137.

LAUNDER, B. E. & SPALDING, D. B. 1972. Lectures in Mathematical Models of Turbulence, London, England, Academic Press.

LAUNDER, B. E. & SPALDING, D. B. 1974. The Numerical Computation of Turbulent Flows. Computer Methods in Applied Mechanics and Engineering, 3, 269-289.

LESIEUR, M. 2008. Turbulence in Fluids, Netherlands, Springer,.

LIANG, H. 2004. Optimization of Blowing and Suction Control on NACA0012 Airfoil using Genetic Algorithm with Diversity Control. PhD Thesis, University of Kentucky.

LIU, Y., CAO, N., WANG, Q. & LI, B. 2012. Numerical Simulation of Two-Dimensional Parallel Blade-Vortex Interactions Using Large Eddy Simulation. Procedia Engineering, 31, 703-707.

LOZANO, M. A., BARTOLOME, J.L., VALERO, A., REINI, M. 1994. Thermoeconomic diagnosis of energy systems. Proceedings of the Third Florence World Energy Research Symposium. Florence: Italy.

M. TAKAO & LEE, Y. W. 2002. Air Turbine Using Self-Pitch-Controlled Blades for Wave Energy Conversion. Twelfth International Offshore and Polar Engineering Conference. Kitakyushu, Japan: The International Society of Offshore and Polar Engineers.

MAEDA, H., SETOGUCHI, T., TAKAO, M., SAKURADA, K., KIM, T. H. & KANEKO, K. 2001. Comparative study of turbines for wave energy conversion. Journal of Thermal Science, 10, 26-31.

MAMUN, M. 2006. The Study on the Hysteretic Characteristics of the Wells Turbine in a Deep Stall Condition. Doctor of Philosophy degree PhD, Saga University.

MAMUN, M., KINOUE, Y., SETOGUCHI, T., KANEKO, K. & ISLAM, A. K. M. S. 2006. Improvement af the Performance of the Wells Turbine by using a Very Thin Elongated Endplate at the Blade Tip. the 3rd BSME-ASME International Conference on Thermal Engineering. Dhaka, Bangladesh: ASME.

MAMUN, M., KINOUE, Y., SETOGUCHI, T., KIM, T. H., KANEKO, K. & INOUE, M. 2004. Hysteretic Flow Characteristics of Biplane Wells Turbine. Ocean Engineering, 31, 1423-1435.

MARIMUTHU, C. & KIRUBAKARAN, V. 2014. A critical review of factors affecting wind turbine and solar cell system power production. International Journal of Advanced Engineering Research and Studies, 3, 143-147.

MARTIN, T., GUITTON, A., SCHMIT, R. & GLAUSER, M. N. 2005. Development of a morphing micro air vehicle wing using the combined POD and LSE technique. Infotech at Aerospace: Advancing Contemporary Aerospace Technologies and Their Integration, AIAA 2005-7158.

MARTINAT, G., BRAZA, M., HOARAU, Y. & HARRAN, G. 2008. Turbulence modeling of the flow past a pitching NACA0012 airfoil at 10^5 and 10^6 Reynolds number, . Journal of Fluids and Structures, 24, 1294-1303.

MASAMI SUZUKI & ARAKAWA, C. 2002. Design Method of Wave Power Generating System with Wells Turbine. Twelfth InternationalOffshoreandPolarEngineeringConference. Kitakyushu,Japan: The International Society of Offshore and Polar Engineers.

MASKELL, E. C. 1958. Approximate Calculation of the Turbulent Boundary Layer In Two Dimensional Incompressible Flow. In: REPORT, M. O. S. (ed.).

MASTERS, G. M. 2004. Wind Power Systems. Renewable and Efficient Electric Power Systems. Hoboken, New Jersey.: John Wiley & Sons, Inc.

MATOS, A. D., PINHO, F. A. A. & SILVEIRA!NETO, A. 1999. Large-eddy simulation of turbulent ~ow over a two! dimensional cavity with temperature ~uctuations. International Journal of Heat and Mass Transfer, 42, 3848.

MAZZEI, L., ANDREINI, A., FACCHINI, B. & TURRINI, F. 2016. Impact of Swirl Flow on Combustor Liner Heat Transfer and Cooling: A Numerical Investigation With Hybrid Reynolds-Averaged Navier–Stokes Large Eddy Simulation Models. Journal of Engineering for Gas Turbines and Power, 138, 051504.

MCCORMICK, D. C., LOZYNIAK, S., MACMARTIN, D. G. & LORBER, P. F. 2001. Compact High Power Boundary Layer Separation Control Actuation Development. ASME Fluids Engineering Division Summer Meeting, New Orleans, ASME FEDSM2001-18279.

MCCORMICK, R. B. A. M. E. 2003. Wave Energy Conversion Elsevier, Ocean Engineering Series, 6, 1-187.

MCCROSKEY, W. J. 1980a. Prediction of Unsteady Separated Flows on Oscillating Airfoils. (AGARD) Advisory Group for Aerospace Research and Development. Paris, France.: AGARD Lecture Series, No.94, p. 12-1.

MCCROSKEY, W. J. 1980b. Some Unsteady Separation Problems for Slender Bodies. , No.94, p.8-1.: AGARD Lecture Series.

MCCULLOUGH, G. B. & GAULT, D. E. 1951. Examples of Three Representative Types of Airfoil- Section Stall at Low Speed. NACA TN-2502, Washington, DC.

MENTER, F. R. 1994. Two-equation eddy-viscosity turbulence models for engineering applications. AIAA Journal, 32, 1598-1605.

MEULLER, T. J., AND BURNS, T.F., " 1982. Experimental Studies of the Eppler 61 Airfoil at Low Reynolds Numbers. AIAA Journal, 82.

MICHIOKA, T., SATO, A., TAKIMOTO, H. & KANDA, M. 2010. Large-Eddy Simulation for the Mechanism of Pollutant Removal from a Two-Dimensional Street Canyon. Boundary-Layer Meteorology, 138, 195-213.

MIGUEL, A. F. & AYDIN, M. 2011. Ocean energy: exergy analysis and conversion. The Global Conferance on Global Warming. Lison, Portugal.

MOHAMED, M. H., JANIGA, G., PAP, E. & THEVENIN, D. 2011. Multi-objective Optimization of the Airfoil Shape of Wells Turbine used for Wave Energy Conversion. Energy, 36, 438-446.

MOHAMED, M. H., JANIGA, G. & TH´EVENIN, D. 2008. Performance Optimization of a Modified Wells Turbine using Non-Symmetric Airfoil Blades. Turbo Expo 2008: Power for Land, Sea and Air GT. Berlin, Germany: ASME.

MOHAMED, M. H. & SHAABAN, S. 2013. Optimization of Blade Pitch Angle of an Axial Turbine Used for Wave Energy Conversion. Energy, 56, 229-239.

MOHAMED, M. H. & SHAABAN, S. 2014. Numerical Optimization of Axial Turbine with Self-pitch-controlled Blades used for Wave Energy Conversion. International Journal of Energy Research, 38, 592–601.

MOIN, P. & BEWLEY, T. 1994. Feedback Control of Turbulence. Applied Mechanics Reviews, 47, S3-S13.

MOIN P, S. K., CABOT W, LEE S. 1991. A dynamic subgrid-scale model for compressible turbulence and scalar transport. Physics Fluids A, 3, 2746–57.

MøRK, G., BARSTOW, S., KABUTH, A. & PONTES, M. T. 2010. ASSESSING THE GLOBAL WAVE ENERGY POTENTIAL. 29th International Conference on Ocean, Offshore Mechanics and Arctic Engineering. Shanghai, China: ASME.

MOROSUK, T. & TSATSARONIS, G. 2008. A new approach to the exergy analysis of absorption refrigeration machines. Energy, 33, 890-907.

MOROSUK, T. & TSATSARONIS, G. 2011. Comparative evaluation of LNG – based cogeneration systems using advanced exergetic analysis. Energy, 36, 3771-3778.

MOROSUK, T., TSATSARONIS, G. & ZHANG, C. 2012. Conventional thermodynamic and advanced exergetic analysis of a refrigeration machine using a Voorhees' compression process. Energy Conversion and Management, 60, 143-151.

MOROSUK T., T. G., BOYANO A., GANTIVA C. 2012. Advanced exergy-based analyses applied to a system including LNG regasification and electricity generation. International Journal of Energy and Environmental Engineering, 3, 1-9.

MOSAFFA, A. H., GAROUSI FARSHI, L., INFANTE FERREIRA, C. A. & ROSEN, M. A. 2014. Advanced exergy analysis of an air conditioning system incorporating thermal energy storage. Energy, 77, 945-952.

MUNDAY, D. & JACOB, J. D. 2002. Active Control of Separation on a Wing with Oscillating Camber. AIAA Journal of Aircraft, 39.

N. ROSTAMZADEH, R. M. K., B.B. DALLY, Z.F. TIAN 2012. An Experimental and Computational Study of Flow over a NACA 0021 Airfoil with Wavy Leading Edge Modification. 18th australian fluid mechanics conference. Australia.

NATERER, G. 2006. Entropy based design of fuel cells. Journal of Fuel Cell Science and Technology 3, 165-174.

NICKERSON, J. D. 1986. A Study of Vortex Generators at Low Reynolds Numbers. AIAA Journal, 1986-0155.

NOMURA, T., SUZUKI, Y., UEMURA, M. & KOBAYASHI, N. 2003. Aerodynamic Forces on a Square Cylinder in Oscillating Flow with Mean Velocity. Journal of Wind Engineering and Industrial Aerodynamics, 91, 199–208.

NUNES, G., VALERIO, D., BEIRãO, P. & Sá DA COSTA, J. 2011. Modelling and control of a wave energy converter. Renewable Energy, 36, 1913-1921.

OKUHARA, S., TAKAO, M., TAKAMI, A. & SETOGUCHI, T. 2013. Wells Turbine for Wave Energy Conversion —Improvement of the Performance by Means of Impulse Turbine for Bi-Directional Flow. Open Journal of Fluid Dynamics, 03, 36-41.

OZGENER, O. 2006. A smallwind turbine system(SWTS) application and its performance analysis. Energy Conversion and Management, 47, 1326-1337.

OZGENER, O. & OZGENER, L. 2007. Exergy and Reliability Analysis of Wind Turbine Systems: A Case Study. Renewable and Sustainable Energy Reviews, 11, 1811-1826.

OZGENER, O., OZGENER, L. & DINCER, I. 2009. Analysis of some exergoeconomic parameters of small wind turbine system. International Journal of Green Energy, 6, 42-56.

ÖZGöKMEN, T. M., ILIESCU, T., FISCHER, P. F., SRINIVASAN, A. & DUAN, J. 2007. Large eddy simulation of stratified mixing in two-dimensional dam-break problem in a rectangular enclosed domain. Ocean Modelling, 16, 106-140.

PADERI, M. & PUDDU, P. 2013. Experimental investigation in a Wells turbine under bi-directional flow. Renewable Energy, 57, 570-576.

PEARCEY, H. H. 1961. Shock Induced Separation and Its Prevention by Design and Boundary Layer Control, England, Pergamon Press, Oxford.

PETRAKOPOULOU, F., TSATSARONIS, G. & MOROSUK, T. 2012a. Advanced exergoenvironmental analysis of a near-zero emission power plant with chemical looping combustion. Environmental Science Technology, 46, 3001–3007.

PETRAKOPOULOU, F., TSATSARONIS, G., MOROSUK, T. & CARASSAI, A. 2012b. Conventional and advanced exergetic analyses applied to a combined cycle power plant. Energy, 41, 146-152.

PIQUET, J. 2013. Turbulent Flows: Models and Physics, Springer Berlin Heidelberg.

POPE, K., DINCER, I. & NATERER, G. F. 2010. Energy and Exergy Efficiency Comparison of Horizontal and Vertical Axis Wind Turbines. Renewable Energy, 35, 2102-2113.

POPE, S. B. 2004. Ten questions concerning the large-eddy simulation of turbulent flows. New journal of Physics, 6, 35.

POZRIKIDIS, C. 2009. Fluid Dynamics - Theory, Computations and numerical Simulation, USA, springer.

PRADO, M. & POLINDER, H. 2013. Direct drive wave energy conversion systems: an introduction. 175-194.

PRANDTL, L. 1904. Über Flüssigkeitsbewegung bei sehr kleiner Reibung (Motion of fluids with very little viscosity). in Verhandlungen des III Internationalen Mathematiker-Kongresses, Heidelberg, (B G Teubner, Leipzig).

PRZEKWAS, A. J., SINGHAL, A. K. & TAM, L. T. 1983. Modeling of two-phase reactive flows in swirl combustion chambers.

RADWAN, A., IBRAHIM, K. A., HANAFY, A. & SAQR, K. M. 2014. On RANS Modeling of Unconfined Swirl Flow. CFD Letters, 6, 159-174.

RAGHUNATHAN, S. 1980. Theory and Performance of Wells Turbine. Queen's University of Belfast, Rept. WE/80/13R.

RAGHUNATHAN, S. 1995a. A methodology for Wells turbine design for wave energy conversion. ARCHIVE: Proceedings of the Institution of Mechanical Engineers, Part A: Journal of Power and Energy 1990-1996 (vols 204-210), 209, 221-232.

RAGHUNATHAN, S. 1995b. The Wells Air Turbine for Wave Energy Conversion. Progress Aerospace Sciences, 31, 335-386.

RAGHUNATHAN, S. & BEATTIE, W. C. 1996. Aerodynamic performance of contra-rotating Wells turbine for wave energy conversion. ARCHIVE: Proceedings of the Institution of Mechanical Engineers, Part A: Journal of Power and Energy 1990-1996 (vols 204-210), 210, 431-447.

RAGHUNATHAN, S., SETOGUCHI, T. AND KANEKO, K. 1991. Aerodynamics of monoplane Wells turbine-A review. Offshore mechanics and Polar Engineering Conference. Edinburgh, U.K.

RAGHUNATHAN, S., TAN, C. & WELLS, N. 1981a. Wind tunnel tests on airfoils in tandem cascade. AIAA Journal, 19, 1490-1492.

RAGHUNATHAN, S., TAN, C. P. & WELLS, N. A. J. 1981b. Wind Tunnel Tests on Airfoils in Tandem Cascade. AIAA Journal, 19, 1490-1492.

RAGHUNATHAN S., CURRAN R. & T., A. W. T. J. 1995. Performance of the Islay Wells air turbine. the Institution of Mechanical Engineers, Part A: Journal of Power and Energy, 209, 55-62.

REDHA, A. M., DINCER, I. & GADALLA, M. 2011. Thermodynamic Performance Assessment of Wind Energy Systems: An Application. Energy, 36, 4002-4010.

RESHOTKO, E. & TUCKER, M. 1957. Approximate calculation of the compressible turbulent boundary layer with heat transfer and arbitrary pressure gradient. NACA TN-4154, Lewis Flight Propulsion Laboratory.

REZAEI, F., ROOHI, E. & PASANDIDEH-FARD, M. 2013. Stall simulation of flow around an airfoil using LES model and comparison of RANS models at low angles of attack. 15th Conference on Fluid Dynamics. The University of Hormozgan, Bandar Abbas, Iran.

RICHEZ, F., MARY, I., GLEIZE, V. & BASDEVANT, C. 2007. Zonal RANS/LES coupling simulation of a transitional and separated flow around an airfoil near stall. Theoretical and Computational Fluid Dynamics, 22, 305-315.

RIDLUAN, A., EIAMSA-ARD, S. & PROMVONGE, P. 2007. Numerical simulation of 3D turbulent isothermal flow in a vortex combustor. International Communications in Heat and Mass Transfer, 34, 860-869.

ROSA, A. V. D. 2012. Fundamentals of Renewable Energy Processes, United States of America, Elsevier Academic Press.

ROSEN, M. 2002. Assessing energy technologies and environmental impacts with the principles of thermodynamics. Applied Energy, 2002, 427-441.

ROSEN, M., DINCER, I. & KANOGLU, M. 2008. Role of exergy in increasing efficiency and sustainability and reducing environmental impact. Energy Policy, 36, 128-137.

RUMSEY, C. L. & NISHINO, T. 2011. Numerical study comparing RANS and LES approaches on a circulation control airfoil. International Journal of Heat and Fluid Flow, 32, 847-864.

S. RAGHUNATHAN, C. P. T., AND N. A. J. WELLS 1987. Theory and Performance of a Wells Turbine. J. Energy, 6, 157-160.

SAEED, F. & SELIG, M. S. 1996. Multipoint inverse airfoil design method for slot-suction airfoils. Journal of Aircraft, 33, 708-715.

SAGAUT, P. 2005. Large Eddy Simulation for Incompressible Flows, Berlin Heidelberg New York, Springer.

SAHIN, A., DINCER, I. & ROSEN, M. 2006a. Development of new spatio-temporal wind exergy maps. Proceedings of ASME2006 Mechanical Engineering Congress and Exposition. November 5-10, Chicago, Illinois, USA.

SAHIN, A., DINCER, I. & ROSEN, M. 2006b. Thermodynamic analysis of wind energy. International Journal of Energy Research, 2006, 553-566.

SALTER, S. 1993. Variable Pitch Air Turbines," Proc Euro Wave Energy Symp, Edinburgh, pp 435-442. Symposium of European Wave Energy. Edinburgh.

SAMPATH, S. & GANESAN, V. k- epsilon MODEL IN TWO-DIMENSIONAL RECIRCULATING FLOWS. In: VEZIROGLU, T. N., ed., 1982 Miami, FL, USA. Univ of Miami, 172-174.

SANKAR, L., ZIBI-BAILLY, J., LE BALLEUR, J., BLAISE, D., ROUZAUD, O. & RHEE, M. 2002. A comparative study of three methodologies for modeling dynamic stall. In: 28th European Rotorcraft Forum, Bristol

SAQR, K. M., ALY, H. S., KASSEM, H. I., SIES, M. M. & WAHID, M. A. 2010. Computations of shear driven vortex flow in a cylindrical cavity using a modified k-ε turbulence model. International Communications in Heat and Mass Transfer, 37, 1072-1077.

SAQR, K. M., KASSEM, H. I., ALY, H. S. & WAHID, M. A. 2012. Computational study of decaying annular vortex flow using the R ε/k-ε turbulence model. Applied Mathematical Modelling, 36, 4652-4664.

SAQR, K. M. & WAHID, M. A. 2014. Effects of Swirl Intensity on Heat Transfer and Entropy Generation in Turbulent Decaying Swirl Flow. Applied Thermal Engineering, 70, 486–493.

SARMENTO AJNA, G. L., AND FALCZO AFDEO 1987. Wave-Energy Absorption by an OWC Device with Blade-Pitch-Controlled Air-Turbine. Proc 6th Int Offshore Mechanics and Arctic Eng Symp, ASME, 2, 465-473.

SAVU, G. & TRIFU, O. 1984. Porous Airfoils in Transonic Flow. AIAA Journal, 22, 989-991.

SB., P. 2000. Turbulent flows. Cambridge University Press.

SCHATZ, M., G¨UNTHER, B. & THIELE, F. 2007. Computational Investigation of Separation Control for High-Lift Airfoil Flows, Berlin, Germany.

SCHMITT, F. G. 2007. About Boussinesq's turbulent viscosity hypothesis: historical remarks and a direct evaluation of its validity. Comptes Rendus Mécanique, 335, 617-627.

SCHOLZ, N. 1978. Aerodynamics of Cascades. AGARD-AG-220. Amsterdam: NATO Science and Technology Organization.

SECCHIAROLI, A., RICCI, R., MONTELPARE, S. & D'ALESSANDRO, V. 2009. Numerical simulation of turbulent flow in a Ranque-Hilsch vortex tube. International Journal of Heat and Mass Transfer, 52, 5496-5511.

SEFOGUCHI, T., KINOUE, Y., MOHAMMAD, M., KANEKO, K. & TAKAO, M. Unsteady flow phenomena of wells turbine in deep stall condition. Proceedings of the International Offshore and Polar Engineering Conference, 2004. 266-271.

SETOGUCHI, T., KINOUE, Y., KIM, T. H., KANEKO, K. & INOUE, M. 2003a. Hysteretic Characteristics of Wells Turbine for Wave Power Conversion. Renewable Energy, 28, 2113-2127.

SETOGUCHI, T., RAGHUNATHAN, S, TAKAO, M, AND KANEKO, K 1997. Air-Turbine with Self-Pitch-Controlled Blades for Wave Energy Conversion (Estimation of Performances in Periodically Oscillating Flow). Int Journal Rotating Machinery, 3, 233-238.

SETOGUCHI, T., SANTHAKUMAR, S., TAKAO, M., KIM, T. H. & KANEKO, K. 2001. Effect of Guide Vane Shape on the Performance of a Wells Turbine. Renewable Energy, 23, 1-15.

SETOGUCHI, T., SANTHAKUMAR, S., TAKAO, M., KIM, T. H. & KANEKO, K. 2003b. A modified Wells turbine for wave energy conversion. Renewable Energy, 28, 79-91.

SETOGUCHI, T. & TAKAO, M. 2006. Current status of self rectifying air turbines for wave energy conversion. Energy Conversion and Management, 47, 2382-2396.

SETOGUCHI, T., TAKAO, M., ITAKURA, K., MOHAMMAD, M., KANEKO, K. & THAKKER, A. 2003c. Effect of Rotor Geometry on the Performance of Wells Turbine. The Thirteenth International Offshore and Polar Engineering Conference. Honolulu, Hawaii, USA: The International Society of Offshore and Polar Engineers.

SETOGUCHI T, T. M., KANEKO K. 1998. Hysteresis on Wells Turbine Characteristics in Reciprocating Flow. International Journal of Rotating Machinery, 4, 17-24.

SETOGUCHI T, T. M., KINOUE Y, KANEKO K, SANTHAKUMAR S, INOUE M. 2000. Study on an impulse turbine for wave energy conversion. International Journal Offshore Polar Eng., 10, 145-52.

SHAABAN, S. 2012. Insight Analysis of Biplane Wells Turbine Performance. Energy Conversion and Management, 59, 50-57.

SHAABAN, S. & ABDEL HAFIZ, A. 2012. Effect of duct geometry on Wells turbine performance. Energy Conversion and Management, 61, 51-58.

SHARMA, D. M. & PODDAR, K. Investigation of dynamic stall characteristics for flow past an oscillating airfoil at various reduced frequencies by simultaneous PIV and surface pressure measurements. PIV13; 10th International Symposium on Particle Image Velocimetry, Delft, The Netherlands, July 1-3, 2013, 2013. Delft University of Technology.

SHEHATA, A. S., SAQR, K. M., SHEHADEH, M., XIAO, Q. & DAY, A. H. 2014. Entropy Generation Due to Viscous Dissipation around a Wells Turbine Blade: A Preliminary Numerical Study. Energy Procedia, 50, 808-816.

SHEHATA, A. S., SAQR, K. M., XIAO, Q., SHEHADEH, M. F. & DAY, A. 2016. Performance Analysis of Wells Turbine Blades Using the Entropy Generation Minimization Method. Renewable Energy1133-1123 ،86 ،.

SHEHATA, A. S., XIAO, Q., SAQR, K. M. & ALEXANDER, D. 2017. Wells turbine for wave energy conversion: a review. International journal of energy research, 41, 6-38.

SHELDAHL, R. E. & KLIMAS, P. C. 1981. Aerodynamic Characteristics of Seven Symmetrical Airfoil Sections Through 180-Degree Angle of Attack for Use in

Aerodynamic Analysis of Vertical Axis Wind Turbines. Sandia National Laboratories energy report. the United States of America.

SHERMAN, E. N. J. A. A. 1937. Airfoil section characteristics as affected by variation of the Reynolds number. NACA Rep., No. 586.

SHIDA, Y., KUWAHARA, K, ONO, K. AND TAKAMI, H. 1987. Computation of Dynamic Stall of a NACA-0012 Airfoil. AIAA Journal, 25, 408-413.

SHIH, T.-H., LIOU, W. W., SHABBIR, A., YANG, Z. & ZHU, J. 1995. A new k-ϵ eddy viscosity model for high reynolds number turbulent flows. Computers & Fluids, 24, 227-238.

SKYLLINGSTAD, E. D. & WIJESEKERA, H. W. 2004. Large-Eddy Simulation of Flow over Two-Dimensional Obstacles: High Drag States and Mixing. Journal of physical oceanography, 34, 94-112.

SMAGORINSKY, J. 1963. General Circulation Experiments with the Primitive Equations. I. The Basic Experiment. Month. Wea. Rev., 91, pp.99-164.

SMITH, B. L. & GLEZER, A. 1997. Vectoring and Small-Scale Motions Effected in Free Shear Flows Using Synthetic Jet Actuators. In: AIAA-97-0213 (ed.) 35th Aerospace Sciences Meeting and Exhibit. Reno, NV.

SMITH, B. L. & GLEZER, A. 1998. The Formation and Evolution of Synthetic Jets. Physics of Fluids, 10, 2281- 2297.

SOLTANMOHAMADI, R. & LAKZIAN, E. 2015. Improved design of Wells turbine for wave energy conversion using entropy generation. Meccanica, Springer Netherlands., 51, 1713-1722.

SPEZIALE, C. G., ABID, R. & ANDERSON, E. C. 1992. Critical evaluation of two-equation models for near-wall turbulence. AIAA Journal, 30, 324-331.

STACK, J. 1944. Tests of airfoils designed to delay the compressibility burble. NACA TN-976, Langley Memorial Aeronautical Laboratory, Langley Field, VA.

STARZMANN, R. 2012. Aero-acoustic Analysis of Wells Turbines for Ocean Wave Energy Conversion. Doctoral Universitat Siegen.

STARZMANN, R. & CAROLUS, T. 2013a. Effect of Blade Skew Strategies on the Operating Range and Aeroacoustic Performance of the Wells Turbine. Journal of Turbomachinery, 136, 011003.

STARZMANN, R. & CAROLUS, T. 2013b. Model-Based Selection of Full-Scale Wells Turbines for Ocean Wave Energy Conversion and Prediction of their Aerodynamic and Acoustic Performances. Proceedings of the Institution of Mechanical Engineers, Part A: Journal of Power and Energy, 228, 2-16.

STRATFORD, B. S. 1959. The Prediction of Separation of the Turbulent Boundary Layer. Journal of Fluid Mechanics, 5, 1-16.

SUNADA, S., SAKAGUCHI, A. & KAWACHI, K. 1997. Airfoil section characteristics at a low Reynolds number. Journal of fluids engineering, Transactions of the ASME, 119, 129-135.

SUZUKI M, A. C., AND TAKAHASHI S 2004. Performance of wave power generating system installed in breakwater at Sakata port in Japan. the 14th International Offshore Polar Engineering Conference, Mountain View, CA, USA. Toulon, France: In: Chung JS.

SZYDLOWSKI, J. & COSTES, M. 2004. Simulation of Flow Around a Static and Oscillating in Pitch NACA 0015 Airfoil Using URANS and DES. ASME 2004 Heat Transfer/Fluids Engineering Summer Conference, Volume 2, Parts A and B, 891-908.

T. J. T. WHITTAKER, F. A. M. 1985a. Design Optimisation of Axisymmetric Tail Tube Buoys. IUTAM, Symposium on Hydrodynamics of Ocean Wave Energy Conversion. Lisbon,July.

T. J. T. WHITTAKER, J. G. L., A. E. LONG AND M. A. MURRAY 1985b. The Queen's university of Belfast Axisymmetric and Multi-resonant Wave Energy Converters. Trans. ASME. J. Energy Resources Tech., 107, pp. 74-80.

T. SETOGUCHI, M. T., S. SANTHAKUMAR AND K. KANEKO 2004. Study of an Impulse Turbine for Wave Power Conversion: Effects of Reynolds Number and Hub-to-Tip Ratio on Performance. Journal of Offshore Mechanics and Arctic Engineering, 126, 137-140.

T. SETOGUCHI, S. S., H. MAEDA, M. TAKAO AND K. KANEKO 2001. A Review of Impulse Turbine for Wave Energy Conversion. Renewable Energy, 23, 261-292.

TAE-HUN KIM, YEON- WON LEE, ILL-KYOO PARK, TOSHIAKI SETOGUCHI & KANG, C.-S. 2002. Numerical Analysis for Unsteady Flow Characteristics of the Wells Turbine. International Offshore and Polar Engineering Conference. Kitakyushu, Japan: The International Society of Offshore and Polar Engineers.

TAGORI, R., ARAKAWA, C. AND SUZUKI, M. 1987. Estimation of prototype performance and optimum design of Wells turbine. proceedings of Research in Natural Energy, SPEY 20 (The Ministry of Education, Science and Culture, Japan).

TAHA, Z., SUGIYONO & SAWADA, T. 2010. A comparison of computational and experimental results of Wells turbine performance for wave energy conversion. Applied Ocean Research, 32, 83-90.

TAHA, Z., SUGIYONO, TUAN YA, T. M. Y. S. & SAWADA, T. 2011. Numerical investigation on the performance of Wells turbine with non-uniform tip clearance for wave energy conversion. Applied Ocean Research, 33, 321-331.

TAKAO, M. & SETOGUCHI, T. 2012. Air turbines for wave energy conversion. International Journal of Rotating Machinery, 2012.

TAKAO, M., SETOGUCHI, T., KIM, T. H., KANEKO, K. & INOUE, M. 2001. The Performance of a Wells Turbine with 3D Guide Vanes. International Journal of Offshore and Polar Engineering, 11, 72-76.

TAKAO, M., SETOGUCHI, T., KINOUE, Y. & KANEKO, K. 2007. Wells Turbine with End Plates for Wave Energy Conversion. Ocean Engineering, 34, 1790-1795.

TAKAO, M., SETOGUCHI, T, KANEKO, K, AND INOUE, M 1997a. Air Turbine with Self-Pitch-Controlled Blades for Wave Energy Conversion. Int Journal Ofihore and Polar Eng, ISOPE, 7, 308-312.

TAKAO, M., SETOGUCHI, T, SANTHAKNMAR, S, AND KANEKO, K 1997b. A Comparative Study of Turbines Using Pitch-Controlled Blades for Wave Energy Conversion. Proc 2nd Int Symp Fluid Mechanics and Heat Transfer. Dhaka.

TAKAO, M., THAKKER, A., ABDULHADI, R. & SETOGUCHI, T. 2006. Effect of Blade Profile on the Performance of a Large-scale Wells Turbine for Wave-energy Conversion. International Journal of Sustainable Energy, 25, 53-61.

TAN, M. & KECEBAŞ, A. 2014. Thermodynamic and economic evaluations of a geothermal district heating system using advanced exergy-based methods. Energy Conversion and Management, 77, 504-513.

TAYLOR, H. D. 1948. Application of Vortex Generator Mixing Principles to Diffusers. Research Department Concluding Report No. R-15064-5, United Aircraft Corporation, East Hartford.

TAYLOR, J. R. M. & CALDWELL, N. J. 1998 Design and Construction of the variable-pitch air-turbine for the Azores wave energy plant. Third European Wave Power Conference. Patras, Greece

TEILLANT, M. V., G.P. ROSATI PAPINI, G. MORETTI, R. VERTECHY, M. FONTANA, K. MONKAND, M. ALVES. 2015. Techno-economic comparison between air turbines and dielectric elastomer generators as power take off for oscillating water column wave energy converters. 11th European Wave & Tidal Energy Conference. Nantes, France.

THAKKER, A. & ABDULHADI, R. 2007. Effect of Blade Profile on the Performance of Wells Turbine under Unidirectional Sinusoidal and Real Sea Flow Conditions. International Journal of Rotating Machinery, 2007, 1-9.

THAKKER, A. & ABDULHADI, R. 2008. The Performance of Wells Turbine Under Bi-Directional Airflow. Renewable Energy, 33, 2467-2474.

THAKKER, A., FRAWLEY, P. & BAJEET, E. S. 2001. Numerical Analysis of Wells Turbine Performance Using a 3D Navier Stokes Explicit Solver. International Offshore and Polar Engineerbtg Conference. Stavanger, Norway.

THAKKER, A., FRAWLEY, P., BAJEET, E. S. & HEFFERNAN, A. 2000a. Experimental Investigation of CA9 Blades on a 0.3m Wells Turbine Rig. the Tenth (2000) International Offshore and Polar Engineering Conference. Seattle, USA: International Society of Offshore and Polar Engineers.

THAKKER, A., FRAWLEY, P., DALY, J. & ABUGHAILIA, Y. 2000b. A 2D CFD study of symmetrical airfoils. PART II: in cascade flow, Cupertino, CA, ETATS-UNIS, International Society of Offshore and Polar Engineers.

THAKKER T, F. P., BAJEET ES. 2001. CA9: analysis of a stall-resistant aerofoil in view of wave power conversion. Proceedings of the 11th International Offshore and Polar Engineering Conference. Stavanger, Norway.

THORPE, T. W. 1995. An Assessment of The Art OSPREY Wave Energy Device, ETSU-R-90, Dti.

THWAITES, B. 1949. Approximate Calculation of the Laminar Boundary Layer. Aeronautical Quarterly, 1, 245-280.

TORRE-ENCISO, Y., ORTUBIA, I., AGUILETA, L. I. L. D. & MARQUES, J. 2009. Mutriku Wave Power Plant: from the thinking out to the reality. Proceedings of The 8th European Wave and Tidal Energy Conference. Uppsala, Sweden.

TORRESI, M., CAMPOREALE, S. & PASCAZIO, G. 2007a. Experimental and Numerical Investigation on the Performance of a Wells Turbine Prototype. Seventh European Wave and Tidal Energy Conference. Porto, Portugal

TORRESI, M., CAMPOREALE, S. & PASCAZIO, G. 2007b. Performance of a Small Prototype of a High Solidity Wells Turbine. Seventh European Conference on Turbomachinery Fluid Dynamics and Thermodynamics. Athens, Greece

TORRESI, M., CAMPOREALE, S. M. & PASCAZIO, G. 2009. Detailed CFD Analysis of the Steady Flow in a Wells Turbine Under Incipient and Deep Stall Conditions. Journal of Fluids Engineering, 131, 071103.

TORRESI, M., CAMPOREALE, S. M., PASCAZIO, G. & FORTUNATO, B. 2004. Fluid Dynamic Analysis of a Low Solidity Wells Turbine. Atti del 59° Congresso Annuale ATI. Genova, Italy.

TORRESI, M., CAMPOREALE, S. M., STRIPPOLI, P. D. & PASCAZIO, G. 2008. Accurate numerical simulation of a high solidity Wells turbine. Renewable Energy, 33, 735-747.

TORRESI, M., D. PRANZO, S.M. CAMPOREALE & PASCAZIO, G. 2011. Improved Design of High Solidity Wells Turbine. the Ninth European Wave and Tidal Energy Conference (EWTEC2011). Southampton, UK.

TSATSARONIS, G. & MOROSUK, T. 2010. Advanced exergetic analysis of a novel system for generating electricity and vaporizing liquefied natural gas. Energy, 35, 820-829.

TSATSARONIS, G., MOROSUK, T., KOCH, D. & SORGENFREI, M. 2013. Understanding the thermodynamic inefficiencies in combustion processes. Energy, 62, 3-11.

TSATSARONIS G. & T., M. 2010. Advanced exergetic analysis of a refrigeration system for liquefaction of natural gas. International Journal of Energy and Environmental Engineering, 1, 1-17.

TSINOBER, A. 2009. An Informal Conceptual Introduction to Turbulence, Netherlands, Springer.

TV, H. 2007. The development of a turbo-generation system for application in OWC breakwaters. In: AFO, F. (ed.) Proceedings of the 7th European Wave Tidal Energy Conference. Porto, Portugal.

TWIDELL, J. & WEIR, T. 2006. Renewable Energy Resources, New York, USA, Taylor & Francis.

UCHE, J. 2006. Exergy costs and inefficiency diagnosis of a dual-purpose power and desalination plant. Journal of Energy Resources Technology, 128, 186-192.

VAKALIS IS, S. A. 2000. Real-time control of OWC with a variable pitch-angle turbine. Proceedings of the Fourth European Wave Energy Conference. Denmark.

VOLINO, R. J., KARTUZOVA, O. & IBRAHIM, M. B. 2011. Separation Control on a Very High Lift Low Pressure Turbine Airfoil Using Pulsed Vortex Generator Jets. Journal of Turbomachinery, 133, 041021.

VOSOUGH, A. & SADEGH, V. 2011. Different Kind of Renewable Energy and Exergy Concept. INTERNATIONAL JOURNAL OF MULTIDISCIPLINARY SCIENCES AND ENGINEERING, 2.

VS, R., M, R. & PM, K. 1993. Experiences on a 150 kW wave energy pilot plant. In: G, E. G. A. C. (ed.) European Wave Energy Symposium, East Kilbride, Scotland. Edinburgh, UK.

VUČKOVIĆ, G. D., STOJILJKOVIĆ, M. M., VUKIĆ, M. V., STEFANOVIĆ, G. M. & DEDEIĆ, E. M. 2014. Advanced exergy analysis and exergoeconomic performance evaluation of thermal processes in an existing industrial plant. Energy Conversion and Management, 85, 655-662.

WATTERSON, J. K., GILLAN, M. A., RAGHUNATHAN, S. & MITCHELL, R. D. 1997. APPLICATIONS OF COMPUTATIONAL FLUID DYNAMICS TO A WAVE ENERGY CONVERSION DEVICE. INTERSOCIETY ENERGY CONVERSION ENGINEERING CONFERENCE(IECEC 97). Honolulu, HI: IEEE.

WATTERSON, J. K. & RAGHUNATHAN, S. 1996. INVESTIGATION OF WELLS TURBINE PERFORMANCE USING 3-D CFD. INTERSOCIETY ENERGY

CONVERSION ENGINEERING CONFERENCE(IECEC 96). Washington, DC: IEEE.

WAVEGEN 2002. Research into the further development of the LIMPET shoreline wave energy plant, Dti, V/06/00183/00/Rep.

WEBB, I., SEAMAN, C. & JACKSON, G. 2005. Marine Energy Challenge Oscillating Water Column Wave Energy Converter Evaluation Report.

WEINIG, F. S. 1964. Theory of two-dimensional flow through cascades. In: HAWTHORNE, W. R. (ed.) Aerodynamics of Turbines and Compressors, Oxford University Press, London

WHITTAKER, T. J. J., MCILWAIN, S. T. AND RAGHUNATHAN, S. 1993a. Islay Shore Line Wave Power Station. Proceedings European Wave Energy Symposium., Paper G6, Edinburgh.

WHITTAKER, T. J. T., STEWART, T. P. & CURRAN, R. 1997. Design synthesis of oscillating water column wave energy converters: performance matching. Proceedings of the Institution of Mechanical Engineers, Part A: Journal of Power and Energy, 211, 489-505.

WHITTAKER, T. J. T. M., S.J. & RAGHUNATHAN, S 1993b. A review of the Islay shoreline wave power station. Proceedings of European Wave Energy Symposium. Edinburgh, Scotland.

WILCOX, D. C. 1988. Reassessment of the scale-determining equation for advanced turbulence models. AIAA Journal, 26, 1299-1310.

WILCOX, D. C. 1993. Comparison of two-equation turbulence models for boundary layers with pressure gradient. AIAA Journal, 31, 1414-1421.

WILCOX, D. C. 1994. Turbulence Modeling for CFD, Glendale, California, USA, Griffin Printing.

WILCOX, D. C. 1998. Turbulence Modeling for CFD, DCW Industries.

WILCOX, D. C. 2006a. Turbulence Modeling for CFD, DCW Industries.

WILCOX, D. C. 2006b. Turbulence Modeling for Computational Fluid Dynamics, DCW Industries, Incorporated.

WILDER, M. C., CHANDRASEKHARA, M. S. & CARR, L. W. 1993. Transition effects on compressible dynamic stall of transiently pitching airfoils. 23rd Fluid Dynamics, Plasmadynamics, and Lasers Conference, Orlando,FL,U.S.A.

WOLFE, W. P. & OCHS, S. S. 1997. Predicting Aerodynamic Characteristics of Typical Wind Turbine Airfoils Using CFD. SANDIA REPORT. the United States of America.

WONG, C. & KONSTANTINOS, K. 2006. Flow control by spanwise blowing on a NACA 0012. 24th AIAA Applied Aerodynamics Conference. San Francisco, CA.

WRIGHT, M. C. M. & NELSON, P. A. 2001. Wind tunnel experiments on the optimization of distributed suction for laminar flow control. Proceedings of the Institution of Mechanical Engineers, Part G: Journal of Aerospace Engineering, 215, 343-354.

XYDIS, G., KORONEOS, C. & LOIZIDOU, M. 2009. Exergy analysis in a wind speed prognostic model as a wind farm sitting selection tool: a case study in Southern Greece. Applied Energy 86, 2411-2420.

Y. WASHIO, H. OSAWA, Y. NAGATA, F. F. & H. FURUYAMA, T. F. 2000. The offshore floating type wave power device 'Mighty Whale': Open sea tests. In: JS, C. (ed.) proceedings of the 10th International Offshore Polar Engineering Conference, Mountain View, CA, USA. Seattle, WA, USA.

YAKHOT, V., ORSZAG, S., THANGAM, S., GATSKI, T. & SPEZIALE, C. 1992. Development of turbulence models for shear flows by a double expansion technique. Physics of Fluids A: Fluid Dynamics (1989-1993), 4, 1510-1520.

YOUSEFI, K., SALEH, R. & ZAHEDI, P. 2014. Numerical study of blowing and suction slot geometry optimization on NACA 0012 airfoil. Journal of Mechanical Science and Technology, 28, 1297-1310.

ZHANG, J. & NIEH, S. 1997. Simulation of gaseous combustion and heat transfer in a vortex combustor. Numerical Heat Transfer; Part A: Applications, 32, 697-713.

ZODIATIS, G., GALANIS, G., NIKOLAIDIS, A., KALOGERI, C., HAYES, D., GEORGIOU, G. C., CHU, P. C. & KALLOS, G. 2014. Wave energy potential in the Eastern Mediterranean Levantine Basin. An integrated 10-year study. Renewable Energy, 69, 311-323.

ZOROVIĆ, D., MOHOVIĆ, R. & MOHOVIĆ, Đ. 2003. Toward Determining the Length of the Wind Waves of the Adriatic Sea. Naše more, 50, 3-4.